QUANTITATIVE METHODS TO ASSESS CEREBRAL HAEMODYNAMICS

Emma L. Hall, M.Sci.

Thesis Submitted to the University of Nottingham

for the Degree of Doctor of Philosophy

July 2012

ABSTRACT

In this thesis methods for the assessment of cerebral haemodynamics using 7 T Magnetic Resonance Imaging (MRI) are described. The measurement of haemodynamic parameters, such as cerebral blood flow (CBF), is an important clinical tool.

Arterial Spin Labelling (ASL) is a non-invasive technique for CBF measurement using MRI. ASL methodology for ultra high field (7 T) MRI was developed, including investigation of the optimal readout strategy. Look-Locker 3D-EPI is demonstrated to give large volume coverage improving on previous studies. Applications of methods developed to monitor functional activity, through flow or arterial blood volume, in healthy volunteers and in patients with low grade gliomas using Look-Locker ASL are described.

The effect of an increased level of carbon dioxide in the blood (hypercapnia) was studied using ASL and functional MRI; hypercapnia is a potent vasodilator and has a large impact on haemodynamics. These measures were used to estimate the increase in oxygen metabolism associated with a simple motor task. To study the physiology behind the hypercapnic response, magnetoencephalography was used to measure the impact of hypercapnia on neuronal activity. It was shown that hypercapnia induces widespread desynchronisation in a wide frequency range, up to $\sim$ 50 Hz, with peaks in the sensory-motor areas. This suggests that hypercapnia is not iso-metabolic, which is an assumption of calibrated BOLD.

A Look-Locker gradient echo sequence is described for the quantitative monitoring of a gadolinium contrast agent uptake through the change in longitudinal relaxation rate. This sequence was used to measure cerebral blood volume in Multiple Sclerosis patients. Further development of the sequence yielded a high resolution anatomical scan with reduced artefacts due to field inhomogeneities associated with ultra high field imaging. This allows whole head images acquired at sub-millimetre resolution in a short scan time, for application in patient studies.

ACKNOWLEDGMENTS

Firstly I would like to thank my supervisors Dr Sue Francis and Professor Penny Gowland for their time, effort and knowledge over the last 3.5 years. Additional thanks goes to Dr Andrew Peters, who has helped with nearly all the MR experiments in this thesis.

Special thanks go to members of "*Team Perfusion*" past and present, especially Ian Driver and Paula Croal. For helping out with experiments, many a RespirAct based conversation and making scanning days a bit more fun!

I would like to thank Ali Al-Radaideh, Anna Blazejewska and Olivier Mougin for their work scanning all the MS volunteers – and to the volunteers themselves for giving up their time.

The SPMMRC Tea Room gang, past and present, for providing plenty of entertainment. Special mentions go to Jim, our long serving original QM, Lesley, Eleanor, Mary, Paula, Becky, Liz, Sue P., Paul and many others who have had the honour of appearing on the board. Thank you to students and staff of the SPMMRC for making studying very enjoyable, and for all the people who volunteered for my studies.

Peter and Lindsey, who have been happy to share the PhD journey with me and other friends who are probably bored of hearing "once I've finished my thesis" (sorry Alan!)

Finally, I must thank Matt and my family; Mum, Dad, Andrew and Steven. Matt, for ensuring I didn't panic through all points of my PhD. My parents for being supportive throughout my education (all 22 years of it!), my brothers for providing ample "constructive criticism" to spur me on! Unfortunately Grandad didn't quite get to see the finished article, but knew I was doing something clever (hopefully this counts!).

TABLE OF CONTENTS

GLOSSARY

AFI: Actual Flip-angle Imaging
ASL: Arterial Spin Labelling

BBB: Blood Brain Barrier
bFFE: Balanced Fast Field Echo (balanced, gradient echo)
BOLD: Blood Oxygenation Level Dependant
BS: Background Suppression

CASL: Continuous Arterial Spin Labelling
CBF: Cerebral Blood Flow
CBV: Cerebral Blood Volume
$CMRO_2$: Cerebral metabolic rate of oxygen consumption
CNR: Contrast-to-Noise Ratio
CVR: Cerebral Vascular Reactivity

DAM: Dual Angle Method (B_1 mapping)

EEG: Electroencephalography
EPI: Echo Planar Imaging

FA: Flip Angle
FAIR: Flow-sensitive Alternating Inversion Recovery
$FiCO_2$: Inspired concentration of carbon dioxide
FID: Free Induction Decay
FiO_2: Inspired concentration of oxygen
fMRI: Functional Magnetic Resonance Imaging
FOCI: Frequency Offset Corrected Inversion
FOV: Field of View

GE: Gradient Echo
GM: Grey Matter
GRASE: GRadient And Spin Echo

HRF: Haemodynamic Response Function
HSC: Hyperbolic secant
Hypercapnia: Increased concentration of CO_2 in the blood
Hyperoxia: Increased concentration of O_2 in the blood
Hypocapnia: Reduce concentration of CO_2 in the blood
Hypoxia: Reduce concentration of O_2 in the blood

IR: Inversion Recovery

LL: Look-Locker

MEG: Magnetoencephalography
MPRAGE: Magnetisation Prepared Rapid Gradient Echo
MRI: Magnetic Resonance Imaging
MRS: Magnetic Resonance Spectroscopy
MS: Multiple Sclerosis

NMR: Nuclear Magnetic Resonance
Normocapnia: Normal levels of CO_2 in the blood

OEF: Oxygen Extraction Fraction

PASL: Pulsed Arterial Spin Labelling
PCASL: Pseudo Continuous Arterial Spin Labelling
$P_{ET}CO_2$: End tidal partial pressure of carbon dioxide
$P_{ET}O_2$: End tidal partial pressure of oxygen
PSIR: Phase Sensitive Inversion Recovery
PW: Perfusion Weighted

R_1: Longitudinal relaxation rate
R_2: Transverse relaxation rate
RF: Radio Frequency

SE: Spin Echo
SENSE: SENSitivity Encoding
SNR: Signal-to-Noise Ratio
SQUID: Superconducting quantum interference device
SSI: Shot-to-Shot Interval

T_1: Longitudinal relaxation time
T_2: Transverse relaxation time
TE: Echo time
TFE: Turbo Field Echo, gradient echo
TI: Post label delay
TR: Sequence repetition time
TrueFISP: Fast Imaging with Steady Precession (balanced gradient echo)
tSNR: Temporal Signal-to-Noise Ratio
TurboFLASH: Fast Low Angle SHot (gradient echo sequence)

UHF: Ultra-High Field (≥ 7.0 T)

WM: White Matter

1 INTRODUCTION

1.1 OUTLINE

The initial developments of magnetic resonance imaging (MRI) were made in the early 1970's. In 1973 Paul Lauterbur at Stony Brook, New York introduced the use of magnetic field gradients to spatially encode signals from a sample [1]. 1974 saw the development of slice selection by Peter Mansfield at the University of Nottingham [2]. These developments allowed the non-invasive imaging of the human body using magnetic fields and both Lauterbur and Mansfield were recognised by the Nobel committee in 2003 for their work.

MRI developed rapidly from this point, by 1996 there were over 10,000 MRI scanners worldwide [3] and 10 years later an estimated 20,000 [4]. The first human images were acquired at field strengths of much less than 1 T; the first commercial cryogen cooled 1.5 T systems were available in 1985, with clinical 3 T systems only becoming available in the late 1990's [4]. The field strength of MRI scanners used for research has increased at a much faster rate; in 1998 Ohio State University installed an 8 T system. The University of Nottingham 7 T scanner was installed in late 2004. This, along with those at Ohio State University and Vanderbilt University were the first 7 T Philips Achieva systems. In 2007, the University of Illinois, Chicago, installed a 9.4 T human scanner and NeuroSpin (CEA, Saclay, France) are currently developing an 11.7 T human system.

The advent of high (3 T) and ultra-high field (≥ 7 T) has provided increased signal, which allows for increased spatial resolution (see Figure 1-1), allowing the human body to be studied in greater detail, with no need for invasive procedures. Human imaging at 7 T began with the development of brain imaging [5], with the first demonstration of functional brain imaging in 2001 [6]. Demonstrations of perfusion [7, 8] and diffusion [9] imaging in the brain followed a few years later. Initial experiments have also been conducted to measure characteristic properties (T_1, T_2, T_2*) of the brain that determine image contrast (e.g. [10-13]). These developments have led to comparisons between field strengths and the possible benefit of 7 T for clinical neuroimaging (e.g. [14]).

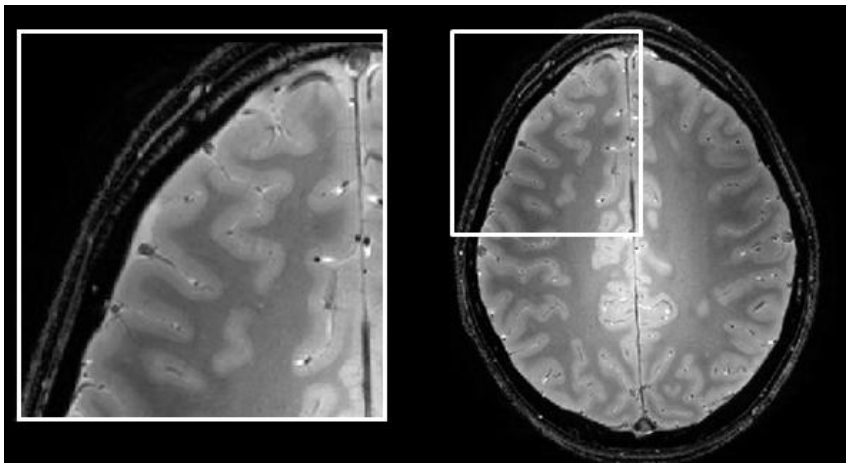

Figure 1-1: T_2* weighted gradient echo images acquired at 7 T with 0.4 x 0.4 x 1.5 mm^3 spatial resolution. Box highlights expanded section shown on the left.

Though the initial developments at ultra high field were for brain imaging, largely due to the availability of RF hardware, imaging of other regions of the body has been demonstrated (Figure 1-2) through the development of local transmit/receive coils. In 2007 Regatte *et al.* [15] demonstrated imaging of the musculo-skeletal system, including knee, leg and ankle in sub-millimetre resolution. Shortly after, this was followed by abdominal imaging by Vaughan *et al*. [16], and subsequently the hand [17] and heart [18] in 2009. Recently in 2011, a demonstration of high resolution kidney imaging has been shown [19].

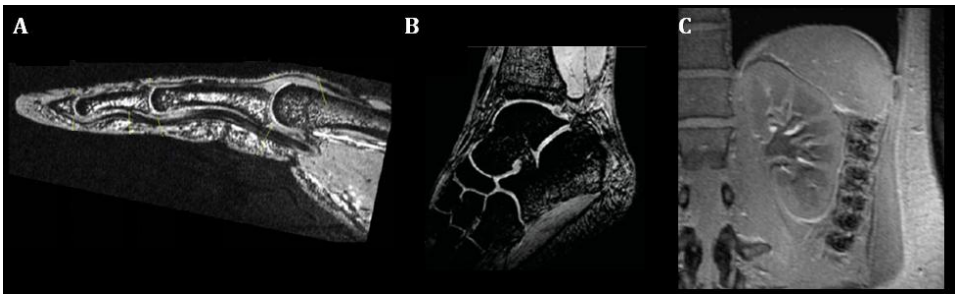

Figure 1-2: Images from non-brain studies at 7 T (A) Finger from [17] using a 3D-gradient echo with 270 x 270 x 300 μm^3 voxels (B) 3D-FLASH images of the ankle acquired at 254 x 254 x 1000 μm^3 from [15] (C) 3D-FLASH image of the kidney, resolution of 1.3 x 1.3 x 1.6 mm^3 from [19]. Images reproduced with kind permission from John Wiley & Sons and Springer Science and Business Media.

After 10 years of 7 T human imaging, techniques still need to be adapted and tailored to take full advantage of ultra-high field strength. There are still developments to be made to ensure the full benefits can be gained by optimising methodology used at clinical field strengths, as well as new specific 7 T techniques.

1.2 SCOPE OF THESIS

This thesis describes the development of methods for the assessment of cerebral haemodynamics using ultra-high field magnetic resonance imaging. Chapters Two – Four describe the theory behind the experimental work presented in Chapters Five – Seven.

Chapters Two and Three detail the theory behind nuclear magnetic resonance (NMR) and MRI. Describing how the behaviour of nuclei in magnetic fields can be exploited to image a sample. The imaging sequences used in the subsequent experimental chapters are introduced. The hardware of the MRI system used for the work in this thesis is also introduced. Also discussed are the safety and ethical considerations required for the use of human subjects in MRI studies.

Chapter Four describes the human brain, the vascular structure and how neuronal activity impacts on the vascular system. The multi-modal methods that are used to gain insight into brain function are introduced. Including the blood oxygenation level dependant (BOLD) contrast mechanism and arterial spin labelling (ASL); a method of measuring blood flow detailed in Chapters 5 and 6.

Chapter Five describes developments of techniques for the measurement of brain perfusion using arterial spin labelling at ultra high field (7 T). The experiments assess image readout type and Look-Locker [20] methods and their applications. The advantages and disadvantages of ultra high field imaging and the impact upon ASL are discussed.

In Chapter Six the effect of inspired carbon dioxide, hypercapnia, on brain function is described. Measurements are made using ASL and BOLD at 7 T to investigate metabolic changes during a motor task. Magnetoencephalography (MEG) is used to assess the impact of hypercapnia on neuronal activity.

Chapter Seven outlines methodology for tracking contrast agent uptake in the brain using longitudinal relaxation time (T_1) changes. This applies Look-Locker methods [20] for fast acquisition times at ultra-high field. Simulations are performed to optimise the MRI sequence parameters. The sequence is used to monitor contrast uptake in Multiple Sclerosis patients, to look for breakdown in the blood-brain barrier and measure cerebral blood volume (CBV). Optimisation of high spatial resolution anatomical imaging for ultra high field imaging is also discussed.

The final chapter concludes the experimental work presented in this thesis and looks to future work that could build on these findings.

1.3 REFERENCES

1. Lauterbur, P., *Image Formation by Induced Local Interactions: Examples Employing Nuclear Magnetic Resonance.* Nature, 1973. **242**: p. 190-191.
2. Garroway, A.N., P.K. Grannell, and P. Mansfield, *Image Formation in NMR by a Selective Irradiative Process.* J. Phys. C: Solid State Phys., 1974. **7**: p. 457-462.
3. McRobbie, D.W., E.A. Moore, M.J. Graves, and M.R. Prince, *MRI: From Picture to Proton*. 2010, Cambridge: Cambridge University Press.
4. Blamire, A.M., *The technology of MRI - the next 10 years?* The British Journal of Radiology, 2008. **81**: p. 601-617.
5. Vaughan, J.T., M. Garwood, C.M. Collins, W. Liu, L. DelaBarre, G. Adriany, P. Andersen, H. Merkle, R. Goebel, M.B. Smith, and K. Ugurbil, *7T vs. 4T: RF power, homogeneity, and signal-to-noise comparison in head images.* Magnetic Resonance in Medicine, 2001. **46**(1): p. 24-30.
6. Yacoub, E., A. Shmuel, J. Pfeuffer, P.-F. Van De Moortele, G. Adriany, P. Andersen, J.T. Vaughan, H. Merkle, K. Ugurbil, and X. Hu, *Imaging brain function in humans at 7 Tesla.* Magnetic Resonance in Medicine, 2001. **45**(4): p. 588-594.
7. Pfeuffer, J., G. Adriany, A. Shmuel, E. Yacoub, P.-F. Van De Moortele, X. Hu, and K. Ugurbil, *Perfusion-based high-resolution functional imaging in the human brain at 7 Tesla.* Magnetic Resonance in Medicine, 2002. **47**(5): p. 903-911.
8. Gardener, A.G., P.A. Gowland, and S.T. Francis, *Implementation of Quantitative Perfusion Imaging Using Pulsed Arterial Spin Labeling at Ultra-High Field.* Mag. Res. Med., 2009. **61**: p. 874-882.
9. Heidemann, R.M., D.A. Porter, A. Anwander, T. Feiweier, K. Heberlein, T.R. Knösche, and R. Turner, *Diffusion imaging in humans at 7T using readout-segmented EPI and GRAPPA.* Magnetic Resonance in Medicine. **64**(1): p. 9-14.
10. Rooney, W.D., G. Johnson, X. Li, E.R. Cohen, S.-G. Kim, K. Ugurbil, and C.S. Springer, *Magnetic Field and Tissue Dependancies of Human Brain Longitudinal ^1H_2O Relaxation in Vivo.* Mag. Res. Med., 2007. **57**: p. 308-318.
11. Wright, P.J., O.E. Mougin, J.J. Totman, A.M. Peters, M.J. Brookes, R. Coxon, P.G. Morris, M. Clemence, S.T. Francis, R. Bowtell, and P.A. Gowland, *Water Proton T1 Measurements in Brain Tissue at 7, 3 and 1.5T using IR-EPI, IR-TSE and MPRAGE: results and optimisation.* Magn. Reson. Mater. Phy, 2008. **21**: p. 121-130.
12. Peters, A.M., M.J. Brookes, F.G. Hoogenraad, P.A. Gowland, S.T. Francis, P.G. Morris, and R. Bowtell, *T2* Measurements in Human Brain at 1.5, 3 and 7T.* Magnetic Resonance Imaging, 2007. **25**: p. 748 - 753.
13. Cox, E.F. and P. Gowland, *Simultaneous Quantification of T2 and T2' Using a Combined Gradient Echo-Spin Echo Sequence at Ultrahigh Field.* Mag. Res. Med., 2010. **64**: p. 1441-1446.
14. Kollia, K., S. Maderwald, N. Putzki, M. Schlamann, J.M. Theysohn, O. Kraff, M.E. Ladd, M. Forsting, and I. Wanke, *First Clinical Study on Ultra-High-Field MR Imaging in Patients with Multiple Sclerosis: Comparison of 1.5T and 7T.* American Journal of Neuroradiology, 2009. **30**(4): p. 699-702.
15. Regatte, R.R. and M.E. Schweitzer, *Ultra-high-field MRI of the musculoskeletal system at 7.0T.* Journal of Magnetic Resonance Imaging, 2007. **25**(2): p. 262-269.
16. Vaughan, J.T., C.J. Snyder, L.J. DelaBarre, P.J. Bolan, J. Tian, L. Bolinger, G. Adriany, P. Andersen, J. Strupp, and K. Ugurbil, *Whole-body imaging at 7T: Preliminary results.* Magnetic Resonance in Medicine, 2009. **61**(1): p. 244-248.
17. Behr, B.r., J.r. Stadler, H. Michaely, H.-G. Damert, and W. Schneider, *MR imaging of the human hand and wrist at 7Â T.* Skeletal Radiology, 2009. **38**(9): p. 911-917.
18. Snyder, C.J., L. DelaBarre, G.J. Metzger, P.F. van de Moortele, C. Akgun, K. Ugurbil, and J.T. Vaughan, *Initial results of cardiac imaging at 7 tesla.* Magnetic Resonance in Medicine, 2009. **61**(3): p. 517-524.
19. Umutlu, L., S. Orzada, S. Kinner, S. Maderwald, I. Brote, A. Bitz, O. Kraff, S. Ladd, G. Antoch, M. Ladd, H. Quick, and T. Lauenstein, *Renal imaging at 7 Tesla: preliminary results.* European Radiology. **21**(4): p. 841-849.
20. Look, D.C. and D.R. Locker, *Time saving in measurement of NMR and EPR relaxation times.* Rev. Sci. Instrum., 1970. **41**: p. 250-1.

2 NUCLEAR MAGNETIC RESONANCE THEORY

2.1 OUTLINE

This chapter will describe the theory of nuclear magnetic resonance (NMR) and how this can be used to measure intrinsic properties of a system. Initially the system is described in terms of quantum mechanics, and then a classical description of the interactions between nuclei and static or time varying magnetic fields is outlined. The description will concentrate on the hydrogen, ^{1}H, nucleus as this is the focus of all the work presented in this thesis.

2.2 NUCLEAR MAGNETIC RESONANCE

Nuclei have three important characteristics; mass, charge and spin. Spin angular momentum, or spin, is an intrinsic property of nuclei; it is not a physical movement of the particle like angular momentum [1]. Spin angular momentum, as described in non-relativistic quantum mechanics, is a vector quantity, **P,** with Cartesian components [$\hbar I_x$, $\hbar I_y$, $\hbar I_z$]. The magnitude of **P** is expressed as,

$$|\mathbf{P}| = \hbar\sqrt{I(I+1)}, \qquad \textbf{2-1}$$

where *I* is the spin quantum number and there *2I+1* quantum states, given by m_I. *I* which can take integer (*bosons*) or half integer (*fermions*) values and is an intrinsic property of the nucleus. The quantum number m_I determines the number of spin states allowed in an applied magnetic field, m_I = *-I, -I+1 … I*. ^{1}H has a spin of ½ and $m_I = \pm ½$. In the absence of a magnetic field the *2I+1* states are degenerate, possessing the same energy. When placed in a magnetic field there is a resulting energy difference between the spin states.

2.3 MAGNETIC MOMENT AND MAGNETISM

Initially the case of a single spin shall be used, in later sections this shall be extended to an assembly of spins. A classical description can be used to explain the behaviour of a nucleus in a magnetic field. The magnetic moment, **μ**, of a nucleus is given by

$$\boldsymbol{\mu} = \gamma\mathbf{P}, \qquad \textbf{2-2}$$

where γ is the gyromagnetic ratio of the nucleus; it is nucleus specific and for ^{1}H it is 267.5 10^6 radT^{-1} [1]. The sign of the gyromagnetic ratio indicates whether the

magnetic moment is parallel to the spin angular momentum (positive γ) or anti-parallel (negative γ), see Table 2-1 for examples.

Nucleus	Spin	Gyromagnetic Ratio (10^6 radT^{-1})	Abundance in the human body
^{1}H, hydrogen	1/2	267.5	88 M
^{23}Na, sodium	3/2	70.8	80 mM
^{31}P, phosphorus	1/2	108.4	75 mM
^{17}O, oxygen	5/2	-36.3	16 mM
^{19}F, fluorine	1/2	251.8	4 μM

Table 2-1: List of nuclei, their spin, gyromagnetic ratio and relative abundance in the human body (M = mole/litre). Adapted from [2].

The associated energy of this magnetic moment when it is placed in a magnetic field, **B**, is

$$E = -\boldsymbol{\mu}.\mathbf{B}, \qquad \textbf{2-3}$$

which indicates that the energy is lowest when the magnetic moment is parallel to the magnetic field. Combining Equation 2-2 with Equation 2-3;

$$E = -\gamma\mathbf{P}.\mathbf{B}\,. \qquad \textbf{2-4}$$

Standard convention for NMR is to define the main magnetic field, $\mathbf{B_0}$, to be along the z-axis, and equal to B_z, hence

$$E = -\hbar\gamma B_z I_z. \qquad \textbf{2-5}$$

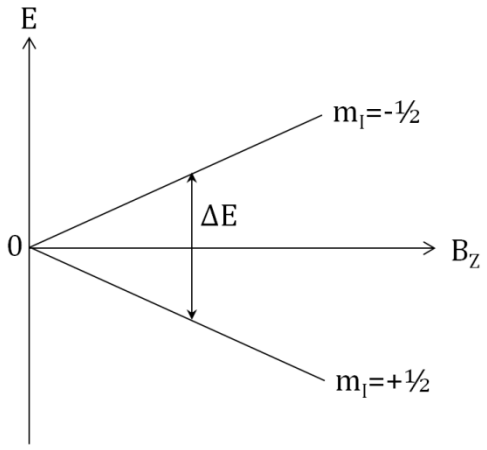

Figure 2-1: Demonstration of the energy gap between the two spin states induced by the application of a static magnetic field.

For a spin ½ system $m_I = \pm ½$ which gives rise to an energy difference between the two states of

$$\Delta E = \hbar\gamma B_z, \qquad \textbf{2-6}$$

when a magnetic field is applied. This is known as Zeeman splitting, shown schematically in Figure 2-1. Transitions between the two energy states can be induced by the absorption or stimulated emission of photons with energy that match the energy gap between states. The frequency of the energy required for this to occur is

$$\nu = \frac{\gamma}{2\pi} B_z, \qquad \textbf{2-7}$$

where ν is frequency in Hz. At 7 T, the frequency required to excite transitions in a ^{1}H sample is ~ 300 MHz, which is in the radiofrequency (rf) range (~ 30 kHz – 300 GHz).

2.4 Classical Description of Magnetic Resonance

The behaviour of a single spin in a static magnetic field can be explored further classically. In the presence of a magnetic field, **B**, a magnetic moment will experience a torque which can be equated to a change in angular momentum:

$$\frac{d\mathbf{P}}{dt} = \boldsymbol{\mu} \times \mathbf{B}. \qquad \textbf{2-8}$$

Substituting for **P** using Equation 2-2 gives an expression in terms of **μ,**

$$\frac{d\boldsymbol{\mu}}{dt} = \gamma \boldsymbol{\mu} \times \mathbf{B}. \qquad \textbf{2-9}$$

Assuming that the magnetic field is parallel to the z-axis this can be described in three components for the x, y and z direction.

$$\begin{aligned} \frac{d\mu_x}{dt} &= \gamma \mu_y B_z, \\ \frac{d\mu_y}{dt} &= \gamma \mu_x B_z, \\ \frac{d\mu_z}{dt} &= 0. \end{aligned} \qquad \textbf{2-10}$$

Solving these differential equations gives;

$$\begin{aligned} \mu_x(t) &= \mu_x|_{t=0} \cos(\gamma B_z t) + \mu_y\big|_{t=0} sin(\gamma B_z t), \\ \mu_y(t) &= -\mu_x|_{t=0} \sin(\gamma B_z t) + \mu_y\big|_{t=0} cos(\gamma B_z t), \\ \mu_z(t) &= \mu_z(t=0). \end{aligned} \qquad \textbf{2-11}$$

This describes the precession of the magnetic moment about the z-axis, with an angular frequency of $-\gamma B_z$, shown schematically in Figure 2-2. This is the *Larmor*

frequency, ω_L, and is equivalent to the frequency required to drive transitions between the two spin states, (Equation 2-7).

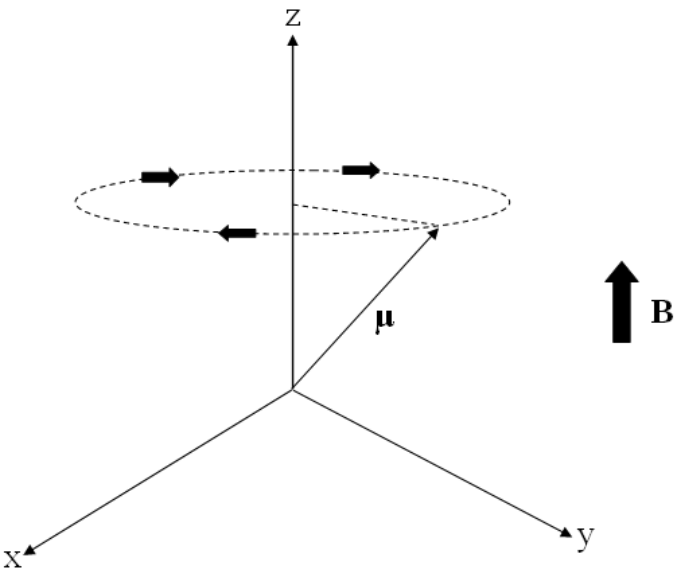

Figure 2-2: Precession of a magnetic moment, μ, due to a static magnetic field, *B*, applied along the z-axis. The small arrows indicate the direction of motion around the z axis.

2.5 INTERACTIONS WITH TIME DEPENDANT MAGNETIC FIELDS

In the presence of a static magnetic field it was shown that a spin precessed with angular frequency $-\gamma B_z$ about the z-axis, now the application of time varying magnetic fields to the system is considered. A time dependant magnetic field, $\mathbf{B_1}(t)$ is applied perpendicular to the main static field and can be expressed as

$$\mathbf{B_1}(t) = 2B_1 \cos(\omega t)\,\hat{\mathbf{x}}. \qquad \textbf{2-12}$$

To simplify the mathematics this can be considered as having a component which rotates anticlockwise (B_a) and one that rotates clockwise (B_c) (shown in Figure 2-3);

$$\mathbf{B_1}(t) = \mathbf{B_a}(t) + \mathbf{B_c}(t),$$
$$\mathbf{B_1}(\boldsymbol{t}) = B_1(\cos(\omega t)\,\hat{\mathbf{x}} + sin(\omega t)\hat{\mathbf{y}}) + B_1(\cos(\omega t)\,\hat{\mathbf{x}} - sin(\omega t)\hat{\mathbf{y}}). \qquad \textbf{2-13}$$

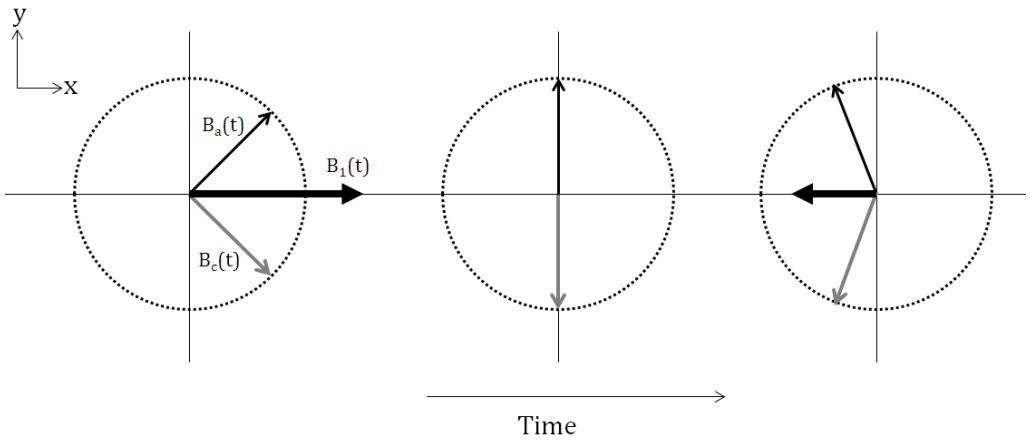

Figure 2-3: Evolution of B_1 (large black arrow), the anticlockwise (thin black arrow) and the clockwise (grey arrow) components with time.

B_a can be discarded as it effectively rotates with a frequency ω which is far off-resonance to the Larmor frequency ($-\gamma B_z$). Hence we only need to include the clockwise component B_c in the equations of motion. Adding the time varying magnetic field into Equation 2-9:

$$\frac{d\boldsymbol{\mu}}{dt} = \gamma\boldsymbol{\mu} \times (B_z\hat{\mathbf{z}} + B_1(\cos(\omega t)\hat{\mathbf{x}} - \sin(\omega t)\,\hat{\mathbf{y}}). \qquad \textbf{2-14}$$

At this stage, to simplify the mathematics, the frame of reference is changed from the laboratory frame to the rotating frame. The rotating frame rotates clockwise about **z** with frequency –ω which has the effect of B_1 appearing stationary, Figure 2-4. The axis system is rotated from [x, y, z] to [x', y', z].

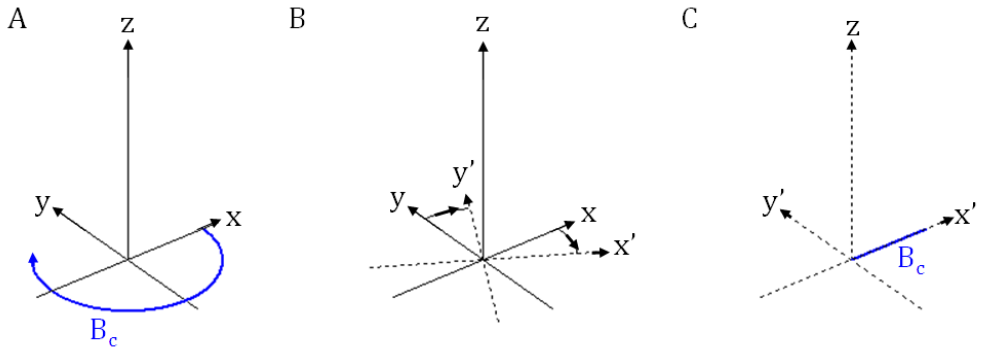

Figure 2-4: (A) The appearance of B_c in the laboratory frame (B) The relationship between the rotating frame (broken lines) and laboratory frame (solid lines) (C) The appearance of B_c in the rotating frame.

From classical mechanics the velocity of vector **r** in the laboratory frame is equal to the velocity of **r** in the rotating frame with the addition of the relative angular velocity between the rotating and laboratory frame ($\boldsymbol{\omega} \times \mathbf{r}$);

$$\left(\frac{d\mathbf{r}}{dt}\right)_{xyz} = \boldsymbol{\omega} \times \mathbf{r} + \left(\frac{d\mathbf{r}}{dt}\right)_{x\prime y\prime z}. \quad \textbf{2-15}$$

Replacing **r** with **μ** to give the expression for the magnetic moment system and equating to Equation 2-14 gives

$$\left(\frac{d\boldsymbol{\mu}}{dt}\right)_{xyz} = \boldsymbol{\omega} \times \boldsymbol{\mu} + \left(\frac{d\boldsymbol{\mu}}{dt}\right)_{x\prime y\prime z\prime},$$

$$= \gamma\boldsymbol{\mu} \times (B_z\hat{\mathbf{z}} + B_1\hat{\mathbf{x}}'). \quad \textbf{2-16}$$

Hence, the velocity of **μ** in the new reference frame (x', y', z) is given by simply rearranging Equation 2-16;

$$\left(\frac{d\boldsymbol{\mu}}{dt}\right)_{x\prime y\prime z} = -\boldsymbol{\omega} \times \boldsymbol{\mu} + \gamma\boldsymbol{\mu} \times (B_z\hat{\mathbf{z}} + B_1\hat{\mathbf{x}}'),$$

$$= \gamma\boldsymbol{\mu} \times \left(\left(B_z - \frac{\omega}{\gamma}\right)\hat{\mathbf{z}} + B_1\hat{\mathbf{x}}'\right),$$

$$= \gamma\boldsymbol{\mu} \times \mathbf{B_{eff}}, \quad \textbf{2-17}$$

where $\mathbf{B_{eff}}$ is the effective magnetic field within the rotating frame of reference. Equation 2-17 represents a precession of the magnetic moment about the axis of $\mathbf{B_{eff}}$. When $\omega = \omega_L$, B_1 is on resonance with the Larmor frequency, $B_z = \omega/\gamma$ and $\mathbf{B_{eff}} = B_1\hat{\mathbf{x}}'$, which describes **μ** precessing about the **x'** axis at an angular frequency of $\omega = -\gamma B_1$. This is represented in Figure 2-5 where the difference between an off-resonance and an on-resonance B_1 field being applied is shown. In a time t, **μ** will have rotated through an angle

$$\theta = \omega t = \gamma B_1 t. \quad \textbf{2-18}$$

This is further discussed in Section 2.6 and in Figure 2-7.

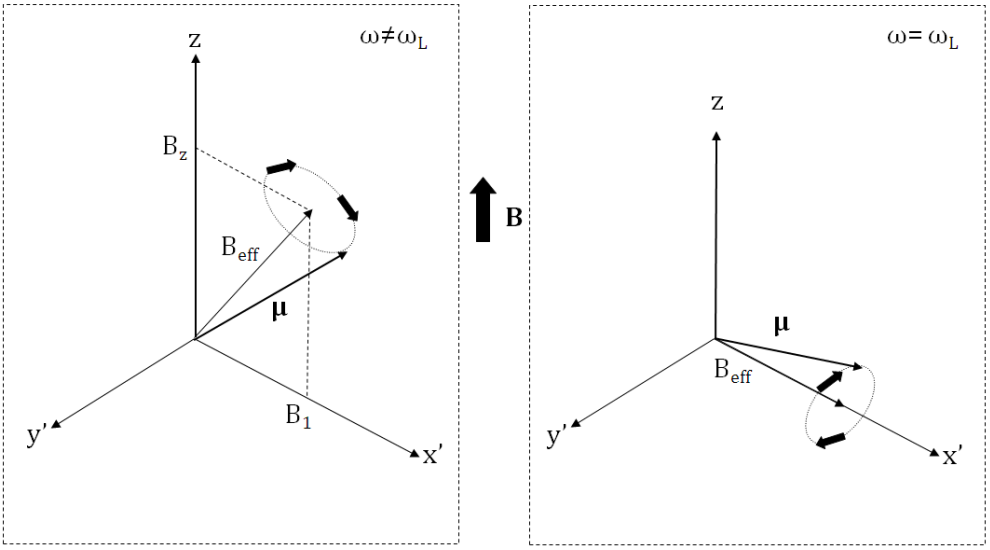

Figure 2-5: Rotating frame of reference and the impact of resonance (A) applied B_1 field is off-resonance (B) applied B_1 field is on-resonance.

It is at this point where this classical treatment of the behaviour of a magnetic moment breaks down. The previous equation suggests that a single magnetic moment can be at any angle relative to the magnetic field. However, from quantum mechanics there are only two possible angles due to the two spin states $|\alpha\rangle$ (parallel to applied field, $m_I = ½$) and $|\beta\rangle$ (anti parallel, $m_I = -½$) for ^1H, yet the classical description can be used to look at an assembly of spins.

2.6 Extension to an Assembly of Spins

Previously, only a single magnetic moment, **μ**, in the magnetic field has been considered. However there will be of the order 10^{20} protons in a single MRI voxel and MRI/NMR experiments consider the signal from these together, or the bulk magnetisation – not on a spin-by-spin basis. The bulk magnetisation, M, is the sum of the individual magnetic moments in the system per unit volume V [2],

$$M = \frac{1}{V} \sum_{\substack{protons\ in \\ V}} \mu_i \qquad \textbf{2-19}$$

as represented schematically in Figure 2-6 A. The spins in the volume are described as a spin isochromat.

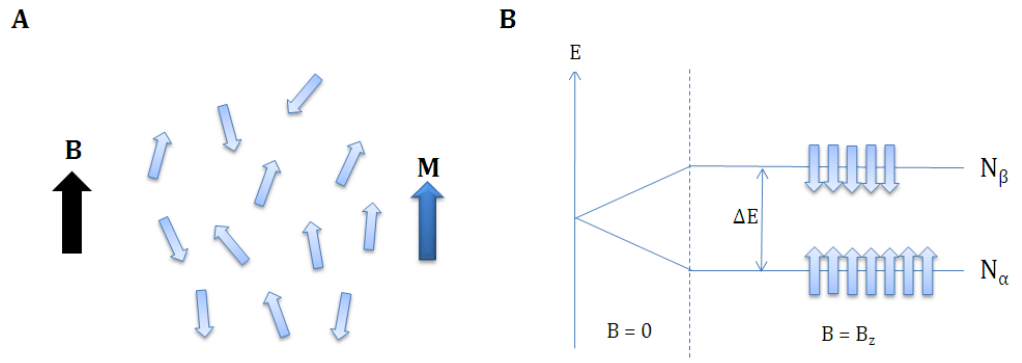

Figure 2-6: (A) Schematic of the concept of net magnetisation showing the applied magnetic field *B* and the net magnetisation *M*, each small arrow represents a spin (B) Zeeman splitting giving rise to an energy gap between the states.

For simplicity, the system is thought to consist of non-interacting spins that precess independently. The distribution of spins in each of the two states $|\alpha\rangle$ and $|\beta\rangle$ at thermal equilibrium in a static magnetic field can be described using the Boltzmann distribution (Figure 2-6 B);

$$\frac{N_\beta}{N_\alpha} = exp\left(-\frac{\Delta E}{k_b T}\right) = exp\left(-\frac{\hbar\gamma B_z}{k_b T}\right), \quad \textbf{2-20}$$

where N_β is the number of spins in the β state, N_α is the number of spins in the α state, ΔE is the energy gap between the levels caused by Zeeman splitting, k_b is the Boltzmann constant and T is the temperature (Kelvin). Looking at the high temperature limit where $k_bT >> \Delta E$ then the exponential term can be approximated using a Taylor series;

$$\frac{N_\beta}{N_\alpha} \approx 1 - \frac{\hbar\gamma B_z}{k_b T}. \quad \textbf{2-21}$$

Hence, the population difference, $n = N_\alpha - N_\beta$ can be approximated as

$$N_a - N_\beta = n = \frac{N_\alpha \hbar\gamma B_z}{2k_b T}. \quad \textbf{2-22}$$

Furthermore, there will only be a small difference in the two states, $N_\alpha \approx N_\beta$, and taking N as the total number of spins ($N = N_\alpha + N_\beta \approx 2N_\alpha$); the population difference is given by

$$n = \frac{N\hbar\gamma B_z}{k_b T}. \quad \textbf{2-23}$$

The fractional difference in spin states (n/N) at 3 T is $\sim 3 \times 10^{-6}$ and at 7 T $\sim 7 \times 10^{-6}$. The magnitude of the net magnetisation can be calculated from this

$$|\mathbf{M}| = N_\alpha \mu_{z\alpha} + N_\beta \mu_{z\beta} = N_\alpha \mu_{z\alpha} - N_\beta \mu_{z\alpha} = n\mu_{z\alpha}, \quad \textbf{2-24}$$

where $\mu_{z\alpha} = \frac{1}{2}\hbar\gamma$ giving

$$|\boldsymbol{M}| = \frac{N(\hbar\gamma)^2 B_z}{4k_b T}. \quad \textbf{2-25}$$

This indicates that the net longitudinal (parallel to field) magnetisation is directly proportional to the magnetic field strength. The transverse (perpendicular to field) magnetisation will vectorally add to zero if there is no phase coherence in the assembly of spins. The bulk magnetisation **M** obeys the same equations of motion as the individual magnetic moments;

$$\frac{d\mathbf{M}}{dt} = \gamma \mathbf{M} \times \mathbf{B}. \quad \textbf{2-26}$$

This equation can be used to predict the time evolution of the bulk magnetisation. RF pulses can be used to tip the magnetisation vector through an angle $\theta = \gamma B_1 t$ where t is the duration of the pulse. The bulk magnetisation can occupy any angle, unlike a single spin. A 90° pulse will cause zero net longitudinal magnetisation, as equal populations are in the two states, but maximum transverse magnetisation. A 180° pulse will invert the longitudinal magnetisation as demonstrated in Figure 2-7.

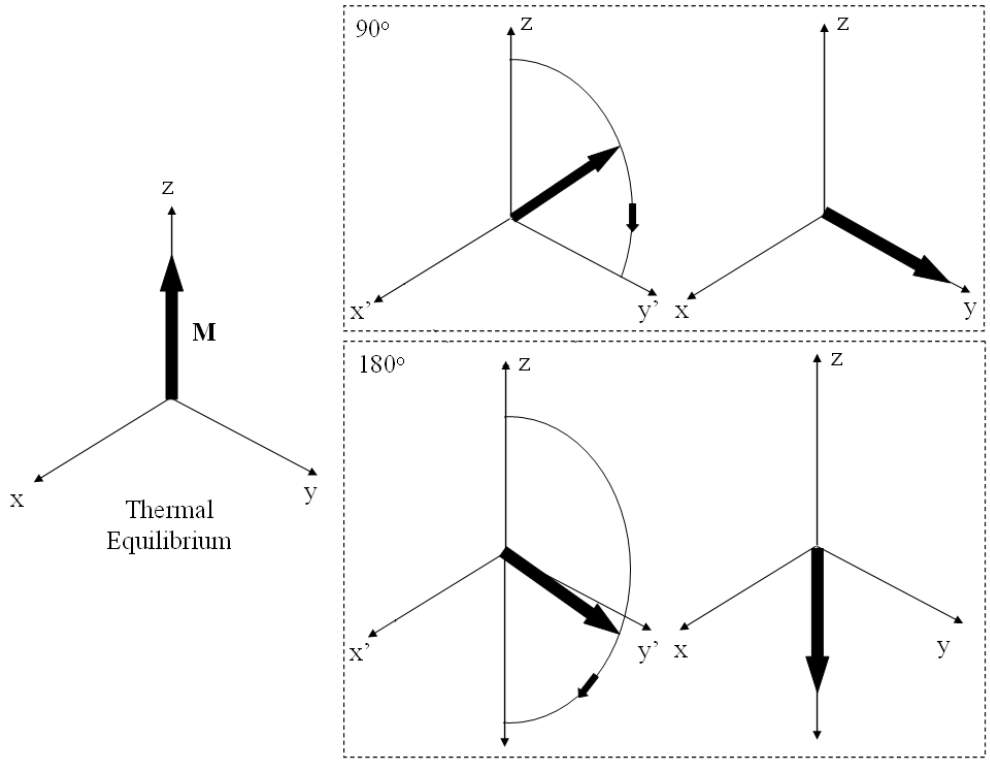

Figure 2-7: Bulk magnetisation in thermal equilibrium, and the process of a 90° and 180° pulse.

2.7 NUCLEI INTERACTIONS AND THE PROCESS OF RELAXATION

The above considered an ensemble of non-interacting spins; however there are interactions between the nuclei in the spin system and these must be accounted for in order to describe the evolution of the bulk magnetisation. Placing a sample in a magnetic field will cause the system to reach thermal equilibrium as described by the Boltzmann distribution. After an RF pulse perturbs the system it will return to equilibrium by a process known as nuclear spin relaxation.

T_1, the longitudinal relaxation time, describes the relaxation processes that cause M_z to return to equilibrium (M_0). Longitudinal relaxation is the process in which the spin system returns energy to the lattice after being placed in a magnetic field or an RF pulse has been applied. T_1 varies dependant on tissue type, in human tissue T_1 is of the order of seconds (see section 2.8.1).

T_2, the transverse relaxation time, is the equivalent time constant for the relaxation processes for M_x/M_y. After an RF pulse, spins in the transverse plane are bought into phase which forms the measured signal. However after time these spins will start to dephase and the net magnetisation will be zero in the transverse plane. The mechanisms behind this are due to interactions between

neighbouring spins and any field inhomogeneities (e.g. due to hardware problems, magnetic susceptibility differences).

For spin ½ nuclei, relaxation arises from the randomly fluctuating magnetic fields caused by the motion of the molecules in the system [1]. As a molecule moves, the magnetic field caused by one spin on a neighbouring spin changes. A second source of changing local fields is chemical shift anisotropy (CSA). CSA is caused by electron currents induced by the external magnetic field. Again, as the molecules move the magnitude and direction of these fields change.

In a system of many spins, they all experience the same externally applied field (ignoring effects from inhomogeneous B_0), but will each experience a slightly different, time varying, transverse magnetic field, B_x. It is assumed that, over either time for one spin or for many spins at the same time, the fluctuating field has zero mean, but a non-zero average magnitude:

$$\langle B_x(t)\rangle = 0,$$
$$\langle B_x^2(t)\rangle \neq 0. \qquad \textbf{2-27}$$

To describe how fast the field fluctuates an autocorrelation function is defined,

$$\mathbb{G}(\tau) = \langle B_x(t)B_x(t+\tau)\rangle \neq 0. \qquad \textbf{2-28}$$

A rapidly fluctuating field will decay away rapidly with τ, conversely a slowing fluctuating field will decay slowly. The corresponding spectral density function, $\mathbb{J}(\omega)$, is defined as twice the Fourier transform of the autocorrelation function;

$$\mathbb{J}(\omega) = 2\int_0^\infty \mathbb{G}(\tau)\exp(-i\omega\tau)\,d\tau. \qquad \textbf{2-29}$$

Assuming that the autocorrelation function, $\mathbb{G}(\tau)$, tends to be large for small τ and zero for large τ, it can be approximated as an exponential decay to simplify the expression for $\mathbb{J}(\omega)$;

$$\mathbb{G}(\tau) = \langle B_x^2\rangle exp\left(-\frac{|\tau|}{\tau_c}\right),$$
$$\Rightarrow \mathbb{J}(\omega) = 2\langle B_x^2\rangle\frac{\tau_c}{1+\omega^2\tau_c^2}, \qquad \textbf{2-30}$$

where τ_c is the correlation time (order of ns), rapid fluctuations have short τ_c whereas slow fluctuations have longer values of τ_c. Equation 2-30 is normally expressed in terms of the normalized spectral density, $\mathcal{J}(\omega)$, which is related to $\mathbb{J}(\omega)$ by $\mathbb{J}(\omega) = 2\langle B_X^2\rangle\mathcal{J}(\omega)$.

The fluctuating transverse field causes transitions between the two spin states,$|\alpha\rangle$ and $|\beta\rangle$. The transition probability is predicted to be equal in the two directions ($|\alpha\rangle \Leftrightarrow |\beta\rangle$) and proportional to the normalised spectral density at the Larmor frequency (ω_L) [1]. This can be used to derive expressions for the relaxation time constants T_1 and T_2 in terms of the normalised spectral density function [1, 3];

$$\frac{1}{T_1} = \frac{3}{10} b^2 \{\mathcal{J}(\omega_L) + 4\mathcal{J}(2\omega_L)\},$$
$$\frac{1}{T_2} = \frac{3}{20} b^2 \{3\mathcal{J}(0) + 5\mathcal{J}(\omega_L) + 2\mathcal{J}(2\omega_L)\}, \quad \textbf{2-31}$$

where b is the dipole-dipole coupling constant;

$$b = -\frac{\mu_0 \gamma^2 \hbar}{4\pi r^3}, \quad \textbf{2-32}$$

and r is the separation of the spins. The expressions for T_1 and T_2 in Equation 2-31 demonstrate that T_1 and T_2 have a strong dependence on correlation time, and as such are temperature dependant. However these expressions cannot describe fully the dependence in biological systems due to their complexity, but are more valid for pure substances [3].

This description assumed that each spin experienced the same applied magnetic field. However, as will be described in Section 2.8.2, this is not true due to hardware inconsistencies and magnetic susceptibility differences in an inhomogeneous system causing non uniform longitudinal magnetisation. These introduce secondary effects that cause further dephasing of the transverse signal.

2.7.1 THE BLOCH EQUATIONS

The equations of motion for the bulk magnetisation need to take into account the relaxation processes. The Bloch equations, in Equation 2-33, describe the evolution of the three components of the net magnetisation and take into account relaxation.

$$\frac{dM_x}{dt} = \gamma M_y \left(B_0 - \frac{\omega}{\gamma}\right) - \frac{M_x}{T_2}$$
$$\frac{dM_y}{dt} = \gamma M_z B_1 - \gamma M_x \left(B_0 - \frac{\omega}{\gamma}\right) - \frac{M_y}{T_2} \quad \textbf{2-33}$$
$$\frac{dM_z}{dt} = \gamma M_y B_1 - \frac{M_z - M_0}{T_1}$$

where M_0 is the equilibrium longitudinal magnetisation. Figure 2-8 demonstrates the evolution of the net magnetisation according to the solutions of the Bloch equations (initial conditions $M_z = 0$, $M_{xy} = M_0$ and $B_1 = 0$) in the laboratory frame (blue) and the rotating frame (red).

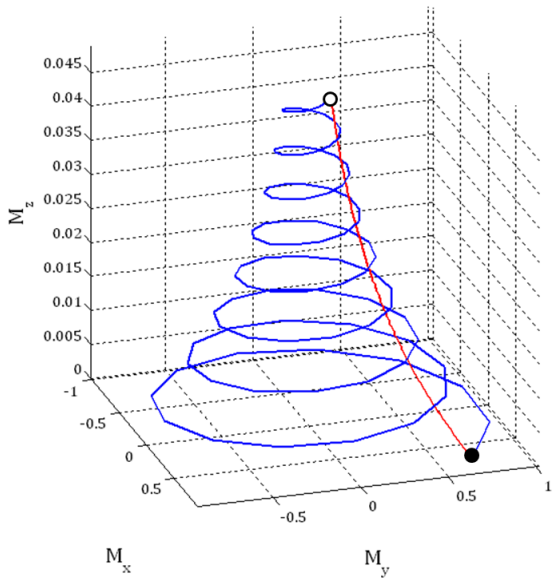

Figure 2-8: Evolution of net-magnetisation in the laboratory frame (blue) and the rotating frame (red) after a 90° pulse. Filled circle indicates starting point (t = 0) and empty circle indicates end point (t = t).

2.8 NMR Experiments – Measuring the FID for T_1 and T_2 Quantification

The application of an RF pulse can produce signal in the transverse plane (M_{xy}) inducing a current in a coil placed close to the sample (according to Faraday's Law, the electromotive force is equal to the rate of change of magnetic flux [4]). The induced current is small, but has a well defined frequency, and decays according to the Bloch equations (Equation 2-27). This is known as the Free Induction Decay (FID), Figure 2-9.

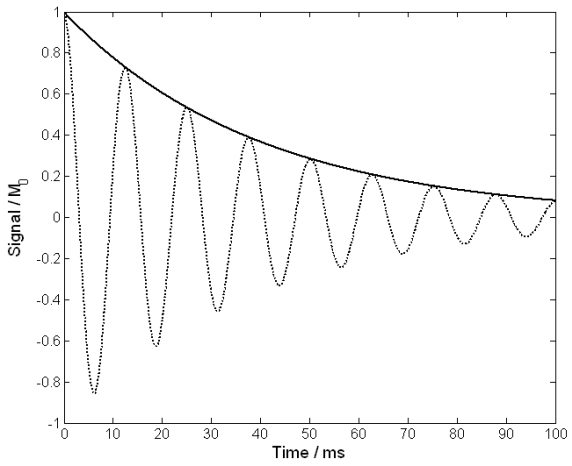

Figure 2-9: FID with sample on resonance (solid line) and off resonance (broken line).

The detection of the FID relies on pre-amplification and a phase sensitive detector as the signal oscillates at 100's of MHz. The phase sensitive detector multiplies the detected signal ($V_{sig} = M_0\sin(\theta)\cos(\omega_L t)\exp(-t/T_2)$) by a reference signal ($A\cos(\omega_0 t)$);

$$s(t) = M_0 A\sin(\theta)\cos(\omega_L t)exp\left(-\frac{t}{T_2}\right)\cos(\omega_0 t)$$
$$= \frac{M_0}{2}A\sin(\theta)exp\left(-\frac{t}{T_2}\right)\left(\cos\left((\omega_L+\omega_0)t\right)+\cos\left((\omega_L-\omega_0)t\right)\right). \quad \textbf{2-34}$$

This is then integrated over a time period δt, which contains many cycles of the high frequency component ($\omega_L + \omega_0$) which average to zero, and the low frequency ($\omega_L - \omega_0$) component which is approximately constant over δt. Simplifying the integration leads to:

$$S(t) = \int_t^{t+\delta t} s(t)dt$$
$$= \frac{M_0}{2}A\sin(\theta)exp\left(-\frac{t}{T_2}\right)\cos\left((\omega_L-\omega_0)t\right)\delta t. \quad \textbf{2-35}$$

This signal does not distinguish between positive and negative differences in phase as it is dependent on the cosine term which is symmetric about zero. To differentiate the sign of the phase, a further phase sensitive detector is commonly used, which has its reference signal 90° degrees out of phase to the first. This is known as *quadrature detection,* and results in a second signal:

$$S_2(t) = \frac{M_0}{2}A\sin(\theta)exp\left(-\frac{t}{T_2}\right)\sin\left((\omega_L-\omega_0)t\right)\delta t. \quad \textbf{2-36}$$

These are added to give the complex FID signal

$$S_{FID}(t) = S(t) + iS_2(t)$$
$$= M_0 \sin(\theta)\, exp\left(-\frac{t}{T_2}\right) \exp(i(\omega_L - \omega_0)t). \quad \textbf{2-37}$$

Figure 2-9 is the FID with a frequency difference between the sample and reference (broken line) and the situation where the reference is on-resonance (solid line). The Fourier Transform of these signals will provide the frequency spectrum. With these tools, simple NMR experiments can be devised to measure the characteristic relaxation time constants of the sample, T_1 and T_2.

2.8.1 MEASURING T_1: INVERSION RECOVERY

T_1 is a useful characteristic as it provides information about the properties of a sample. In healthy tissue T_1 is related to the concentration of macromolecules, water binding and water content [5]. It allows discrimination of different samples, e.g. white and grey brain matter, as demonstrated in Table 2-2.

Tissue Type	T_1 / ms
Cortical grey matter	2132 [6], 1939 [7]
White matter	1220 [6], 1130 [7]
CSF	4425 [6],
Blood	2587 [6],

Table 2-2: Example longitudinal relaxation times (T_1) at 7 T.

The inversion recovery sequence is the most common method of T_1 measurement, and is shown in Figure 2-10.

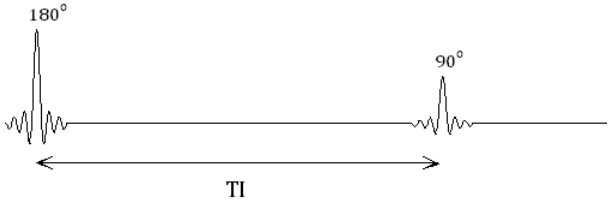

Figure 2-10: Simple pulse diagram of inversion recovery sequence.

The magnetisation starts in thermal equilibrium, M_0, a 180° inversion pulse is then applied which inverts the longitudinal magnetisation to $-M_0$. There is then a time delay termed the inversion time TI, between the inversion pulse and the 90° pulse used to generate the transverse signal that is measured by the receive coil. The inversion time is used to allow the longitudinal magnetisation to begin to recover towards thermal equilibrium with T_1. The magnetisation measured at a

time TI is given by the solution of the Bloch equations, using initial conditions at t = 0; $M_z = -M_0$, $M_x = M_y = 0$;

$$M(TI) = M_0\left(1 - 2\exp\left(-\frac{TI}{T_1}\right)\right). \quad \textbf{2-38}$$

To measure T_1, a series of delay times is used to sample the inversion recovery curve from inversion as it returns back to thermal equilibrium, as shown in Figure 2-11.

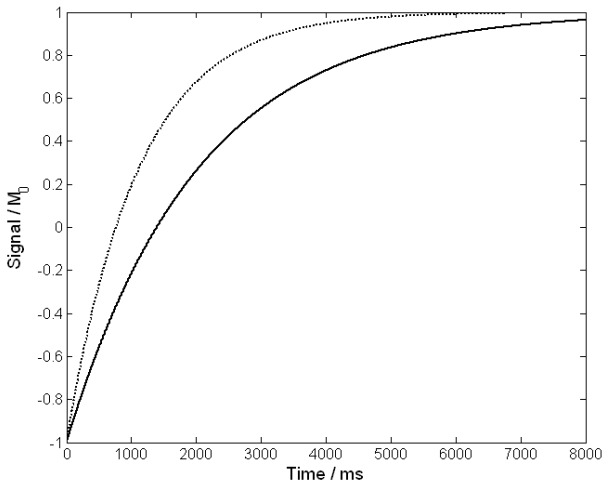

Figure 2-11: Longitudinal signal recovery during IR sequence for white matter (T_1 = 1.1 s, broken line) and grey matter (T_1 = 2 s, solid line) at 7 T.

2.8.2 MEASURING T_2 TRANSVERSE DECAY: SPIN ECHO

T_2 is the time constant that characterises the decay of the transverse magnetisation due to the fluctuations in the resonant frequencies of the nuclei causing dephasing. The causes of the transverse magnetisation being destroyed can be split into two types; spin-spin and those due to B_0 inhomogeneities [3]. Therefore a new expression for T_2 is formed. T_2* takes into account all the dephasing effects, spin-spin effects are characterised by T_2 and B_0 inhomogeneities (e.g. due to susceptibility differences at air/tissue interfaces) are described by T_2' a non-time varying decay constant. The relationship between these three rate constants is

$$\frac{1}{T_2^*} = \frac{1}{T_2} + \frac{1}{T_2'}. \quad \textbf{2-39}$$

To measure T_2 the effects of T_2' need to be removed. Effects leading to T_2' decay remain constant over time whereas T_2 decay effects vary over time. A spin-echo (SE) sequence is used [8], which refocuses the effects due to T_2' as these remain constant throughout the experiment allowing measurement of T_2.

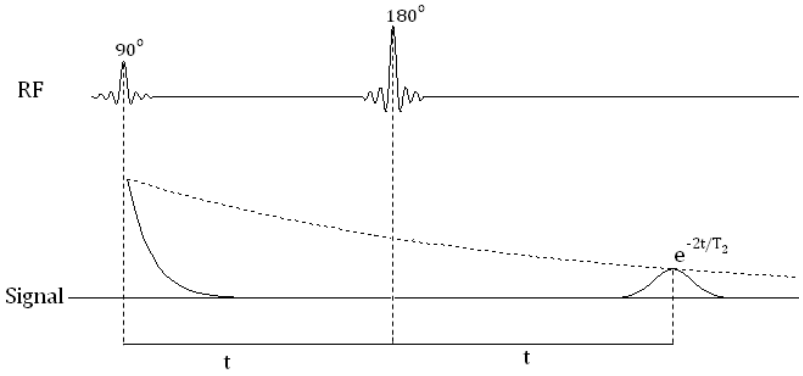

Figure 2-12: Simple schematic of spin echo RF pulse sequence to measure T_2 and corresponding signal.

The spin-echo sequence, Figure 2-12, consists of a 90° and a 180° pulse separated by time t, the signal is then sampled at a time t following the 180° pulse (the 180° is about the y'-axis; rather than inverting the magnetisation). The classical picture of the evolution of the bulk magnetisation can be used to explain how the SE sequence works.

After the 90° pulse, the spin isochromat is in the transverse plane (Figure 2-13 A). Due to slightly different precession frequencies the spins begin to dephase, after a time t the spin isochromat will have fanned out. Some of the spins will have a precessional frequency faster than the Larmor frequency, others slower (Figure 2-13 B). In the rotating frame this will appear as spins going in different directions.

The 180° pulse causes the spins to be flipped about the y' axis (Figure 2-13 C); they begin to return back towards the y' axis and rephase (Figure 2-13 D). This will form the observed signal at time 2t since the first pulse.

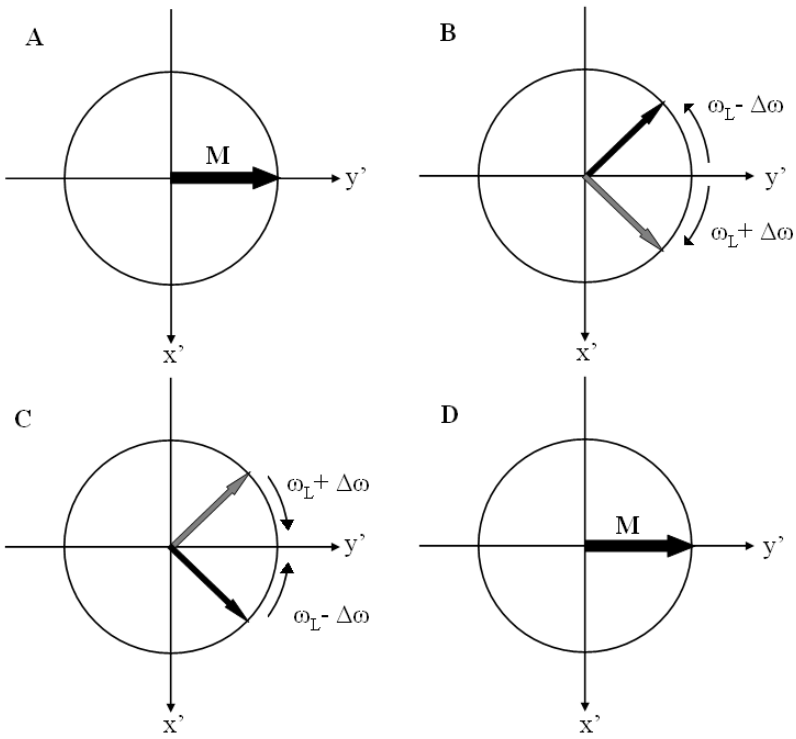

Figure 2-13: Schematic of the spin evolution in a spin echo. (A) Magnetisation after initial 90° pulse (B) Spins have dephased over the time period t (C) 180° pulse causes spins to move back towards y' (D) After further time t spins have rephased.

The spin echo experiment will rephase any effects that are the same in the two sections of the pulse sequence – e.g. susceptibility differences caused by air/tissue interfaces. Molecular motion will change throughout the experiment, and as such these effects will not be rephased. Effects of static field inhomogeneities will be rephased. Similarly to the measurement of T_1, this experiment is repeated using different values of t to measure T_2 by fitting to $M_0\exp(-2t/T_2)$. The echo time of the experiment, TE, is equal to 2t.

T_2, measured with a GESSE (gradient and spin echo) sequence, has been shown to be approximately 45 ms in gray and white matter in the human brain at 7 T [9].

The expression for the transverse magnetisation can be expressed to include a diffusion term [10];

$$M_{xy} = M_0 exp\left(-\frac{TE}{T_2}\right)\exp(-bD), \quad \textbf{2-40}$$

where D is the diffusion coefficient and b (known as the *b value* of the sequence) for a constant applied gradient (G) is

$$b = \frac{\gamma^2 G^2 t^3}{3}, \quad \textbf{2-41}$$

where t is the time of the echo. Hence diffusion will cause further signal dephasing and possible underestimation of T_2 if not taken into account. At high field, the relative diffusion contribution to signal dephasing is increased due to a reduction in T_2. Carr-Purcell (CP) [11] and Carr-Purcell Meiboom-Gill (CPMG) [12] sequences can be used for the measurement of T_2 accounting for diffusion to minimise errors in T_2 quantification, Figure 2-14. This can be used to measure the T_2 of blood, and determine oxygenation (e.g. [13]).

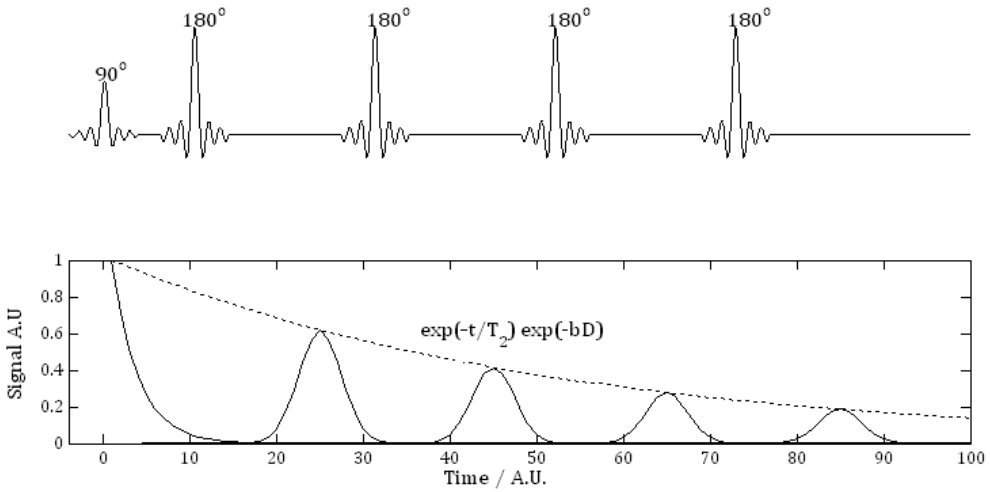

Figure 2-14: Schematic of the RF pulse sequence and envelope of the transverse signal from a CPMG sequence.

2.8.3 MEASURING T_2 TRANSVERSE DECAY*

The measured transverse signal after an RF pulse is proportional to $\exp(-t/T_2^*)$, where t is the measurement time after the RF pulse, as demonstrated in Figure 2-9. Measurements performed at different times, t, will allow for T_2^* to be found with a mono-exponential fit.

At 7 T T_2^* was measured to be 33.2 ± 1.3 ms in grey matter and 26.8 ± 1.2 ms in white matter using a multiple echo EPI sequence [14]. At lower field strengths

T_2* increases, e.g. grey matter at 3 T is approximately 66 ms and at 1.5 T 84 ms causing less signal dephasing. T_2* will be dependant on sample thickness, due to through plane dephasing of the spins, thicker slices will shorten T_2*.

2.9 CONCLUSIONS

This chapter has introduced the basics of the interactions between a nucleus and both a static and time varying magnetic field. This has been extended to an ensemble of spins, and to include the interactions between spins and how they are characterised through decay times (T_1, T_2 and T_2*). The measurement of these was demonstrated. This forms the basis of magnetic resonance imaging; which is discussed in Chapter 3.

2.10 REFERENCES

1. Levitt, M.H., *Spin Dynamics*. 2006, Chichester: John Wiley & Sons Ltd.
2. Haacke, M., R. Brown, M. Thompson, and R. Venkatesan, *Magnetic Resonance Imaging: Physical Principles and Sequence Design*. 1999, New York: Wiley-Liss.
3. Morris, P.G., *Nuclear Magnetic Resonance Imaging in Medicine and Biology*. 1986, Oxford: Clarendon Press.
4. Pollack, G.L. and D.R. Stump, *Electromagnetism*. 2002, San Francisco: Addison Wesley.
5. *Quantitative MRI of the Brain*, ed. P. Tofts. 2003, Chichester: Wiley.
6. Rooney, W.D., G. Johnson, X. Li, E.R. Cohen, S.-G. Kim, K. Ugurbil, and C.S. Springer, *Magnetic Field and Tissue Dependancies of Human Brain Longitudinal ^1H_2O Relaxation in Vivo.* Mag. Res. Med., 2007. **57**: p. 308-318.
7. Wright, P.J., O.E. Mougin, J.J. Totman, A.M. Peters, M.J. Brookes, R. Coxon, P.G. Morris, M. Clemence, S.T. Francis, R. Bowtell, and P.A. Gowland, *Water Proton T1 Measurements in Brain Tissue at 7, 3 and 1.5T using IR-EPI, IR-TSE and MPRAGE: results and optimisation.* Magn. Reson. Mater. Phy, 2008. **21**: p. 121-130.
8. Hahn, E.L., *Spin Echoes.* Physical Review, 1950. **80**(4): p. 580-594.
9. Cox, E.F. and P. Gowland, *Simultaneous Quantification of T2 and T2' Using a Combined Gradient Echo-Spin Echo Sequence at Ultrahigh Field.* Mag. Res. Med., 2010. **64**: p. 1441-1446.
10. Cox, E., *Quantitative Whole Body Imaging at High Field*, in *School of Physics and Astronomy*. 2009, University of Nottingham: Nottingham.
11. Carr, H.Y. and E.M. Purcell, *Effects of Diffusion on Free Precession in Nuclear Magnetic Resonance Experiments.* Physical Review, 1954. **94**(3): p. 630-638.
12. Meiboom, S. and D. Gill, *Modified Spin Echo Method for Measuring Nuclear Relaxation Times.* Review of Scientific Instruments, 1958. **29**(8): p. 688-691.
13. Thulborn, K.R., J.C. Waterton, P.M. Matthews, and G.K. Radda, *Oxygenation dependence of the transverse relaxation time of water protons in whole blood at high field.* Biochimica et Biophysica Acta (BBA) - General Subjects, 1982. **714**(2): p. 265-270.
14. Peters, A.M., M.J. Brookes, F.G. Hoogenraad, P.A. Gowland, S.T. Francis, P.G. Morris, and R. Bowtell, *T2* Measurements in Human Brain at 1.5, 3 and 7T.* Magnetic Resonance Imaging, 2007. **25**: p. 748 - 753.

3 MAGNETIC RESONANCE IMAGING AND HARDWARE

3.1 OUTLINE

This chapter will outline the theory behind magnetic resonance imaging and the imaging techniques that are used in the experimental work presented in this thesis. The MR scanner hardware will also be introduced, concentrating on the 7 T Philips Achieva system. Safety and ethical considerations are also outlined.

3.2 IMAGING

Previous discussion of NMR theory in Chapter 2 has concentrated on the total signal arising from the entire sample that has been excited by the RF pulse. However, for magnetic resonance imaging the signal needs to be encoded in such a way that signals from different parts of the sample can be discriminated. To do this, several techniques allow for the spatial separation of the signals. The concepts of magnetic field gradients slice selection, frequency and phase encoding shall be introduced. A number of imaging sequences that are used in the experimental work are also shown.

3.2.1 MAGNETIC FIELD GRADIENTS FOR SPATIAL ENCODING

Previously in Chapter 2 the case where the entire sample was excited was shown, commonly however only signal from a specific volume of interest is required. From Chapter 2 it was shown that the frequency of precession is linearly proportional to the magnetic field. Thus, by spatially varying the magnetic field, the Larmor frequency will also vary spatially, giving a degree of spatial specificity. To achieve this, magnetic field gradients can be applied, these can be applied along the three axes so that the Larmor frequency differs in every position. A gradient, **G**, is fully expressed as a tensor, with gradient field components along all three axis (B_x, B_y and B_z). However, as the main field is applied along the z-axis, the gradient can be simplified to only include the B_z components as at high field such as 7T it is assumed that the other components will have little effect on the resonant frequency of the spins;

$$\boldsymbol{G} = G_x\hat{\mathbf{x}} + G_y\hat{\mathbf{y}} + G_z\hat{\mathbf{z}} = \frac{\partial B_z}{\partial x}\hat{\mathbf{x}} + \frac{\partial B_z}{\partial y}\hat{\mathbf{y}} + \frac{\partial B_z}{\partial z}\hat{\mathbf{z}}, \qquad \textbf{3-1}$$

This means the expression for the Larmor frequency experienced at a point **r** is now

$$\omega(\boldsymbol{r}) = \gamma(B_0 + \mathbf{G}.\mathbf{r}). \quad \textbf{3-2}$$

This can then be substituted into the equation for the FID, described in Chapter 2 (Eq. 2-37), so that the signal from the sample is

$$S(t) = \int \rho(\mathbf{r}) \exp(i\gamma \mathbf{G}.\mathbf{r}t)\, dr^3, \quad \textbf{3-3}$$

which is the integral over the three dimensional volume. ρ(**r**) is the density of nuclear spins and $\mathbf{k} = \gamma \mathbf{G} t$ can be substituted, where **k** refers to k-space, a spatial frequency (dimensions of length^{-1}), to give

$$S(t) = \int \rho(\mathbf{r}) \exp(i\mathbf{k}.\mathbf{r})\, dr^3. \quad \textbf{3-4}$$

This can be converted to give spin density (ρ(**r**)) by inverse Fourier transforming the expression for signal;

$$\rho(\mathbf{r}) = \frac{1}{16\pi^3} \int S(t) \exp(-i\mathbf{k}.\mathbf{r})\, dk^3. \quad \textbf{3-5}$$

This allows the image to be formed from the signal (S(t)) providing adequate sampling of k-space has been performed using the field gradients, **G**.

K-space comprises different spatial frequency components; generally the centre of k-space provides information on bulk image intensity whilst the higher spatial frequencies provide edge information. This is demonstrated in Figure 3-1, showing the effect of applying different k-space filters to an MR image.

The sampling of k-space is related to the spatial resolution and field of view (FOV) in image space. The FOV is given by $1/\Delta k$ where Δk is the step between samples in k-space (this can be asymmetric in the phase and frequency encode directions). The spatial resolution, or voxel size, is given by the inverse of the largest spatial frequency – or FOV in k-space [1].

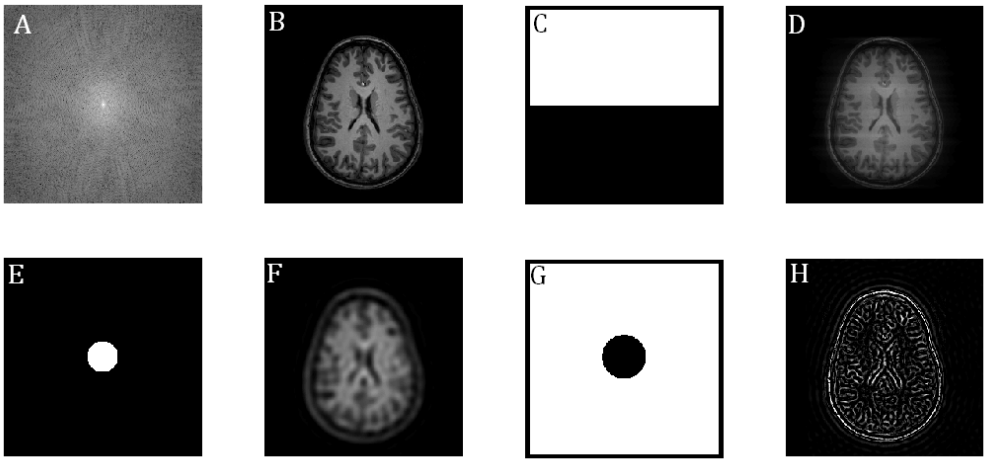

Figure 3-1: (A) K-space representation of the image in (B), (C, E, G) K-space filters where black indicates the signal that has been removed, (C) is half of k-space (E) is the centre of k-space and (G) is the high k-space frequencies only and resulting images (D, F and H).

3.2.1.1 Slice Selection

The previous section has looked at signal arising from the entire excited 3D volume. However, commonly only a 2D image is needed, acquired by exciting a slice of the sample. This is known as *slice selection*. A linear gradient is applied along one axis (e.g. z), and an RF pulse of the same frequency and bandwidth as the slice of interest is applied so that only those spins are excited [2]. The RF pulse typically used for slice selection is a truncated sinc pulse, an infinite sinc pulse would give a square pulse profile (given by the Fourier transform), and truncation will cause an imperfect profile (ringing at the boundary).

The bandwidth of the RF pulse determines the range of frequencies that are excited and hence the slice thickness. The slice thickness is proportional to the RF bandwidth ($\Delta\omega$) scaled by the gradient strength (G_z),

$$\Delta z = \frac{\Delta\omega}{\gamma G_z}, \qquad \textbf{3-6}$$

as shown schematically in Figure 3-2.

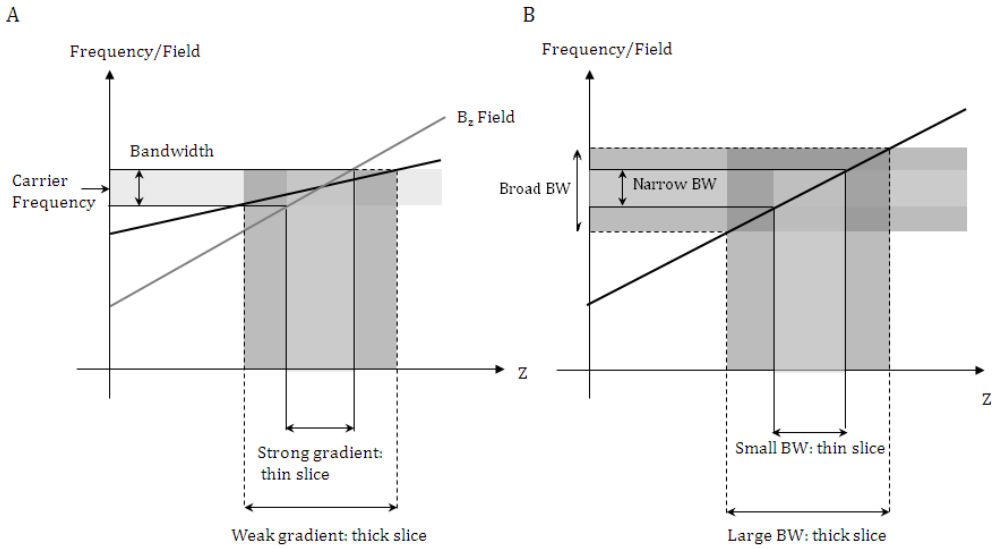

Figure 3-2: Schematic diagram of slice selection using magnetic field gradients. (A) The effect of gradient strength on slice thickness, (black line is a weak gradient, grey line a strong gradient) (B) The effect of bandwidth (BW) on slice thickness, adapted from [1].

This ensures that the measured signal will only come from the slice of interest as outside the slice of interest the spins will be off resonance. To facilitate multiple slice imaging, multiple excitation pulses with different carrier frequencies are required to select different slices within the sample.

The slice select gradient pulse applied is a positive lobe followed by a negative lobe of half the duration, demonstrated in Figure 3-3. The negative lobe is used to rephase the signal, which is dephased by the application of the gradient, to maximise the measured signal.

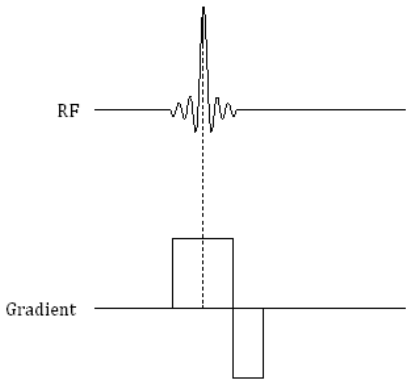

Figure 3-3: Slice select RF pulse and gradient.

3.2.1.2 Frequency Encoding

Spatial specificity now needs to be incorporated into the measured signals; slice selection or volume excitation means the signal will originate from a specified volume but more information is needed. Frequency encoding (FE) uses a similar principle to slice selection; however the spatial dependence of the resonant frequency is used for spatially separating the measured signals. The frequency encoding gradient is applied after the RF excitation, so only affects the spins in the excited slice/volume. Commonly, a gradient is applied along the x-axis so that

$$\omega(x) = \gamma(B_0 + \mathrm{G_x}x). \quad \textbf{3-7}$$

The resonant frequency varies linearly across the sample, along the x-axis. Hence the frequency of the received signal will provide spatial localisation, allowing a projection across a sample to be built up.

3.2.1.3 Phase Encoding

Frequency encoding allows a one dimensional image to be identified. To extend this to a 2D image, phase encoding, where the phase of the detected signals is dependent on their y-axis position, is used. A G_y gradient is applied for a short time to cause a phase change across the sample in the y direction; this is applied before the readout gradient.

This means that each voxel in the image can be characterised by a unique frequency/phase combination allowing an image to be built up from different samples covering k-space. The use of x and y gradients to sample the k_x-k_y plane is shown schematically in Figure 3-4.

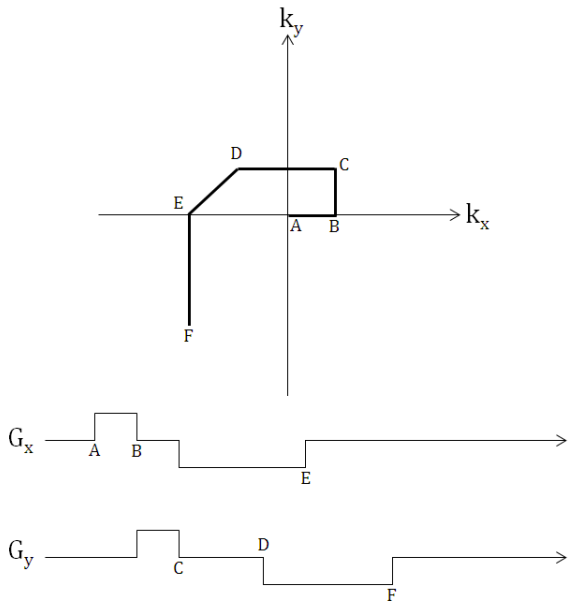

Figure 3-4: Example of how G_x and G_y magnetic field gradients can be used to traverse k-space.

3.2.2 IMAGING SEQUENCES

Image contrast depends on the intrinsic properties of the sample; the proton density (PD), longitudinal relaxation time (T_1) and transverse relaxation times (T_2 and T_2*). Sequence design and parameters will determine which contrast is dominant. For example, a gradient echo sequence with long echo time (TE) would give rise to contrast between tissues based on T_2*. Similarly, a spin echo image with long TE would have T_2 contrast. A T_1 weighted sequence normally employs a preparation pulse that either saturates or inverts the longitudinal magnetisation prior to sampling. The delay between the preparation pulse and imaging will change the contrast. A sequence that has short TE and very long TR will reduce the dependence on relaxation effects and becomes proton density (PD) weighted.

The contrast required depends on the information required. For example, multiple sclerosis (MS) lesions can be identified using a T_1 weighted sequence called FLAIR (fluid attenuated inversion recovery) or DIR (dual inversion recovery) as their T_1 differs from the local white matter. FLAIR uses an inversion pulse to null the signal from the fluid (e.g. CSF), whereas DIR uses two inversion pulses to null two tissues with different T_1 values (e.g. CSF and white matter) to aid lesion identification. T_2* weighted images highlight vessels due to the difference in T_2* between blood and tissue.

There are many different techniques used for imaging, the sequence chosen will be dependent on many factors including the area of interest, contrast, spatial and temporal resolution required. Here the basic imaging sequence of spin warp and the main sequences that are used in the experimental work in this thesis are described.

3.2.2.1 Basic Imaging – Spin Warp

Spin warp imaging samples k-space in a regular grid, moving across the k_x-axis and stepping through k_y to sample 2D k-space [3], allowing an image to be formed. To step through k-space, k_y phase encode gradients are applied along the y-axis, their strength being varied to target different spatial frequencies. A read gradient is applied along the x-axis to traverse k_x. A negative read gradient is initially applied to move in the negative k_x, a positive readout gradient of twice the duration is then applied to cover the whole of k_x. This gives rise to a symmetric signal as the spins are rephased during the first half of the positive gradient and then begin to dephase.

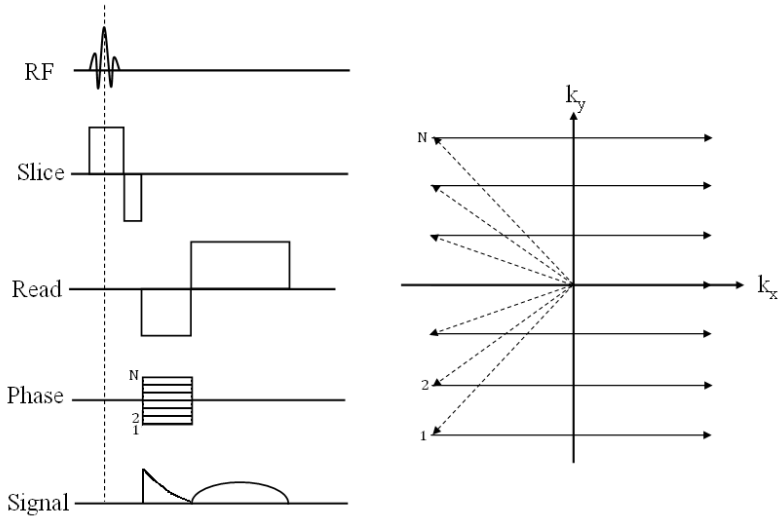

Figure 3-5: Schematic of the pulse sequence and k-space trajectory for spin-warp imaging.

The spin warp sequence is a robust imaging sequence, however it takes a long time to acquire each image due to the acquisition of only one line of k-space per excitation. For maximum signal there needs to be a long time between the RF pulses to allow for recovery, if a flip angle of 90° is used. Dependant on the size of the image and the spatial resolution, this could be 256 lines taking approximately 40 minutes per image.

To speed up the acquisition the TR, the time between RF pulses, is shorter than the time required for full recovery causing saturation of the signal, and so the flip angle is chosen to maximise the signal. The steady state signal, M_{ss}, which is the signal that is created after a train of RF pulses, can be calculated using the Bloch equation for longitudinal recovery. Assuming all the transverse magnetisation is spoilt between RF pulses and does not contribute to the signal, this gives

$$M_{ss} = \frac{M_0 \sin(\theta)\left(1 - exp\left(-\frac{TR}{T_1}\right)\right)}{1 - \cos(\theta) exp\left(-\frac{TR}{T_1}\right)}, \quad \textbf{3-8}$$

where TR is the time between RF pulses and M_0 is the equilibrium magnetisation. Differentiating Equation 3-8 with respect to θ, leads to the angle which maximises the measured signal, this is known as the Ernst angle [4]

$$\theta = \cos^{-1}\left(exp\left(-\frac{TR}{T_1}\right)\right). \quad \textbf{3-9}$$

For example, to maximise the signal for grey matter at 7 T (T_1 = 2 s [5]) with a TR of 50 ms, a flip angle of approximately 13° is needed. White matter with a shorter T_1 of 1.2 s [5] would require a larger flip angle of 16° to maximise the signal. Using a short TR, e.g. 50 ms, reduces the time to acquire a single slice to only a few seconds but M_{ss} and so the signal-to-noise ratio (SNR) will be reduced compared to a longer TR.

3.2.2.2 TFE

TFE (Turbo Field Echo) or TurboFLASH (Turbo – Fast Low Angle SHot) is a gradient echo technique, typically a 2D sequence [6, 7]. This steps through k_y as in Spin-Warp imaging and uses a short TR (order of ms) to acquire images rapidly whilst the flip angle is low to reduce suppression of the signal. The echo time, TE, of TFE, is the time from the centre of the RF pulse to the centre of the positive read gradient lobe.

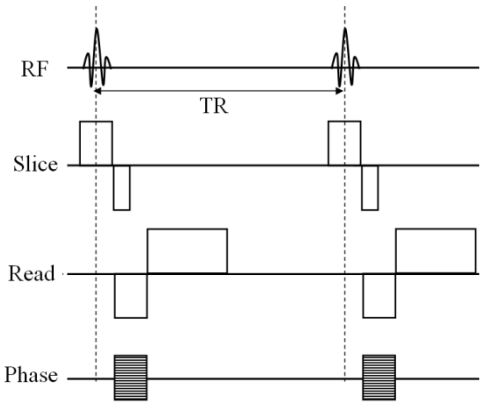

Figure 3-6: Section of pulse sequence diagram for TFE, this will loop ~100 times for a single slice. RF spoiling or gradient spoiling may be incorporated to give T_1 weighting.

Figure 3-7 shows example 7 T TFE images (2 x 2 x 3 mm^3, FA = 15°, TE/TR = 2.5/5 ms, FOV = 192 x 192 x 12 mm^3). TFE images are often preceded by a spin preparation pulse, e.g. inversion or saturation. A TFE image with an inversion preparation pulse is commonly known as an MPRAGE (Magnetisation Prepared RApid Gradient Echo), which is a T_1 weighted scan with contrast dependant on the delay between inversion and readout. It is often used for anatomical reference scans. TFE is used in the experimental work described in Chapter 5.

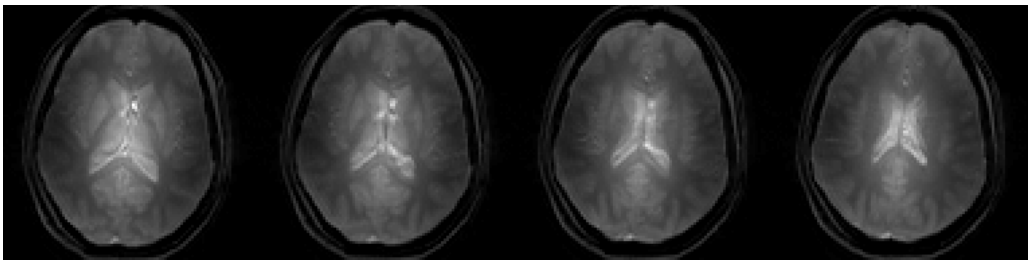

Figure 3-7: Example TFE images (2 x 2 x 3 mm^3, FA = 15°, TE/TR = 2.5/5 ms, FOV = 192 x 192 x 12 mm^3).

3.2.2.3 bFFE

bFFE (balanced Fast Field Echo), balanced steady-state free precession (bSSFP) or TrueFISP is a 2D gradient echo technique [8, 9]. In contrast to TFE, this uses a train of high flip angle (~ 50°) RF pulses and uses both transverse and longitudinal magnetisation to build up the steady state signal [10]. The gradients are balanced which means the phase of the transverse magnetisation is retained and the evolution of magnetisation is equivalent between each TR, independent of the phase and read gradients.

Commonly the first RF pulse of the bFFE train (order of 100 pulses per slice) has flip angle $\alpha/2$, whilst the remainder have a flip angle α. This is to stabilise the

signal and to reduce oscillations. To try and stabilise the measured signal further pre-scans where no data is recorded are normally inserted prior to data recording to ensure that the magnetisation is in the steady state. The contrast in bFFE is a mixture of T_1 and T_2 weighted, and is very dependent on the TR chosen.

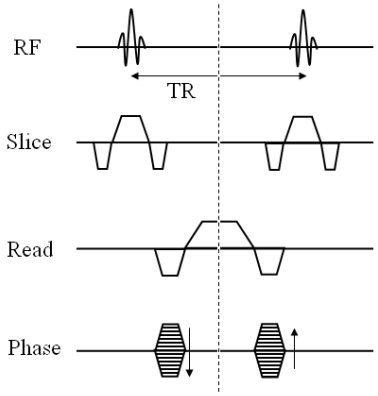

Figure 3-8: Pulse sequence for bFFE.

Figure 3-9 shows example bFFE images acquired at 7 T (2 x 2 x 3mm^3, TE/TR = 1.8 / 3.6 ms, FA = 50°, FOV = 192 x 192 x 3 mm^3). In the lower slice this shows a characteristic banding artefact associated with bSSFP techniques, which occurs in areas of large frequency offsets. This can be reduced by improved shimming techniques, and changing the TR of the readout. TR should be less than the inverse of the off resonance frequency to maintain phase coherence between the RF pulses. bFFE imaging is used in the ASL development work described in Chapter 5.

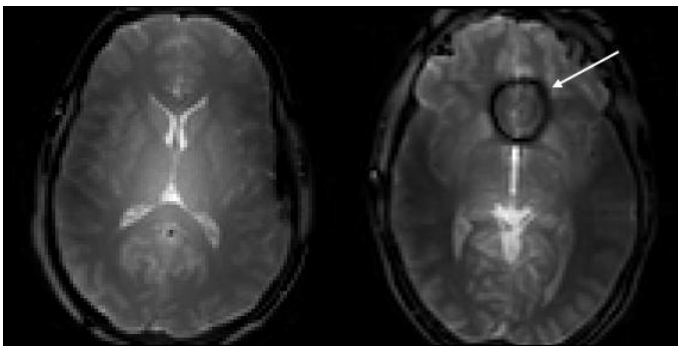

Figure 3-9: Example bFFE images at a higher and lower axial position, arrow indicates banding artefact (2 x 2 x 3 mm^3, FA = 50°, TE/TR = 1.8/3.6 ms, FOV = 192 x 192 x 3 mm^3).

3.2.2.4 Echo Planar Imaging

Many applications require high temporal resolution to allow monitoring of dynamic processes within the body. For example, functional MRI (fMRI) relies on temporal resolution of a few seconds to monitor the haemodynamic response.

Similarly bolus tracking of contrast agents requires high temporal resolution. Spin-warp imaging, as described above, would not be able to deliver high temporal resolution due to the slower k-space sampling trajectory.

EPI was developed by Mansfield *et al*. in 1977 [11] which was the advent of fast imaging techniques. EPI samples all of 2D k-space after a single excitation pulse – a single slice can be acquired in tens of milliseconds. To achieve this, the gradients are rapidly switched to traverse the entire 2D k-space after a single RF pulse, the most common trajectory is shown in Figure 3-10. Initial gradients move the sampling to a corner of k-space, they then scan back and forth across k_x, with small steps in k_y as shown schematically in the k-space diagram.

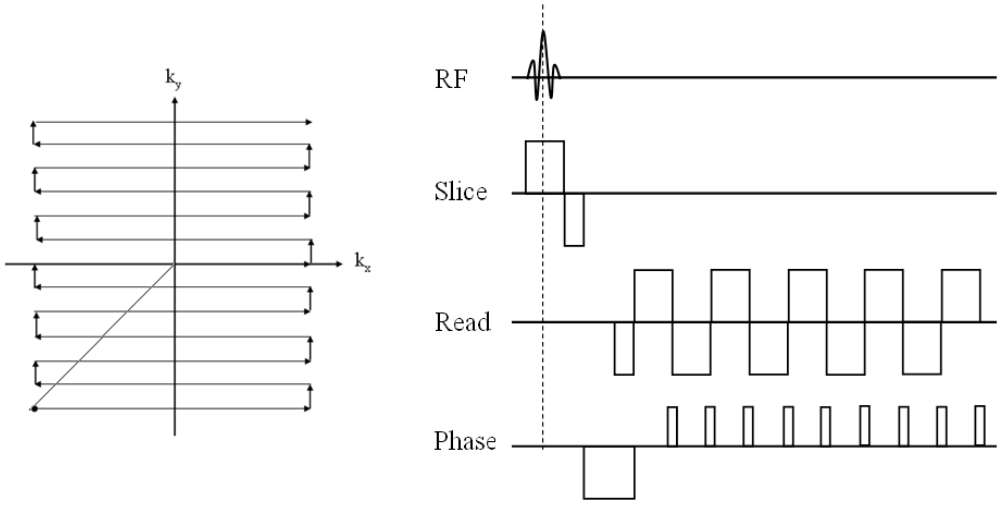

Figure 3-10: K-space trajectory and pulse sequence for 2D echo-planar imaging (not to scale, read gradients typically ~ 10 times strength of phase encode gradients).

Prior to Fourier transforming to reconstruct the image, the acquired signals must be reordered to account for the change in direction that k-space is sampled.

The EPI readout can be divided into sections (segmented EPI), where a few lines of k-space are acquired following each excitation. This can avoid the signal decaying excessively with T_2* due to the length of the readout and reduce some of the common artefacts associated with EPI (as detailed in Section 3.4), but can also introduce artefacts. Similar to spin warp imaging the Ernst angle is used to maximise the steady state signal, allowing for short TR imaging – acquiring slices in rapid succession.

3.2.2.5 3D EPI

In Section 3.2.2.4 2D-EPI was used to acquire an image but it can be adapted by two possible methods to image a 3D volume. One method is echo volumar imaging (EVI) [12] which samples the entirety of 3D k-space after a single excitation. Alternatively, 3D-EPI can be used which uses multiple excitations, following each a plane of k_x-k_y space is acquired, and steps through k_z with every excitation (Figure 3-11) [13]. The RF excitation is applied to the entire volume which increases the SNR as the signal comes from a volume rather than a single slab.

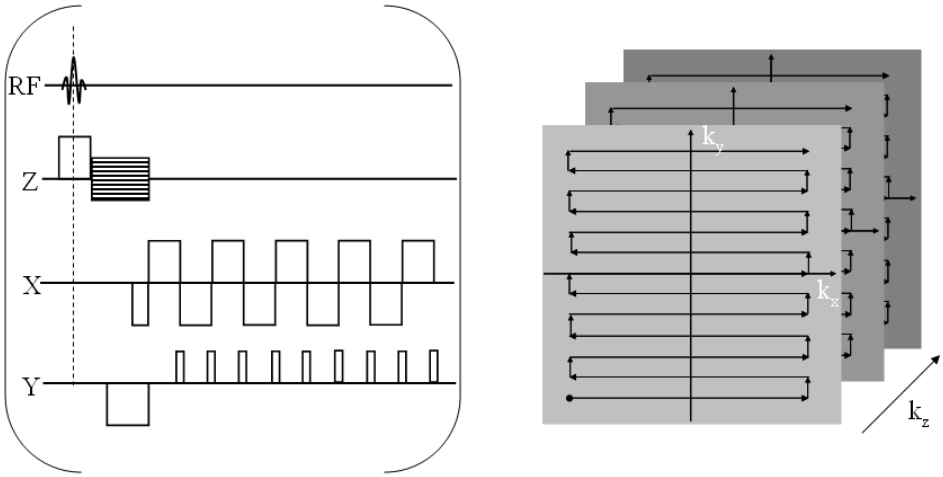

Figure 3-11: Pulse diagram and k-space trajectory for 3D-EPI.

EVI is not commonly used due to the long acquisition times causing signal decay with T_2*; this is more problematic at higher magnetic field strengths as T_2* shortens [14] increasing dephasing. 3D-EPI is more commonly used and more applicable for higher field imaging as it does not rely on long T_2*. It has been used for fMRI at 7 T, as the 3D technique increases SNR over the 2D technique for a given volume [13]. The flip angle is typically low (~ 15°) so as not to suppress the signal for successive planes of k-space, which has the advantage of reducing SAR (see Section 3.6).

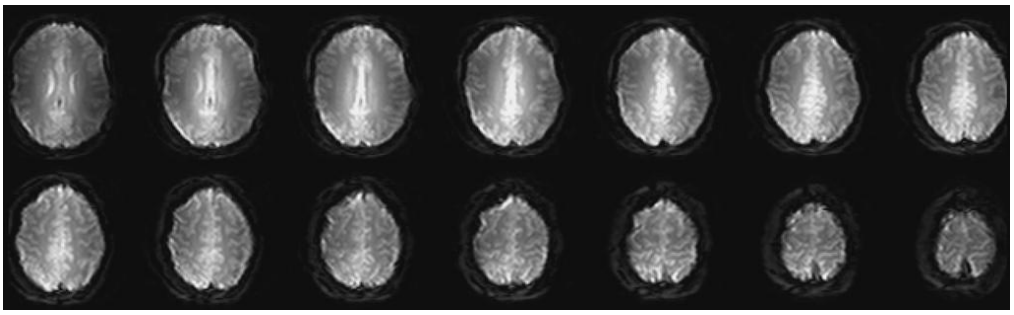

Figure 3-12: Example 3D-EPI images (2 x 2 x 3 mm^3, FA = 14°, TE/TR = 10/27 ms, FOV = 192 x 192 x 42 mm^3).

Figure 3-12 shows 3D-EPI images obtained at 7 T (TE/TR = 10/27 ms, voxel size of 2 x 2 x 3 mm^3, FOV 192 x 192 x 42 mm^3, flip angle (FA) = 14°). The benefit of 3D sequences is that the centre of k-space is acquired simultaneously; the slices are not staggered in time which is helpful for fMRI. The SNR increases as the signal arises from a large volume rather than a small slice. Also, the slice profiles within the 3D volume are better as they are not defined by the slice-selective RF pulses used in 2D imaging. 3D-EPI is used for perfusion imaging which is described in Chapter 5.

3.3 SPEEDING UP IMAGE ACQUISITION

For many applications, such as fMRI, cardiac imaging and perfusion imaging, the image acquisition needs to be fast. This could be to track a contrast agent, monitor function or to reduce motion artefacts. By speeding up the acquisition, distortions and image artefacts can be reduced. Several different techniques are often used. In the following sections segmented k-space, partial Fourier and parallel imaging (or SENSE) are discussed.

3.3.1 SEGMENTED K-SPACE ACQUISITION

If T_2/T_2^* decay is affecting image quality due to a long echo time, segmenting the acquisition can be helpful. Segmenting the readout divides the acquisition into multiple shorter *segments*, acquiring a section of k-space. This reduces the individual readout times following an excitation pulse, hence reducing signal decay due to T_2/T_2^*. However this generally increases the time to acquire the image volume, also patient movement can be a problem as they can move between (acquisition of) segments. Segmentation has been used to allow higher spatial resolution (e.g. for ASL perfusion imaging [15] and fMRI [16]).

3.3.2 PARTIAL FOURIER IMAGING

K-space is well characterised, the real component is symmetric and the imaginary component anti-symmetric about the centre, demonstrated in Figure 3-1 C/D. The relationship between the k-space signal, *s*, and the complex conjugate, *s**, is [2]:

$$s^*(k_x, k_y, k_z) = s(-k_x, -k_y, -k_z). \quad \textbf{3-10}$$

This can be used to reduce the amount of k-space sampled, the missing section can be estimated from the acquired section of data using these properties. Acquiring a fraction (> ½) of k-space can allow echo times to be reduced and/or reduced image acquisition time dependant on the direction that the partial imaging is applied. Reduced k-space acquisition in the frequency encode reduces the TE, reduction in the phase encode reduces the number of phase encode steps, and reduces the total acquisition time.

This is beneficial in certain techniques, like fMRI where high temporal resolution is required and in breath-hold MRI for body imaging where fast acquisitions are necessary. The main benefit is to reduce the echo time for high resolution imaging, reducing imaging distortions. However as less k-space is acquired the SNR of the image is reduced.

3.3.3 SENSE

Sensitivity encoding (SENSE) was introduced by Pruessmann *et al*. [17] in 1999. It is a commonly used technique to reduce scan time when a receive coil with multiple elements is used, these type of methods are known as *parallel imaging*. By accounting for each receiver coil having a specific sensitivity profile you can reduce the amount of k-space that is sampled.

To achieve this the distance between the sampled points in k-space is increased, but the maximum k-space values are unaffected thus maintaining spatial resolution. Reducing the sampling frequency would typically reduce the FOV causing aliasing (signal outside the FOV to wrap back into the image, shown in Figure 3-13) however with SENSE the FOV is maintained.

Prior to acquiring a scan with SENSE, a reference scan is performed that measures the sensitivities of all the receive elements. The reference scan used on the 7 T is typically a gradient echo with large FOV, coarse voxel size and low flip

angle (FOV = 300 x 300 x 450 mm^3, 4.69 mm isotropic voxels, FA = 1°). This creates an aliased image for each receive element (Figure 3-13).

The subsequent images are then reconstructed based on this reference scan to remove the aliased images and to produce an image with the full FOV. The SENSE factor of a scan, is the amount that sampled k-space has been reduced by, which is limited by the number of receive coil elements.

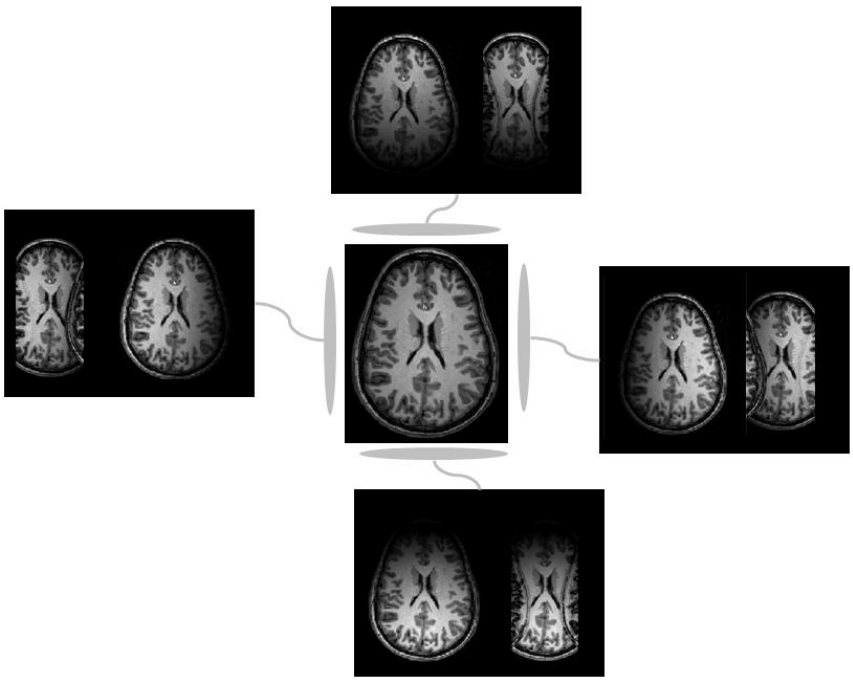

Figure 3-13: Schematic diagram of SENSE. A 4 coil receive set up is shown. For each coil the full FOV image and the reduced FOV image due to reduced k-space sampling frequency are shown.

3.4 IMAGE ARTEFACTS

Image artefacts can arise from a number of factors; distortions caused by image acquisition, T_2* effects, chemical shift effects, image wrap, patient movement and sampling errors. The cause of these, the impact on the image and how they can be improved upon will be briefly summarised.

3.4.1 DISTORTIONS

Image distortions, how much the MR image deviates from the sample, is dependant upon the imaging sequence. The receive bandwidth (BW) is the range of frequencies which the receiver will accept. It is dependant upon the readout, gradient strength and sampling rate, it impacts upon SNR as

$$SNR \propto \frac{1}{\sqrt{BW}}. \quad \textbf{3-11}$$

Hence a small bandwidth increases SNR, but it can increase image distortions. The receive bandwidth determines the amount which a signal is shifted due to the chemical shift. The spatial shift can be quantified as

$$\Delta x = \frac{\Delta\omega}{BW_{pixel}} x, \quad \textbf{3-12}$$

where Δx is the spatial shift of the signal in mm, BW_{pixel} is the receiver bandwidth per pixel (frequency of k-space sampling), $\Delta\omega$ is the frequency shift from the Larmor frequency (γB_0) and x is the voxel size in mm. Hence in areas of magnetic field inhomogeneity large image distortions can arise due to large $\Delta\omega$. This is most problematic for EPI due to a small bandwidth increasing the distortions (typically the BW_{pixel} is much shorter in the phase than the read direction, causing different distortions in the two directions).

3.4.2 CHEMICAL SHIFT

Further problems can be caused by chemical shift effects. The resonant frequency of a proton will be dependent on their chemical environment. This causes the protons in water and fat to have a different resonant frequency as they experience slightly different magnetic fields [2]. This can cause an artefact due to the spatial shift of the fat signal (Figure 3-14 A) in the frequency encode direction due to the frequency shift between fat/water [2]. The spatial shifting of the fat signal will be a problem if the frequency difference between fat and water is of the same order as the bandwidth per voxel. In brain imaging, the fat signal is generated from the scalp fat, this can be reduced by a technique called *fat suppression*, where either a suppression RF pulse at the resonant frequency of the fat is applied or an inversion pulse is used (e.g. STIR, short TI inversion recovery) prior to image acquisition to reduce the signal arising from the fat.

3.4.3 *SAMPLING ERRORS*

Artefacts can arise due to the method of sampling k-space. The Nyquist theorem states that the highest frequency, f_{max}, that can be sampled is:

$$f_{max} = \frac{1}{T_{sample}}, \quad \textbf{3-13}$$

where T_{sample} is the period between samples. If the FID contains signals with frequency greater than f_{max} ($f_{max}+\delta f$) they will be mapped to frequency $f_{max}-\delta f$. Image wrap (Figure 3-14 B) can occur when the field of view (FOV) is smaller than the volume being excited. Signals from outside the FOV have frequencies > f_{max} and wrap into the opposite side of image. This can be resolved by either making the FOV larger or using suppression pulses (*rest slabs*) that suppress the signal from outside the imaging volume. Often sequences incorporate fold-over suppression where k-space is oversampled to reduce fold over artefacts.

In EPI, due to the alternate direction of lines in k-space a phenomena called the Nyquist or N/2 ghost can occur. Some of the sampled lines of k-space need to be inverted to take account of the two read directions. However if the lines are acquired off centre due to imperfect acquisition this will cause a ghost image in the reconstructed image.

3.4.4 *MAGNETIC SUSCEPTIBILITY*

Magnetic susceptibility is defined as the ratio of the induced magnetisation **M** to the external magnetisation **H**;

$$\chi = \frac{\mathrm{M}}{\mathrm{H}} \quad \textbf{3-14}$$

Materials are split into three categories dependant on their χ value; diamagnetic materials have low negative values, paramagnetic materials have low positive values and ferromagnetic materials have high positive values. Diamagnetic materials, when placed in a magnetic field, acquire a magnetisation proportional to the applied field but in the opposite direction. Paramagnetic materials acquire magnetisation in the same direction as the magnetic field; both diamagnetic and paramagnetic materials lose their magnetisation when the field is removed. Ferromagnetic materials interact more strongly with applied fields, and can be permanent magnets – sources of magnetic fields [18]. Where there are boundaries of different magnetic susceptibilities, this causes a change in the local

magnetic field. The sinuses cause particular problems due to the large pocket of air next to the brain tissue, and EP images at this level are commonly distorted (Figure 3-14 C).

Magnetic field inhomogeneity can stem from underlying poor magnet homogeneity, as well as disturbances to the magnetic field when a sample is placed in the magnetic field due to different magnetic susceptibilities. The decay of the signal after the RF excitation pulse due to T_2* effects can be problematic, more so for EPI as the time between excitation and measurement is long. This is a problem in areas of poor magnetic field homogeneity where T_2* is short as $\Delta R_2^* \propto \Delta B_0$ [19]. To improve image quality good shimming of the magnetic field is required to increase homogeneity. This can be achieved by using shim coils to apply a further field, or by placing blocks of diamagnetic materials (e.g. [20]) around the sample to correct the field inhomogeneities. Images can also be improved by reducing the echo time (e.g. through segmented acquisitions, SENSE or partial Fourier) as described in Section 3.3.

3.4.5 PATIENT MOTION

Patient movement can also cause significant artefacts – this is more commonly associated with body imaging where respiration causes organ motion. However subjects unfamiliar with the scanner environment can often move and can be a problem for brain imaging especially in patients and at high resolution. 3D scans are more susceptible to motion artefacts as the entire volume of k-space is sampled together. Figure 3-14 D is a 3D T_2* weighted scan that took approximately 10 minutes to acquire and motion artefacts can be seen as blurring of the image, seen around the front of the brain. Motion can also cause image ghosting, where further faint reproductions of the image are seen around the main image. This is due to the time taken to acquire the phase encode lines, periodic motion such as respiration will cause ghosting, whereas other motion will cause general diffuse noise. Fast imaging techniques are used to reduce motion artefacts e.g. EPI / bFFE.

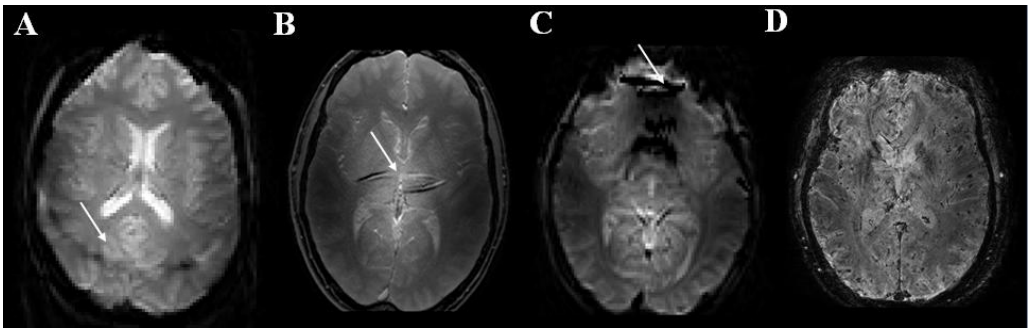

Figure 3-14: Image artefacts (A) cause by fat (B) fold over (C) susceptibility differences and (D) patient motion.

3.5 HARDWARE

The work presented in this thesis was performed on a Philips 7.0 T Achieva system. Therefore, specific hardware information will be provided for this system. A schematic diagram of an MRI scanner is shown in Figure 3-15.

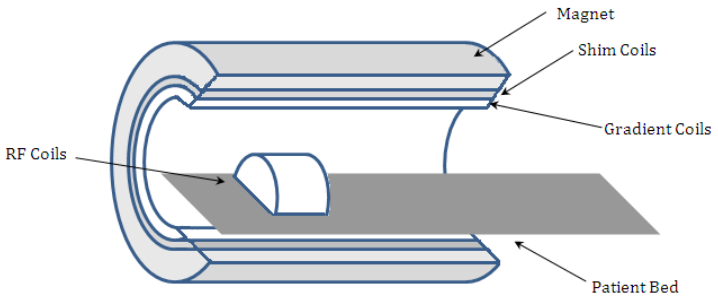

Figure 3-15: Schematic of an MRI scanner with local transmit/receive coils.

3.5.1 MAGNET

The magnet is a 7.0 T horizontal bore solenoid superconducting magnet produced by Magnex now Varian. Liquid helium is used to keep the coils superconducting, a cryostat and cryocoolers are used to keep the helium cool and reduce boil-off (older systems would have used a jacket of liquid nitrogen rather than a cryocooler). The stability of the magnet is 0.10 ppm in a 25 cm diameter spherical volume. To shield the magnet, an iron box weighing 200 tonnes surrounds the magnet to reduce the extent of the fringe field. The extent of the fringe field needs to be short to limit the field outside the building which would be dangerous for people with contraindications to strong magnetic fields (see section 3.6.1). A 5 Gauss (5 mT) line is marked, to indicate when you are entering the magnetic field.

3.5.2 *SHIM COILS*

Shimming is the process of making the static B_0 field more homogeneous to avoid distortions/signal drop-outs in the image. Passive shimming uses small pieces of diamagnetic material to compensate for inhomogeneities in the magnetic field (e.g. [21]). Active shimming uses current passing through small shim coils to correct the field; these are optimised for that particular session/subject. The scanner can implement its own optimisation of the shim fields using the FASTMAP technique. However, image based shimming provides the most robust technique, such as that developed by Poole and Bowtell [22] which was used in this thesis. This uses a B_0 field map taken prior to the main image to optimise the shim fields to minimise the variation in the static B_0 field.

3.5.3 *GRADIENT COILS*

Gradient coils are required to set up the linear gradients in all three directions (x, y and z) for imaging. The shape of the coils depends on the gradient required. As high currents are required to produce the required gradients the coils are cooled, typically water-cooled, to reduce the temperature due to resistive heating. The gradient coils on the 7 T can produce a maximum field gradient of 40 mT/m with a slew rate of 200 mT/m/ms (maximum rate of change). However to reduce PNS (see Section 3.6.3) these are limited to 33 mT/m and 166 mT/m/ms in the work in this thesis.

3.5.4 *RF COILS*

Here the set-up for brain MRI is described where separate transmit and receive coils are used. For transmission, a head volume transmit coil is used. A 16 or 32 channel coil within the transmit coil is used for receive (Figure 3-16). The multiple receive elements allow for SENSE techniques to reduce acquisition times. At ultra high field the wavelength of the RF pulse is decreased (order of 1m) this causes increased interactions between the RF pulse and the sample due to the comparable length scales [23]. This causes RF inhomogeneity and hence SAR profile inhomogeneities [23]. To reduce absorbed power the coil designs at 7T have been generally restricted to volume coils as shown here.

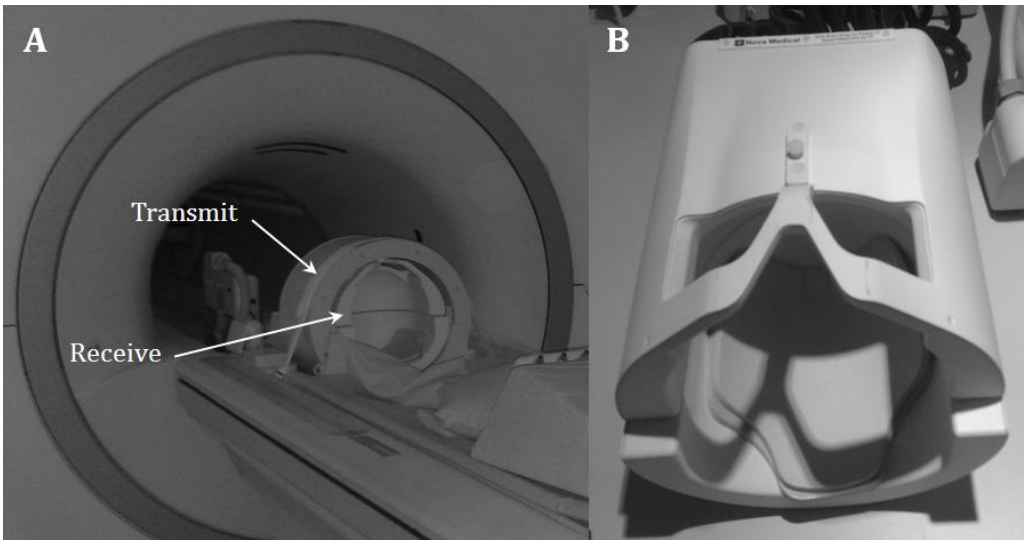

Figure 3-16: (A) 7 T scanner showing RF volume transmit and 32-channel receive coils (B) 32 channel receive coil. Photos courtesy of Dr O. Mougin, SPMMRC.

3.5.5 CONSOLE

The scanner is controlled through a console, which allows the user to set up a sequence. This calculates the RF and gradient waveforms, and then relays these to the spectrometer. The received signals, measured using a phase sensitive detector, will be amplified before being reconstructed and displayed on the console. The console's software calculates SAR limits and monitors gradient temperature to ensure safe running of the scanner.

3.6 SAFETY

MRI utilises low frequency radiation of comparatively low energy and as such does not pose the risks that techniques that use ionising radiation, such as X-rays, do. However there are still dangers associated with MRI scanners, and precautions must be taken to ensure the safety of the volunteers and the scanner operators. Here the concerns associated with the static field, RF and gradients are considered separately.

3.6.1 STATIC MAGNETIC FIELDS

The static magnetic field used to create the MR images are potentially hazardous due to the attraction of magnetic objects towards the scanner bore. Large objects would be pulled with significant force, acting as a projectile. Also, implants such as aneurysm clips and pacemakers could malfunction due to the interaction with the magnetic field. To avoid these types of incidents, all subjects with access to the magnet must be screened for pacemakers and clips, all metal objects (e.g.

belts, keys) need to be removed beforehand. The areas that you can be exposed to magnetic fields greater than 5 Gauss (0.5 mT) are marked with red/white tape (5 Gauss line).

To reduce stray fields the 7 T is shielded in an iron box, this is to ensure that people passing are not affected by the magnetic field. The field is contained so that access to the magnetic field can be restricted. The magnet room of the 7 T is situated in a control room behind a coded door – this is to stop accidental access to the magnet.

The static field can also cause people to feel nauseous, dizzy (vertigo), and give a metallic taste in the mouth or to see small flashes when moving through the field [24]. These can be avoided by moving slowly when around the magnet, and moving subjects into the magnet slowly. Particular care should be taken when swapping coils.

3.6.2 RF FIELD

RF radiation can potentially cause tissue heating due to the power deposited into the tissue. This could damage tissues particularly those that are not well perfused as the blood flow is not present to cool the area down by dissipating the heat. The measure of RF power deposition is called the Specific Absorption Rate (SAR), which is calculated by the scanner for each scan and coil configuration. SAR is dependent on the sequence (e.g. flip angle, pulse timings) and the tissue size/density. SAR is measured in Watts per kilogram of body weight.

SAR limits are in place to avoid excessive tissue heating, the Health Protection Agency recommends for normal procedures that whole body temperature rises should not exceed 1°C and to follow the 2004 ICNIRP (International Commission on Non-Ionizing Radiation Protection) guidelines on whole body SAR, which are 2 W/Kg for normal clinical procedures and 4 W/Kg for other procedures.

Furthermore, RF fields can heat metallic objects which in contact with skin/tissue could cause burns. This risk is diminished by eliminating metal inside the bore of the magnet as far as possible and insulating where necessary (e.g. call button, VCG leads) and volunteers are screened for metal implants. Metal based or conductive dyes can also be present in inks used for tattooing – old, dark tattoos can cause skin burns. Again, patient screening is used to avoid this occurring. In

addition, circulating currents can be induced in the body, subjects are placed in the scanner without arms or legs crossing to avoid this.

Patients need to be positioned in the magnet without their arms or legs crossing, or loops being formed due to the other equipment in the scanner. This can cause current loops to be set up and burns may result.

3.6.3 GRADIENT FIELD

The rapidly switching gradients that are used for imaging can induce currents along the nerves in the body. This effect is called Peripheral Nerve Stimulation, or PNS, and can cause discomfort. It is avoided by keeping the gradient switching rate low (< 60 mT/m/ms) [25]. As described previously, the gradients used in the experimental work described in this thesis were limited to a strength of 33 mT/m and slew rate of 166 mT/m/ms.

3.6.4 OTHER SAFETY CONSIDERATIONS

Another safety concern is the acoustic noise generated by the scanner during imaging (values of 100 dB for fast imaging sequences at 3 T [26]). All volunteers must wear ear protection, as must anybody working around the magnet during operation. This is a concern in foetal imaging, as the sound can be transmitted through the mother so the sequences are designed to be quieter.

MRI scanners use cryogens (e.g. liquid helium and nitrogen) to keep the magnet superconducting. A quench of the magnet, or emergency discharge of these cryogens due to the wires becoming resistive rather than superconducting resulting in heating, would release these as the form of gases. These would displace the oxygen if they were discharged into a closed/un-ventilated room, and asphyxiate the occupants. Oxygen depletion alarms are used to warn scanner operators of this situation. If working with cryogens, protective equipment (mask, gloves) must be worn to prevent cold burns and training given.

3.7 ETHICS

When scanning patients and healthy volunteers all studies must be approved by an ethics committee to ensure appropriate guidelines are followed. All the studies in this thesis were approved by the University of Nottingham ethics committee, and all volunteers provided informed, written consent to take part in the studies.

A concern when scanning patients is the possibility of incidental abnormal findings on scans. A protocol is in place in the event of an abnormal finding, the volunteer is not shown their images and the images are sent to a radiologist for review. Scans are not routinely sent for investigation as incidental findings can impact on the subject's ability to obtain insurance, work or a mortgage. In the written consent, subjects must confirm their willingness to be informed of incidental findings.

3.8 REFERENCES

1. McRobbie, D.W., E.A. Moore, M.J. Graves, and M.R. Prince, *MRI: From Picture to Proton*. 2010, Cambridge: Cambridge University Press.
2. Haacke, M., R. Brown, M. Thompson, and R. Venkatesan, *Magnetic Resonance Imaging: Physical Principles and Sequence Design*. 1999, New York: Wiley-Liss.
3. Edelstein, W.A., J.M.S. Hutchison, G. Johnson, and T. Redpath, *Spin warp NMR Imaging and Applications to Human Whole-Body Imaging.* Phys. Med. Biol., 1980. **25**: p. 751.
4. Ernst, R.R. and W.A. Anderson, *Application of Fourier Transform Spectroscopy to Magnetic Resonance.* The Review of Scientific Instruments, 1966. **37**(1): p. 93-102.
5. Wright, P.J., O.E. Mougin, J.J. Totman, A.M. Peters, M.J. Brookes, R. Coxon, P.G. Morris, M. Clemence, S.T. Francis, R. Bowtell, and P.A. Gowland, *Water Proton T1 Measurements in Brain Tissue at 7, 3 and 1.5T using IR-EPI, IR-TSE and MPRAGE: results and optimisation.* Magn. Reson. Mater. Phy, 2008. **21**: p. 121-130.
6. Haase, A., J. Frahm, D. Matthaei, W. Hanicke, and K.D. Merboldt, *FLASH imaging. Rapid NMR imaging using low flip-angle pulses.* Journal of Magnetic Resonance (1969), 1986. **67**(2): p. 258-266.
7. Haase, A., *Snapshot flash mri. applications to t1, t2, and chemical-shift imaging.* Magnetic Resonance in Medicine, 1990. **13**(1): p. 77-89.
8. Oppelt, A., R. Graumann, H. Barfuss, H. Fischer, W. Hartl, and W. Schajor, *FISP - a new fast MRI sequence.* Electromedica, 1986. **54**: p. 15-18.
9. Haacke, E.M., P.A. Wielopolski, J.A. Tkach, and M.T. Modic, *Steady-state free precession imaging in the presence of motion: application for improved visualization of the cerebrospinal fluid.* Radiology, 1990. **175**: p. 545-552.
10. Cox, E., *Quantitative Whole Body Imaging at High Field*, in *School of Physics and Astronomy*. 2009, University of Nottingham: Nottingham.
11. Mansfield, P., *Multi-planar image formation using NMR spin echoes.* J. Phys. C: Solid State Phys., 1977. **10**(L55-L58).
12. Mansfield, P., A.M. Howseman, and R.J. Ordidge, *Volumar imaging using NMR spin echoes: echo-volumar imaging (EVI) at 0.1T.* J. Phys. E: Sci. Instrum, 1989. **22**: p. 324-330.
13. Poser, B.A., P.J. Koopmans, T. Witzel, L.L. Wald, and M. Barth, *Three dimensional echo-planar imaging at 7 Tesla.* NeuroImage, 2010. **51**: p. 261-266.
14. Peters, A.M., M.J. Brookes, F.G. Hoogenraad, P.A. Gowland, S.T. Francis, P.G. Morris, and R. Bowtell, *T2* Measurements in Human Brain at 1.5, 3 and 7T.* Magnetic Resonance Imaging, 2007. **25**: p. 748 - 753.

15. Feinberg, D., S. Ramanna, and M. Gunther. *Evaluation of new ASL 3D GRASE sequences using Parallel Imaging, Segmented and Interleaved k-space at 3T with 12- and 32-channel Coils.* in *Proceedings of the 17th Annual Meeting of ISMRM*. 2009. Hawaii, USA: 623.
16. Hoogenraad, F.G.C., P.J.W. Pouwels, M.B.M. Hofman, S.A.R.B. Rombouts, C. Lavini, M.O. Leach, and E.M. Haacke, *High-resolution segmented EPI in a motor task fMRI study.* Magnetic Resonance Imaging, 2000. **18**(4): p. 405-409.
17. Preussmann, K.P., M. Weiger, M.B. Scheidegger, and P. Boesiger, *SENSE: Sensitivity Encoding for Fast MRI.* Mag. Res. Med., 1999. **42**: p. 952-962.
18. Pollack, G.L. and D.R. Stump, *Electromagnetism*. 2002, San Francisco: Addison Wesley.
19. Kurland, R.J. and F.G.H. Ngo, *Effect of Induced Field Inhomogeneity on Transverse Proton NMR Relaxation in Tissue Water and Model Systems.* Mag. Res. Med., 1986. **3**: p. 425-431.
20. Yang, Q.X., W. Mao, J. Wang, M.B. Smith, H. Lei, X. Zhang, K. Ugurbil, and W. Chen, *Manipulation of image intensity distribution at 7.0 T: Passive RF shimming and focusing with dielectric materials.* Journal of Magnetic Resonance Imaging, 2006. **24**(1): p. 197-202.
21. Wilson, J.L. and P. Jezzard, *Utilization of an Intra-Oral Diamagnetic Passive Shim in Functional MRI of the Inferior Frontal Cortex.* Mag. Res. Med., 2003. **50**: p. 1089-1094.
22. Poole, M. and R. Bowtell, *Volume parcellation for improved dynamic shimming.* Magnetic Resonance Materials in Physics Biology and Medicine, 2008. **21**(1-2): p. 31-40.
23. Lattanzi, R., D.K. Sodickson, A.K. Grant, and Y. Zhu, *Electrodynamic Contraints on Homogeneity and Radiofrequency Power Deposition in Multiple Coil Excitations.* Mag. Res. Med., 2009. **61**: p. 315-334.
24. Chakeres, D.W. and F. de Vocht, *Static magnetic field effects on human subjects related to magnetic resonance imaging systems.* Progress in Biophysics and Molecular Biology. **87**(2-3): p. 255-265.
25. Ham, C.L.G., J.M.L. Engels, G.T. van de Wiel, and A. Machielsen, *Peripheral Nerve Stimulation during MRI: Effects of High Gradient Amplitudes and Switching Rates.* JMRI, 1997. **7**: p. 933-937.
26. Price, D.L., J.P. De Wilde, A.M. Papadaki, J.S. Curran, and R.I. Kitney, *Investigation of acoustic noise on 15 MRI scanners from 0.2 T to 3 T.* Journal of Magnetic Resonance Imaging, 2001. **13**(2): p. 288-293.

4 INTRODUCTION TO BRAIN FUNCTION AND FUNCTIONAL BRAIN IMAGING TECHNIQUES

4.1 OUTLINE

This chapter describes basic brain anatomy and the metrics used to describe brain function. Methods to measure brain function with emphasis on MR methods of brain function are introduced; PET, SPECT, MEG, EEG, BOLD, arterial spin labelling (ASL), contrast agent based perfusion measures and magnetic resonance spectroscopy (MRS). The methodology for ASL is discussed in more detail including the mathematical model for perfusion quantification, as this forms an emphasis of this thesis.

4.2 BRAIN FUNCTION PHYSIOLOGY

The brain is only about 2 % of total body weight but uses a disproportionate amount of resources; 20 % of total oxygen consumption [1], 25 % of glucose, and approximately 14 % of the total cardiac output [1] at rest. The brain is supplied by four main arteries, the left and right carotid arteries and the left and right vertebral arteries (Figure 4-1 A). The vertebral arteries merge to form the basilar artery, which joins the carotid arteries at the Circle of Willis [1]. The large arteries branch into arterioles and capillaries to allow for perfusion of water, CO_2, O_2 and waste products between blood and tissue cells (Figure 4-1 B). These capillaries merge into venules and a network of smaller veins before the blood drains into the sagittal sinus and jugular vein in the neck.

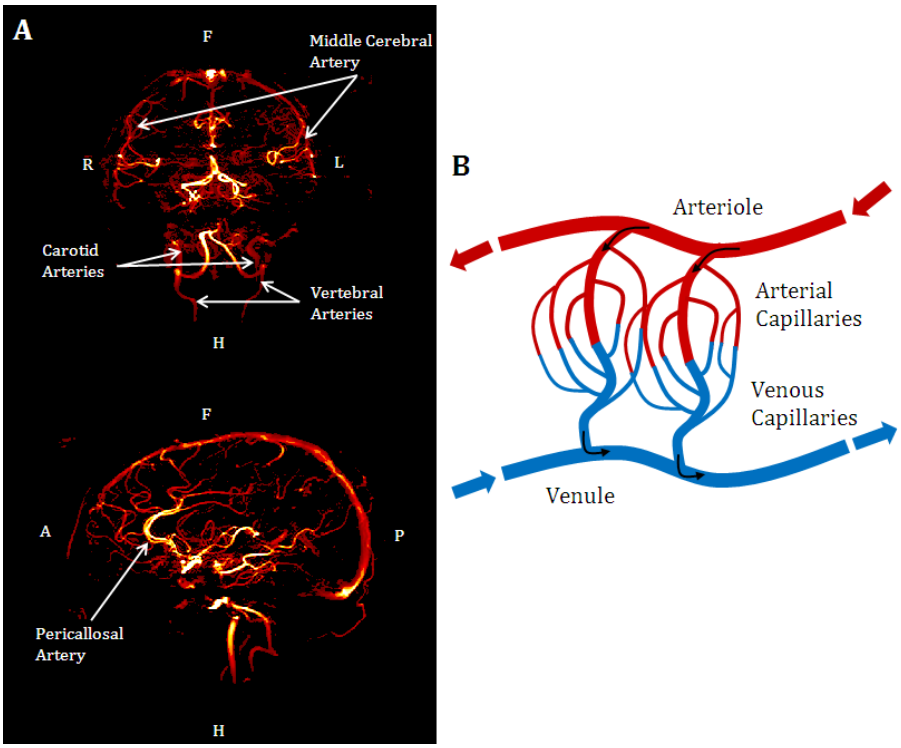

Figure 4-1: (A) 7 T MR angiogram images of vessels in the brain and neck in coronal and sagittal planes, (B) schematic of capillary vasculature, arrows indicate direction of blood flow.

The blood-brain barrier (BBB) allows essential molecules, such as glucose and oxygen, to enter the brain from the blood but restricts the movement of large molecules [2]. It aims to protect the brain from infections/viruses crossing from the blood, however some substances that could treat disorders cannot cross into the tissue due to the BBB. In comparison the capillaries in the rest of the body generally allow transport of larger molecules, e.g. hormones, which can be beneficial as well as harmful. Breakdown of the BBB can be seen in certain clinical conditions, such at Multiple Sclerosis (MS), bacterial meningitis, Alzheimer's and AIDS (acquired immune deficiency syndrome) [3].

To monitor the function of the brain a number of measurable quantities are defined and summarised in Table 4-1.

Metric	Symbol	Definition	Units
Cerebral Blood Flow	CBF	Volume of arterial blood that is delivered to 100 g of brain tissue per minute	ml/100g/min
Cerebral Blood Volume	CBV	Volume of blood present in 100g of tissue	ml/100g
Oxygen Extraction Fraction	OEF	Amount of oxygen extracted by the brain from the available oxygen in the blood	-
Cerebral metabolic rate of oxygen consumption	$CMRO_2$	Amount of oxygen metabolised by the brain per minute	μmol/min

Table 4-1: Summary of metrics used to describe brain function.

4.3 FUNCTIONAL BRAIN IMAGING

Magnetic resonance imaging provides a method of imaging structures in the body, which can aid in the identification of abnormalities e.g. tumours. However it can also provide a measure of *function* to aid our understanding of how the body works and to improve clinical practices. In addition to MRI, other imaging modalities can provide a measure of brain function; PET (positron emission tomography), SPECT (single photon emission computed tomography), EEG (electroencephalography) and MEG (magnetoencephalography).

PET uses radiopharmaceuticals that contain an isotope (e.g. ^{15}O, ^{13}N, ^{18}F) which emit positrons. These, on colliding with an electron, emit two photons in opposite directions. The photons are detected by a ring of detectors; coincident detected pairs of events can be used to detect where the photons originated from. However this technique does have limited spatial resolution. The radiopharmaceuticals used tend to have a short half life, making it generally necessary to manufacture them on-site using a cyclotron leading to PET being expensive. Dependant on the tracer used, different aspects of tissue function can be investigated, e.g. $CMRO_2$ and OEF.

SPECT uses tracers that emit gamma rays (e.g. ^{99}Tc, ^{123}I), which are then detected by a gamma camera. SPECT imaging is complicated by scattering of the photons, as pairs of events are not being monitored photons that have scattered off objects can be reconstructed to the wrong origin. However, SPECT is less expensive than

PET and can be used for many of the same measurements, commonly for the assessment of CBF [4].

EEG and MEG both work on the principle that neurons within the brain have small electric currents passing through them which generate small electric and magnetic fields [4]. EEG uses an array of electrodes placed in contact with the scalp using a cap and conductive gel. The electric potentials generated by neuronal firing, which are of the order of micro volts, can then be measured. The measurements made on the surface of the scalp can be projected back into the brain to localise the active brain area. However, this is a mathematically ill-posed problem (no unique solution) and requires complex source localisation algorithms. The EEG signal can be corrupted by interference from the subject's heart beat, eye and muscle movement. Furthermore, the different conductivities of the brain, scalp and skin can disturb the electric fields, limiting the accuracy of the source localisation, resulting in low spatial resolution. However EEG has the benefit of being a relatively inexpensive method making it a useful clinical technique [4].

MEG uses the magnetic fields produced by neuronal firing to monitor brain function. Using SQUID (superconducting quantum interference device) magnetometers the small magnetic field (of the order of fT) produced by neurons can be detected [4]. Source localisation is better in MEG than EEG, as the magnetic field is not distorted by the skull/scalp. But, the spatial resolution is still low compared to other techniques, and like EEG, interference arises from eye and muscle movement. MEG is an expensive technique, due to the requirement of a magnetically shielded room, and liquid helium for the SQUIDS. However, it has superior temporal resolution to MRI (further detail on MEG is provided in Chapter 6).

4.4 BRAIN FUNCTION MEASUREMENTS MADE WITH MR

The common MR measures used to probe brain function are summarised in Figure 4-2. Upon neuronal activity there are changes in cerebral blood flow, cerebral blood volume, and the cerebral metabolism of oxygen resulting in a change in deoxyhaemoglobin levels. Four MR functional imaging techniques, Arterial Spin Labelling (ASL), Blood Oxygenation Level Dependant (BOLD) contrast, MR spectroscopy (MRS) and the use of exogenous contrast agents, are common ways of measuring these aspects of brain function. Contrast agents and ASL can also be used to measure resting values of cerebral blood flow and blood volume, and MRS of metabolite levels respectively.

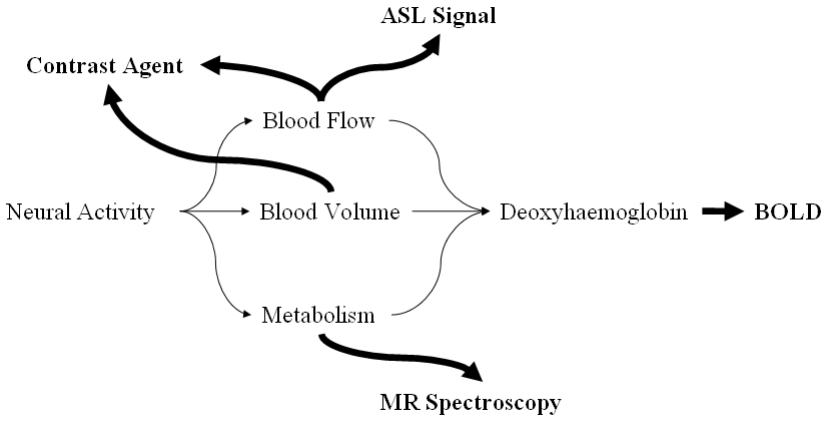

Figure 4-2: Methods of measuring brain function using MR.

4.4.1 *BOLD*

The most common technique for monitoring brain activation is functional magnetic resonance imaging (fMRI) which uses the BOLD (blood oxygenation level dependant) contrast mechanism. The biophysics of the BOLD response has yet to be fully understood; however can be described simply as a change in the relative levels of deoxy- and oxyhaemoglobin in the blood [5]. Deoxyhaemoglobin is a paramagnetic molecule whereas oxyhaemoglobin is diamagnetic. Deoxyhaemoglobin in the blood causes a susceptibility difference between the blood vessel and tissue which causes variations in the local T_2*, dependant on the concentration of deoxy- and oxyhaemoglobin [6].

Upon neuronal activation, blood flow increases to supply the active area with more oxyhaemoglobin. This is induced by the release of neurotransmitters from the activated neurons which cause the local vessels to dilate reducing resistance

in the vessels increasing flow [7]. Vessels further upstream also dilate to allow the increase in flow, this effect has been attributed to different mechanisms (e.g. flux of potassium ions, nitrous oxide, adenosine (see [7])). Oxygen is then extracted from the blood to the cells at a slightly higher rate than at rest to keep up with demand, schematically represented in Figure 4-3. These changes result in an excess of oxyhaemoglobin (less deoxyhaemoglobin) and hence an increase in the MR signal, due to an increase in T_2* resulting in less extravascular dephasing of the MR signal [5]. At higher field strengths (> 4 T) the intravascular contribution is reduced due to a reduction in blood T_2 [8].

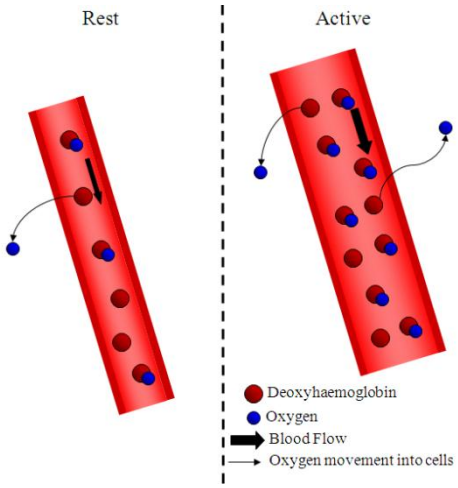

Figure 4-3: Schematic of the origins of the BOLD effect.

The time course of this BOLD signal can be monitored by rapid image acquisition during the presentation of a stimulus (e.g. flashing checkerboard) or whilst the subject is performing a task (e.g. finger tapping). Functional imaging is performed using a sequence sensitive to T_2* to monitor the changes in susceptibility, hence the standard sequence used is a gradient-echo (GE) EPI acquisition. The GE-EPI echo time chosen is crucial for optimal fMRI contrast. A sufficient echo time (TE) is needed for the difference in T_2* between the two states (active and rest) to be apparent, but the echo time should not be so long that the signal has decayed. It can be shown that the optimal TE is that equal to the T_2* of the grey matter [9], through maximising the difference between the two signals accounting for a small change in T_2* between activation and rest.

The BOLD signal change is delayed relative to the start of the stimulus; this is due to the haemodynamic response, it takes a few seconds for the vascular system to respond to the change in neuronal activity. The BOLD haemodynamic response can be characterised in terms of three main components. There is a possible

initial dip, thought to be due to an immediate increase in oxygen consumption [10]. The duration of the initial dip is short (~ 1s) compared to the other features of the BOLD response. It is thought that the initial dip has good spatial localisation to the site of the neuronal activity [11, 12]. The second feature is the main positive response or overshoot, which is delayed by a few seconds with respect to the stimulus and persists for a few seconds. The magnitude of the BOLD response is dependant on field strength, echo time and stimulus/location of activation, but is of the order of 6 % at 7 T and 4 % at 3 T. The third feature of the BOLD haemodynamic response is the post stimulus undershoot. The origin of the post stimulus undershoot is still debated [13, 14] but is thought to be most likely to be due to either a delayed vCBV recovery or prolonged elevation in $CMRO_2$. The post stimulus undershoot can persist for many seconds (~ 45 s) after the positive response has ended.

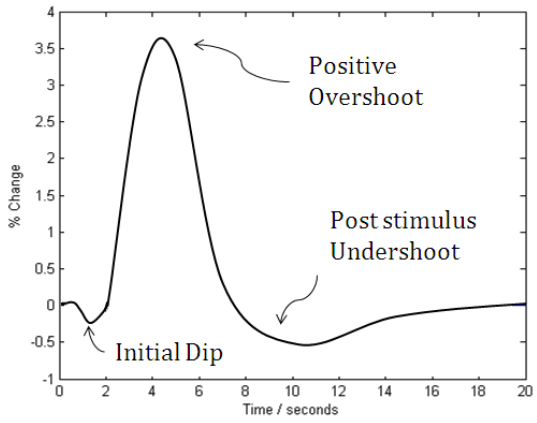

Figure 4-4: BOLD haemodynamic response function (hrf) to an event stimulus applied at t = 0s.

4.4.1.1 fMRI Data Analysis

An fMRI experiment can be performed in two main ways; event related or a block design. Event related uses brief stimuli, whereas a block design will have several repeats of the same task, shown schematically in Figure 4-5, to prolong the BOLD response for measurement. The task is typically repeated several times with periods of rest between.

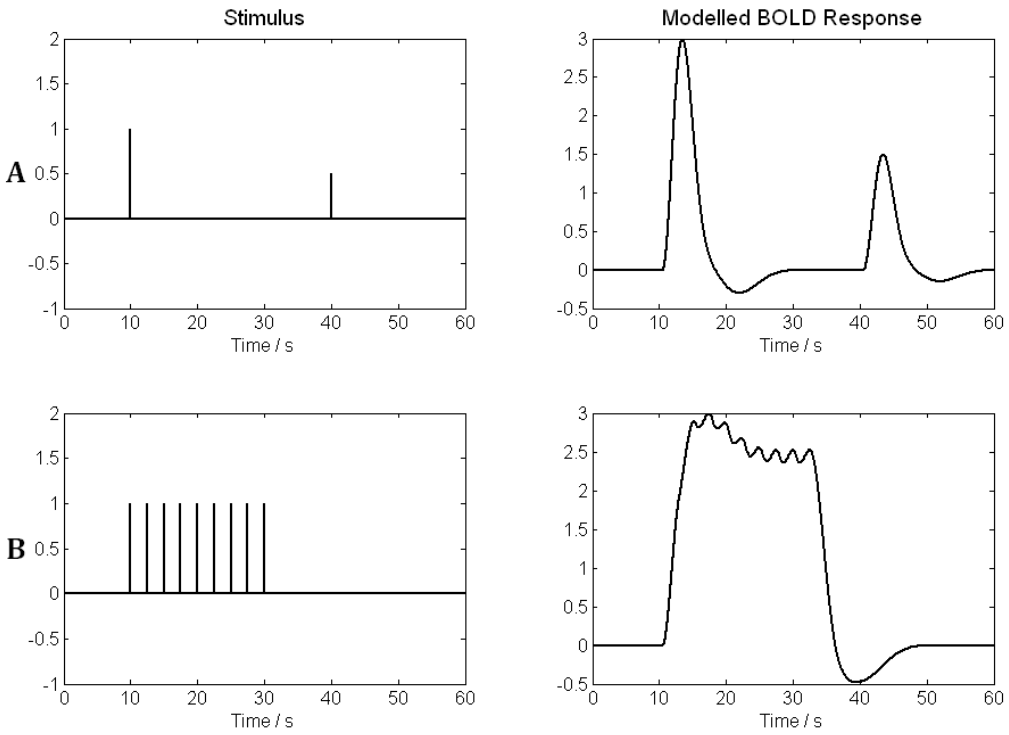

Figure 4-5: Schematic of (A) event related and (B) a block design fMRI experiment showing the stimulus and modelled BOLD response.

To localise active brain areas in response to a stimulus, the fMRI timecourse is fitted to a BOLD model (e.g. minimisation of square of residuals between data and fit), as described above. Prior to this, several processing steps are performed to maximise the success of detecting active voxels. The main pre-processing steps are motion correction (realignment), spatial smoothing and temporal filtering of the data.

Motion correction realigns all the data across time into the same space, reducing errors introduced by patient motion. This is normally performed using a 6 parameter, rigid body transformation, including three translation and three rotation corrections [15].

Sources of noise in fMRI data include thermal noise, physiological noise (heart beat, respiration), and non-task related neuronal activity [7]. Spatial and temporal smoothing are performed to increase the signal-to-noise ratio (SNR).

Spatial smoothing is often performed using a Gaussian kernel with FWHM of a few mm, this increases the signal-to-noise ratio of the data by averaging neighbouring signals. Applying too much spatial smoothing blurs the response and reduces sensitivity as active voxels are averaged with non-active regions, typically the smoothing kernel should match the size of activation. A degree of

spatial smoothing is also introduced by the motion correction performed (and associated interpolation).

Temporal smoothing helps remove noise that can arise from scanner drift (very low frequency noise), physiological noise (pulsatility effects) and thermal noise. Temporal smoothing can be achieved using linear or polynomial detrending to remove low frequency drift and filtering (e.g. a Gaussian) can be applied to remove specific frequency bands. The temporal smoothing applied needs to be carefully chosen so as not to remove the effect of interest and the typical cut off period is twice the task cycle duration.

The effect of physiological noise can be further reduced by use of RETROICOR [16], a retrospective software correction method for fMRI data. Physiological data, respiratory and cardiac cycle time courses, are recorded during fMRI acquisition. The fMRI timecourse assumed to be corrupted by additive noise from respiration and the cardiac cycle. The physiological noise is modelled as a 2nd order Fourier series based on the phase of the respiratory and cardiac cycle, which is then subtracted from the timecourse to reduce contributions from physiological noise.

Modelling the BOLD data to find active brain areas is most commonly performed using a general linear model (*GLM*) [17]. This assumes that the BOLD data (a vector **X,** with dimensions number of voxels *x* number of time points) is a linear combination of the stimuli (**G,** number of effects/stimuli *x* number of time points) plus noise (**e**).

$$\boldsymbol{X = G\beta + e.} \qquad \textbf{4-1}$$

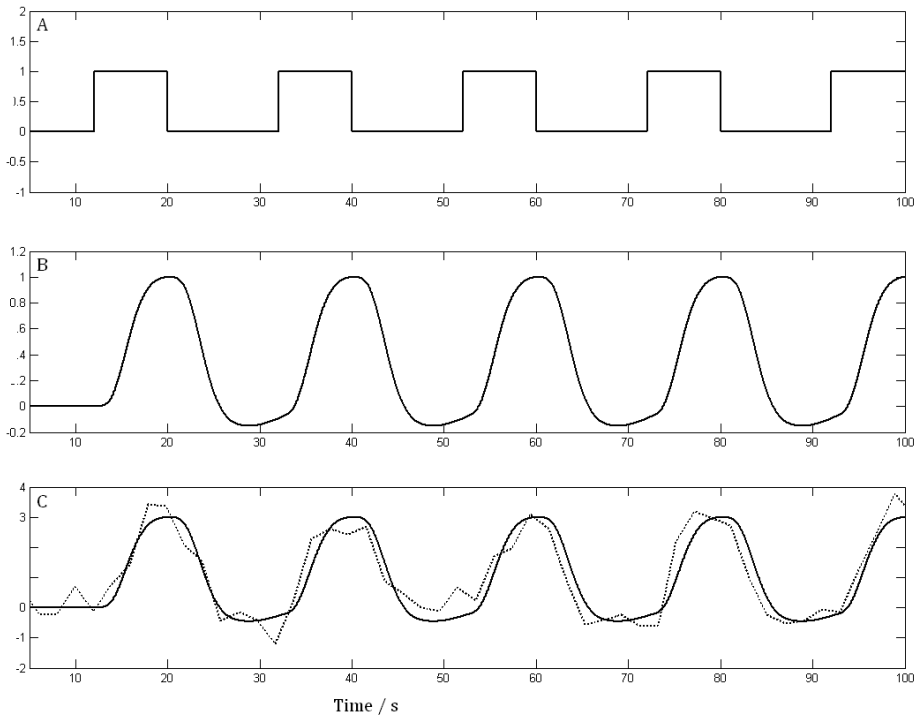

Figure 4-6: Schematic of GLM analysis (A) a binary representation of the stimulus (B) the BOLD hrf convolved with the stimulus to give *G* (C) simulated BOLD response (broken line) to the stimulus and the fitted curve with β = 3.

By convolving the input stimulus with the expected BOLD hrf, an expression for **G** is found. This is then fitted to each voxel timecourse to determine the value of β, this is shown in Figure 4-6. A statistical map is then formed, a T value is given by the estimate of β normalised by the uncertainty in that value (β/standard error (β)). T values can be converted to probability (p), and a threshold applied based upon the p value (e.g. $p < 0.01$). However due to the number of voxels analysed in a typical fMRI experiment, there would be a large numbers of voxels shown to be active by chance. To reduce the false-positive rate a further correction is applied to account for multiple comparisons (e.g. Gaussian random field theory), and the p-value is referred to as *corrected*.

4.4.2 *ARTERIAL SPIN LABELLING*

Arterial spin labelling (ASL) is a non-invasive technique for measuring perfusion, which is the delivery of blood and subsequent exchange of nutrients to a tissue or organ [18]. This thesis will present ASL developments and the applications of this technique for ultra high field (≥ 7 T) human brain imaging. Here, the basic theory for ASL is described and the standard terms used to describe different sequences are defined.

ASL uses the magnetic labelling of inflowing blood to the tissue; two sets of images are taken, one where the inflowing blood water is labelled (the label image), the second without labelling applied termed the control image [19]. The difference between these signals will give an image of the labelled blood water which will have perfused into the tissue. This is summarised schematically in Figure 4-7. A post-label delay (TI), the time between labelling and imaging, allows time for the labelled blood to arrive at the tissue and perfuse into the tissue. The signal changes measured by ASL are small, ~1 % in grey matter at 3 T, so many measurements (~ 50) are made and the average of these taken.

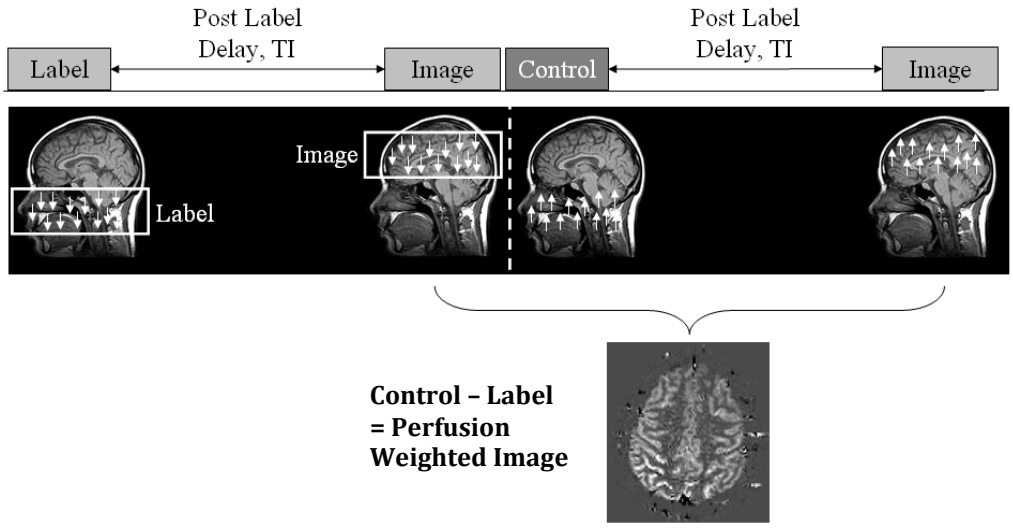

Figure 4-7: Basic method of Arterial Spin Labelling (ASL) perfusion imaging (this schematic ignores the effect of longitudinal relaxation on the labelled blood bolus).

By modelling the expected ASL signal change, this perfusion weighted signal can be converted into physiological units of perfusion in ml/100g/min [18]. In the human brain, CBF ~ 70ml/100g/min for grey matter and ~ 20ml/100g/min for white matter [20]. As well as measurements of cerebral perfusion, ASL has also been used to measure perfusion in skeletal muscle [21], kidney [22], thyroid [23], pancreas [24] and heart tissue [25]. ASL techniques can be used to measure cerebral blood flow (CBF), arterial cerebral blood volume (aCBV) and transit times (time for blood to arrive at the arteries, tissue or to travel through tissue) [26].

ASL can be used to measure (i) perfusion at rest to assess the vasculature, this is often used in patient groups where the blood flow is disturbed (e.g. stroke [27]) or (ii) the change in blood flow due to an external stimulus, thus performing fMRI using perfusion, a direct quantitative measure, rather than BOLD contrast (e.g.

[28]). Combining BOLD and ASL studies allows for the spatial comparison of BOLD and ASL changes, with BOLD arising predominantly from the venous side of the blood supply and ASL signal from the arterial side [29]. In addition, combined experiments allow further insight into the BOLD mechanism for BOLD modelling [30] and can be used in calibrated BOLD studies, as described in Chapter 6 [31].

In addition, ASL can provide measures of how arteries are feeding the brain tissue. In a technique called territorial ASL (TASL or selective ASL [32]) the major arteries are selectively labelled allowing identification of the vascular territories of the brain, typically the basilar artery and left and right carotid arteries are selectively labelled [33]. TASL is useful in the treatment of patients; for example in strokes where the blood vessels are blocked, which can lead to hypoperfusion due to a lack of blood supply [27].

4.4.2.1 Labelling Schemes

The labelling schemes for ASL can be divided into three main categories; PASL (Pulsed Arterial Spin Labelling [34]), CASL (Continuous Arterial Spin Labelling [35]) and PCASL (Pseudo Continuous Arterial Spin Labelling [36]), and these schemes are summarised in Figure 4-8. All the experiments presented in this thesis use PASL but a brief description of the three ASL schemes is included here.

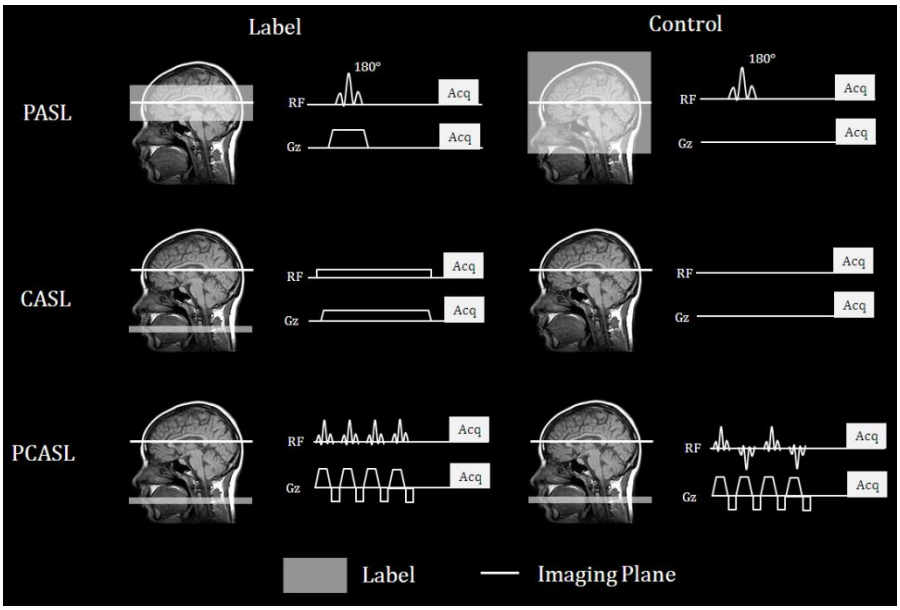

Figure 4-8: Schematic diagram representing the RF and gradient waveforms for PASL (FAIR scheme), CASL and PCASL. *Acq* represents the image acquisition module.

PASL typically uses short duration RF pulses to label (usually invert) a slab of spins. The two most common RF pulse shapes for labelling are hyperbolic secant (hsc) or frequency offset correction inversion pulses (FOCI). An hsc pulse has the form $(A_0\text{sech}(\beta t))^{1+i\mu}$ where A_0 is the maximum B_1 field, β is a modulation angular frequency and μ is dimensionless [37]. The bandwidth of this pulse, which determines the slice thickness (as well as the applied gradients), is given by $\mu\beta/\pi$. FOCI pulses were introduced to reduce spatial localisation errors due to frequency offsets for spectroscopy by giving a sharper pulse profile [38]. A FOCI pulse is based on a hsc pulse but scaled by a further factor A(t) which is 1 in the middle of the pulse, and larger than 1 at the ends to reshape the B_1, gradients and frequency offsets. The parameters can be optimised to provide the most efficient inversion.

There are many different pulsed labelling schemes proposed for PASL, Figure 4-9 summarises three of these schemes. The labelling schemes require that there is a difference between the two states for only the inflowing blood not the static tissue. A control condition is used to match magnetisation transfer (transfer of longitudinal magnetisation between macromolecules and free water) and other effects such as eddy currents.

FAIR (flow alternating inversion recovery [39]) uses a selective and a non-selective 180° inversion pulse for labelling the inflowing blood, centred in the middle of the imaging volume. This matches the RF power between label and control.

STAR (signal targeting with alternating radio frequency [40]) uses a 180° below the imaging slice to label the inflowing blood and then two 180° pulses for the control, equivalent to a 360°. This matches the power and MT effects between the label and control images.

PICORE (proximal inversion controlling for off resonance effects [28]) uses an identical label to STAR but does not have a gradient for the control condition. This ensures that the same RF power has been deposited into the tissue to match MT effects, but labelling only occurs when the gradient and RF excite the same frequency of spins.

The choice of labelling scheme is some what dependant upon scanner hardware capabilities. For example, STAR requires a 360° pulse to be made from two 180°

pulses; requiring very good B_1 homogeneity. Also STAR and PICORE require a sharp profile for the inversion to prevent the label bleeding into the imaging plane and the need for a large gap between the image volume and label.

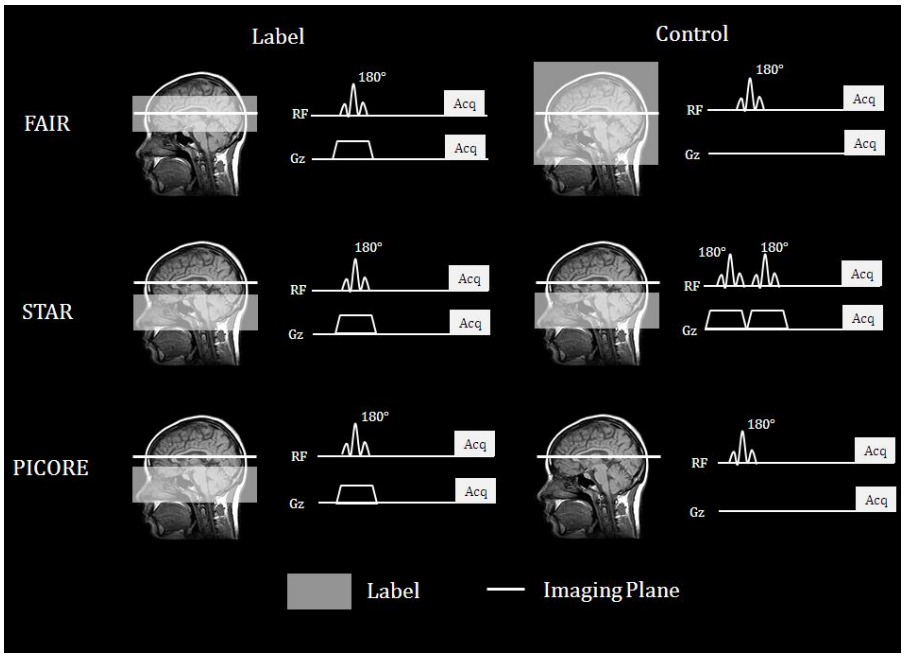

Figure 4-9: Schematic of three different ASL labelling schemes, solid line indicates imaging plane, broken line indicates placement of inversion pulse.

CASL uses a long low power RF pulse to label the spins so that labelling takes a few seconds. The labelling is applied at a single location in the neck. The advantage of CASL is that it maximises the perfusion signal [18]. However the long RF pulse increases the power deposited in the tissue (SAR), which can limit the technique at higher magnetic field strengths. CASL can also require a separate transmit coil for labelling the spins to reduce SAR. When using a separate labelling coil magnetisation transfer effects are removed providing the two coils are decoupled [41].

PCASL uses a train of small, short-duration RF pulses to imitate CASL The control condition is achieved by alternating the sign of the RF pulses in the train to give average B_1 of zero, but the RF power is matched maintaining MT effects between label/control.

CASL/PCASL both have higher SAR relative to PASL due to the higher RF power, so can be limited at higher field strength. CASL can exceed SAR limits at 3 T if using the body coil for transmission, separate labelling coils must be developed to reduce SAR. Homogenous B_1 is required for efficient labelling which is harder

to achieve at higher field with current hardware, PCASL was shown to be more dependant on B_1 than PASL at 7 T [42]. This is due to the labelling for PCASL being applied in the neck where B_0 (large offset frequencies) and B_1 are less homogeneous (RF wavelength reduced increasing RF/tissue interactions).

4.4.2.2 Modelling the ASL Signal

To convert the perfusion weighted images into a quantifiable parameter in ml/100g/min a basic physiological model for ASL is needed, an example is shown in Figure 4-10. This shows the vascular tree, from a large artery, to arterioles into the tissue capillary bed and then the venous compartment. For pulsed ASL the label can be modelled to have a temporal width W, which takes a time Δ_a for the leading edge to reach the imaging slice, this remains in the blood vessels for an exchange time δ before perfusing the tissue. This will then leave the tissue through venous flow, by which point the label will have decayed. The tissue perfusion curve, Figure 4-10 B, reflects this model, as until a time $\Delta_a + \delta$ there is no tissue signal, the labelled blood then flows in for a time W after which unlabelled blood flows in. The imaging module should be used to sample the peak of this curve for maximum signal, but using a number of inversion times is optimal as this allows transit times to be assessed improving the accuracy of the perfusion quantification.

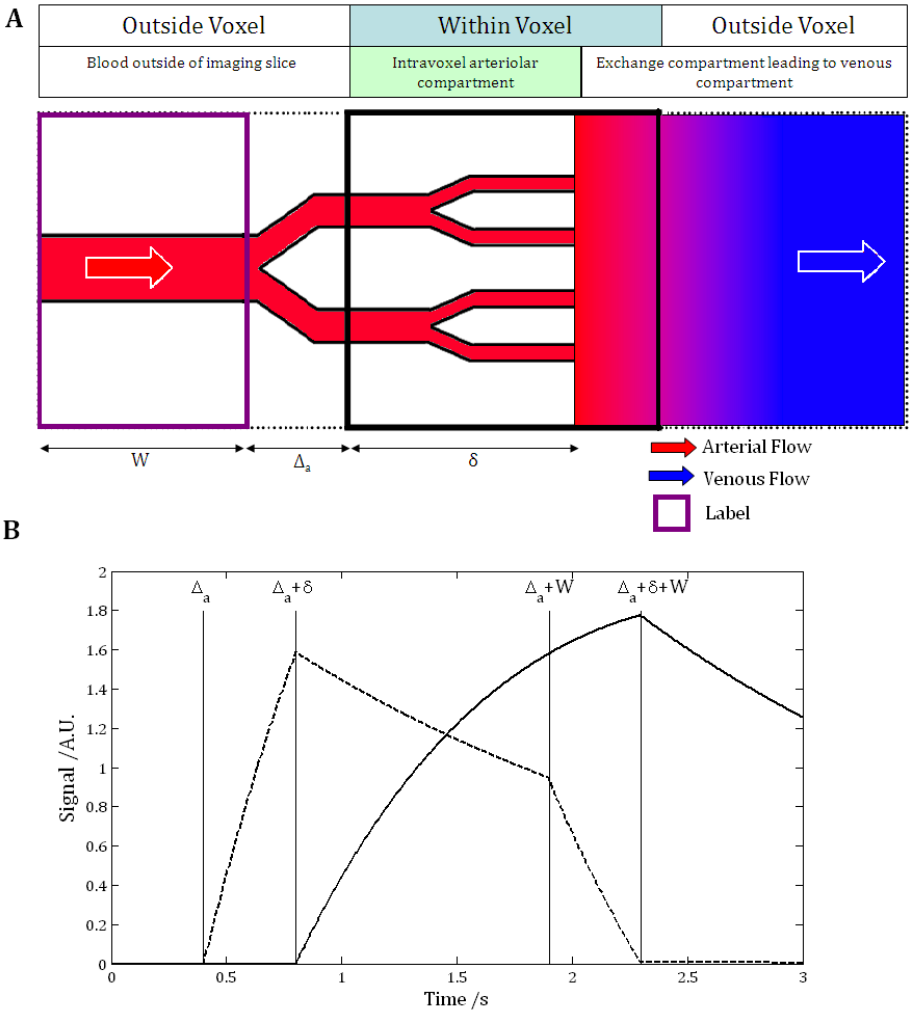

Figure 4-10: (A) Model of ASL compartments from Francis *et al.* [26] (B) Difference signal from blood compartment (broken line) and tissue compartment (solid line).

Different methods for modelling the ASL signal have been proposed. The first model for PASL was proposed in separate studies by Kim [39] and Kwong *et al.* [43]. It is based upon the single compartment model and the Bloch equation incorporating a flow component that was initially proposed by Detre *et al.* [44]:

$$\frac{dM}{dt} = \frac{M_0 - M}{T_1} + fM_b - \frac{f}{\lambda}M \qquad \textbf{4-2}$$

where M is the tissue magnetisation, M_b is the blood signal, M_0 is the equilibrium tissue signal, f is flow and λ is the blood-brain partition coefficient. The $+fM_b$ term represents the magnetisation flowing into the compartment, and $-fM/\lambda$ is the magnetisation flowing out. The factor of $1/\lambda$ converts from blood magnetisation to tissue magnetisation [45] as

$$\lambda = \frac{M_0}{M_{b,0}} \qquad \textbf{4-3}$$

T_1 is the tissue T_1 for non-selective inversion, which is modified to apparent T_1, $T_{1,app}$, when accounting for flow as for the selective inversion;

$$\frac{1}{T_{1,app}} = \frac{1}{T_1} + \frac{f}{\lambda} \qquad \textbf{4-4}$$

Using Equations 4-2 and 4-4, the signal difference for a FAIR scheme between a non-selective (M_{ns}) and a selective signal (M_s) can be shown as

$$M_s(t) - M_{ns}(t) = M_0\left(1 - 2e^{-t/T_{1,app}}\right) - M_0\left(1 - 2e^{-t/T_1}\right)$$
$$M_s(t) - M_{ns}(t) = 2M_0\left(e^{-t/T_1} - e^{-t/T_{1,app}}\right)$$
$$\Rightarrow M_s(t) - M_{ns}(t) = 2M_0 e^{-t/T_1}\left(1 - e^{-ft/\lambda}\right) \qquad \textbf{4-5}$$

assuming that TR >> T_1, allowing full recovery. For times such that $ft/\lambda << 1$ then

$$\Delta M(t) = 2\alpha\frac{f}{\lambda}M_0 t e^{-t/T_1} \qquad \textbf{4-6}$$

where ΔM is the measured difference signal and α is the fractional labelling efficiency where α = 1 indicates complete inversion. This assumes that a sufficiently long time has passed so that the entire labelled bolus has reached the imaging voxel [46]. This is a simple model as it does not take account of transit times.

The modified Bloch equations can also be used to account for the different transit times of the blood, as used in Gardener *et al.* [47]. Solving the modified Bloch equations assuming plug flow and complete refreshment between TR periods it can be shown that

$$\Delta M(t) = \begin{cases} 0 & t < \Delta_{tissue} \\ 2\alpha M_0 \dfrac{f}{\lambda\left(\frac{1}{T_{1app}} - \frac{1}{T_{1,b}}\right)} e^{\frac{-\Delta_{tissue}}{T_{1,b}}}\left(e^{\frac{-(t-\Delta_{tissue})}{T_{1,b}}} - e^{\frac{-(t-\Delta_{tissue})}{T_{1,app}}}\right) & \Delta_{tissue} < t < \Delta_{tissue} + W \\ 2\alpha M_0 \dfrac{f}{\lambda\left(\frac{1}{T_{1app}} - \frac{1}{T_{1,b}}\right)} e^{\frac{-\Delta_{tissue}}{T_{1,b}}}\left(e^{\frac{-W}{T_{1,b}}} - e^{\frac{-W}{T_{1,app}}}\right) e^{\frac{-(t-\Delta_{tissue}-W)}{T_{1,app}}} & t > \Delta_{tissue} + W \end{cases} \qquad \textbf{4-7}$$

where Δ_{tissue} is the tissue transit time (equal to $\Delta_a+\delta$ in Figure 4-10) and $T_{1,b}$ is the T_1 or arterial blood. By acquiring data with a range of TI values it can be fitted for f, W and Δ_{tissue} using the above equations.

For quantification of CBF an estimation of the M_0 of blood is needed, and there are different methods that are used [48]. The measurement of $M_{0,b}$ directly from vessel filled voxel is difficult, primarily due to the typical coarse spatial resolution increasing partial volume effects. Equilibrium magnetisation values of white

matter or CSF can be converted to $M_{0,b}$ by accounting for differences in proton density and T_2* between WM/CSF and blood. However the more popular method is that the M_0 of tissue can be measured (e.g. using inversion recovery) and converted to $M_{0,b}$ using the relationship in Equation 4-3. This can be performed globally, using an average value of M_0 as the value of $M_{0,b}$ is constant over the brain. However often it is performed voxelwise, as this allows for correction of other effects (e.g. T_2*, coil sensitivity profiles) [48].

4.4.2.3 Single TI Methods

The most common use of ASL is the single TI method, where only one post-label delay time is used of ~ 1400 ms, as shown in Figure 4-7. The advantage to this is that it is easier to implement and easier to model the perfusion signal. However, perfusion is a dynamic process, and by only taking one time point the effect of transit time is not taken into account. Transit time is the time taken for the labelled bolus to arrive in the tissue (the time of zero signal change in Figure 4-11). The transit time varies across the brain [49] and with age [50] and can lead to perfusion quantification errors. Buxton [46] provided several recommendations to ensure errors are minimised; these included waiting a sufficient time (~ 1200 ms) for the entire bolus to have reached the tissue.

To assess transit time effects, the single TI experiment can be repeated at several different post-label delays (for example [49, 51]). This allows for mapping of perfusion and the transit time, however this method is slow.

The imaging module used in combination with ASL can be of any type, however fast readout methods, such as EPI, are required. The magnetic label decays with T_1 and hence there is a time limit before the perfusion signal decays to zero. An example ASL signal curve is shown in Figure 4-11. The echo-time chosen for ASL should be short, to ensure maximum signal change and reduce the contribution from BOLD. In addition, St Lawrence and Wang demonstrated that perfusion can be underestimated with a long echo time [52]. They concluded that at higher field strengths the reduced T_2* of blood will reduce the capillary contribution to the ASL signal, underestimating CBF.

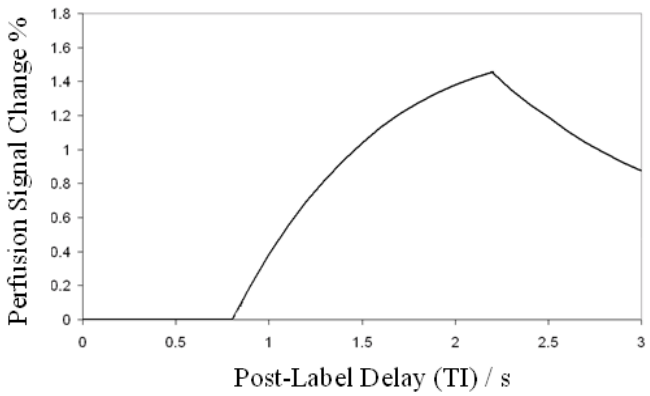

Figure 4-11: Perfusion signal change as a function of post label delay. Simulation parameters $T_{1,b}$ = 2.1 s, T_1 = 2.1 s, W = 1.2 s, Δ_{tissue} = 0.8 s, f = 90 ml/100g/min.

4.4.2.4 Multiple TI Methods

As explained above, perfusion of blood into the tissue is a dynamic process, which has temporal characteristics that vary between brain regions [49]. Single inversion time imaging, as described above, does not take these temporal characteristics into account. A Look-Locker (LL) readout [53] allows several readouts to be acquired per shot, this method is commonly applied to T_1 mapping (e.g. [54]) but has been combined with an ASL readout [26, 55-57]. The labelling scheme is applied and followed by several low flip angle readouts acquired prior to the next labelling module, as shown in Figure 4-12. This has the advantage of increased temporal information without increasing the scan time. However the application of multiple readout pulses perturbs the recovery of the magnetisation, resulting in lower signal and a more complex model for perfusion quantification [26, 56].

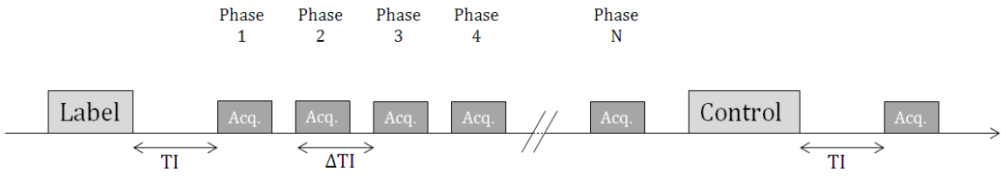

Figure 4-12: Schematic of the Look-Locker ASL sequence.

To fit the signal, the signal is modelled using the model in Figure 4-10 A, modelling the blood outside the voxel, intravoxel blood and the exchange compartment [26]. The signals are modelled in small time increments so that the effect of the RF pulses on the signal can be fully modelled as spins could experience many RF pulses whilst in the imaging voxel.

The *blood outside the voxel* will be an inversion recovery, and is unaffected by the RF pulses:

Selective	$M_{in}(t) = M_{b,0}\left(1 - 2e^{-t/T_{1,b}}\right)$	$t < \Delta_a$	**4-8**
	$M_{in}(t) = M_{b,0}$	$t > \Delta_a$	
Non Selective	$M_{in}(t) = M_{b,0}\left(1 - 2e^{-t/T_{1,b}}\right)$	$t < \Delta_a + W$	
	$M_{in}(t) = M_{b,0}$	$t > \Delta_a + W$	

where t is the time since the inversion pulse, $M_{b,0}$ is the equilibrium magnetisation of the blood and $T_{1,b}$ is the longitudinal relaxation time of the blood.

The *intravoxel arteriolar blood* remains in the vessels for a time δ before reaching the capillary bed (the exchange compartment). The magnetisation of this compartment, $M_b(t)$ can be described by

$$\frac{d}{dt}M_b(t) = \frac{M_{b,0} - M_b(t)}{T_{1,b}} + FM_{in}(t) - FM_{out}(t) \quad \textbf{4-9}$$

where F is the arterial blood flow, M_{out} is the magnetisation flowing out of the blood compartment into the exchange compartment, this will depend on the RF pulses the blood has experienced in time δ. The arterial blood volume (CBVa) is given by Fδ.

The magnetisation in the *exchange compartment* can be described by the modified version of Equation 4-2;

$$\frac{d}{dt}M_{tissue}(t) = \frac{M_{tissue,0} - M_{tissue}(t)}{T_{1,tissue}} + \frac{f}{\lambda}M_{out}(t) - fM_{tissue}(t) \quad \textbf{4-10}$$

where $M_{tissue,0}$ is the equilibrium magnetisation of the tissue, λ is the blood:brain partition coefficient, M_{out} is the magnetisation flowing out of the intravoxel arteriolar compartment into the exchange compartment and f is the tissue perfusion. This compartment is perturbed by the application of the RF pulses and each of these must be modelled.

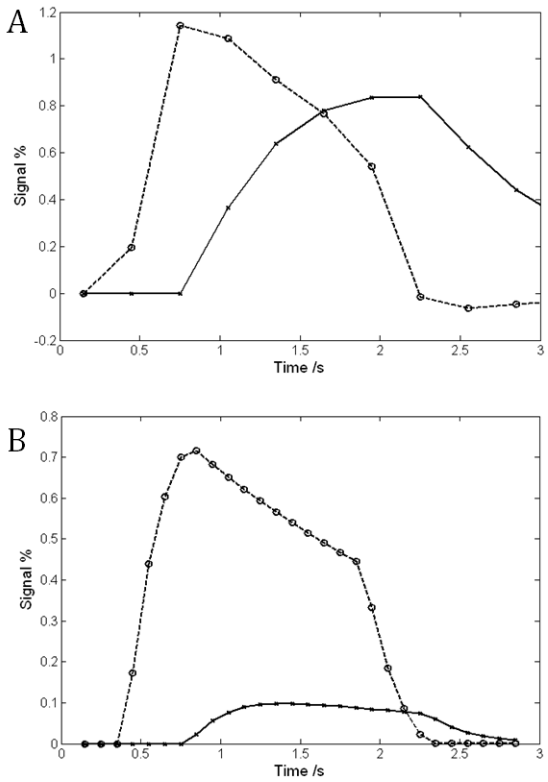

Figure 4-13: LLEPI FAIR signals for the arteriolar (broken line) and exchange (solid line) compartments with sequence parameters (A) TI/ΔTI = 150/300 ms flip angle = 35° (B) TI/ΔTI = 150/100 ms flip angle = 45°. Common parameters are f = 90 ml/100g/min, F = 180 ml/100g, δ=0.4s. Δ_a = 0.4s, W = 1.5s.

Example LLEPI signals for two different sets of scan parameters are shown in Figure 4-13. For CBF quantification the contribution from the blood signal should be reduced, and that from the tissue signal increased to improve the fitting for CBF. This can be achieved by using a reasonably low flip angle (35°) and long ΔTI (~ 300 ms) so that the tissue signal is not suppressed extensively ensuring adequate SNR (Figure 4-13 A). To reduce the blood signal vascular crushing (see 4.4.2.5) can be used to remove large vessel contributions.

In addition to measuring CBF LL-ASL has been applied to measure arterial blood volume (CBVa) [55]. This uses the blood signal, thus the blood signal needs to be maximised and the tissue signal minimised. This is achieved by reducing the initial TI (~100 ms), increasing the flip angle (~ 45°) and reducing the ΔTI (~ 100 ms). The rapid application of high flip angle pulses suppresses the tissue signal, but the blood signal is continually refreshed due to fresh blood flowing in, giving high blood signal (Figure 4-13 B)

An alternative method for Look Locker ASL is the model-free approach of Petersen *et al.* [57]. Here two scans are acquired, one with and one without the use of vascular crushing. The difference signal between the non-crushed and

crushed timecourses gives signal that is weighted towards the arterial blood volume as the tissue perfusion has been removed:

$$CBVa = \frac{\int_{-\infty}^{\infty}(\Delta M_{ncr}(t) - \Delta M_{cr}(t))\exp\left({}^{1}/_{T_{1,b}}\right)dt}{2M_{0,b}\alpha W} \quad \textbf{4-11}$$

where ΔM_{ncr} is the perfusion difference signal from the non-crushed data, ΔM_{cr} is the perfusion difference signal from the crushed data, $T_{1,b}$ is the T_1 of arterial blood, W is the bolus duration, α is the inversion efficiency and $M_{0,b}$ the equilibrium magnetisation of arterial blood.

From the difference signal the arterial input function (AIF) is defined from a voxel containing a large artery. The CBVa is used to weight the AIF for each voxel to take into account blood volume fraction, then the perfusion is calculated by deconvolution of the perfusion timecourse with the local AIF. The method estimated grey matter perfusion in healthy volunteers to be 38 ± 2 ml/100g/min and CBVa as 0.93 ± 0.06 % which are on the lower bounds of literature values. The simulations performed in that study also predicted an underestimation of perfusion using this *model free* approach [57].

LL-ASL has been applied to monitor functional changes. Brookes *et al.* [55] investigated the effect of a motor task on CBVa using LL-EPI ASL. Ho *et al.* have looked at the impact of hypercapnia and visual stimulation on blood volume, transit time and perfusion [58, 59]. This method has also been applied in patient studies, e.g. Parkinson's [60] and Alzheimer's [61].

Generally 2D-EPI is used in conjunction with Look-Locker ASL but other implementations have been shown. Wang *et al.* [62] demonstrated at 3 T the feasibility of combining a Look-Locker scheme with a FLASH readout for blood velocity mapping, and TrueFISP has been incorporated in a LL-readout for kidney perfusion imaging at 1.5 T [63].

4.4.2.5 Vascular Crushing

ASL is typically used to assess tissue perfusion, rather than the arterial blood signal (e.g. [55]). To reduce arterial blood signal contaminating the perfusion signal, techniques are used to decrease the contribution from the arterial blood. One way is to use a long post-labelling delay so that all the labelled blood has moved from the arterial blood into the tissue compartment. However for transit time mapping and more accurate perfusion quantification it is common to take

several measurements at different post-labelling delays (for example [49]). For this, *vascular crushing* is used to suppress the signal from arterial blood [64].

Vascular crushing is achieved by applying a bipolar gradient after the RF excitation and prior to the readout gradients. Bipolar gradients with two lobes of equal duration and magnitude but opposite polarity will cause no resultant phase shift of stationary spins. However, moving spins will acquire a phase shift as they move during the application of the gradients as they do not experience both gradients equally [65]. For spins of a constant velocity the phase shift ϕ acquired during the bipolar gradient pair is linearly proportional to velocity ($\phi = \gamma\delta\Delta G v$, where γ is the gyromagnetic ratio, v is velocity, δ is the duration of a gradient lobe, G the strength of the gradient and Δ is the distance between the centres of the gradient lobes [65]). Hence an expression for the encoding velocity can be formed;

$$v_{enc} = \frac{\pi}{\gamma G \delta \Delta}. \qquad \textbf{4-12}$$

The encoding velocity is the cut-off velocity, above which the spins will be dephased (calculated when $\phi = \pi$); below this level the spins will still be visible in the final image. Example encoding velocity levels for a 5 ms bipolar pair lobe duration and required gradient strengths are shown in Table 4-2.

V_{enc} [mm s^{-1}]	Gradient Strength [mT m^{-1}]	b-value (s/mm^2)
15	31	5.7
25	19	2.1
35	13.5	1.1
50	9.5	0.5
75	6.3	0.2
100	4.7	0.1

Table 4-2: Example encoding velocities for vascular crushing (5 ms lobe duration). Typical values used in the experimental work presented in Chapters 5 and 6 shown highlighted.

4.4.2.6 Saturation Pulses

Saturation pulses, to null the signal in the imaging plane are applied prior to the labelling (pre-saturation) and directly after the label (post-saturation) [28], an example scheme is shown in Figure 4-14. The benefit of these pulses is that the tissue is always in the same state at the beginning of each TR period, without needing a long TR to allow recovery to simplify modelling. In-plane saturation can also be used to remove any effects of inversion of the inferior blood spins due to imperfect inversion pulse profiles.

Saturation can be achieved using sinc or WET (water suppression enhanced through T_1 effects [66]) pulses. WET uses four RF pulses of different flip angles to achieve greater B_1/T_1 independence. The flip angles are optimised for a range of typical T_1 and B_1. WET pulses have the disadvantage of increased SAR due to multiple RF pulses.

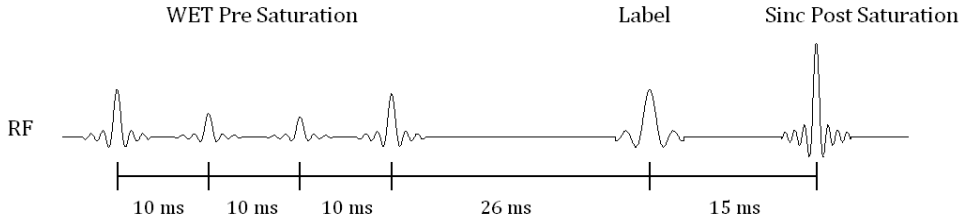

Figure 4-14: Schematic of the RF scheme for PASL with WET pre-saturation and sinc post-saturation pulses with typical timings shown.

4.4.2.7 Background Suppression

ASL suffers from low signal as the theoretical signal change due to perfusion is only ~ 1 – 2 % of M_0 at 7 T, therefore a number of different methods have been suggested to improve the signal-to-noise ratio of CBF measurements. To improve the sensitivity of ASL, Ye *et al.* [67] suggested the use of inversion pulses to reduce fluctuations in the static signal which can contaminate the perfusion signal. Background suppression (BGS) uses one or more inversion pulses to ensure that the static tissue signal is at its null point when the images are acquired [68]. Ye *et al.* [67] demonstrated a substantial reduction, ~ 70 %, in the variance in the measured perfusion signal with background suppression as fluctuations in static signal were suppressed.

The timings of the BGS pulses need to be optimised for the post label delay, TI, and the longitudinal relaxation time (T_1) of the tissue of interest. For example, Figure 4-15 shows a tissue recovery curve for grey and white matter at 7 T, having been saturated at t = 0. To find the optimum values of TI1 and TI2 the solutions of the Bloch equations for the longitudinal component of magnetisation are used to model the recovery of the magnetisation between the inversion pulses. At time t = TI the magnetisation is some fraction, ε, of M_0 and it can be shown that

$$\frac{(\varepsilon - 1)e^{\frac{TI}{T1}} + 1}{2} = e^{\frac{TI1}{T1}} - e^{\frac{TI2}{T1}} \qquad \textbf{4-13}$$

Equation 4-13 can then be used to compute the required TI1/TI2 pairs for suppression of a tissue of longitudinal relaxation time T_1 to have signal εM_0 at time TI. The BGS pulses typically used are such that the data is not acquired as it crosses the null point ($\varepsilon > 0$), otherwise sign correction of the data would need to be performed prior to image subtraction. For example, grey matter at 7 T with a post-label delay of 1.5 s then TI1/TI2 = 402/1041 ms ($\varepsilon = 0.1$, these values are used in the experimental work in Chapter 5).

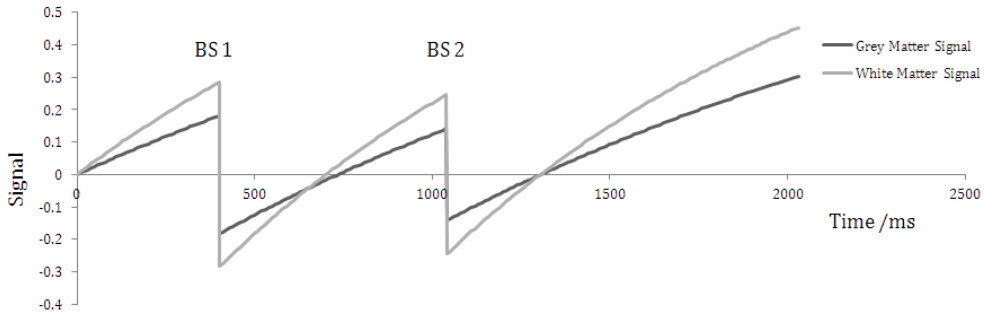

Figure 4-15: Example recovery curves for BGS pulses at 402 and 1041 ms for grey (T_1 = 2 s) and white (T_1 = 1.2 s) matter after pre-saturation.

4.4.2.8 Applications of ASL

ASL has the major benefit of being a non-invasive technique and is now being used in clinical imaging. Wolf and Detre [18] highlighted the benefit of ASL to study conditions such as cerebrovascular disease (e.g. stroke), vascular malformations, tumours of the central nervous system, epilepsy and in the study of degenerative diseases. Pollock *et al.* [69] discussed the benefit of ASL over conventional imaging techniques which may miss some abnormalities due to a non-structural origin, for example in epilepsy and migraines. The work presented in Chapter 5 shows developments to methodology to allow more flexibility in the assessment of patients, and has been used to assess blood flow in Low Grade Gliomas.

4.4.3 *CONTRAST AGENTS FOR MR PERFUSION IMAGING*

In this thesis work on T_1 mapping at 7 T (Chapter 7) and its application to steady state contrast agent monitoring for the measurement of CBV will be demonstrated. This section will briefly describe the principles of MR contrast agents for perfusion imaging and their clinical benefit.

The use of contrast agents is the clinical standard for assessment of cerebral perfusion using MRI [70]. ASL has the advantage of being a non-invasive technique, however as it is a relatively new technique requiring different scanner capabilities and it is not, to-date, a standard clinical tool. Currently contrast agents have higher sensitivity and are generally quicker to acquire. A contrast agent for MR imaging is commonly a paramagnetic agent e.g. a Gadolinium chelate. These are non-diffusible tracers and do not cross the BBB, unless it is damaged (as shown by Figure 4-18); contrast agents work by shortening the T_1, T_2 and T_2* of the blood. The local tissues can be affected by the contrast agent due to susceptibility differences and water exchange occurring between the blood and tissue also reducing, also reducing T_2/T_2* of the tissue by diffusion [71].

As a free ion Gadolinium is extremely toxic so it is chelated with other compounds for administration. The side effects of gadolinium contrast agent administration are possible anaphylactic shock due to an allergic reaction or NSF (nephrogenic systemic fibrosis) [72] which is a concern for patients with poor kidney function. Although, this is very dependant on the particular chelate used.

There is a linear relationship between the concentration of contrast agent and R_1 ($1/T_1$) which allows for the use of T_1 weighted imaging for contrast agent monitoring and CBV quantification. There is also a linear relationship with change in R_2^* ($1/T_2$*), which is proportional to the blood volume; allowing for CBV quantification. The administration of a contrast agent is typically monitored in one of two ways – dynamic monitoring in time for CBV, CBF and vascular permeability measures or steady state for CBV quantification.

4.4.3.1 Dynamic Measurement

Dynamic monitoring uses rapidly acquired images with T_1 or T_2^* weighting during a quick infusion of contrast agent, to see the contrast agent flow into the imaging slice. This can lead to measurement of CBF, CBV (blood volume) and MTT (mean transit time). CBV is the fraction of the voxel occupied by blood, MTT is the time taken for the contrast agent to pass through the voxel [71]. Using the central volume principle CBF can be calculated as

$$CBF = \frac{CBV}{MTT}. \qquad \textbf{4-14}$$

Further temporal parameters including onset time and time to peak can also be calculated.

The draw backs of dynamic contrast agent monitoring include the recirculation of the contrast agent which makes it difficult to isolate the first pass curve. A measurement of the arterial input function in a major vessel needs to be made to calibrate the other CBV values. Measurement of MTT is complicated by bolus dispersion caused by the finite duration of the injection – hence the signal curves are normally deconvolved using the AIF (arterial input function, time course from large artery Figure 4-16) to counteract this.

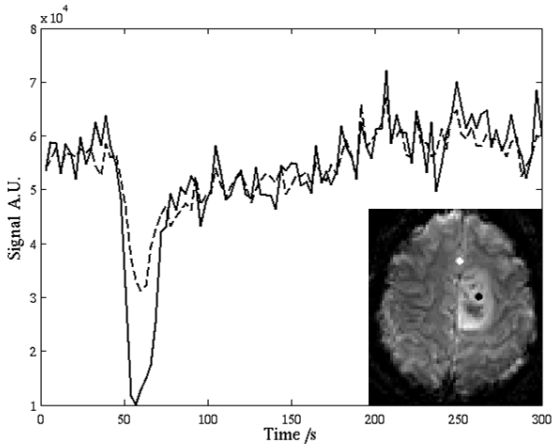

Figure 4-16: Example T_1 weighted timecourse from an arterial vessel (AIF, solid line) and an area of tumour (broken line). Voxel positions shown inset.

Further analysis can look at rate constants of the transfer of the contrast agent using pharmokinetic modelling. For example, K_{trans} is the rate constant describing the movement of contrast from blood to the tissue of interest. This can be a measure of 'leakiness'.

Gadolinium uptake curves can also be used to measure vascular permeability. Figure 4-17 shows a two compartment model used for contrast agent analysis [73]. The two compartments of the blood plasma and extravascular-extracellular space are shown, with contrast agent arriving with rate k_a and being eliminated with rate k_e. The rate constants k_{12} and k_{21} describe the movement of contrast agent between them.

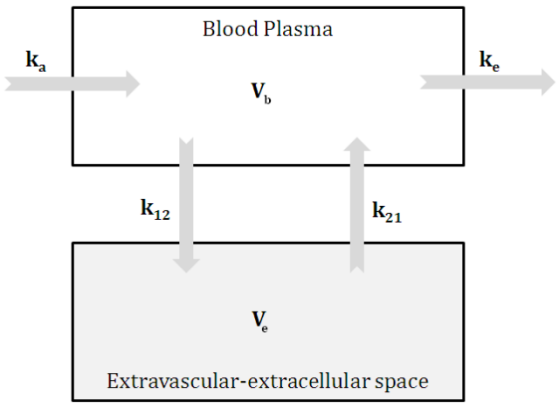

Figure 4-17: Two compartment model for contrast agent uptake modelling. k denotes a rate constant for the process shown by arrows and V_b/V_e are the volumes of the two compartments. Adapted from [73].

The net flux of contrast agent into the tissue is

$$\frac{d}{dt}C_t(t) = k_{12} \cdot C_b(t) - k_{21} \cdot C_t(t) \qquad \textbf{4-15}$$

where C_t is the concentration of the agent in the tissue and C_b is the concentration in the blood. The solution of this yields

$$C_t(T) = K^{trans} \int_0^T C_p(t) \cdot e^{K^{trans}/V_e(T-t)} dt \qquad \textbf{4-16}$$

where C_p is the concentration in the plasma ($C_p(t) = (1-h) \cdot C_b(t)$, h is the haematocrit), K^{trans} is $E \cdot F \cdot (1-h)$ (E is the extraction fraction and F the blood flow) and V_e is the extravascular-extracellular volume fraction. C_p and C_t are measured during the administration of a contrast agent and K^{trans} and V_e can be calculated from fitting the data to Equation 4-16.

4.4.3.2 Steady State Measurement

Steady state techniques use pre and post contrast images, with several minutes between them to allow the uptake of contrast agent. Pre and post contrast images show where any gadolinium has been distributed; this can be used for CBV calculation. Areas of BBB breakdown (Figure 4-18) will be visible on steady state images as the contrast agent will reach the tissue. As this is not a rapid measurement, high resolution images, with large coverage can be acquired.

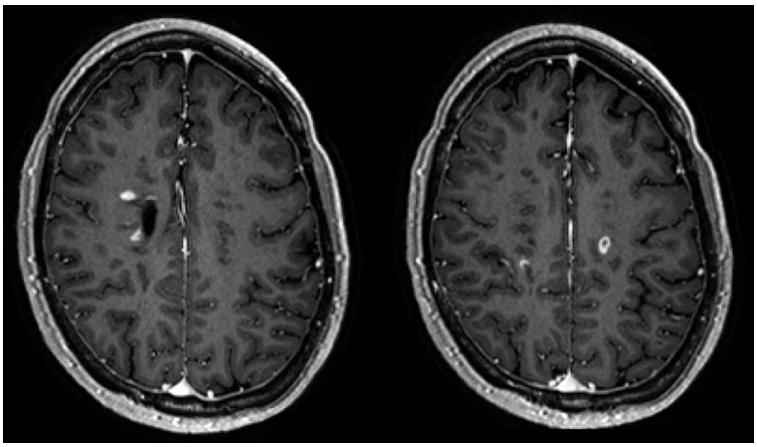

Figure 4-18: BBB breakdown shown in MS lesions after gadolinium contrast administration (post contrast MPRAGE, 0.8mm isotropic acquired at 3 T).

4.4.4 *MR SPECTROSCOPY*

MRI, generally, uses only the ^{1}H molecule to provide structural and functional information. MR spectroscopy (MRS) can be performed to assess the chemical contribution of the signal rather than image the structure directly. MRS exploits the fact that the resonant frequency of a spin is dependent on the environment that it is in. This allows different molecules to be identified by their resonant frequency [74], from which metabolite levels and rates of change can be measured [4].

Proton, ^{1}H, spectroscopy can be used to look at N-acetyl-aspartate (NAA) and compounds containing choline, creatine and glutamine, an example spectrum is given in Figure 4-19. NAA is thought to be related to neuron density, choline containing compound concentrations can be perturbed in disease and glutamate is an excitatory neurotransmitter [75]. Phosphorous (^{31}P) is also widely used as it can provide information on oxidative metabolism; carbon-13 spectroscopy can look at glucose metabolism (through the tricarboxylic acid (TCA) cycle rate [76]) but requires administration of a ^{13}C labelled compound due to the low natural abundance (1.1 %) [4].

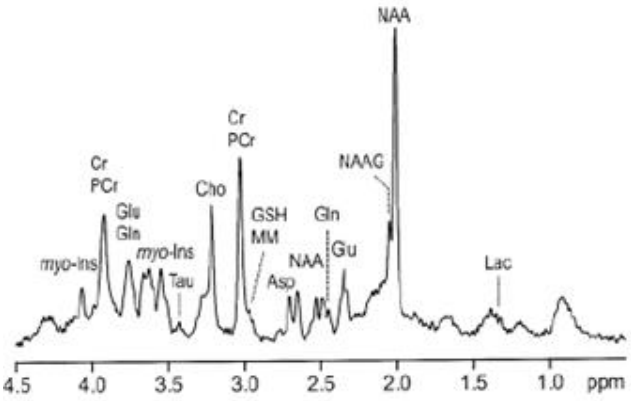

Figure 4-19: Example ^{1}H spectrum from human brain acquired at 7 T, reproduced from [77] with kind permission from John Wiley & Sons.

4.5 CONCLUSION

This chapter has introduced methods for monitoring brain function, through the measurement of physiological parameters or through monitoring how the brain reacts to performing certain tasks. Arterial spin labelling has been introduced, including basic theory and physiological model of the process of measuring perfusion non-invasively. Other measures of brain function using MR (BOLD, contrast agents and MRS) have been included to illustrate how MR can aid in the monitoring of brain function and activity.

4.6 REFERENCES

1. Klabunde, R.E., *Cardiovascular Physiology Concepts*. 2005, Baltimore: Lippincott Williams & Wilkins.
2. Rubin, L.L. and J.M. Staddon, *The Cell Biology of the Blood-Brain Barrier.* Annu. Rev. Neurosci., 1999. **22**: p. 11-28.
3. Vries, H.E.d., J. Kuiper, A.G.d. Boer, T.J.C.V. Berkel, and D.D. Breimer, *The Blood-Brain Barrier in Neuroinflammatory Diseases.* Pharmacological Reviews, 1997. **49**(2): p. 143-156.
4. Orrison, W.W., J.D. Lewine, J.A. Sanders, and M.F. Hartshorne, *Functional Brain Imaging*. 1995, St-Louis: Mosby.
5. Ogawa, S., T.M. Lee, A.R. Kay, and D.W. Tank, *Brain magnetic resonance imaging with contrast dependent on blood oxygenation.* Proceedings of the National Academy of Sciences, 1990. **87**(24): p. 9868-9872.
6. Thulborn, K.R., J.C. Waterton, P.M. Matthews, and G.K. Radda, *Oxygenation dependence of the transverse relaxation time of water protons in whole blood at high field.* Biochimica et Biophysica Acta (BBA) - General Subjects, 1982. **714**(2): p. 265-270.
7. Huettel, S., A.W. Song, and G. McCarthy, *Functional Magnetic Resonance Imaging*. 2nd ed. 2009, Massachusetts: Sinauer Associates Inc.
8. Moonen, C.T.W. and P.A. Bandettini, *Functional MRI*. Medical Radiology; Diagnostic Imaging, ed. A.L. Baert, K. Sartor, and J.E. Youker. 2000, Berlin: Springer.
9. Clare, S., S. Francis, P.G. Morris, and R. Bowtell, *Single-shot T_2* measurement to establish optimum echo time for fMRI: Studies of the visual, motor, and auditory cortices at 3.0 T.* Magnetic Resonance in Medicine, 2001. **45**(5): p. 930-933.

10. Yacoub, E., A. Shmuel, J. Pfeuffer, P.-F. Van De Moortele, G. Adriany, K. Ugurbil, and X. Hu, *Investigation of the initial dip in fMRI at 7 Tesla.* NMR in Biomedicine, 2001. **14**(7-8): p. 408-412.
11. Duong, T.Q., D.-S. Kim, K. Uğurbil, and S.-G. Kim, *Spatiotemporal dynamics of the BOLD fMRI signals: Toward mapping submillimeter cortical columns using the early negative response.* Magnetic Resonance in Medicine, 2000. **44**(2): p. 231-242.
12. Yacoub, E., T.H. Le, K. Ugurbil, and X. Hu, *Further Evaluation of the Initial Negative Response in Functional Magnetic Resonance Imaging.* Mag. Res. Med., 1999. **41**: p. 436-441.
13. Mandeville, J.B., J.J.A. Marota, B.E. Kosofsky, J.R. Keltner, R. Weissleder, B.R. Rosen, and R.M. Weisskoff, *Dynamic functional imaging of relative cerebral blood volume during rat forepaw stimulation.* Magnetic Resonance in Medicine, 1998. **39**(4): p. 615-624.
14. Frahm, J., J.r. Baudewig, K. Kallenberg, A. Kastrup, K.D. Merboldt, and P. Dechent, *The post-stimulation undershoot in BOLD fMRI of human brain is not caused by elevated cerebral blood volume.* Neuroimage, 2008. **40**(2): p. 473-481.
15. Jenkinson, M., P. Bannister, M. Brady, and S. Smith, *Improved Optimization for the Robust and Accurate Linear Registration and Motion Correction of Brain Images.* NeuroImage, 2002. **17**: p. 825-841.
16. Glover, G.H., T.Q. Li, and D. Ress, *Image-based method for retrospective correction of physiological motion effects in fMRI: RETROICOR.* Magnetic Resonance in Medicine, 2000. **44**(1): p. 162-167.
17. Friston, K.J., A.P. Holmes, K.J. Worsley, J.-P. Poline, C.D. Frith, and R.S.J. Frackowiak, *Statistical Parametric Maps in Functional Imaging: A General Linear Approach.* Human Brain Mapping, 1995. **2**: p. 189-210.
18. Wolf, R. and J.A. Detre, *Clinical Neuroimaging using Arterial Spin-Labeled Perfusion MRI.* Neurotherapeutics, 2007. **4**(3): p. 346-359.
19. Williams, D.S., J.A. Detre, J.S. Leigh, and A.P. Koretsky, *Magnetic resonance imaging of perfusion using spin inversion of arterial water.* Proc. Natl. Acad. Sci. USA, 1992. **89**: p. 212-216.
20. Parkes, L.M., W. Rashid, D.T. Chard, and P.S. Tofts, *Normal cerebral perfusion measurements using arterial spin labeling: Reproducibility, stability, and age and gender effects.* Magnetic Resonance in Medicine, 2004. **51**(4): p. 736-743.
21. Frank, L.R., E.C. Wong, L.J. Haseler, and R.B. Buxton, *Dynamic imaging of perfusion in human skeletal muscle during exercise with arterial spin labeling.* Magnetic Resonance in Medicine, 1999. **42**(2): p. 258-267.
22. Martirosian, P., U. Klose, I. Mader, and F. Schick, *FAIR TrueFISP Perfusion Imaging of the Kidneys.* Magnetic Resonance Imaging, 2004. **51**: p. 353-361.
23. Schraml, C., A. Boss, P. Martirosian, N.F. Schwenzer, C.D. Claussen, and F. Schick, *FAIR true-FISP perfusion imaging of the thyroid gland.* Journal of Magnetic Resonance Imaging, 2007. **26**(1): p. 66-71.
24. Schraml, C., N.F. Schwenzer, P. Martirosian, C.D. Claussen, and F. Schick, *Perfusion imaging of the pancreas using an arterial spin labeling technique.* Journal of Magnetic Resonance Imaging, 2008. **28**(6): p. 1459-1465.
25. Poncelet, B.P., T.M. Koelling, C.J. Schmidt, K.K. Kwong, T.G. Reese, P. Ledden, H.L. Kantor, T.J. Brady, and R.M. Weisskoff, *Measurement of Human Myocardial Perfusion by Double-Gated Flow Alternating Inversion Recovery EPI.* Mag. Res. Med., 1999. **41**: p. 510-519.
26. Francis, S.T., R. Bowtell, and P.A. Gowland, *Modeling and Optimization of Look-Locker Spin Labeling for Measuring Perfusion and Transit Time Changes in Activation Studies Taking into Account Arterial Blood Volume.* Mag. Res. Med., 2008. **59**: p. 316-325.
27. Chalela, J.A., D.C. Alsop, J.B. Gonzalez-Atavales, J.A. Maldjian, S.E. Kasner, and J.A. Detre, *Magnetic Resonance Perfusion Imaging in Acute Ischemic Stroke Using Continuous Arterial Spin Labeling.* Stroke, 2000. **31**(3): p. 680-687.
28. Wong, E.C., R.B. Buxton, and L.R. Frank, *Implementation of quantitative perfusion imaging techniques for functional brain mapping using pulsed arterial spin labeling.* NMR in Biomedicine, 1997. **10**(4-5): p. 237-249.
29. Detre, J.A. and J. Wang, *Technical aspects and utility of fMRI using BOLD and ASL.* Clinical Neurophysiology, 2002. **113**(5): p. 621-634.
30. Buxton, R.B., E.C. Wong, and L.R. Frank, *Dynamics of blood flow and oxygenation changes during brain activation: The balloon model.* Magnetic Resonance in Medicine, 1998. **39**(6): p. 855-864.
31. Davis, T.L., K.K. Kwong, R.M. Weisskoff, and B.R. Rosen, *Calibrated functional MRI: Mapping the dynamics of oxidative metabolism.* Neurobiology, 1998. **95**: p. 1834-1839.
32. Davies, N.P. and P. Jezzard, *Selective arterial spin labeling (SASL): Perfusion territory mapping of selected feeding arteries tagged using two-dimensional radiofrequency pulses.* Magnetic Resonance in Medicine, 2003. **49**(6): p. 1133-1142.

33. Hendrikse, J., E.T. Petersen, A. Cheze, S.M. Chng, N. Venketasubramanian, and X. Golay, *Relation Between Cerebral Perfusion Territories and Location of Cerebral Infarcts.* Stroke, 2009. **40**(5): p. 1617-1622.
34. Edelman, R.R., B. Siewart, D.G. Darby, V. Thangaraj, A.C. Nobre, M.M. Mesulam, and S. Warach, *Qualitative mapping of cerebral blood flow and functional localization with echo-plan MR imaging and signal targeting with alternating radio freqeuncy.* Radiology, 1994. **192**: p. 513-520.
35. Detre, J.A., W. Zhang, D.A. Roberts, A.C. Silva, D.S. Williams, D.J. Grandis, A.P. Koretsky, and J.S. Leigh, *Tissue specific perfusion imaging using arterial spin labeling.* NMR in Biomedicine, 1994. **7**(1-2): p. 75-82.
36. Dai, W., D.M. Garcia, C. de Bazelaire, and D.C. Alsop, *Continuous Flow Driven Inversion for Arterial Spin Labeling Using Pulsed Radiofrequency and Gradient Fields.* Mag. Res. Med., 2008. **60**(6): p. 1488-1497.
37. Bernstein, M.A., K.F. King, and X.J. Zhou, *Handbook of MRI Pulse Sequences*: Elsevier Academic Press.
38. Ordidge, R.J., M. Wylezinska, J.W. Hugg, E. Butterworth, and F. Franconi, *Frequency Offset Corrected Inversion (FOCI) Pulses for Use in Localized Spectroscopy.* Mag. Res. Med., 1996. **36**: p. 562-566.
39. Kim, S.-G., *Quantification of relative cerebral blood flow change by flow-sensitive alternating inversion recovery (FAIR) technique: Application to functional mapping.* Magnetic Resonance in Medicine, 1995. **34**(3): p. 293-301.
40. Edelman, R.R. and Q. Chen, *EPISTAR MRI: Multislice mapping of cerebral blood flow.* Magnetic Resonance in Medicine, 1998. **40**(6): p. 800-805.
41. Talagala, S.L., F.Q. Ye, P.J. Ledden, and S. Chesnick, *Whole-Brain 3D Perfusion MRI at 3.0T Using CASL With a Separate Labeling Coil.* Magnetic Resonance in Medicine, 2004. **52**: p. 131-140.
42. Teeuwisse, W.M., A.G. Webb, and M.J.P. Van Osch, *Arterial Spin Labeling at Ultra-High Field: All That Glitters is Not Gold.* Int J Imaging Syst Technol, 2010. **2**: p. 62-70.
43. Kwong, K.K., D.A. Chesler, R.M. Weisskoff, K.M. Donahue, T.L. Davis, L. Ostergaard, T.A. Campbell, and B.R. Rosen, *Mr perfusion studies with t1-weighted echo planar imaging.* Magnetic Resonance in Medicine, 1995. **34**(6): p. 878-887.
44. Detre, J.A., J.S. Leigh, D.S. Williams, and A.P. Koretsky, *Perfusion Imaging.* Mag. Res. Med., 1992. **23**: p. 37-45.
45. Roberts, D.A., R. Rizi, R.E. Lenkinski, and J.S. Leigh, *Magnetic Resonance Imaging of the Brain:Blood Partition Coefficient for Water: Application to Spin-Tagging Measurement of Perfusion.* JMRI, 1996. **6**: p. 363-366.
46. Buxton, R.B., *Quantifying CBF With Arterial Spin Labeling.* Journal of Magnetic Resonance Imaging, 2005. **22**: p. 723-726.
47. Gardener, A.G., P.A. Gowland, and S.T. Francis, *Implementation of Quantitative Perfusion Imaging Using Pulsed Arterial Spin Labeling at Ultra-High Field.* Mag. Res. Med., 2009. **61**: p. 874-882.
48. Cavusoglu, M., J. Pfeuffer, K. Ugurbil, and K. Uludag, *Comparison of pulsed arterial spin labeling encoding schemes and absolute perfusion quantification.* Magnetic Resonance Imaging, 2009. **27**(8): p. 1039-1045.
49. Gallichan, D. and P. Jezzard, *Variation in the shape of pulsed arterial spin labeling kinetic curves across the healthy human brain and its implications for CBF quantification.* Magnetic Resonance in Medicine, 2009. **61**(3): p. 686-695.
50. Campbell, A.M. and C. Beaulieu, *Pulsed arterial spin labeling parameter optimization for an elderly population.* Journal of Magnetic Resonance Imaging, 2006. **23**(3): p. 398-403.
51. MacIntosh, B.J., K.T.S. Pattinson, D. Gallichan, I. Ahmad, K.L. Miller, D.A. Feinberg, R.G. Wise, and P. Jezzard, *Measuring the effects of remifentanil on cerebral blood flow and arterial arrival time using 3D GRASE MRI with pulsed arterial spin labelling.* J Cereb Blood Flow Metab, 2008. **28**(8): p. 1514-1522.
52. St. Lawrence, K.S. and J. Wang, *Effects of the apparent transverse relaxation time on cerebral blood flow measurements obtained by arterial spin labeling.* Magnetic Resonance in Medicine, 2005. **53**(2): p. 425-433.
53. Look, D.C. and D.R. Locker, *Time saving in measurement of NMR and EPR relaxation times.* Rev. Sci. Instrum., 1970. **41**: p. 250-1.
54. Deichmann, R., *Fast high-resolution T1 mapping of the human brain.* Magnetic Resonance in Medicine, 2005. **54**(1): p. 20-27.
55. Brookes, M.J., P.G. Morris, P.A. Gowland, and S.T. Francis, *Noninvasive Measurement of Arterial Cerebral Blood Volume Using Look-Locker EPI and Arterial Spin Labeling.* Mag. Res. Med., 2007. **58**: p. 41-54.
56. Gunther, M., M. Bock, and L.R. Schad, *Arterial Spin Labeling in Combination With a Look-Locker Sampling Strategy: Inflow Turbo-Sampling EPI-FAIR (ITS-FAIR).* Mag. Res. Med., 2001. **46**: p. 974-984.

57. Petersen, E.T., T. Lim, and X. Golay, *Model-Free Arterial Spin Labeling Quantification Approach for Perfusion MRI.* Mag. Res. Med., 2006. **55**: p. 219-232.
58. Ho, Y.-C.L., E.T. Petersen, and X. Golay, *Measuring arterial and tissue responses to functional challenges using arterial spin labeling.* NeuroImage, 2010. **49**(1): p. 478-487.
59. Ho, Y.-C.L., E.T. Petersen, I. Zimine, and X. Golay, *Similarities and differences in arterial responses to hypercapnia and visual stimulation.* J Cereb Blood Flow Metab, 2011. **31**(2): p. 560-571.
60. Kamagata, K., Y. Motoi, M. Hori, M. Suzuki, A. Nakanishi, K. Shimoji, S. Kyougoku, R. Kuwatsuru, K. Sasai, O. Abe, Y. Mizuno, S. Aoki, and N. Hattori, *Posterior hypoperfusion in parkinson's disease With and without dementia measured with arterial spin labeling MRI.* Journal of Magnetic Resonance Imaging, 2011. **33**(4): p. 803-807.
61. Yoshiura, T., A. Hiwatashi, T. Noguchi, K. Yamashita, Y. Ohyagi, A. Monji, E. Nagao, H. Kamano, O. Togao, and H. Honda, *Arterial spin labelling at 3-T MR imaging for detection of individuals with Alzheimer's disease.* European Radiology, 2009. **19**(12): p. 2819-2825.
62. Wang, Y., S.-E. Kim, E.V.R. DiBella, and D.L. Parker, *Flow measurement in MRI using arterial spin labeling with cumulative readout pulses - Theory and validation.* Medical Physics, 2010. **37**(11).
63. Hoad, C., E. Cox, D. Anblagan, and S.T. Francis. *Multiphase True-FISP ASL in the Kidney*. in *ISMRM*. 2010. Stockholm: 327.
64. Ye, F.Q., V.S. Mattay, P. Jezzard, J.A. Frank, D.R. Weinberger, and A.C. McLaughlin, *Correction for vascular artifacts in cerebral blood flow values measured by using arterial spin tagging tachniques.* Mag. Res. Med., 1997. **37**(2): p. 226-235.
65. Schepers, J., M.J.P. van Osch, and K. Nicolay, *Effect of Vascular Crushing on FAIR Perfusion Kinetics, Using a BIR-4 Pulse in a Magnetization Prepared FLASH Sequence.* Mag. Res. Med., 2003. **50**: p. 608-613.
66. Ogg, R.J., P.B. Kingsley, and J.S. Taylor, *WET, a T1 and B1 Insensitive Water-Suppression Method for in Vivo Localized 1H NMR Spectroscopy.* Journal of Magnetic Resonance, Series B, 1994. **104**: p. 1-10.
67. Ye, F.Q., J.A. Frank, D.R. Weinberger, and A.C. McLaughlin, *Noise reduction in 3D perfusion imaging by attenuating the static signal in arterial spin tagging (ASSIST).* Magnetic Resonance in Medicine, 2000. **44**(1): p. 92-100.
68. Garcia, D.M., G. Duhamel, and D.C. Alsop, *Efficiency of inversion pulses for background suppressed arterial spin labeling.* Magnetic Resonance in Medicine, 2005. **54**(2): p. 366-372.
69. Pollock, J.M., H. Tan, R.A. Kraft, C.T. Whitlow, J.H. Burdette, and J.A. Maldjian, *Arterial Spin Labeled MRI Perfusion Imaging: Clinical Applications.* Magn Reson Imaging Clin N Am, 2009. **17**(2): p. 315-338.
70. Jackson, A., *Analysis of dynamic contrast enhanced MRI.* The British Journal of Radiology, 2004. **77**: p. S154-S166.
71. Barbier, E.L., L. Lamalle, and M. Decorps, *Methodology of Brain Perfusion Imaging.* Journal of Magnetic Resonance Imaging, 2001. **13**: p. 496-520.
72. Deo, A., M. Fogel, and S.E. Cowper, *Nephrogenic Systemic Fibrosis: A Population Study Examining the Relationship of Disease Development to Gadolinium Exposure.* Clinical Journal of the American Society of Nephrology, 2007. **2**(2): p. 264-267.
73. Yankeelov, T.E. and J.C. Gore, *Dynamic Contrast Enhanced Magnetic Resonance Imaging in Oncology: Theory, Data Acquisition, Analysis and Examples.* Curr. Med. Imaging. Rev., 2009. **3**(2): p. 91-107.
74. Talos, I.-F., A.Z. Main, K.H. Zou, L. Hsu, D. Goldberg-Zimring, S. Haker, J.G. Bhagwat, and R.V. Mulkern, *Magnetic resonance and the human brain: anatomy, function and metabolism.* Cell. Mol. Life Sci., 2006. **63**: p. 1106-1124.
75. Stephenson, M.C., *Multi-Nuclear Magnetic Resonance Spectroscopy of Human Energy Metabolism at High and Ultra-High Field*, in *Physics and Astronomy*. 2009, University of Nottingham.
76. Chhina, N., E. Kuestermann, J. Halliday, L.J. Simpson, I.A. Macdonald, H.S. Bachelard, and P.G. Morris, *Measurement of human tricarboxylic acid cycle rates during visual activation by 13C magnetic resonance spectroscopy.* Journal of Neuroscience Research, 2001. **66**(5): p. 737-746.
77. Tkac, I., P. Andersen, G. Adriany, H. Merkle, K. Ugurbil, and R. Greutter, *In Vivo 1H NMR Spectroscopy of the Human Brain at 7T.* Mag. Res. Med., 2001. **46**: p. 451-456.

5 OPTIMISING ASL FOR 7T

5.1 OUTLINE

Ultra-high field (UHF, ≥ 7 T) brings advantages and challenges to Arterial Spin Labelling (ASL) [1, 2]. The lengthened longitudinal relaxation times of tissue and blood [3, 4] mean the peak of the perfusion signal is broader than at lower field strength, this coupled with the increased signal-to-noise ratio (SNR) gives improved contrast-to-noise (CNR) in the ASL images [2]. However, with this are challenges; shortened transverse relaxation time (T_2*) causes increased signal dephasing, increased specific absorption rate (SAR), greater B_0 and B_1 field inhomogeneities leading to distortions resulting in image artefacts. To take full advantage of the increased signal that ultra-high field brings, imaging sequences used at 3T have to be modified and optimised for higher field strength.

In this chapter methods for ultra-high field ASL imaging sequences are discussed. The experimental work in this chapter is divided into two main sections. The first is the development of ASL readout schemes; including the development of (1) high spatial resolution gradient-echo EPI, (2) the use of Balanced Fast Field Echo (bFFE) and Turbo Field Echo (TFE) and (3) the implementation of 3D-EPI. The second section of the chapter describes Look Locker (LL) multiple post-label delay (TI) ASL methods for 7 T imaging. This includes (1) the measurement of arterial cerebral blood volume at rest and during motor activation, (2) the combination of 3D-EPI with a Look Locker readout for increased high volume coverage imaging over 2D-EPI and (3) the assessment of the haemodynamics of Low Grade Gliomas with Look Locker TFE.

5.2 READOUT SCHEMES FOR ULTRA HIGH FIELD ASL

5.2.1 2D-EPI: EFFECT OF SPATIAL RESOLUTION

ASL data are generally acquired at coarse spatial resolution, typical in-plane resolution ~ 3 mm with 5 – 8 mm slice thickness (~ 60 µl voxel volume). The spatial resolution is restricted by the intrinsically low perfusion-weighted ASL signal, of the order of 1 % at 3 T, and the image and temporal signal-to-noise ratio (iSNR / tSNR) available at conventional field strengths [5]. At this reasonably

coarse spatial resolution ASL voxel dimensions exceed the brain's cortical thickness, which ranges from 1.5 to 4.5 mm [6].

Only a small number of prior studies have collected high resolution ASL data; single slice segmented TrueFISP ASL has been acquired at 3 T (1 mm in-plane and 6 - 8 mm slice thickness) [7], at 7 T a surface coil has been used to collect high resolution EPI data with a limited field of view (FOV) (1.5 x 1.5 x 3 mm^3) [8], and the use of segmented GRASE has been demonstrated (1.5 x 1.5 x 5 mm^3) [9]. Duyn *et al*. [10] demonstrate the feasibility of high resolution (1.5 x 1.5 x 2 mm^3) ASL data using an EPI acquisition at 3 and 7 T in their study on the technological improvements for ASL perfusion imaging.

Studies using dynamic susceptibility contrast (DSC) MRI [11, 12] and ASL [13-15] have suggested partial volume effects (PVE) at low spatial resolution lead to an underestimation of grey matter and overestimation of white matter perfusion. Partial volume effects arise due to a voxel containing different tissue types; this is made worse with coarse resolution/large voxel sizes. Donahue *et al.* [13] compared perfusion measurements (blood flow) made using PET with TILT (transfer insensitive labelling technique) pulsed ASL. Data were acquired at in-plane spatial resolutions of 2.75, 3.0, 3.75, 5.0 and 7.5 mm with 3 mm slice thickness. Frontal grey matter (GM) cerebral blood flow (CBF) was found to increase from 48.8 to 54.4 ml/100g/min, and occipital GM CBF increased from 49.3 to 58.3 ml/100g/min with reducing voxel size. These studies are suggestive of the benefit of high spatial resolution to avoid confounding results due to PVE.

In this first experiment high spatial resolution ASL data is collected at 7 T in 10 minutes using background suppressed, pulsed ASL with a gradient echo EPI readout. The feasibility of increasing spatial resolution and the improved cortical delineation of the grey matter perfusion weighted signal is demonstrated.

5.2.1.1 Methods

Five healthy subjects participated in the study, age 23 ± 3 yrs; all subjects gave informed written consent. Procedures were conducted with approval from the local ethics committee.

Data were acquired using a Philips Achieva 7 T system with 16-channel SENSE receive coil. A FAIR labelling scheme (selective inversion 10 mm wider than imaging volume, 250 mm spatially limited non-selective inversion) employing an

optimised FOCI inversion pulse was used with in-plane saturation provided by WET (water suppression enhanced through T_1 effects) pre-saturation and sinc post-saturation pulses [2]. To minimise head motion, subjects' heads were stabilised using foam padding.

To correct for field inhomogeneities and minimise geometric distortions, an image-based shimming technique [16] was used which minimises the magnetic field inhomogeneity over a cuboid region within a field map placed over the slices of interest. Field maps were generated using a B_0-mapping sequence which acquired two gradient echo images at echo times TE1/TE2 of 6/6.5 ms. The phase difference ($\Delta\varphi$) between these two images is proportional to the local magnetic field offset, echo time and gyromagnetic ratio (γ) allowing for the calculation of the field offset;

$$\Delta\varphi(r) = \gamma \cdot \Delta TE \cdot \Delta B_z(r),$$
$$\Rightarrow \Delta B_z(r) = \frac{\Delta\varphi(r)}{\gamma \cdot \Delta TE}, \qquad \textbf{5-1}$$

where r is position, and ΔTE is the difference in echo time [17].

ASL data sets were acquired at voxel dimensions of 3 mm isotropic, 2 x 2 x 3 mm^3, and 1.5 x 1.5 x 3 mm^3, with FOV = 192 x 192 x 15 mm^3. Gradient echo EPI images were acquired using SENSE acceleration 2, (TE = 25 ms, 3/5 subjects) and a half scan (partial k-space) factor of 0.8 to achieve an echo time (TE) of 16 ms (2/5 subjects). An identical TE and a constant bandwidth of 21.2 Hz per pixel in the phase-encode direction was used for all spatial resolutions resulting in a readout time of 42 (TE = 16) / 51 (TE = 25) ms per slice at each resolution.

All datasets were reconstructed to 1.5 x 1.5 mm^2 in-plane resolution (128 x 128 matrix) to allow the same grey matter masks to be applied to the different spatial resolution data sets for voxel-wise comparison. Ninety two dynamics (~ 10 minutes) were acquired at 1.5 and 2 mm in-plane resolution, and 52 dynamics at the 3 mm in-plane.

Five contiguous axial slices were acquired in ascending order with minimal temporal spacing. ASL data were acquired with a post-label delay of 1550 ms, and TR of 6 s per pair. Data were acquired using background suppression [18] (inversion pulses at TI1 = 402 ms and TI2 = 639 ms) to limit the effect of differing physiological noise contributions across different spatial resolutions [19]. At each

spatial resolution a base EPI equilibrium magnetisation image was acquired with a long TR.

In addition an inversion recovery (IR) EPI series was acquired at 1.5 x 1.5 x 3 mm^3 to form a $T_{1,tissue}$ map (data collected with an identical EPI acquisition to the ASL data to match geometric distortions, with TI = 100 – 2500 ms).

Data Analysis

At each spatial resolution, ASL data were first pairwise subtracted and averaged across dynamics. Difference images (ΔM) were quantified voxel-by-voxel using the general kinetic model (Equation 4-6, assuming 0 transit delay), with $M_{0,blood}$ estimated from grey matter (GM) $M_{0,tissue}$ using the blood-brain partition coefficient (λ = 0.98 ml/100g), this was done voxelwise to account for image inhomogeneities [20], and a value of $T_{1,blood}$ of 2100 ms. IR-EPI data were fitted to a 3 parameter mono-exponential recovery for $M_{0,tissue}$, $T_{1,tissue}$ and inversion flip angle and grey matter masks generated from $T_{1,tissue}$ maps. GM voxels were identified from the $T_{1,tissue}$ maps by thresholding from 1900 – 2300 ms. The $T_{1,tissue}$ based grey matter mask derived at 1.5 mm was then used to determine the mean perfusion rate at each spatial resolution (2 and 3 mm data reconstructed to 1.5 mm).

To quantify the effect of spatial resolution on cortical definition, the spatial correlation between the perfusion weighted images and the T_1 maps was assessed using the Pearson correlation coefficient at the three spatial resolutions. The T_1 map provides high resolution structural information, and high correlation coefficients would reflect improved structural information in the perfusion weighted images.

The temporal signal-to-noise (tSNR) was calculated as the mean voxel perfusion weighted signal divided by the standard error in the voxel time course. This was averaged over the GM mask defined from T_1 values. The perfusion contrast-to-noise (CNR) was calculated from the mean GM perfusion weighted (PW) signal divided by the standard error in the white matter (WM) PW signal (WM defined as 1200 – 1400 ms on the T_1 map). These metrics were calculated for all subjects' at all three spatial resolutions.

5.2.1.2 Results

Figure 5-1 shows example perfusion weighted images acquired at 3 mm and 1.5 mm in-plane resolution. The expanded sections demonstrate the cortical structure that is visible at the two spatial resolutions. It can clearly be seen that the high spatial resolution data provides better information on cortical structure without significant loss of signal-to-noise.

The average CBF value for all 5 subjects across the three spatial resolutions is shown in Figure 5-2, and summarised in Table 5-1 along with tSNR, CNR and correlation measures. The CBF measured at 1.5 mm in-plane is significantly ($P < 0.05$) higher than that measured at 2 mm and 3 mm in-plane resolution. Temporal SNR decreases with voxel volume, the 1.5 mm tSNR is significantly lower than at 2 and 3 mm spatial resolutions. However CNR is improved in the 1.5 mm data compared to the lower resolutions. Correlation coefficients between the T_1 map and the perfusion weighted images did not show a trend across the resolutions.

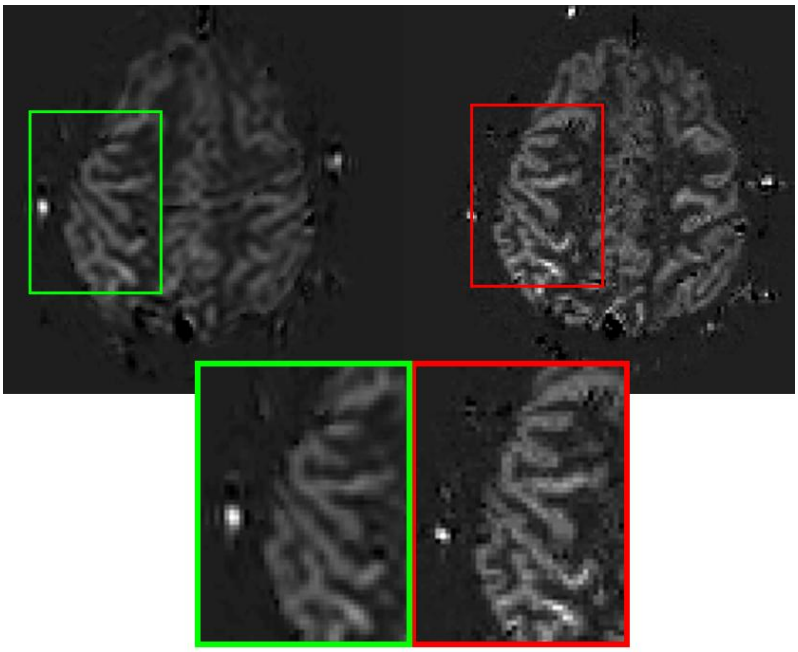

Figure 5-1: Perfusion weighted images acquired at 3 mm (green) and 1.5 mm (red) in-plane resolutions, demonstrating that high spatial resolution provides improved cortical information than the lower spatial resolution data.

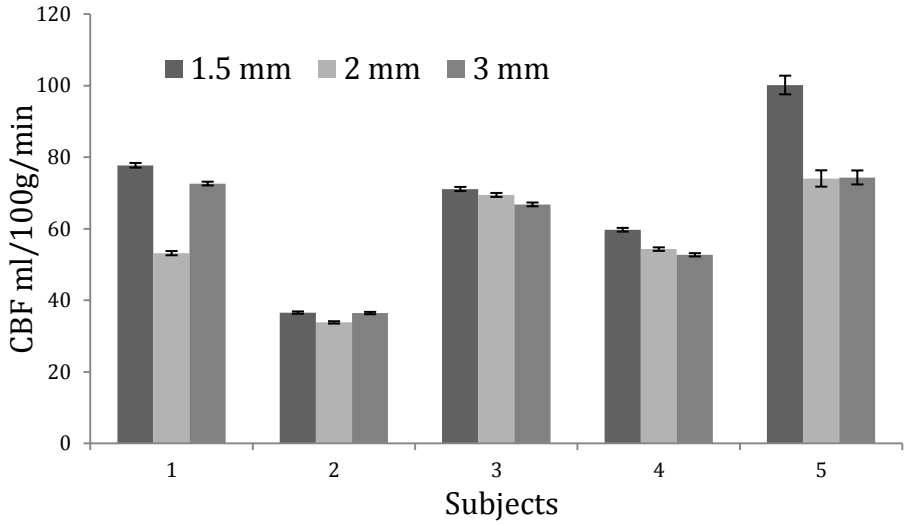

Figure 5-2: CBF for each subject for all three spatial resolutions. Error bars represent standard error across grey matter mask.

	1.5 mm (6.75 µl)	2 mm (12 µl)	3 mm (27 µl)
CBF (ml/100g/min)	69 ± 12 $^{+\$}$	57 ± 8 *	61 ± 8 *
tSNR	5.5 ± 0.8 $^{+\$}$	6.7 ± 1.4 *	7.3 ± 1.5 *
CNR	91 ± 23 $^{+}$	71 ± 18 *	76 ± 17
Correlation Coefficient	0.58 ± 0.08	0.54 ± 0.10	0.62 ± 0.08

Table 5-1: CBF, tSNR, CNR and Pearson correlation coefficient between T_1 map and perfusion weighted images averaged across all subjects for the three spatial resolutions, (* indicates significant difference with 1.5 mm, + indicates significant difference with 2 mm, $ indicates significant difference with 3 mm).

5.2.1.3 Discussion

This study presents high resolution FAIR ASL data collected at ultra-high field (7 T) with a full field of view using a single shot, gradient echo EPI acquisition. This has shown that ultra-high field allows high spatial resolution ASL data to be acquired in relatively short acquisition times (10 minutes).

The improved spatial resolution is shown to provide improved structural delineation in perfusion images, this is visually apparent in Figure 5-1. This is particularly evident in regions with high surface-to-volume ratios and high tortuosity such as the primary somatosensory cortex and the motor cortex. High spatial resolution ASL acquisitions in these areas will, for example, allow improved assessment of functional changes to somatosensory [21] and motor [22] paradigms. This would allow for more strict comparisons of BOLD and ASL

contrast fMRI, as highlighted by [23]. The improved spatial specificity associated with the high resolution acquisition would benefit clinical studies, and the comparison of perfusion data with anatomical information.

tSNR was shown to reduce with increasing spatial resolution, tSNR reduced by a factor of 1.3 between 1.5 and 3 mm, which is less than the 4 fold reduction in voxel volume. This is likely due to the reduced partial volume effects at 1.5 mm increasing the GM signal. CNR increased at 1.5 mm compared to 2 mm in-plane resolution, again likely due to reduced partial volume effects.

An increase in measured mean GM perfusion at higher spatial resolution was found (1.5 mm in-plane: 69 ± 12 ml/100g/min, 3 mm in-plane: 61 ± 8 ml/100g/min). A similar trend for increased GM perfusion was also shown by Donahue *et al.* [13] who collected 3 T data at spatial resolutions up to 2.5 x 2.5 x 3 mm^3. There was less difference in this study due to small changes in voxel size, 7 - 27 mm^3 compared to the 19 - 169 mm^3 range of voxel volumes used in [13].

Correction methods have been suggested to correct for partial volume effects at coarse spatial resolution to allow the assessment of pure grey matter perfusion. However, many proposed correction methods rely on measurement of white matter perfusion [24] or an assumed ratio between white and grey matter perfusion [14], all of which require accurate partial volume fraction estimation. Furthermore, correction methods cannot recover the improved structural delineation provided by high spatial resolution data. It is better to acquire the data at high spatial resolution for perfusion quantification than to apply post processing methods to correct for the coarse acquisition.

In conclusion, ultra-high field provides improved SNR and perfusion contrast allowing ASL data to be collected at high spatial resolution, reducing partial volume effects and leading to improved delineation of cortical structure. This is likely to have particular applications in defining functional changes, improved delineation of borders for stroke and tumour lesions, and the quantification of perfusion with ageing due to brain atrophy or in patient groups where cortical thickness is reduced.

5.2.2 COMPARISON OF TFE AND BFFE WITH EPI

Echo Planar Imaging (EPI) is highly sensitive to B_0-inhomogeneities and susceptibility effects, resulting in geometric distortions and signal drop out, as

discussed in Section 3.4. Furthermore, as spatial resolution (and matrix size) increase, the EPI echo time (TE) increases, leading to a reduction in perfusion weighted signal [25]. To fully exploit the benefits of 7 T to acquire high spatial resolution ASL data, image readout schemes robust to these effects must be explored.

Alternative ASL image readout acquisition schemes include gradient-echo based acquisitions such as a Fast Field Echo (FFE or FLASH (fast low-angle shot)) [26], Turbo Field Echo (TFE, or TurboFLASH) [27-31], and balanced FFE (bFFE, or True-FISP (true-fast imaging with steady-state precession)) [32-37]; spin-echo techniques such as SE-EPI [38], RARE (rapid acquisition with relaxation enhancement) [39], HASTE (half-Fourier single-shot turbo spin-echo) [40], and 3D fast spin-echo (FSE) [41, 42]; or combined gradient-echo and spin-echo (GRASE) contrast [39, 43]. Spin-echo (SE) techniques are advantageous due to reduced susceptibility effects from insensitivity to through-plane gradients. However, in-plane distortions and some T_2* weighting will remain in SE-EPI, particularly at high spatial resolution and UHF due to the shortened T_2* and long EPI readout (parallel imaging can limit this effect) [8, 44]. In addition, at 7 T SE readouts can be limited by SAR [45], particularly when considered in conjunction with labelling and background suppression schemes [18]. Single-shot 3D-GRASE (gradient and spin-echo) is widely used at 3 T to provide rapid simultaneous acquisition of a whole brain volume. However, this uses many refocusing pulses and so becomes SAR limited at 7 T, and typically spatial resolution is coarse (> 3 x 3 x 5 mm^3) [43]. Multiple-shot GRASE [46] allows increased spatial resolution at the detriment of loss of temporal resolution and stability, and again is SAR limited.

Here, GE-EPI, TFE, and bFFE readout schemes for pulsed Arterial Spin Labelling at 7 T are evaluated. ASL data is collected using the three schemes at 2 and 1 mm in-plane spatial resolution. Image and temporal SNR (*iSNR* and *tSNR*), geometric distortions, perfusion-weighted contrast-to-noise ratio (*CNR*), and absolute perfusion quantification (*CBF*) are quantitatively assessed for each gradient-echo readout scheme.

5.2.2.1 Methods

Simulations

The theoretical *iSNR* (image SNR) and point-spread function (PSF) of grey matter (GM) for each readout scheme (GE-EPI, TFE, bFFE) was simulated at 1 and 2 mm spatial resolution assuming a T_1 of 2000 ms and T_2* of 30 ms for grey matter at 7 T [3, 47], and sequence parameters given below (Data Acquisition).

iSNR: For TFE and bFFE the magnetisation at the centre of k-space was modelled iteratively accounting for the effect of each RF pulse and relaxation period by repeated application of Bloch equations (including start-up echoes). The GE-EPI signal at the centre of k-space is simply given by $M_0 exp(-TE/T_2^*)$. Thermal noise for TFE and bFFE schemes was scaled according to the acquisition bandwidth of each sequence. Simulated *iSNR* values for all readouts were then scaled to the measured *iSNR* of the GE-EPI acquisition at 2 mm in-plane resolution.

PSF: For TFE and bFFE, the full width at half maximum (FWHM) of the PSF was calculated by ordering the simulated magnetisation in a centric phase encoding scheme (including start-up echoes), and performing a discrete Fourier transform [48]. The GE-EPI PSF was calculated assuming the GM signal exponentially decayed with T_2* during the GE-EPI acquisition. All signals accounted for the post-saturation pulses in the ASL module resulting in an initial magnetisation of $M_0(1\text{-}e^{-TI/T1})$ and were convolved with a Riesz filter of width 80 % (to reflect the filtering applied by the Philips scanner system to the acquired k-space data) before Fourier transforming. A Riesz filter has the form

$$w(x) = 1 - \left|\frac{x}{x_{max}}\right|^2 \qquad \textbf{5-2}$$

where x_{max} is the maximum x value. A width of 80 % refers to the middle 80 % of the filter being set to 1 (Figure 5-3).

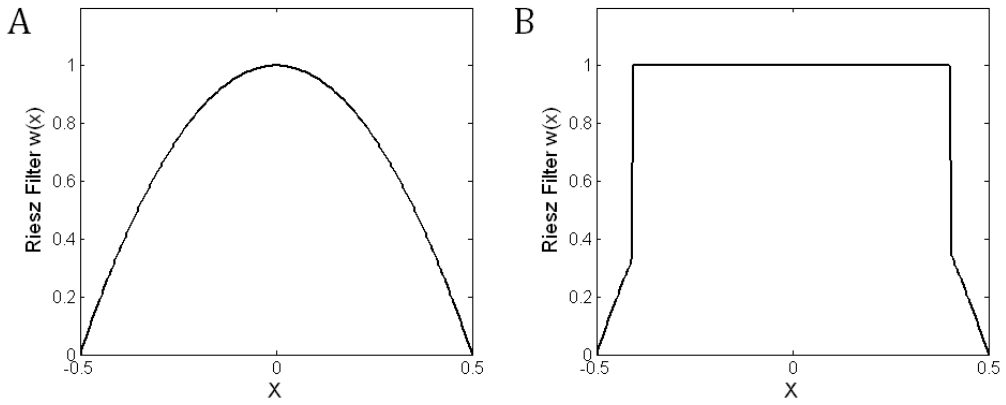

Figure 5-3: (A) Riesz filter of the form given by Equation 5-2, (B) Riesz filter as in (A) but with a width of 80 %.

Data Acquisition

Ten healthy subjects participated in the study and procedures were conducted with University of Nottingham ethics approval. Data was acquired on a Philips Achieva 7 T system with head volume transmit coil and 16-channel SENSE receive coil.

The FAIR scheme comprised a 25 mm selective inversion (control) and a 250 mm wide non-selective inversion (label). WET pre-saturation and sinc post-saturation pulses [2] were applied around the inversion pulse. All ASL data was collected at a post-label delay (TI) of 1550 ms with an ASL pair collected in a TR_{ASL} of 6.2 s.

Image-based shimming [16] was used to correct field inhomogeneities. B_0-field maps were generated from two interleaved gradient-echo images at echo times TE_1 / TE_2 = 6 / 6.5 ms.

For each readout scheme, axial ASL data was collected with 192 x 192 mm^2 FOV, and SENSE factor 2. Images were acquired at two in-plane spatial resolutions: 2 mm (n = 8) and 1 mm (n = 6), with 3 mm slice thickness for all schemes. Ninety ASL pairs (~ 9 min) were acquired at 2 mm in-plane resolution and 125 pairs (~ 13 min) at 1 mm in-plane resolution.

GE-EPI Sequence: Multislice (4 slice) single shot gradient-echo-echo planar images (GE-EPI) were collected: TE = 10 ms at 2 mm in-plane resolution and TE = 24 ms at 1 mm in-plane resolution (minimum achievable TE in both cases). The acquisition bandwidth per pixel was 29.3 / 10.9 Hz in the EPI phase direction (2225 / 1406 Hz in the frequency encoding direction) with a single slice readout

time of 30 and 73 ms for 2 mm and 1 mm respectively. GE-EPI ASL data were collected with background suppression (BGS) [18] using two inversion pulses at 402 and 639 ms.

TFE Sequence: 2 mm and 1 mm data was collected with a single shot TFE readout of TE/TR of 2.5 / 5.0 ms, 15° flip angle and centric phase-encoding (to optimise perfusion contrast [34]), with six start-up echoes. The acquisition bandwidth was 506 Hz/pixel, resulting in a total slice readout time of 165/315 ms for 2/1 mm data. The acquisition was limited to four slices (with no spacing between slices) without BGS due to SAR limits.

bFFE Sequence: bFFE images were collected with TE/TR of 1.8/3.6 ms and 2.1/4.1 ms for 2 / 1 mm resolution respectively. An $\alpha/2$ preparation pulse and 12 pre-scans were followed by successive alternating 50° pulses. The acquisition bandwidth was 1642 Hz/pixel with a readout time per slice of 120/260 ms for 2/1 mm data. A non-segmented acquisition was implemented, and SAR constraints limited the acquisition to a single slice with no background suppression pulses. A four slice acquisition would require a TR_{ASL} of ~11 s/pair with a readout spacing of 522 ms between slice acquisitions.

The slices were positioned in the cortical grey matter for half the subjects (*superior* slices) and an *inferior* level (level of deep gray matter) for the remaining subjects.

For each readout, tissue equilibrium magnetisation was measured from the base images (acquired with long TR). For grey matter segmentation, inversion recovery (IR) data was collected at 10 inversion times of 100, 200, 300, 500, 700, 1000, 1300, 1500, 2100 and 2600 ms, with a TR of 10s. To assess image SNR (*iSNR*), 20 repeats of a scan with zero RF power were acquired to estimate noise (noise scaling factors estimated in 1 subject). In one additional subject, 20 repeats of the base images were acquired to assess temporal SNR (*tSNR*),

Data Analysis

Label and control datasets were subtracted and the resulting images averaged to form perfusion-weighted (PW) images. Perfusion maps were created assuming all signal arose from the centre of k-space using Equation 4-6, assuming zero transit delay. To estimate $M_{0,blood}$ a blood-brain partition coefficient λ of 0.98 ml

blood/g tissue was used to correct the equilibrium magnetisation of grey matter $M_{0,GM}$, [20], and $T_{1,blood}$ assumed to be 2100 ms [49].

IR data were fitted to a mono-exponential recovery for $M_{0,tissue}$, $T_{1,tissue}$ and inversion efficiency; for each readout, a grey matter mask was then formed by thresholding T_1 maps from 1900 – 2300 ms. For each subject, the average perfusion signal was found within the grey matter mask. Any voxels in the GM mask with an ASL percentage signal change of > 5% (~ 400ml/100g/min) were excluded, to remove any voxels with large vessels.

Grey matter image and temporal SNR (*iSNR* and *tSNR*), and perfusion-weighted *CNR* were estimated for each readout scheme. *iSNR* was defined from S/σ, where S is the mean GM signal in the base image and σ is the mean of the standard deviation in the noise image timecourse in a 17 x 17 ROI. *tSNR* was estimated from S/σ_{GM} where σ_{GM} is the variance in the GM time course of repeated acquisitions of the base image. *CNR* was defined as $(S_{SEL}\text{-}S_{NS})_{GM}/\sigma)$ where $(S_{SEL}\text{-}S_{NS})$ is the PW signal. The Coefficient of Variation in grey matter perfusion ($CoV_{CBF}(\%)$) between subjects was also estimated from the variance in CBF between subjects divided by the mean value. All statistical analysis was performed in IBM SPSS Statistics v19. A Friedman's Two-Way ANOVA by ranks including pairwise comparison (correcting for Type I error) was used for *iSNR*, *CNR* and CBF comparisons, with a significance threshold of $P < 0.05$.

5.2.2.2 Results

Simulations

Figure 5-4 shows the simulated (A) theoretical *iSNR* and (B) FWHM of the PSF for grey matter. At 2 mm the GE-EPI readout has the highest simulated *iSNR* and TFE the lowest; whilst at 1 mm spatial resolution the *iSNR* of GE-EPI is significantly reduced to closer to that of bFFE. Considering the point spread function, GE-EPI has the narrowest FWHM at 2 mm; at 1 mm spatial resolution all three readouts have a similar FWHM.

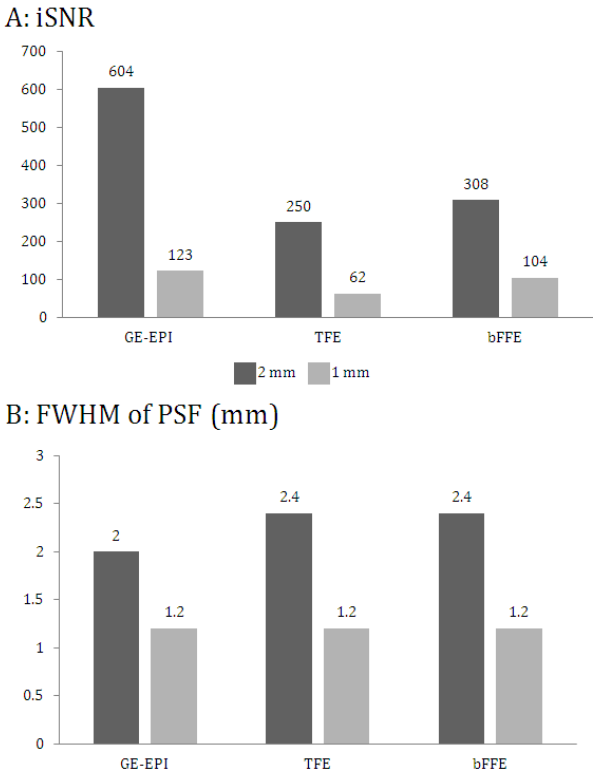

Figure 5-4: Simulations showing (A) theoretical image SNR (all values scaled to measured 2 mm GE-EPI result) and (B) point spread function FWHM (mm) for the 2 and 1 mm resolution data. Simulations assume a low-high acquisition, T_1=2000 ms and T_2*=33 ms used for grey matter and imaging parameters as described in the Methods section (5.2.2.1).

In-vivo Experiments

Figure 5-5 shows example base images of GE-EPI, TFE, and bFFE for superior-inferior planes (data shown for four subjects (i-iv)). GE-EPI images display signal dropout, whilst for one subject the characteristic bFFE banding artefact was seen (arrows, Figure 5-5). TFE images show less field inhomogeneity effects, but have reduced signal compared to GE-EPI and bFFE.

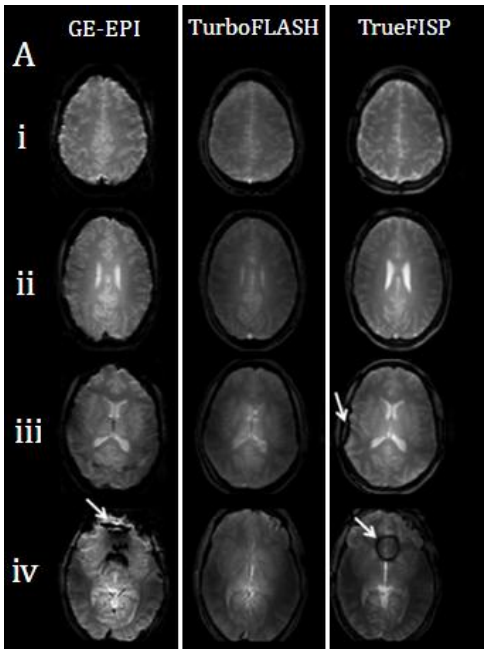

Figure 5-5: Equilibrium base magnetisation images acquired at 2 x 2 x 3 mm^3 for GE-EPI, TFE and bFFE readout schemes. Example data shows a single corresponding slice (of the multi-slice set for GE-EPI and TFE) for four axial planes (i- iv).

Figure 5-6 summarises measured *iSNR*, *tSNR*, *CNR* and CBF. At 2 mm spatial resolution, the *iSNR* of GE-EPI was significantly higher than TFE. In addition, the *tSNR* of GE-EPI at 2 mm was significant highly than bFFE, which in turn was higher than TFE ($P < 0.05$, t-test for means for *tSNR*). This reduction in *tSNR* in the TFE data at 2 mm is reflected in the perfusion maps, Figure 5-7, which was significantly higher for GE-EPI than bFFE. For 1 mm data, *iSNR* was significantly larger for GE-EPI than TFE, there was no significant difference between GE-EPI and bFFE, or bFFE and TFE. At 1 mm, *tSNR* was significantly largest for bFFE, and GE-EPI significantly higher than TFE ($P < 0.05$).

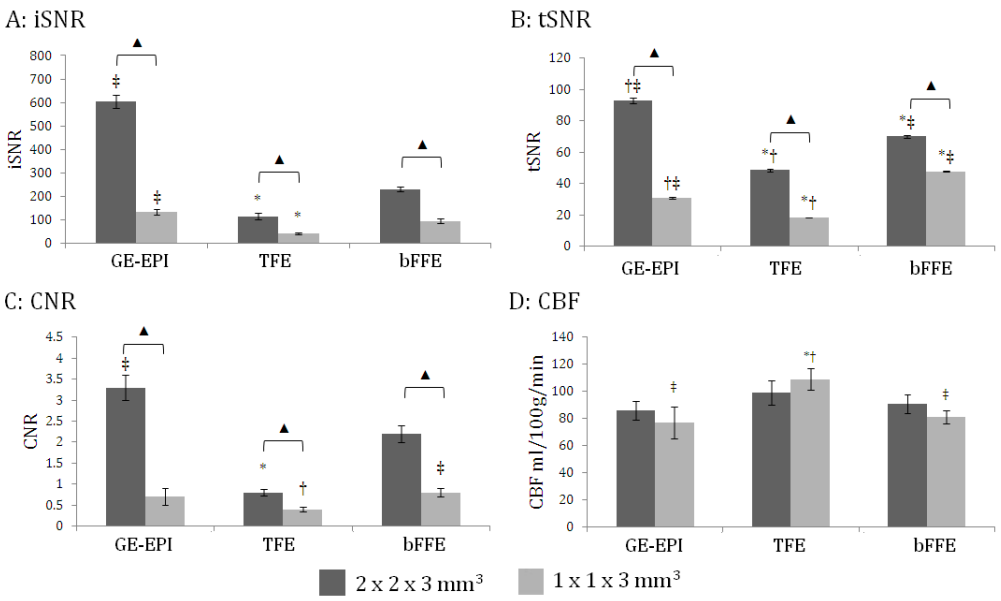

Figure 5-6: (A)Measured image (*iSNR*) and (B) temporal SNR (*tSNR*), (C) perfusion-weighted *CNR* (D) measured perfusion (*CBF*) for each of the three acquisition methods at both spatial resolutions. Mean ± standard error across subjects provided for A, C-D and mean ± standard error across grey matter for B. * P<0.05, comparison with GE-EPI; † P<0.05, comparison with bFFE; ‡ P<0.05, comparison with TFE, ▲ indicates P<0.05 comparison between the resolutions.

Figure 5-7 shows GE-EPI, TFE and bFFE equilibrium images and corresponding quantified perfusion maps for 2 and 1 mm resolution, for both superior and inferior planes. The increased *iSNR* and perfusion contrast (*CNR*) of bFFE at higher spatial resolution is clear. Quantified perfusion values within the GM mask, averaged over all subjects, are given in Figure 5-6 D. At 2 mm, the GE-EPI readout measured a significantly lower CBF than TFE ($P < 0.05$) (shown for each subject in Figure 5-8 A). Comparing calculated values at 1 mm in-plane resolution, the GE-EPI resulted in a large variability across subjects as reflected by the high coefficient of variation (CoV_{CBF}, Table 2), and the lowest measured CBF value of each of the readouts (Figure 5-8 B); significantly lower than for TFE.

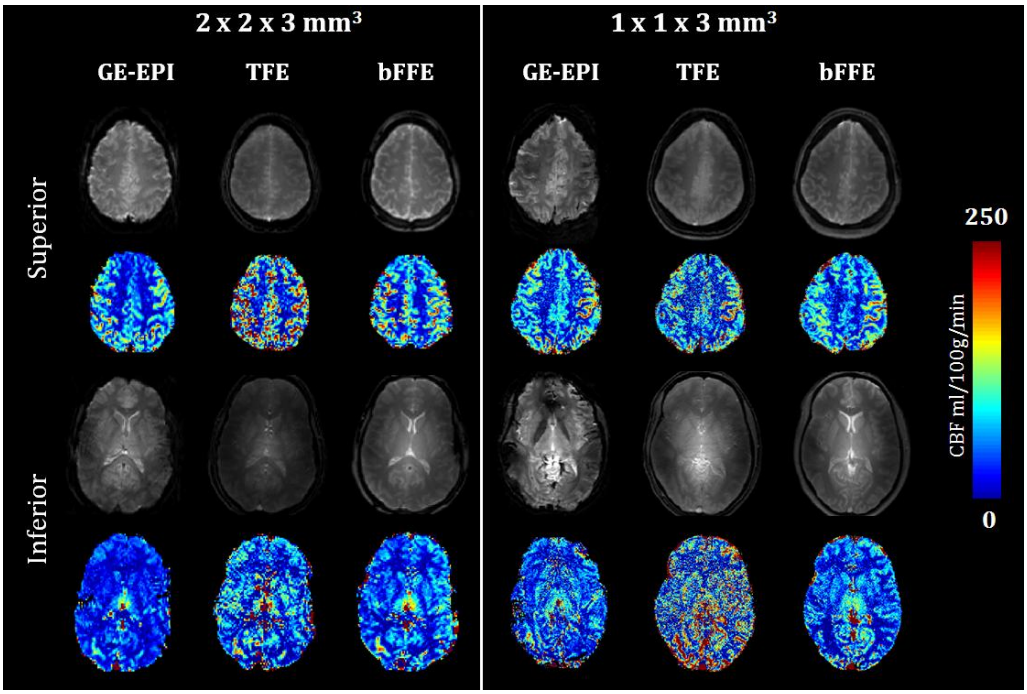

Figure 5-7: 2 mm and 1 mm equilibrium magnetisation images and corresponding CBF maps calculated for GE-EPI, TFE and bFFE. *iSNR* and perfusion-weighted 2 mm images shown are equivalent slices across the readouts, 1 mm images are the first slice in the multi-slice stack to match the post-label delay (TI).

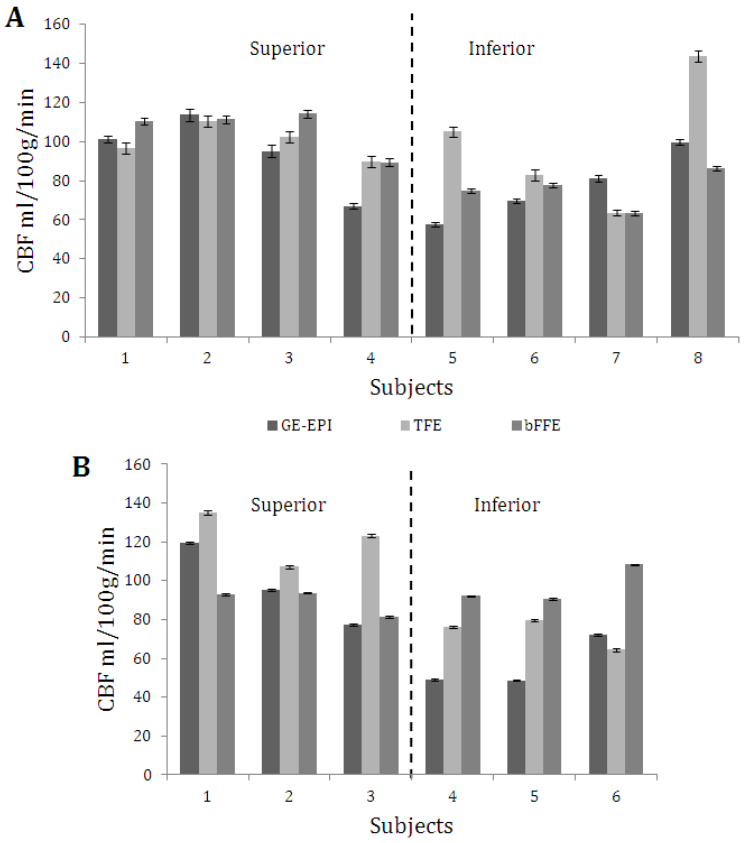

Figure 5-8: (A) Average GM CBF (ml/100g/min) calculated for each readout scheme at 2 mm in-plane spatial resolution (*n* = 8). (B) Average GM CBF (ml/100g/min) for all 6 subjects at 1 mm in-plane resolution. Data divided to show *superior* and *inferior* planes separately. Error bars represent standard error in the mean.

Comparing readout schemes between 2 and 1 mm spatial resolutions, showed a significant reduction in *CNR* ($P < 0.05$), *iSNR* (assessed using Mann-Whitney U test, and Bonferroni corrected) and *tSNR* (t-test for means, Bonferroni correction) at 1 mm, as expected. There was also a tendency for CBF values to be higher at 1 mm compared to 2 mm for TFE (not significant accounting for multiple comparisons). *tSNR* reduced by a similar amount from 2 to 1 mm for GE-EPI and TFE (factor > 2.5), and a lower factor (~ 1.5) for bFFE. GE-EPI had the largest reduction in *CNR* between the resolutions ($\sim$ factor 4), whilst TFE and bFFE reduced by ~ 2.5, approximately equivalent to the voxel volume.

Comparing superior and inferior planes, for the 2 mm data no significant differences were found in *CBF*, *iSNR* or *CNR* (Kruskal-Wallis, Bonferroni corrected for multiple comparisons), although the GE-EPI *CNR* tended to be lower for the inferior plane (not significant accounting for multiple comparisons ($P = 0.102$)).

5.2.2.3 Discussion

Ultra-high magnetic field provides a theoretical increase in perfusion-weighted CNR, however increased magnetic field inhomogeneities result, leading to geometric distortions and signal loss, meaning these gains may not be fully realised for GE-EPI acquisitions. Here GE-EPI, bFFE and TFE ASL readouts were compared at 7 T.

At 2 mm resolution, GE-EPI had higher *iSNR* than TFE; however, the *iSNR* of GE-EPI reduced rapidly with increasing spatial resolution due to an increased echo time (despite using parallel imaging). As expected, TFE and bFFE showed reduced distortion effects and signal voids compared to GE-EPI, with artefacts that appeared reduced compared to images previously shown in the literature [32, 33], likely due to the use of parallel imaging.

Vascular crushing was not used in this study as bipolar gradients would significantly lengthen the GE-EPI echo time, and incorporating vascular crushing into TFE and bFFE acquisitions is challenging [27, 30]. Instead, a long post-label delay was used to limit vascular contributions. Some vascular signal was visible in PW images, to ensure this did not bias average grey matter perfusion values, voxels with PW signal > 5 % were excluded. Measured GM CBF was higher for bFFE ($P = 0.098$) and TFE ($P < 0.05$) than GE-EPI. This may be attributed to the short TR of TFE reducing the tissue signal compared to the blood signal, Boss *et al.* [32] reported a similar increase ($\sim$15 %) for bFFE from the expected

physiological range. The larger difference in values at 1 mm may also be attributed to a significant reduction in *iSNR* of GE-EPI at high resolution, or differences in T_2* between blood and brain tissue at 7 T [25].

TFE and bFFE provide the advantage of a short TE. However, slice acquisition time is significantly increased compared to GE-EPI (TFE/bFFE/GE-EPI: 2 mm in-plane 165/120/30 ms; 1 mm in-plane 315/260/73 ms) reducing the number of slices which can be collected and leading to different perfusion weighting between low and high k-space frequencies, although centric acquisition minimises this. A further constraint is that for TFE and bFFE readouts SAR limitations are met for a TR_{ASL} of 6.2 s, despite using PASL, which has lower SAR than other ASL methods (CASL and PASL). These limits prohibited the use of background suppression for TFE and bFFE, and multi-slice acquisition for bFFE.

In conclusion, the choice of readout at 7 T depends on the site to be imaged, coverage and spatial resolution required; for large spatial coverage at reasonable spatial resolution in areas of low susceptibility GE-EPI is recommend. TFE has low CNR, but has low sensitivity to field inhomogeneity and is less SAR limited than bFFE, allowing the acquisition of multi-slice data with low geometric distortions and signal drop-out in a reasonable temporal resolution. bFFE provides a high SNR technique for use when high spatial resolution but limited coverage is sought.

5.2.3 3D-EPI ASL

2D-EPI is commonly used for the ASL image acquisition due to the short imaging time of the EPI readout allowing several slices to be acquired during the peak of the perfusion curve. 3D sequences have been noted to be of benefit to ASL due to the entire signal from the volume being acquired simultaneously, ensuring that each slice in the volume has the same perfusion weighting [50].

There is a desire for large volume coverage in ASL measures, but this can be limited by the need to acquire slices within the peak of the ASL perfusion curve for adequate SNR. Wide coverage is important for assessment of vascular abnormalities in patients, and functional studies where changes can be widespread [51], such as attention and working memory tasks and pain studies where areas of interest range from inferiorly in the cerebellum to superior slices in the postcentral gyrus [52].

3D-GRASE is the most popular 3D acquisition used in combination with ASL at lower field strengths (1.5 and 3 T) e.g. [43, 50]. 3D-GRASE uses a train of 180° pulses to form a refocused echo train with both gradient and spin echo contrast. Günther *et al.* [50] compared single slice 2D-EPI with 18-slice 3D-GRASE at 1.5 T at a spatial resolution of 2.5 x 3.4 x 6 mm^3. SNR in grey and white matter increased by a factor of ~ 3 for 3D-GRASE, CBF quantification was unaffected. However, the implementation of 3D-GRASE at 7 T is challenging due to the shortened T_2^*, and the necessity to accurately refocus pulses which can be difficult to implement due to B_1-inhomogeneity, and high SAR. Fast spin echo (3D-FSE) has been implemented for ASL-fMRI [53], but again is restricted at 7 T by SAR and B_1 inhomogeneity. 3D-EPI is becoming widely used for BOLD fMRI at 3 T [54] and 7 T ([55, 56]) providing improved image SNR, sensitivity and temporal SNR compared to 2D-EPI. Poser *et al.* [55] showed this increased sensitivity is more prominent at high resolution (< 1.5 mm in-plane) and further benefits from using a parallel imaging acceleration factor in both readout axes to speed up image acquisition. 3D-EPI has not commonly been implemented with ASL, Gai *et al.* [57] demonstrated its advantages at 3 T to produce a 24 slice (resolution ~ 3 x 3 x 4 mm^3) perfusion map.

This experiment implements 3D EPI for large volume coverage ASL at 7 T. Simulations are performed to assess the impact of the readout parameters on the point spread function and perfusion quantification. In-vivo demonstrations of the optimised sequences are provided.

5.2.3.1 Methods

A schematic of the 3D-EPI sequence is shown in Figure 5-9. There is a train of small tip angle RF pulses, separated by a time TR. After each pulse a plane of K_z space is acquired, this is repeated until the whole of 3D k-space has been sampled.

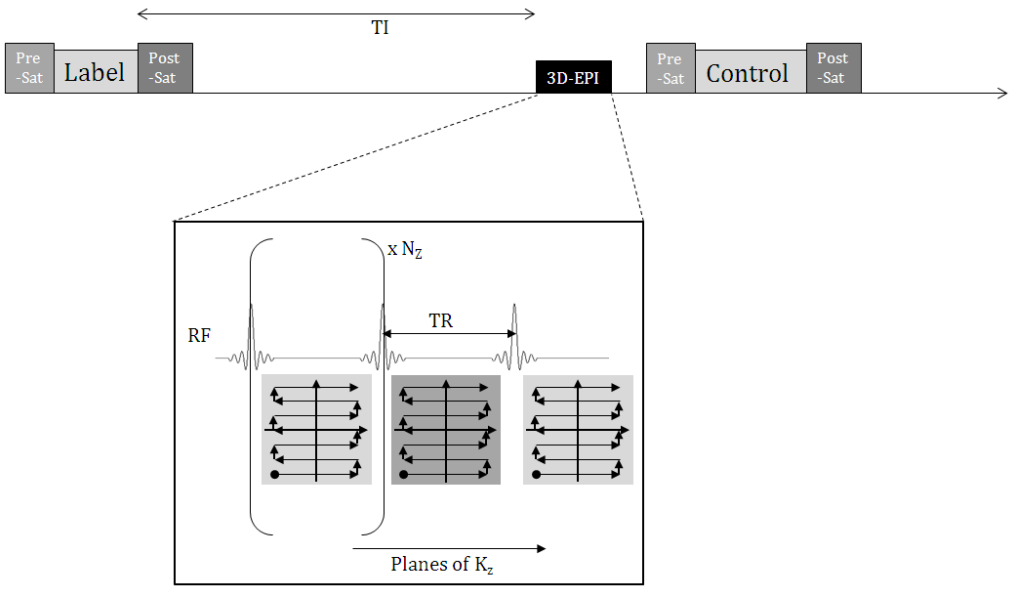

Figure 5-9: Schematic of 3D-EPI ASL acquisition, showing the pre-sat, label and post-sat of the ASL scheme followed by the 3D-EPI acquisition. In 3D-EPI, after each RF pulse a plane of K_z space is acquired and this is repeated N_z times until the entirety of 3D k-space has been sampled.

5.2.3.1.1 Simulations

The effects of the sequence parameters on image quality (e.g. blurring) and perfusion quantification were theoretically assessed. The signal for the 3D-EPI readout can be formed by solving the Bloch equations. The measured transverse signal can be shown to be;

$$M_{xy}(1) = M_0 \sin(\alpha)$$

$$M_{xy}(2) = \left(\frac{M_{xy}(1)\cos(\alpha)}{\sin(\alpha)} exp\left(-\frac{TR}{T_1}\right) + M_0\left(1 - exp\left(-\frac{TR}{T_1}\right)\right)\right)\sin(\alpha)$$

$$\vdots \qquad \textbf{5-3}$$

$$M_{xy}(n) = \left(\frac{M_{xy}(n-1)\cos(\alpha)}{\sin(\alpha)} exp\left(-\frac{TR}{T_1}\right) + M_0\left(1 - exp\left(-\frac{TR}{T_1}\right)\right)\right)\sin(\alpha),$$

for $n > 1$, where M_{xy} is the transverse magnetisation after pulse n, α is the readout flip angle and TR is the time between readout pulses. This assumes complete spoiling of the transverse magnetisation between readout pulses.

It was assumed that there were 23 RF pulses per 3D-EPI block and that TE = 10 ms for both 2D and 3D acquisition of 2 mm in-plane resolution for a 192 x 192 mm^2 FOV with 25 slices. K-space was acquired in a centric ordering with Cartesian sampling.

Point Spread Function

The point spread function (PSF) of the 2 x 2 x 3 mm^3 3D-EPI readout was investigated by simulating the signal of a point source in k-space using rotation and relaxation operators to model the effect of the train of RF pulses assuming a centric k-space acquisition. The k-space signal was Fourier Transformed to give the signal in image space. The PSF was interpolated and the full width at half maximum (FWHM) of the PSF used to assess blurring; the effects of the 3D-EPI parameters of flip angle (10° - 20°) and TR (5 - 30 ms) on the PSF were simulated.

Effect of a 3D-EPI readout on Perfusion Quantification

The nature of the 3D-EPI acquisition (introduced in Chapter 3) will cause the ASL perfusion signal to vary through the acquisition i.e. planes of k_z space will have different perfusion weighting. Simulations were performed to assess this effect on perfusion quantification for a FAIR labelling scheme. The ASL perfusion signal was modelled using a three compartment model (compartments comprising blood outside imaging voxel, blood within voxel and tissue within voxel) as described in Francis *et al.* [58] for a Look-Locker readout scheme (simulation parameters summarised in Table 5-2).

The model was adapted to estimate the transverse signal through k-space for the 3D-readout, by Fourier transforming the k-space signal the image can be formed. The k-space signal following the selective and non-selective signals were each simulated, and then subtracted and Fourier Transformed to provide the difference signal in image space. Due to the linearity of the Fourier transform the order of subtraction/Fourier Transform is inconsequential. The peak magnitude of the FT is taken to be the measured signal.

Parameter	Value
Perfusion rate, f (ml/100g/min)	90
Longitudinal relaxation time of grey matter, T_1 (ms)	2100
Longitudinal relaxation time of blood, T_{1b} (ms)	2100
Equilibrium magnetisation, M_0	1
Bolus duration, W (ms)	1500
Blood : brain partition coefficient, λ (ml/g)	0.98
δ (ms)	400
Δ (ms)	400
Blood volume, CBVa (ml/100g)	1.2
Grey matter transverse relaxation rate (ms)	33
Single-TI post labelling delay (ms)	1500

Table 5-2: Parameters used for 3D-EPI simulations.

To quantify perfusion, the fractional signal change relative to tissue equilibrium magnetisation, M_0, weighted by the blood brain barrier coefficient, λ, was calculated. The fractional signal change was calculated by simulating measurement of M_0 using 3D-EPI, simulated as described above. The relative signal change for a 3D-EPI readout $(\Delta M/M_0)_{3D}$, was then compared to that of a 2D-EPI readout $(\Delta M/M_0)_{2D}$ with 90° flip angle, to examine the effects of fitting the 3D data with a model typically used for a 2D acquisition.

5.2.3.1.2 In-Vivo Study

Two healthy volunteers were scanned with the optimised readout parameters; 2 x 2 x 3 mm^3, FOV = 192 x 192 mm^2, matrix 96 x 96, TR/TE = 26/11 ms, SENSE reduction 3.5 (P)/ 1.5 (S), partial Fourier factors 0.879 (Y) / 0.9 (Z), linear phase encode order, flip angle 14° and bandwidth of 2538 Hz in EPI frequency direction (38.2 Hz/pixel). With these optimised parameters, the number of encoding steps and duration of the readouts is summarised in Table 5-3 for a range of 3D volume coverage values.

Number of Slices	Number of Encoding Steps	Duration of Readout / ms
8	7	181
12	11	283
16	13	334
20	17	437
24	21	539

Table 5-3: Number of encoding steps and acquisition length for optimised 2 x 2 x 3 mm^3 3D EPI acquisition

5.2.3.2 Results

5.2.3.2.1 Simulations

Point Spread Function: The FWHM of the PSF was largely unaffected by changes in TR, except at the larger flip angles (> 16°). The PSF broadened as flip angle increased leading to image blurring as demonstrated in Figure 5-10 A. The PSF can be seen to increase at larger flip angles due to increased signal decay across the readouts, the largest flip angle whilst remaining within a reasonable point spread function was chosen. Thus, a 14° flip angle was used for all 3D-EPI readouts.

Effect of 3D-EPI readout on Perfusion Quantification: The simulations demonstrate a tendency for the 3D-EPI acquisition to lead to an overestimation of the fractional signal change. Figure 5-10 B shows the dependence of this overestimation in fractional signal change on flip angle and TR. For a given TR, varying the flip angle from 5 - 20° resulted in a small difference (~ 2 %) in the accuracy of perfusion quantification. Varying TR had a larger impact, with perfusion being further overestimated as TR increased (resulting in a lengthened readout train).

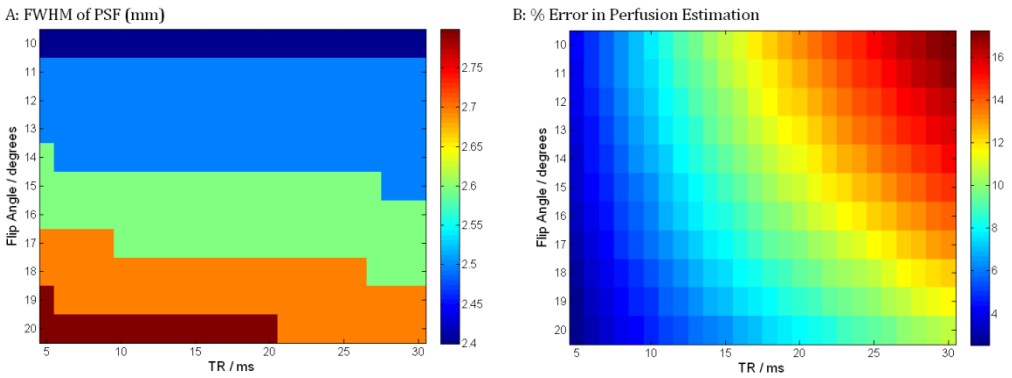

Figure 5-10: (A) Full width at half maximum (FWHM) of the point spread function (PSF) for the 2 mm in-plane readout and (B) error in the perfusion estimation of 3D-EPI readout as a function of flip angle and TR.

These simulations demonstrate that the TR should be kept to a minimum to reduce errors in perfusion quantification and that the flip angle should be around 14° to reduce image blurring whilst providing adequate SNR.

5.2.3.2.2 In-Vivo Study

The quality of the 3D-EPI base images is shown in Figure 5-11, the signal and contrast is consistent across the majority of the slices. The lowest slices show

lower signal due to the extent of the coil – also seen in the scout image is the signal drop off due to the coil.

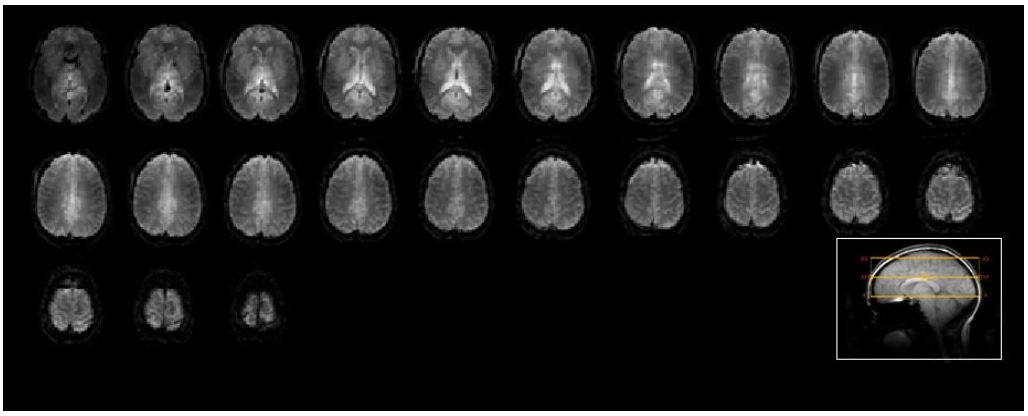

Figure 5-11: Example 3D-EPI base images, scout image with slice coverage shown inset. Images acquired at 2 x 2 x 3 mm^3, with a readout duration of ~ 500ms.

Figure 5-12 shows perfusion weighted 3D-EPI images acquired with two different slice positions, firstly with imaging volume and selective inversion centred within the brain in the foot-head direction, and secondly the imaging volume was moved upwards such that the slice selective inversion extended outside of the head. Artefacts were found to be associated with the selective being within the head as highlighted by white arrows. These artefacts are only present in the difference images; they are not visible in the label or control images. This is likely to be due to slight image wrap in the foot-head (FH) direction. This can be eradicated by widening the selective slab such that it extends out of the top of the head in the superior direction (Figure 5-12 B).

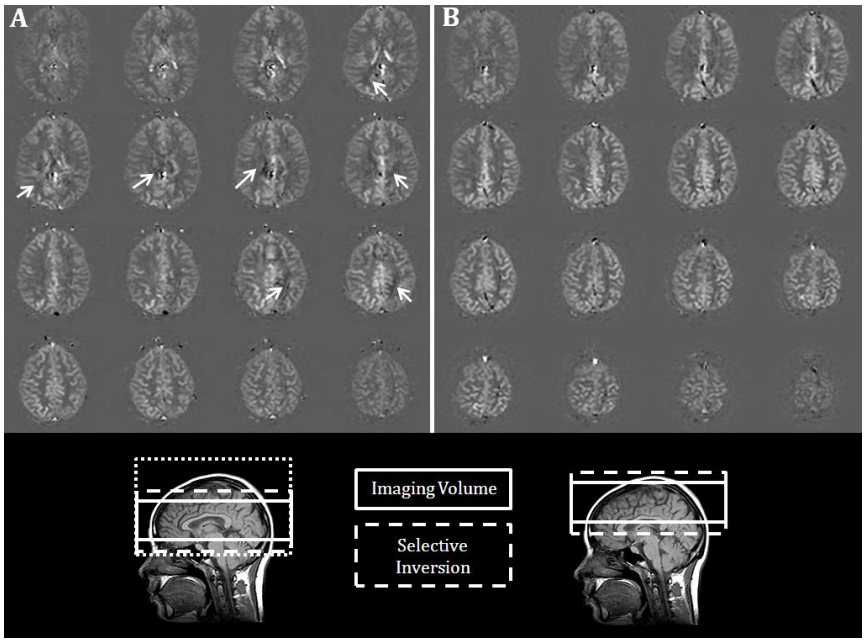

Figure 5-12: Perfusion weighted images where the selective slab is (A) inside the head (dotted box represents widening the selective inversion to reduce image artefacts) and (B) outside the head due to the stack being moved upwards. White arrows indicate position of artefact.

Figure 5-13 shows the perfusion weighted images obtained from the optimised 3D-EPI readout (2 x 2 x 3 mm^3, FOV = 192 x 192 mm^2, matrix 96 x 96, TR/TE = 26/11 ms, SENSE reduction 3.5 (P)/ 1.5 (S), partial Fourier factors 0.879 (Y) / 0.9 (Z), flip angle 14°). The added benefit of the 3D acquisition is the ability to reslice the data into coronal and sagittal views as each axial slice has the same perfusion weighting. The images show the extent of the slice coverage, with inferior coverage of the occipital cortex up to more superior coverage of the motor cortex.

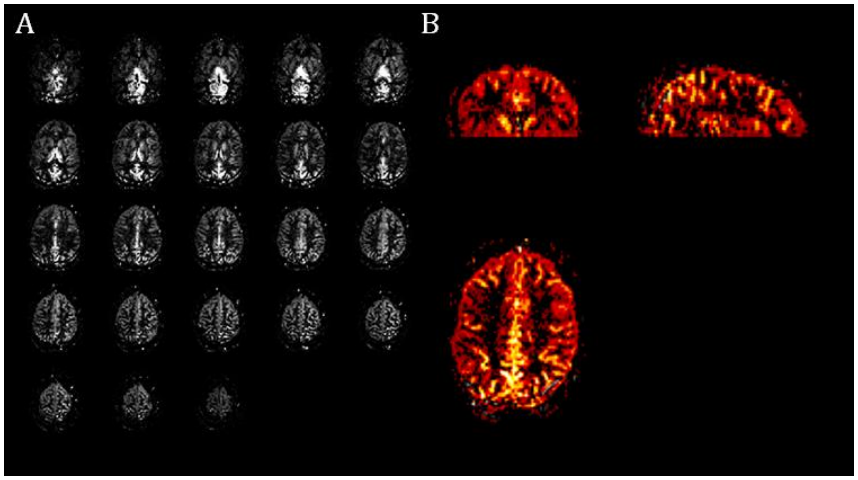

Figure 5-13: 3D-EPI perfusion weighted images shown as (A) all 23 axial slices and (B) coronal, sagittal and transverse views. Scan parameters 2 x 2 x 3 mm^3, FOV = 192 x 192 mm^2, matrix 96 x 96, TR/TE = 26/11 ms, SENSE reduction 3.5 (P)/ 1.5 (S), partial Fourier factors 0.879 (Y) / 0.9 (Z), linear phase encode order, flip angle 14°.

5.2.3.3 Discussion

Figure 5-13 shows the high quality of 3D-EPI ASL perfusion weighted images feasible at 7 T. These images show very good spatial coverage, with good image quality even in inferior slices towards the end of the RF coil. Artefacts that were initially seen were removed by widening the FAIR selective slab thickness slightly to encompass the top slices of the brain (represented by dotted box in Figure 5-12 A), this will cause the magnetisation transfer effects to differ between the selective and non-selective but this effect will be minimal. With the optimised parameters coverage is 72 mm, which covers the majority of the cortex of the brain (excludes cerebellum).

A previous implementation of 3D-EPI for perfusion imaging suggested modulating the readout flip-angle along the train [57]. This has also been suggested for MPRAGE [59] and FSE [60] anatomical imaging to reduce image blurring due to the reduction in signal for the outer lines of k-space (shown in Figure 5-14 A). By modelling the RF pulses it can be shown that to maintain the signal in the pulse train at a constant level the flip angle must be modulated in the following way;

$$f_n = \sin^{-1}\left(\left(\frac{m_{xy}\cos f_{n-1}\exp\left(-\frac{TR}{T_1}\right)}{\sin f_{n-1}} + M_0\left(1-\exp\left(-\frac{TR}{T_1}\right)\right)\right)^{-1} m_{xy}\right), \quad \textbf{5-4}$$

for $n > 1$ where f_n is the flip angle of the n^{th} pulse, m_{xy} is the transverse signal being maintained which is dependent on the initial flip angle chosen ($m_{xy} = M_0 \sin(f_1)$), M_0 is the equilibrium magnetisation, TR is the time between RF pulses and T_1 is the longitudinal relaxation time of interest. For a TR of 30 ms and T_1 of 2 s, starting at 14°, the 19th pulse would be 52°, beyond that it is not possible to maintain the signal at that level (shown in Figure 5-14 B).

Modulating the RF pulse not only restricts the number of slices that it is possible to collect when trying to maintain the signal, but it will also increase SAR due to the large increase in flip angle. In addition the first few flip angles step up by less than one degree –which would be difficult to implement in practice. The accuracy of achieving such specific flip angles, especially at high field, would be extremely difficult and signal decay will not be eliminated. Figure 5-14 A demonstrates the effect of B_1 inhomogeneity on the k-space signal. The shaded region indicates how the signal could vary if there was a ± 20 % error in the flip angle. This

demonstrates that due to the high flip angles required at the end of the train the signal could deviate significantly from the ideal. Initial point spread function simulations and acquired data are indicative of minimal blurring. Therefore the use of modulated flip angles was not further pursued.

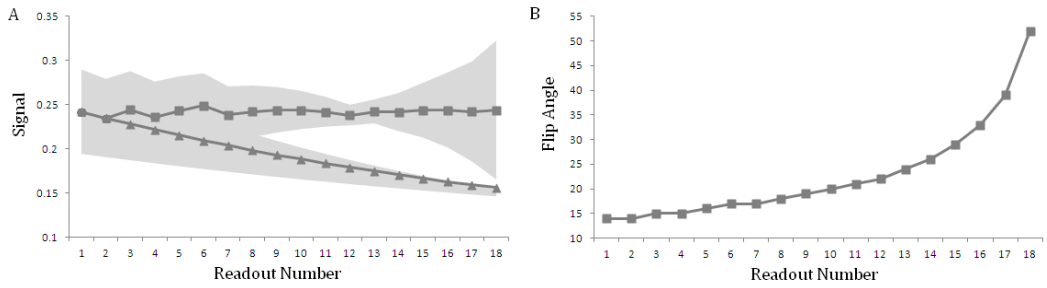

Figure 5-14: (A) Transverse signal due to constant flip angle (▲) and modulated flip angle (■), the flip angle has been rounded to an integer causing small signal oscillations. Shaded areas indicate signal where the flip angle achieved has an error of ± 20 % (B) Theoretical modulation of flip angle required to maintain the signal shown in (A).

3D-EPI provides a fast way of achieving large volume coverage suitable for perfusion imaging. This is faster than the equivalent 2D-EPI acquisition as SENSE acceleration can be applied along both readout directions, as can partial Fourier acquisition. Further gains of a 3D-EPI scheme are that the perfusion weighting is identical across the slices as both the background signal and underlying perfusion signal are not altered across the readout volume.

5.3 LOOK LOCKER ASL: ACQUISITION SCHEMES AND APPLICATIONS

The standard methodology for ASL is to acquire an image at a single post-label delay (TI), by modelling the transit of labelled spins the perfusion can be estimated. However, as demonstrated in Gallichan *et al.* [61] the perfusion timecourse across brain areas is very different due to the different tortuous routes of the labelled blood from vessels in the neck to the tissue bed, causing the labelled blood to arrive at very different times. For example, the arrival time in the caudate nucleus and putamen is approximately 0.2 s but this is increased to nearer 1 s in the occipital regions [61].

Single TI ASL methods to account for such delays, such as QUIPSS/QUIPSSII [62], aim to remove such transit time dependence by applying an additional saturation pulse to define a fixed bolus. However, repeating the ASL acquisition at different post-label delay times allows for a better model fit by accounting for the different temporal characteristics. However, this lengthens the total scan time making it less appropriate in some studies, for example in patients where movement is an

issue. The development of Look-Locker methods for 7 T imaging is important to allow for transit times to be taken into account whilst benefitting from the increased SNR and lengthened T_1.

Look-Locker (LL) techniques [63] proposed for use with an ASL labelling scheme include the work of Francis *et al.* [58], Günther *et al.* [64] and Petersen *et al.* [65] for the measurement of perfusion and transit times. These can be also referred to as QUASAR [65] or multi-phase ASL [66] and the pulse sequence is shown schematically in Figure 5-15. Brookes *et al.* [67] used LL-ASL to measure arterial cerebral blood volume (CBVa), as opposed to cerebral blood flow (CBF). These LL based methods allow for temporal characteristics, e.g. arrival time and transit time, to be found in addition to CBF. This can be particularly useful for functional studies or in patient studies where the transit time is thought to be disrupted. Currently LL-based ASL methods have been applied in healthy people to investigate visual stimulation [68] and combined visual stimulation/hypercapnia [69], as well as in patient groups (e.g. Parkinson's disease [70]).

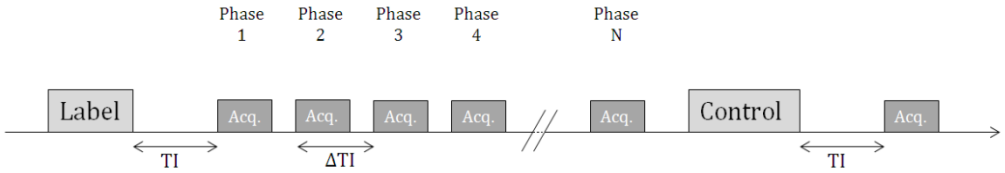

Figure 5-15: Schematic of Look-Locker ASL. TI is the post-label delay, ΔTI is the phase interval or time between readouts and N is the total number of readouts.

The following describes the development of three Look-Locker based methodologies for 7 T which build on the readout schemes developed for ASL in Section 5.2; (1) The measurement of arterial cerebral blood volume (aCBV or CBVa) using Look-Locker FAIR with a 2D-EPI readout; (2) The combination of Look-Locker FAIR with a 3D-EPI readout scheme to increase volume coverage; (3) The study of perfusion using Look-Locker with a TFE readout and applications in patients with low grade gliomas.

5.3.1 *MEASUREMENT OF ARTERIAL BLOOD VOLUME USING LLEPI FAIR*

When using MRI, studies of brain activation commonly use BOLD fMRI due to the high SNR of the technique allowing high spatial and temporal resolution data to be collected. CBF, assessed using ASL, is advantageous for functional assessment due to the measurement of a physiological quantifiable value. Initially the arterial cerebral blood (CBVa) signal was not thought to be of interest as it was assumed

that the predominant change occurred in the venous CBV (CBVv) due to a ballooning of the elastic vessel walls [71]. However a study by Lee *et al.* [72] demonstrated that in fact the arterial blood volume changes on activation (up to a 60 % increase due to hypercapnia, accompanied by only a 10 % change in CBVv). Measurement of CBVa has now become an important measure for understanding fMRI changes. This study demonstrates the measurement of CBVa at ultra high field (7 T) using Look-Locker ASL, and applies the technique to assess the effect of a motor task on CBVa and transit time.

5.3.1.1 Methods

Theory

It has been shown that CBVa can be measured using a Look-Locker ASL scheme, as outlined in Chapter 4. For the Look-Locker EPI sequence to be sensitive to arterial blood volume the signal from the tissue compartment must be suppressed. This can be achieved using closely spaced high flip angle pulses (~ 45° - 50°) in contrast to lower flip angles (~ 35°) used in the measurement of CBF [67]. Also, since the arterial blood signal arrives quickly at the imaging slice leading to a short transit delay, the initial post label delay must be short (~ 150 ms) to adequately sample the inflow of the arterial blood signal.

The model of Brookes *et al.* [67] used a compartmental model to iteratively model the effect of the RF readout pulses in three compartments; the blood flowing into the voxel, the blood in the voxel and the perfusion into the tissue. This allows for measurement of CBVa from estimation of δ, the time the blood remains in the voxel, and F, the bulk flow as

$$CBVa = F\delta \qquad \textbf{5-5}$$

Further parameters in the model include the bolus duration (W) and the time for the bolus to arrive (Δ_a).

Data Acquisition

Data were acquired using a Philips Achieva 7 T system with a head volume transmit and 16-channel SENSE receive coil. Volunteers were positioned in the scanner and foam padding was used to minimise head motion during scanning.

To correct for field inhomogeneities and minimise geometric distortions in the EPI images, a parcellated shimming technique [16] was used. Field maps were

generated using a standard B_0-mapping sequence, which acquired two gradient echo images at echo times TE1/TE2 of 6 / 6.5 ms.

Baseline Study: 4 healthy volunteers took part in the initial study (3 female, 1 male, 24 ± 3 years old). A Look-Locker EPI FAIR sequence was used with a selective inversion thickness of 13 mm and a 230 mm spatially limited non-selective inversion. Optimised FOCI pulses were used for labelling, together with an optimised WET (water suppression enhanced through T_1 effects) pre-saturation and sinc post-saturation scheme for in-plane saturation.

Data were collected with 192 x 192 mm^2 FOV, SENSE acceleration factor of 2, half scan partial factor of 0.8, LLEPI readout flip angle 45°, TI = 150 ms, ΔTI = 100 ms, TE = 10 ms, 21 phases per TR with a TR of 4.8 s per tag/control pair (see Figure 5-15). Images were acquired with a resolution of 2 x 2 x 3 mm^3. 15 contiguous axial slices were acquired. A 15-slice LLEPI-FAIR acquisition was achieved by acquiring one slice per dynamic, and the slices acquired sequentially (as shown in Figure 5-16 for the motor task). 150 dynamics were acquired in 12 minutes this gave 10 averages for each of the 15 slices. Only 10 averages were collected due to the high SNR from the blood signal. A *base* EP image with TR = 10 s was acquired for M_0 estimation.

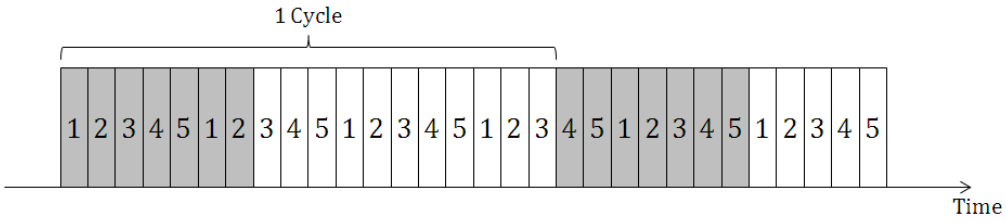

Figure 5-16: Schematic of the aCBV functional paradigm. Numbers 1-5 represent the slice acquired (each slice, represented by a block, takes 4.8s to acquire). Shaded blocks denote the periods of finger tapping, unshaded blocks represent the rest periods.

Motor task: 6 healthy subjects participated in the study, 4 females and 2 males, age 27 ± 5 years. A BOLD localiser scan was used to localise the motor cortex and so identify the slices for the functional task during perfusion data acquisition. The BOLD localiser comprised of 4 cycles of right handed finger tapping, 24 s tapping, and 24 s rest. A visual prompt was used to queue the subject to the finger tapping task, displaying a '+' during rest periods and 'TAP' to tell the volunteer to tap the fingers on their right hand. BOLD data was analysed on-line using IView-BOLD software to locate areas of motor activation. The EPI readout scan parameters for the BOLD localiser were as for the baseline study but with TE = 25 ms and 21

contiguous axial slices acquired. Look-Locker ASL scan parameters were identical to those used for the baseline study except: 180 tag/control pairs were acquired, 1 slice (2 subjects) or 5 (4 subjects) contiguous axial slices were acquired. The functional paradigm during which perfusion data was acquired was a right handed finger tap with 10 cycles of 33.6 s tapping and 52.8 s rest (shown schematically in Figure 5-16).

Data Analysis

Baseline study: Label and control data were subtracted, visually inspected for motion and data averaged across the dynamics. The perfusion weighted images were then fitted to the model of Brookes *et al.* [67] for CBVa, arrival time Δ_a and exchange time δ (assumed W is infinite and that tissue signal is suppressed). $M_{0,b}$ was estimated from the base image intensities in a major vessel. It was assumed that $T_{1,b}$ = 2100ms.

Motor task: Label and control data were subtracted, visually inspected for motion and data averaged across rest and active time periods to give perfusion weighted images at both rest and on activation. The rest and active data sets were then fitted separately, in a similar manner to the data collected in the baseline study.

Spatial smoothing of 3 mm and a high pass temporal filter of 5 * TR, and FILM prewhitening was performed prior to GLM analysis (FEAT, FSL, FMRIB, Oxford, UK) to identify the activate motor region. For the CBVa data, the mean of the 1st eight phases was entered into the GLM. For BOLD analysis, the last phase of the control data was used, giving the same temporal resolution of 4.8 s for BOLD and CBVa measurements. Statistical maps were thresholded at $Z > 2.3$ with a cluster threshold of $P < 0.05$ to form an ROI of the motor area. The CBVa and transit time was calculated at rest and during activation, by taking the average of the CBVa and transit time maps in this motor ROI. Differences in CBVa and transit time between activation and rest were assessed using a non parametric Wilcoxon sign rank test.

Correlation analysis was also performed on the functional data. The correlation coefficient between the stimulus convolved with a Poisson haemodynamic response function and the fMRI data was taken (Correlate, MEDX). Maps of the correlation coefficient for CBVa and BOLD data were produced.

The average CBVa in the grey matter and the major vessels was found from the baseline study and the rest periods of the motor task. Grey matter was defined as voxels which had a signal change between 0.5 and 5 % in the 7th readout phase, as by this readout time (750 ms) the early large vessel blood signal has dissipated and only small vessels in grey matter remain. A vessel mask was defined from those voxels with a signal change > 3 % in the 2nd phase images. The average LLEPI timecourses for the grey matter and vessels was also calculated and the mean CBVa and transit time estimated.

5.3.1.2 Results

An example single slice LLEPI perfusion weighted image across the 21 phases (1 of 15 slices shown) is shown in Figure 5-17. The first few phases clearly show vessels (for example, along the midline).

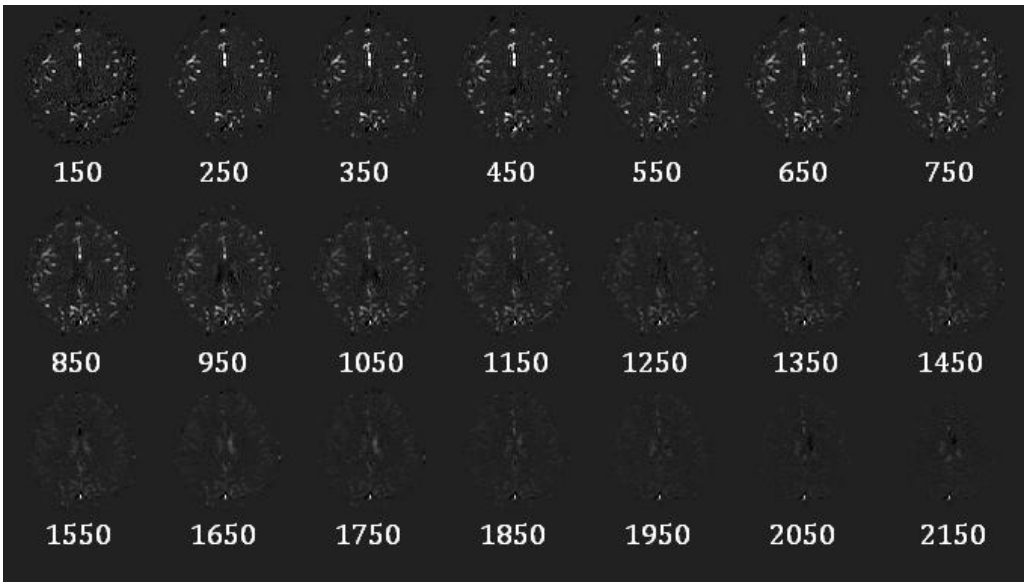

Figure 5-17: Example perfusion weighted LLEPI-CBVa data (1 of the 15 slices shown). The effective post labelling delay is given beneath in ms.

The fitted multislice maps of CBVa are shown in Figure 5-18 for the 4 subjects scanned for the baseline study. As each slice was acquired in a separate dynamic with the same timings, the final images can be re-sliced into three orthogonal views. The grey matter clearly shows high CBVa values in the cortex, with vessels displaying very high CBVa values. An example LLEPI timecourse for the grey matter and arterial vessels is shown in Figure 5-19, it can be seen that the blood arrives and leaves the large vessels much sooner compared to grey matter voxels, with a much larger amplitude signal change.

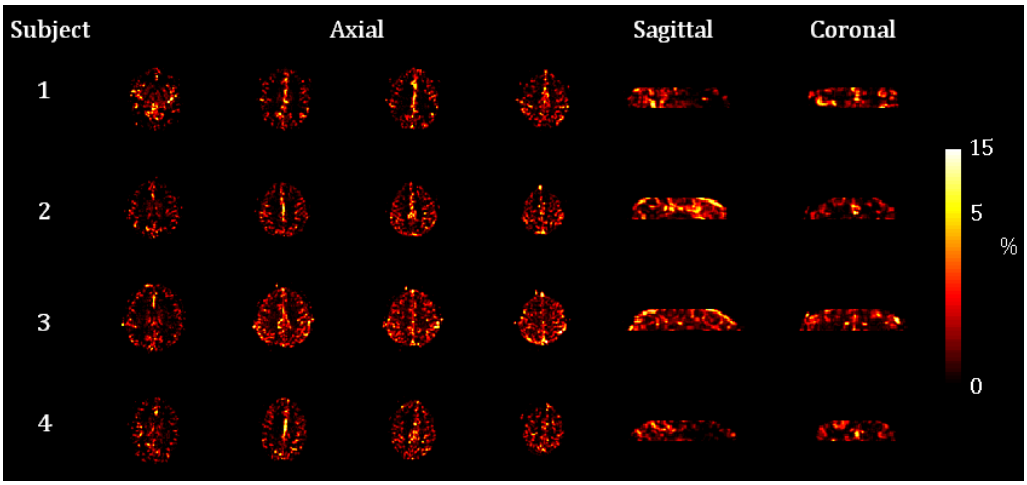

Figure 5-18: Resting CBVa maps for each of the 4 subjects scanned for the baseline study. Four axial slices shown along with a sagittal and coronal view.

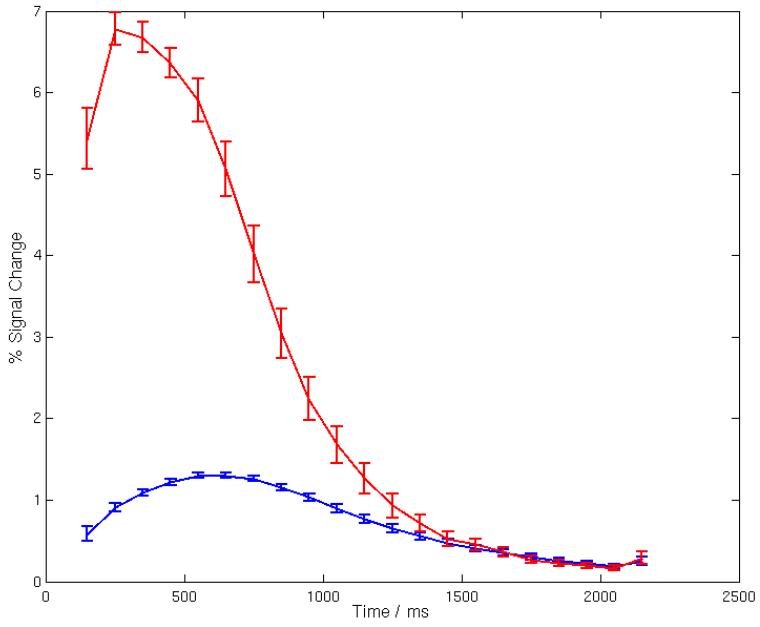

Figure 5-19: CBVa weighted LL-EPI timecourses from grey matter (blue) and large vessels (red). Data is shown subject averaged ± standard error.

The average grey matter CBVa, Δ_a and δ at baseline averaged over all 10 subjects are shown in Figure 5-20. The subject average grey matter CBVa was 3.0 ± 0.1 %, whilst the average arterial vessel CBVa was 9.2 ± 0.6 %. Δ_a was 145 ± 11 and 79 ± 4 ms for grey matter and vessels respectively, whilst δ was 538 ± 2 and 302 ± 17 ms respectively. CBVa was significantly ($P < 0.05$) higher in vessels compared to grey matter, and Δ_a and δ were both significantly ($P < 0.05$) shorter in vessels as expected.

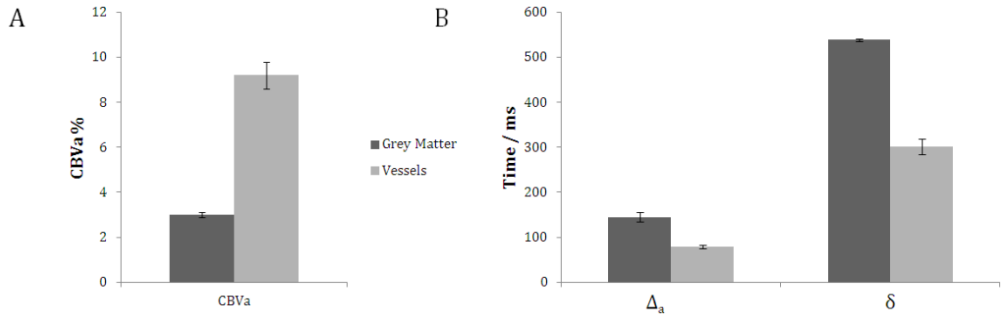

Figure 5-20: Results of the baseline CBVa measurements for all 10 subjects, (A) CBVa and (B) Δ_a and δ. Significant differences were found between grey matter and vessels for all three metrics (Wilcoxon sign rank test, P < 0.05). Error bars represent standard error across subjects.

Example maps of Δ_a and δ are shown in Figure 5-21. These demonstrate that the arrival and exchange time (Δ_a and δ) is typically longer in the occipital brain regions, and watershed areas. White matter is shown to have long Δ_a and δ, this is likely due to be an artefact of the low signal to noise in the white matter. Additionally the spatial maps of Δ_a and δ show similarities, this could be due to physiology or dependence of the two parameters in the data fitting.

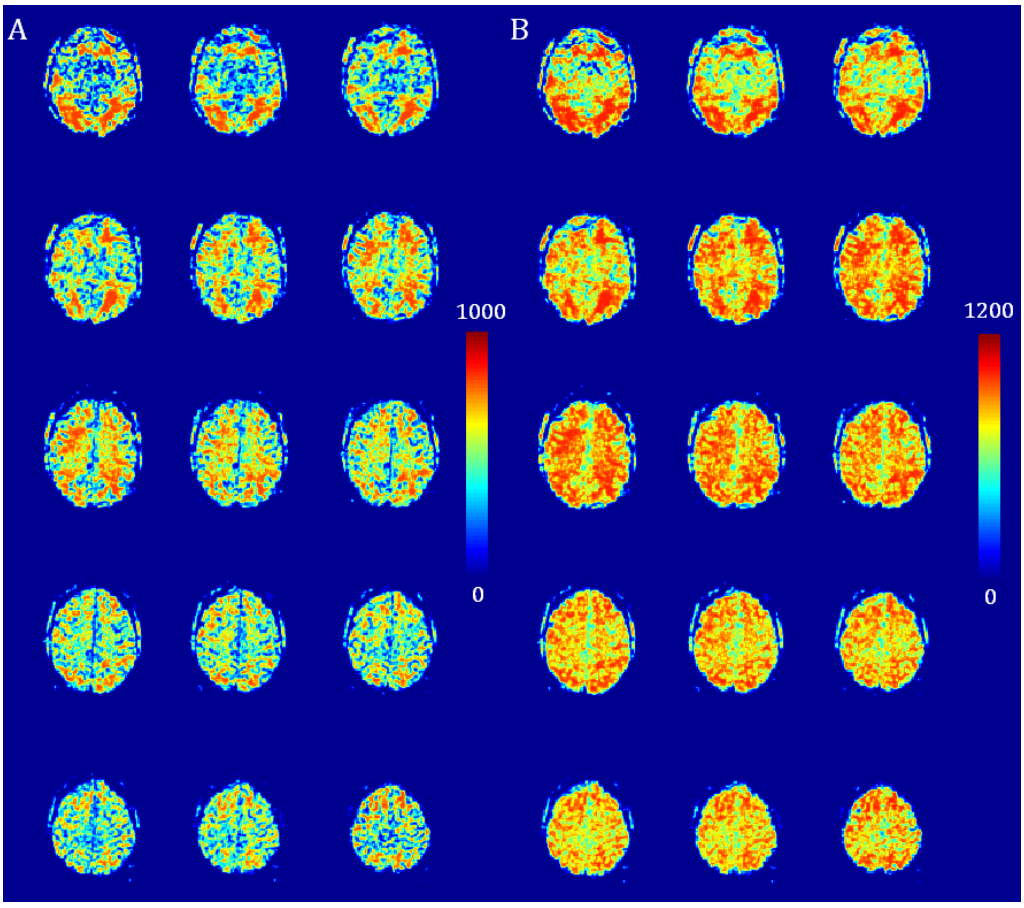

Figure 5-21: Example maps of (A) Δ_a and (B) δ for a representative subject. Colour bar in ms.

Motor Task

One subject did not exhibit a significant BOLD response to the motor task, so was excluded from further data analysis.

An example of the regions active in response to a unilateral motor challenge is shown in Figure 5-22 for both CBVa and BOLD data for a single representative subject. This demonstrates that the CBVa activation is more localised than the BOLD. In addition, BOLD activation is typically seen in the supplementary motor area (SMA) in addition to the primary motor cortex.

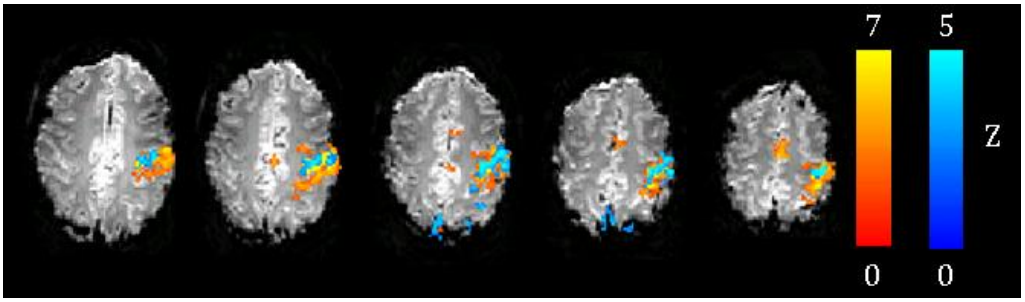

Figure 5-22: Active motor regions from GLM analysis of BOLD (red) and CBVa (blue) timecourses. Representative subject shown.

BOLD is more adversely affected by temporal fluctuations than CBVa, since the CBVa analysis is a subtraction technique this is more robust to low frequency temporal noise effects as the subtraction acts as a high pass filter, as demonstrated by a correlation analysis to detect motor activity, Figure 5-23, where the BOLD activity correlation maps show large fluctuation in the background compared to the CBVa correlation maps. The correlation analysis supports the fact that the CBVa activation is more localised, and that the smaller ROI in Figure 5-22 is not only be due to reduced SNR as the peak correlation coefficients are 0.84 for CBVa and 0.72 for BOLD.

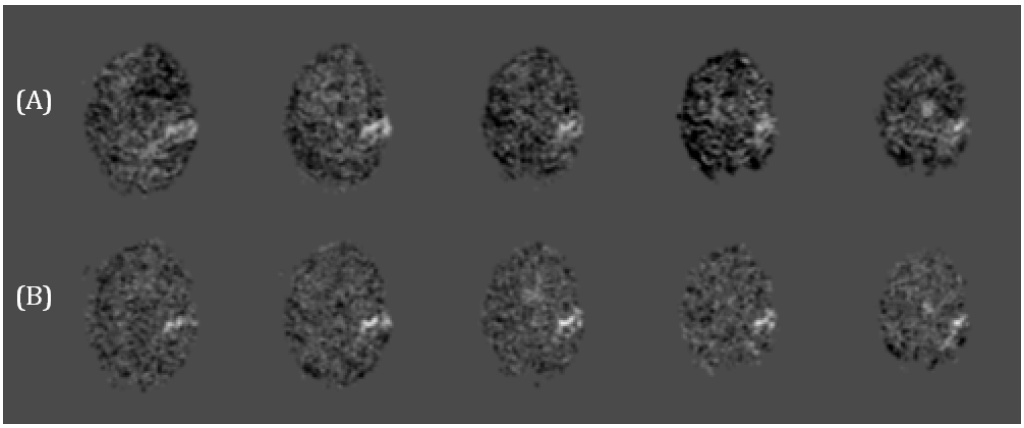

Figure 5-23: Correlation coefficient maps from correlation analysis to locate motor activity in (A) BOLD and (B) CBVa data.

Figure 5-24 shows the LLEPI timecourse from the CBVa GLM motor ROI averaged across the 5 subjects. This shows a clear difference in peak height and delay between rest and activation, with the fitted parameters shown in Figure 5-25. CBVa increased significantly on activation by 36 ± 4 %, from 2.0 ± 0.5 % to 2.7 ± 0.2 % ($P < 0.05$). Both arterial and capillary transit delays reduced from rest, Δ_a by 26 ± 6 % ($P < 0.05$) and δ by 4 ± 2 % ($P = 0.068$).

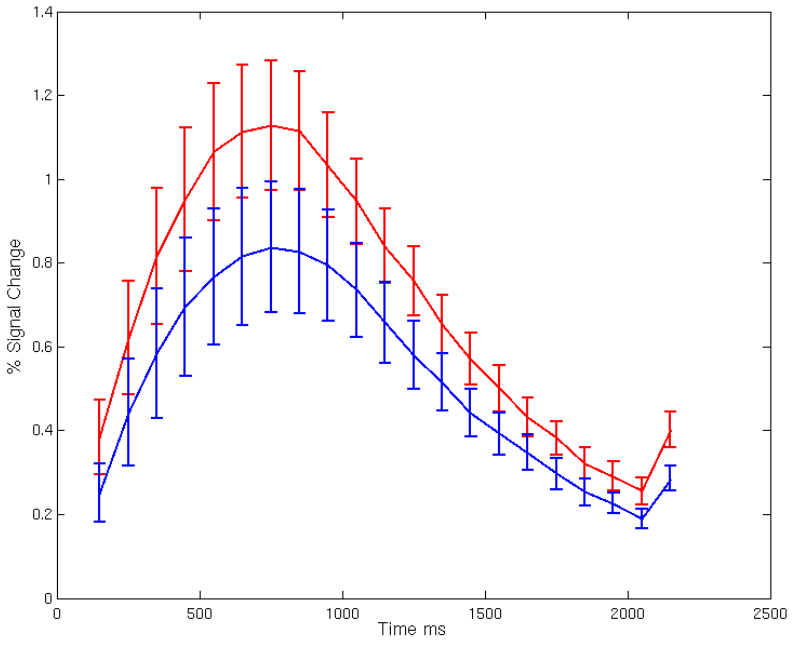

Figure 5-24: Subject averaged CBVa weighted timecourses in the CBVa motor ROI during rest (blue) and finger tap (red). Error bars represent standard error across subjects.

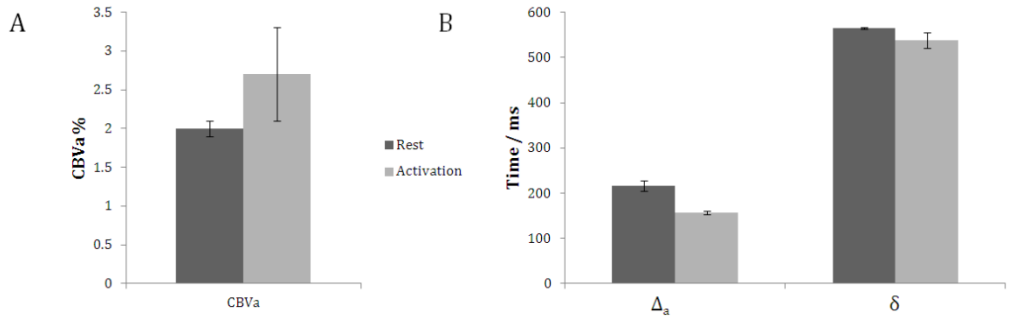

Figure 5-25: Subject averaged results for the motor experiment. Significant differences were found between rest and activation for CBVa and Δ_a assessed using a Wilcoxon sign rank test ($P < 0.05$). Error bars represent standard error across subjects.

5.3.1.3 Discussion

This experiment has shown the feasibility of the measurement of arterial cerebral blood volume at 7 T using Look-Locker EPI ASL. The increased SNR at 7 T has allowed high spatial resolution data of 2 x 2 x 3 mm^3 to be acquired, with only 10 averages required to measure CBVa, taking less than 50 s to acquire a CBVa map per slice. 7 T has allowed an increase in the spatial resolution of CBVa measurements, 2 x 2 x 3 mm^3, compared to those used at lower fields (e.g. 3.75 x 3.75 x 7 mm^3 [65], 3 x 4 x 6 mm^3 [67]).

A grey matter CBVa of 3 % was found which is comparable to that of 2.8 % found by Brookes *et al.* using this same method at 3 T [67]. Vessel CBVa was found to be 9.2 %, again in agreement with the previous value of 9.3 % in Brookes *et al*. Significant differences in transit time between grey matter and large vessels, with blood arriving quicker and exchanging quicker in the large vessels compared to grey matter was found, as expected. At the increased spatial resolution used here the vessel CBVa is anticipated to be higher as partial volume effects are reduced compared to [67] (3 x 4 x 6 mm^3). This was not seen, however the method of defining vessel ROI were different between the two studies. Here vessels were defined from those voxels which had high signal changes at TI = 250 ms, whereas in [67] 10 voxels containing vessels were manually selected. The method used here will include more voxels and those containing smaller vessels will be included, reducing the average CBVa.

Subjects showed a large increase in perfusion weighted signal in the motor cortex on activation (Figure 5-24). An average increase in CBVa of 36 ± 4 % was measured upon activation, which corresponds well with the 33 ± 14 % measured

at 3 T, in addition to the increase in CBVa, a significant reduction in Δ_a by 26 ± 6 % ($P < 0.05$) was seen.

In this study only the steady state effect of activation on CBVa was studied. An extension of this would be to assess the temporal dynamics of the CBVa response to the motor task as in a previous study [67] it was shown that the CBVa undershoots after stimulus cessation.. Due to the acquisition method for multiple slice functional LLEPI data used here, the temporal dynamics would be difficult as there will only be one measurement at each time point, reducing SNR and fitting accuracy.

5.3.2 LOOK-LOCKER 3D-EPI

Current implementations of Look-Locker ASL are limited in slice coverage, as the entire multi-slice data set must be collected in the short time between the multiphase readouts (generally < 300 ms for CBF measurement). Previous studies have typically acquired a maximum of 7 slices [70, 73, 74], and so whole brain coverage can only be achieved by increasing slice thickness (> 6 mm) and including a slice gap. However this is detrimental as areas are missed and partial volume effects increase.

This study combines 3D-EPI with a multi phase readout, providing the advantage of higher volume coverage per unit time compared to Look-Locker 2D EPI. The optimisation of the 3D-EPI readout previously performed in Section 5.2.3 is used here to demonstrate the feasibility of Look Locker 3D-EPI ASL.

5.3.2.1 Simulations

Using the model of Francis *et al.* [58] the Look Locker signal for the 3D-EPI readout was modelled. The haemodynamic parameters for all simulations were F = 180 ml/100g/min, f = 90 ml/100g/min, $\delta/\Delta_a/W$ = 400 / 400 / 1500 ms with $T_{1,b}/T_{1,t}$ = 2.1 s (symbols as in Chapter 4). Standard 3D-EPI simulation parameters are TI/ΔTI = 340 / 300 ms, FA = 14°, TR = 16 ms and m = 10. The impact of TR, flip angle and the number of RF pulses per shot, here called m, was investigated. In addition the 3D-EPI readout was compared to a standard 2D-EPI acquisition (TI/ΔTI = 340 / 300 ms, FA = 35°).

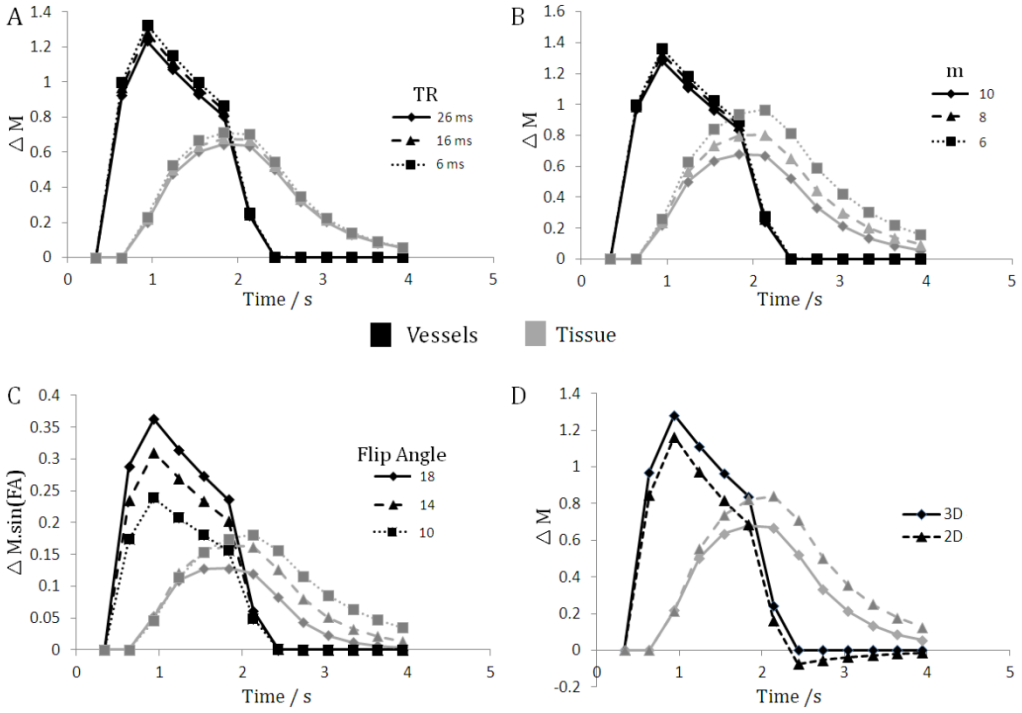

Figure 5-26: LL-3D-EPI simulations showing the effect of (A) choice of 3D-EPI interpulse spacing (TR) (B) number of readout pulses per 3D-EPI block, m and (C) flip angle. (D) LLEPI curves for a 3D-EPI and a 2D-EPI readout. Signal from the arteriolar compartment shown in black and tissue signal shown in grey.

Figure 5-26 shows the simulated perfusion timecourses for the arteriolar and the exchange compartments. These simulations demonstrate that interpulse spacing, TR, has little impact on either the blood or tissue signals. The number of readouts per 3D-EPI block, m, which is related to the number of slices acquired, does not impact the blood signal significantly but does suppress the tissue signal. This differing effect between blood and tissue results from the high flow rate of the blood in arterioles, meaning the signal in this compartment is refreshed at a faster rate, experiencing less RF pulses and suppression than the tissue compartment. Increasing the flip angle is shown to increase the arteriolar signal but reduce the tissue signal, as the blood is suppressed less due to the high flow and the blood signal is increased proportional to sin(FA). The comparison of the 2D-EPI and 3D-EPI curves in Figure 5-26 D demonstrates that the signals are of similar magnitude between the two readouts and that the reduced flip angle of the RF pulses in 3D-EPI acquisition compensates for the increased number of RF pulses which could otherwise suppress the signal. For 2D-EPI there is one pulse per phase, whereas for 3D-EPI there are m pulses per phase where m is dependant on the number of slices.

A factor not included in these simulations is that the signal to noise of the 3D sequence will be proportional to the number of slices acquired, $SNR \propto \sqrt{N_{slice}}$ as the signal arises from the entire volume [55]. This would mean that when the number of RF pulses is increased, which suppresses the signal, the SNR will increase as the number of slices acquired will have increased. The perfusion signal change was suppressed by a factor of 1.2 on increasing m from 8 to 10, but the SNR would improve by approximately 1.1 partially compensating. The SNR of the first phase of a LL acquisition is evaluated in Figure 5-27, this shows that after 7 slices the 3D-EPI has increased SNR compared to 2D-EPI due to the increased volume coverage (simulations look at signal from the grey matter in the first readout-phase after a post-saturation pulse, assuming TI/ΔTI = 340/300ms, T_1 = 2000 ms, TE = 10 ms, TR_{3D} = 16 ms FA = 14°/35° for 3D and 2D respectively).

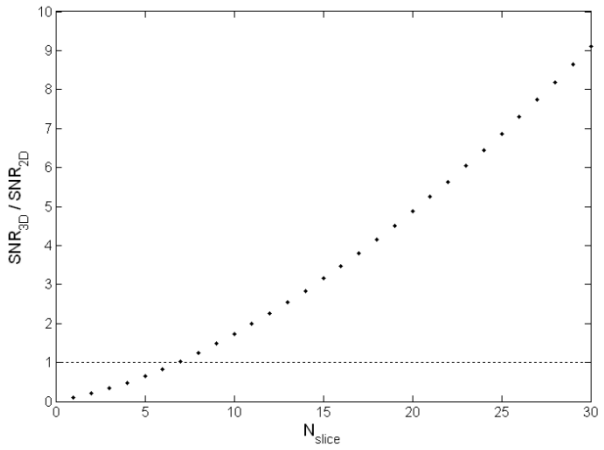

Figure 5-27: The effect of slice number on the relative SNR of the first phase of LL-3D-EPI and LL-2D-EPI acquisition, assuming TI/ΔTI = 340/300ms, T_1 = 2000 ms, TE = 10 ms, TR_{3D} = 16 ms FA = 14°/35° for 3D and 2D respectively.

5.3.2.2 Phantom and In-Vivo Investigation

All imaging was performed on the Philips Achieva 7 T system with head volume transmit and 32-channel SENSE receive coil. All volunteers gave written consent.

Table 5-4 shows the duration of the 2 mm and 3 mm in-plane 3D-EPI acquisitions, with and without vascular crushing using the optimised parameters as described in Section 5.2.3. Common imaging parameters were FOV = 192 x 192 mm^2 and FA = 14°.

Number of Slices	2 x 2 x 3 mm³		3 mm isotropic	
	Non vascular crushed, TE/TR = 11/26 ms	*Vascular crushed, TE/TR = 21/36 ms*	*Non vascular crushed, TE/TR = 7/16 ms*	*Vascular crushed, TE/TR = 17/26 ms*
5	113	155	90	115
10	241	335	155	249
14	344	479	221	356
18	395	551	253	409
22	498	696	318	516
Average time per slice	23 ± 1	32 ± 1	15 ± 1	24 ± 1

Table 5-4: Scan acquisition timings for 2 mm and 3 mm in-plane resolutions, with and without vascular crushing.

Phantom Experiments

To ensure that no systematic artefacts were introduced into the perfusion weighted images when using a 3D-EPI readout, as found in the single TI 3D-EPI method in Section 5.2.3, phantom studies were performed. A quadrant gel phantom that was doped with gadolinium was used; each quadrant had a different T_1 and T_2. Imaging parameters were: 2 x 2 x 3 mm^3, 10 slices, 5 phases, 5 averages, TI = 300 ms and ΔTI = 350 ms. The ASL acquisition was repeated with different FAIR selective inversion thicknesses of 40, 50, 60 and 70 mm, using a hyperbolic secant pulse for the inversion. In addition, two data sets with vascular crushing were acquired (strength 10 mT/m, lobe duration = 5 ms) with selective thickness of 40 and 70 mm. Further investigation into the effect of vascular crushing was performed by acquiring a LL-3D-EPI scan with 3 gradient strengths of vascular crushing, 0, 5 and 10 mT/m. Scan parameters: TE = 21 ms, TI/ΔTI/TR = 150/300/4000 ms, 12 phases, 8 slices of 2 x 2 x 3 mm^3, selective inversion extended outside phantom.

An artefact was present in the LL-3D-EPI ASL difference images acquired on a phantom, to investigate the origins of this an image with readout RF amplitude set to zero was acquired. This allowed determination of whether any signal was arising from the label, due to rephasing of the signal or foldover. This was repeated with increased initial TI to 450 ms, and another scan with reduced phase interval to 300 ms as this could impact on signal that has been rephased. Also investigated were the height of the gradient spoilers applied after the label, and the effect of using a FOCI pulse (A_0 = 4.42, β = 4.33 and μ = 7.75, symbols discussed in Section 4.4.2.1) instead of a hyperbolic secant for labelling.

In-vivo Study

In healthy volunteers LL-3D-EPI data was collected with a range of scan parameters to assess the flexibility of the technique. These scans are summarised in Table 5-5. All data was acquired with FOV 192 x 192 mm^2, selective thickness 20 mm wider than imaging volume and non-selective of 250 mm.

Parameters	
TI/ΔTI/TR/TE = 150/400/3000/7 ms, 5 phases, 20 slices 3 mm isotropic	For large volume coverage
TI/ΔTI/TR/TE = 150/300/3000/11 ms, 9 phases, 8 slices 2 x 2 x 3 mm^3 , 50 averages	To demonstrate high resolution
TI/ΔTI/TR/TE = 150/300/4000/21 ms, 12 phases, 8 slices 2 x 2 x 3 mm^3 , 40 averages Acquired with and without vascular crushing.	To draw comparison with QUASAR [65]
TI/ΔTI/TR/TE = 340/300/5000/7 ms, 13 phases, 10 slices 3 mm isotropic	To draw comparison with the coverage of QUASAR [65]

Table 5-5: Overview of in-vivo LL-3D-EPI scan parameters.

5.3.2.3 Results

Phantom Experiments

Initial experiments using the LL-3D-EPI sequence showed possible artefacts in the middle slices of the stack, similar to those seen in the single TI 3D-EPI ASL discussed earlier in Section 5.2.3. Figure 5-28 (A) shows the 10 slice 2 x 2 x 3 mm^3 LL-3D-EPI difference image acquired on a phantom with 5 phases with a 40 mm selective thickness. The middle slices display a significant artefact. Figure 5-28 (B) demonstrates the effect of altering selective inversion thickness on this artefact. As the selective thickness widens it is seen that the artefact is reduced. This is also seen in data acquired with vascular crushing, Figure 5-28 (C), where additional ripple artefacts are present.

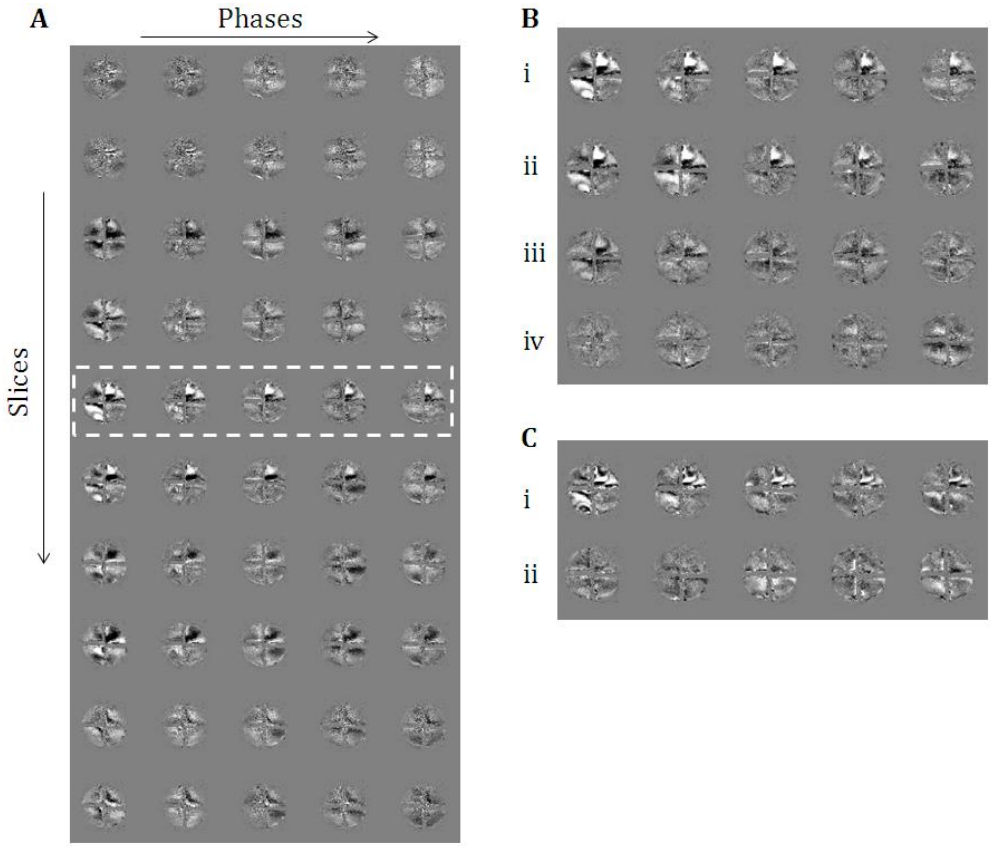

Figure 5-28: (A) 2 x 2 x 3 mm³ LL-3D-EPI difference image acquired on a phantom (10 slices, 5 phases, 5 averages, TI = 300 ms, TI = 350 ms, selective thickness = 40 mm) (B) Middle slice of LL-3D-EPI images (represented by dashed box in (A)) for selective thicknesses of (i) 40mm (ii) 50 mm (iii) 60 mm (iv) 70 mm. (C) LL-3D-EPI difference images with vascular crushing (strength 10mT/m, lobe duration = 5 ms) at selective thickness of (i) 40 mm and (ii) 70 mm.

Figure 5-29 shows LL-3D-EPI images acquired with different levels of vascular crushing, it is seen that the artefact is more prominent in the acquisition with crusher gradients applied. The artefact varies across the phases, and has a common spatial signature between the two vascular crushing levels. The difference in vascular crushing levels has not significantly changed the magnitude of the artefact but changes the readout in which it is most prominent. This signature at the different phases suggests the signal is being rephased by successive application of the RF pulses and spoiler gradients.

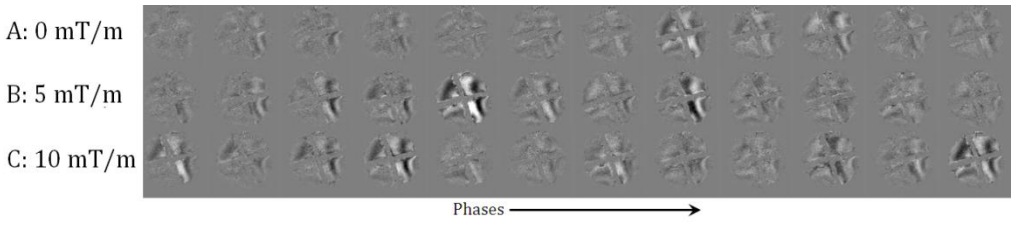

Figure 5-29: LL-3D-EPI difference images with gradient strengths of (A) 0 mT/m (B) 5 mT/m and (C) 10 mT/m all acquired with matched TE. One slice shown.

Figure 5-30 shows the images acquired with RF set to 0, and shows a significant signal contribution (artefact) in the first phase suggesting signal remains from the label and arises from the difference between the selective and non-selective inversion as the artefact is not present in the raw images. Reducing the phase interval was found not to have an impact (B). However, increasing the initial TI to 450 ms was found to remove the artefact in the first phase (C). Varying the heights of the gradient spoilers applied after the label was found to have little impact on the difference images. Altering the pulse for inversion, from a hyperbolic secant to a FOCI (A_0 = 4.42, β = 4.33 and μ = 7.75) was found to make the artefact significantly worse (D).

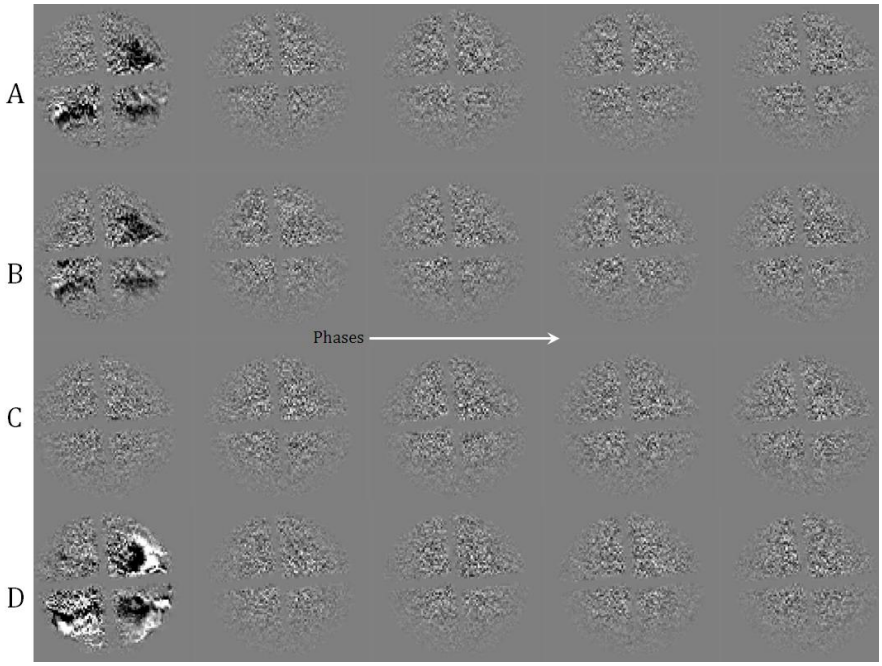

Figure 5-30: RF = 0 LL-3D-EPI difference images (A) 5 phase acquisition (B) with reduced phase interval to 300 ms (C) Increased initial TI to 450 ms and (D) inversion pulses type FOCI rather than hyperbolic secant. One slice shown.

In-Vivo Experiments

Figure 5-31 shows the 20 slice 5 phase 3 mm LLEPI acquisition, acquired with 30 dynamics. This clearly shows the early blood signal in the first phase as no vascular crushing has been used, and the tissue perfusion which is predominant in the 3rd phase. Again the benefit of a 3D-EPI acquisition is visible with all the slices having the same perfusion signal weighting from simultaneous acquisition of all the slices, due to this and the large coverage it clearly shows how the transit times are very different across the brain, for example the signal persists longer in

the occipital regions due to the longer arrival times in that region [61]. This is further demonstrated in Figure 5-32, where the timecourse from an occipital ROI and a sensorimotor ROI are shown.

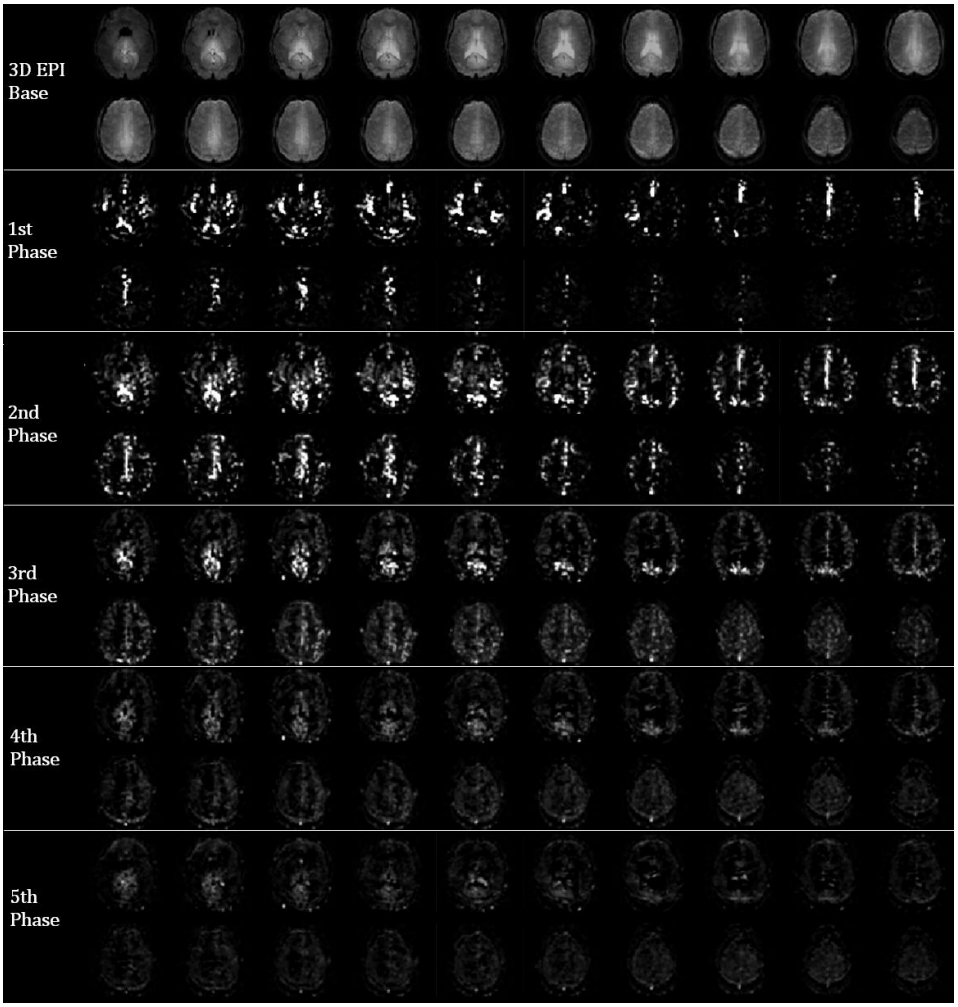

Figure 5-31: 20 slice 5 phase LL-3D-EPI ASL acquisition, base images and the 5 phase are shown separately, all slices shown.

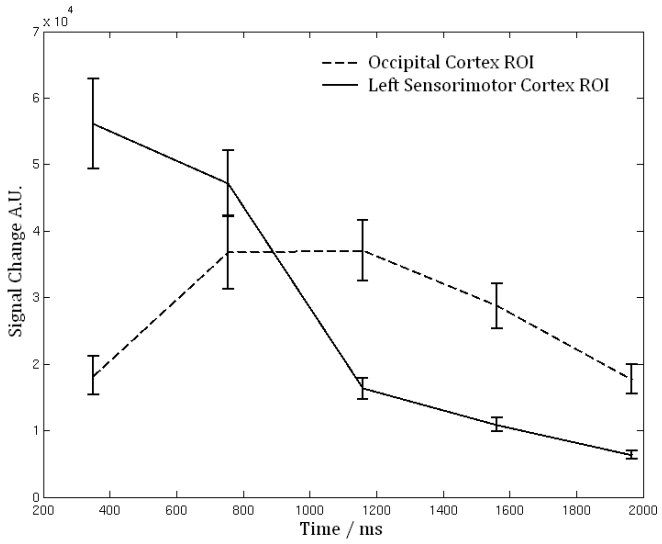

Figure 5-32: LL-3D-EPI perfusion weighted timecourse from an occipital cortex ROI (broken line) and a left sensorimotor ROI (solid line) from data shown in Figure 5-31. Error bars represent standard error across voxels in the ROI.

Figure 5-33 shows a 9 phase, 8 slice 2 x 2 x 3 mm^3 LL-3D-EPI acquisition. The high resolution allows the structure of both the vessels and the cortex to be clearly seen. There is a slight image artefact in the first phase of some of the slices. As seen with the phantom experiments, a short TI (here 150 ms) can exacerbate this artefact.

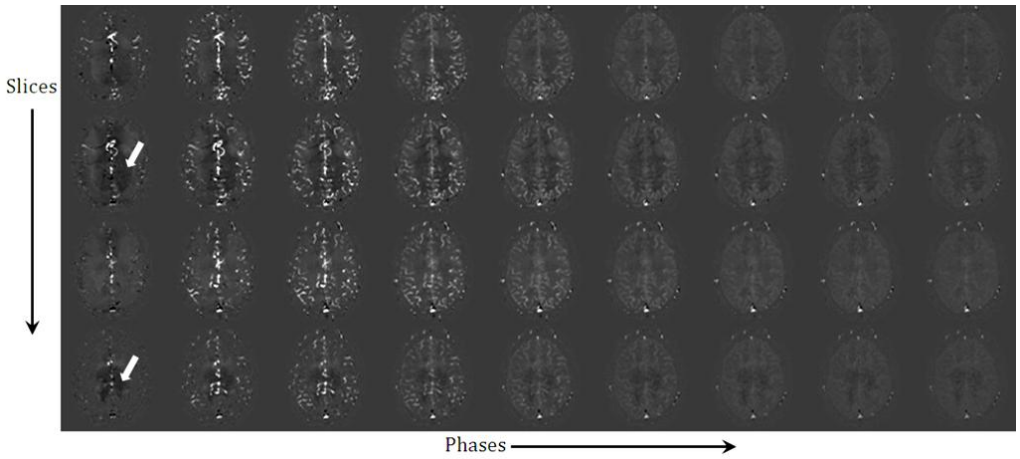

Figure 5-33: 4/8 slices of the 2 x 2 x 3 mm^3 9 phase acquisition. White arrows indicate presence of artefact that is predominant in the first phase but persists through the phases.

Figure 5-34 shows example slices from the (A) non vascular crushed and (B) vascular crushed acquisition. The difference image (A-B) between the two acquisitions clearly shows the blood signal which arrives early and has mainly gone by the 4^{th} phase. Artefacts are more pronounced in the vascular crushed acquisition, as the signal is of lower amplitude making artefacts more easily

visible, and the phantom experiments suggest additional affects may be present due to the vascular crushing.

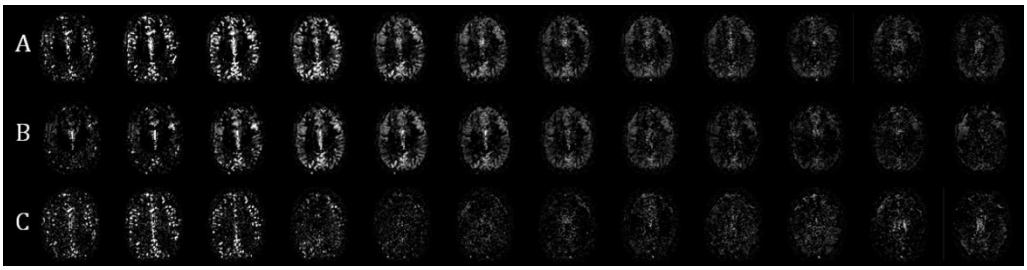

Figure 5-34: LLEPI data acquired, 9 phases, 8 slices, 2 x 2 x 3 mm^3, TE = 21 ms. (A) without vascular crushing and (B) with vascular crushing, (C) = (A)-(B), the difference signal between the two showing the blood signal that is predominant in the first 3 phases. One slice out of eight shown.

Figure 5-35 is the 13 phase acquisition, TR_{ASL} = 10 s/pair, to assess the signal at longer post labelling delays. The signal persists well into the 9th phase and into the 10th phase which has an effective post label delay of 3,040 ms. This is demonstrated in the perfusion timecourses shown in Figure 5-36. The large vessel signal has mainly gone after a post labelling delay of a 1 s, but the tissue signal peaks later due to the longer transit time to the tissue bed, and the tissue signal can be seen to persist until approximately 3 seconds at 7 T.

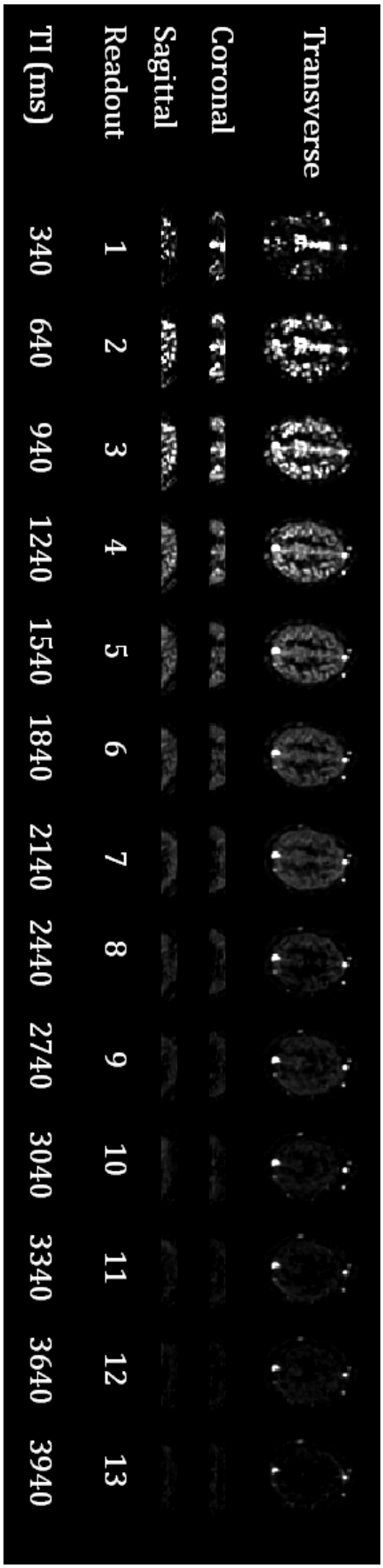

Figure 5-35: 13 phase, 10 slice, 3 mm isotropic LL-3D-EPI acquisition shown in transverse, coronal and sagittal orientations.

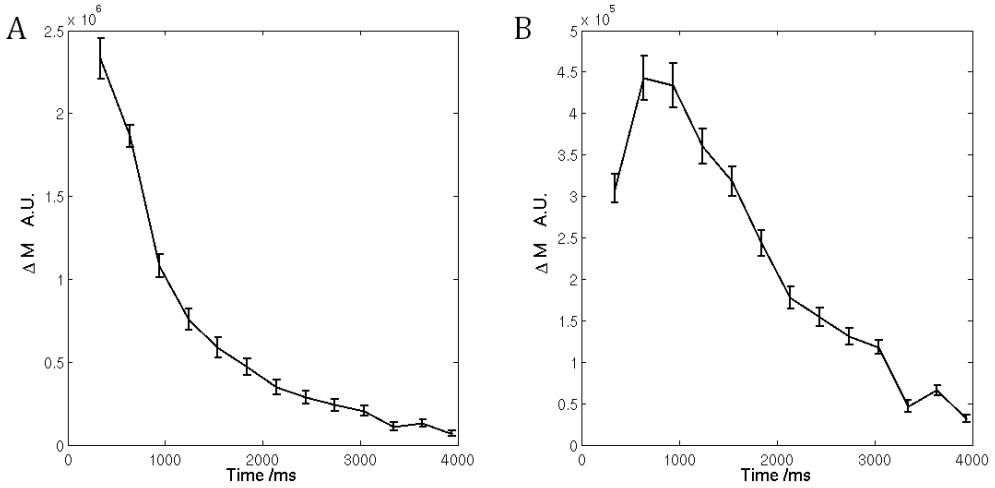

Figure 5-36: Timecourse of the perfusion weighted signal in (A) large vessels and (B) grey matter. Error bars represent standard error across voxels in the ROI.

5.3.2.4 Discussion

This experiment has shown that LL-3D-EPI ASL is feasible at 7 T, and that it allows high volume coverage ASL data to be acquired with high temporal resolution through the readout. It was demonstrated that the LL-3D-EPI acquisition can exceed the coverage and resolution that is currently implemented using QUASAR at 3 T [65], that of 7 slices acquired at 3.75 x 3.75 x 6 mm^3 with interpulse spacing of 300 ms [70, 74].

Simulations showed that the 3D-EPI readout should not suppress the signal much greater than that of a similar 2D-EPI acquisition, even though the number of RF pulses is significantly increased. Interpulse spacing was shown to have little impact on the signal from either the blood or the exchange compartments. Number of RF pulses per readout (linked to number of slices) and flip angle were shown to affect the tissue signal more, due to the prolonged time the label remains in the voxel compared to the blood.

Phantom studies have shown artefacts that are dependant on the width of the selective thickness, as with the single TI 3D-EPI ASL shown in Section 5.2.3. This work shows a need for further development of the technique; investigation of the origin of the artefact is needed to make the technique more robust. The dependence on the selective thickness and the presence of an artefact when the readout RF amplitude was set to zero suggests that the artefact is linked to the label. Varying the gradient spoiling of the label did not have any significant impact. Further investigation would concentrate on variable height gradient spoiling after the label with each TR period and the use of RF spoiling [75].

The use of bipolar gradients was also shown to give rise to large artefacts in the phantom data, which again were reduced on increasing the selective thickness. Vascular crushing is necessary to remove blood signal for CBF quantification and functional studies may wish to look at the variation in tissue perfusion with a functional task rather than the blood compartment. Currently the vascular crushing appears to make the appearance of the artefact worse; this could be due to the application of extra gradients rephasing the artefactual signal.

An additional area for investigation would be the labelling scheme, as artefacts appear to be associated with the non-selective inversion. It would be important to investigate whether this artefact is reduced with a different labelling scheme, such as PICORE or STAR. These could help as the labelling slabs are applied inferior to imaging, whereas in FAIR the inversion slabs are centred on the imaging slices. Look-Locker methods could be combined with CASL/PCASL but this would reduce the temporal resolution of a tag/control pair as the labelling scheme takes $\sim$ 1s, which for functional studies would be problematic. In addition, the SAR and inversion efficiency of these techniques at 7 T is likely to prohibit their use [1].

Further investigation would look at the impact of the RF pulse used for inversion. Here only the comparison between a hyperbolic secant and one FOCI (A_0 = 4.42, β = 4.33 and μ = 7.75) was performed. Optimisation of the RF pulse shape could improve the profile, reducing the artefact seen in the difference images.

A model to allow quantification of the different haemodynamic parameters needs to be developed from the simulations. Current fitting for LL-ASL, as used for the CBVa measurement, assume one RF pulse per slice, whereas here a train of small tip angle pulses are applied. The model used here for simulation has many parameters which would make data fitting difficult due to number of degrees of freedom but could be adapted for data fitting. Similarly the development of such a model would aid the quantification of LL TFE ASL data (Section 5.3.3) as that also uses a train of RF pulses for data acquisition. Further development, initially through simulation, could determine whether arterial blood volume could be measured through a similar methodology as used for the 2D-EPI where the tissue signal is deliberately suppressed. The use of high flip angle readout would achieve this, however this would cause large signal decay during the 3D readout which was found to cause perfusion quantification errors for the single TI

method. A method similar to that of Petersen *et al.* [65] could be implemented where data is acquired with and without vascular crushing, as in Figure 5-34.

LL-3D-EPI is the first implementation of a 3D sequence with a Look-Locker readout for ASL imaging. 3D-GRASE is the most common 3D method for ASL imaging [76] and uses a train of 180° refocusing pulses after excitation, example images acquired at 3 T are shown in Figure 5-37. 3D-GRASE suffers from significant through plane blurring, and due to the use of a long train of high flip angle pulses is also at the upper limits of SAR, which would be exacerbated if combined with a LL readout strategy, especially at 7 T. Achieving high resolution is difficult with 3D GRASE due to the long echo train length, segmentation and parallel imaging are often used to achieve higher spatial resolution [9]. 3D GRASE has not currently been implemented at 7 T.

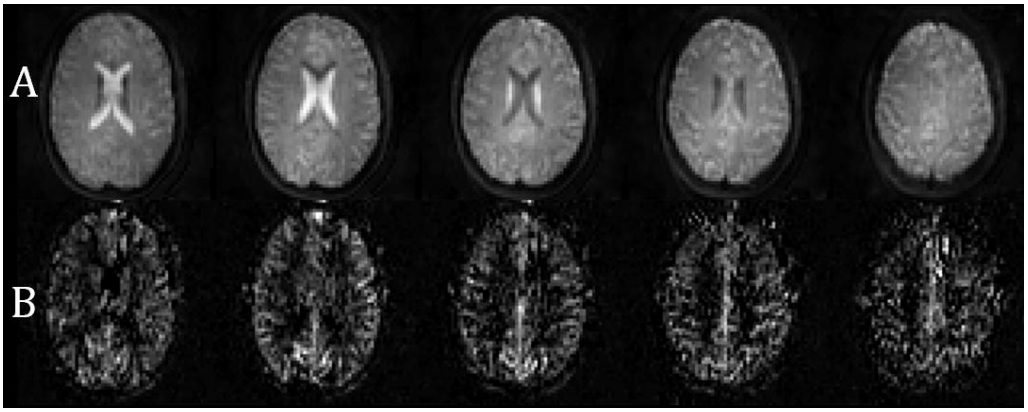

Figure 5-37: (A) Example GRASE images acquired at 3 T with scan parameters TSE = 11, EPI = 27, 10 slice, 3 x 3 x 5 mm, FOV = 192 x 192 x 50 mm, TE = 22ms, TR = 3s (B) Perfusion weighted images using a FAIR labelling scheme with post-label delay of 1400 ms, non-selective = 250mm, selective = 60 mm.

Development of a robust LL-3D-EPI method with associated fitting algorithm would have applications in several areas. The large volume coverage, for example Figure 5-31, would be useful for the definition of vascular territories through the assessment of voxelwise perfusion timecourses. This would be useful in the study of different pathologies that are expected to affect cerebral perfusion (e.g. aging, vascular diseases such as stroke). Also fMRI using perfusion would benefit from larger volume coverage when studying areas with non-focal activation, for example cognitive tasks.

Overall LL-3D-EPI has been shown to be a promising technique for the acquisition of large volume coverage, high temporal resolution perfusion data at 7 T. The 32 channel coil allows for parallel imaging to be applied in two

dimensions to speed up image acquisition. With each shot, over 100 slices can be acquired every 3 seconds. The high SNR available at 7 T allows high signal perfusion weighted images to be acquired in less than 5 minutes. Through further investigation it should be feasible to implement a robust method, and for it to be applied in the study of vascular territories and functional MRI studies.

5.3.3 LOOK-LOCKER TFE: APPLICATION IN LOW GRADE GLIOMAS

As with single TI ASL, presented in Section 5.2, the use of image acquisition methods that are less affected by geometric distortions is important for Look-Locker (LL) ASL at high field. Wang *et al.* [77] demonstrated the feasibility of combining a Look-Locker scheme with a FLASH readout for blood velocity mapping at 3 T, and bFFE has been incorporated in a Look-Locker scheme for kidney perfusion imaging at 1.5 T [66]. TFE and bFFE were introduced in Section 5.2.2 and shown to be more robust to geometric distortions than GE-EPI. bFFE would not be suitable to be combined with Look-Locker style readout at 7 T due to SAR constraints as bFFE uses a long train of high flip angle pulses, however using TFE this is possible.

Here the combination of TFE with a Look-Locker readout to provide undistorted, perfusion weighted images at multiple readout times for use in clinical setting was investigated. The technique was applied to the assessment of cerebral tumours where transit time measures are required to interpret perfusion weighted maps due to abnormal vasculature.

5.3.3.1 Methods

The study was approved by the local ethics committees; 4 low grade glioma (LGG) patients (2 female, age range 28 – 63 years old) gave informed written consent. Experiments were performed on a Philips Achieva 7 T system, with a head volume transmit coil and 16-channel SENSE receive coil.

In a healthy volunteer LL-TFE was demonstrated with a 2 mm and a 1 mm in plane resolution readout, at an inferior and superior axial plane. 75 dynamics were acquired at 2 mm, and 100 dynamics at 1 mm. In the Glioma patients data was acquired at 2 mm in-plane resolution. All scan parameters were matched between the two resolutions.

ASL parameters: FAIR labelling scheme (selective thickness 25 mm, non-selective thickness 230 mm, in-plane pre- and post-saturation pulses, ASL TR of 6 s per tag/control series with 50 averages collected), with a LL-readout (TI = 350 ms, ΔTI = 404 ms between readouts, 5 readouts) comprising a TFE readout scheme: (2 x 2 x 3 mm^3, flip angle = 15°, TR/TE = 5/2.5 ms, FOV = 192 x 192 mm^2). The ΔTI was long due to the length of the readout (315 ms at 1 mm) and to keep within SAR limits. In addition an equilibrium magnetisation base image with a long TR was acquired.

In patients, single-TI TFE data were acquired, (2 x 2 x 3 mm^3, TI = 1500 ms, 5 slice, 90 averages, TR = 6s / pair), imaging parameters as for LL-TFE. 50 averages were acquired in 5 minutes. Tumour borders were defined using a 3D-FSE (0.7 x 0.7 x 1.6 mm^3, FOV: 220 x 220 x 19 mm^3, TR/TE = 2500/315 ms, refocusing angle 40°, SENSE 2).

In a healthy volunteer EPI base images were acquired to compare distortions (2 x 2 x 3 mm^2, 192 x 192 mm^2 FOV, TE = 10 ms, SENSE 2, FA = 90°).

5.3.3.2 Analysis

Single TI label and control data were subtracted, inspected for motion and averaged across the dynamics. Any subjects that showed large motion (> 1 voxel) were discarded. LL-TFE data was subtracted and each phase was averaged across the dynamics. The FSE anatomical image was realigned to the LL-TFE anatomical space using FLIRT (FSL, Oxford).

5.3.3.3 Results

The results from a healthy volunteer are shown in Figure 5-38, where 2 mm and 1 mm data were acquired at two locations in the superior and inferior planes. The TFE is more robust to susceptibility differences (Figure 5-38 E), compared to EPI. At both locations the perfusion weighted signal shows excellent cortical structure throughout the five readouts.

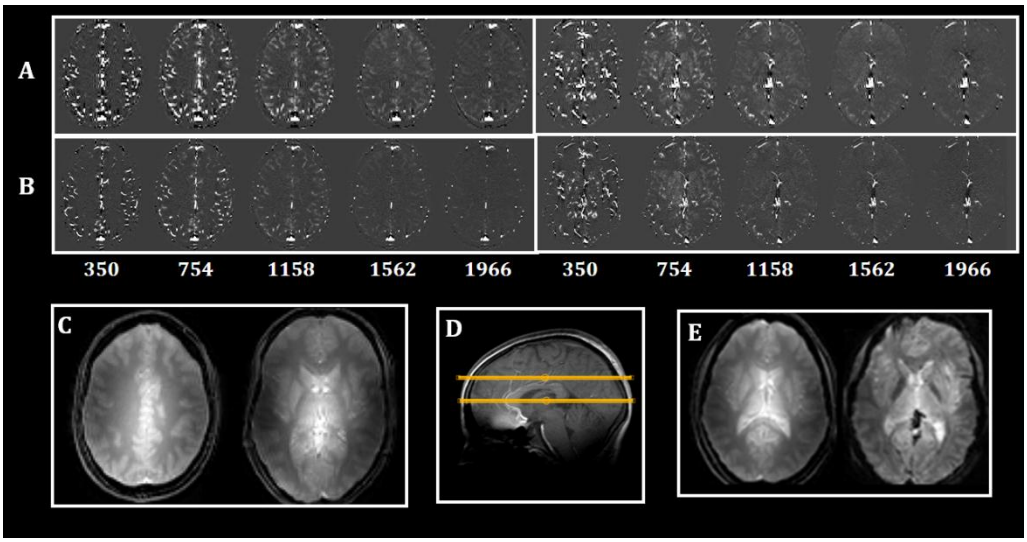

Figure 5-38: Demonstration of LL-TFE in a healthy subject at (A) 2mm and (B) 1mm in plane resolution, effective post-label delay shown below in ms (C) Base TFE images at the two locations (shown in (D)) and (E) demonstrates the distortions that EPI can have (right) compared to TFE (left).

Two patients had small lesions (< 5 mm) located in deep structures not easily distinguishable from neighbouring healthy tissue, hence were excluded; the other two patients had large lesions.

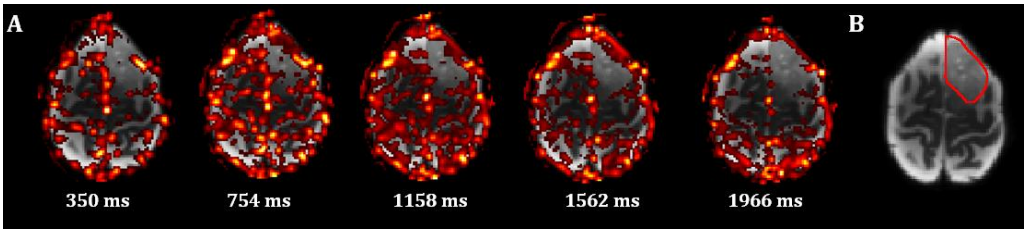

Figure 5-39: ASL LL-TFE data for patient with (A) LGG overlaid on their 3D-FSE image, post label delay shown below in ms; (B) tumour outlined as red ROI on 3D-FSE.

Figure 5-39 shows the ASL LL-TFE PW data for a patient with a low grade glioma overlaid onto their co-registered FSE image. The tumour corresponds to an area of low perfusion and the LL acquisition provides clear evidence that this is not an artefact of a change in transit time as no blood is seen to arrive at any time point.

Figure 5-40 shows LL-TFE and single TI TFE data, of a second patient, again overlaid on their FSE. The 4th phase is approximately equivalent to the single TI inversion time ASL acquisition. It can be seen that the Look-Locker acquisition provides information on the early arrival of tumour blood flow which has washed out by the time of the single TI acquisition (shown by white arrow). This further demonstrated in Figure 5-41 where LL-TFE timecourses are shown for an ROI in the tumour and the cortex.

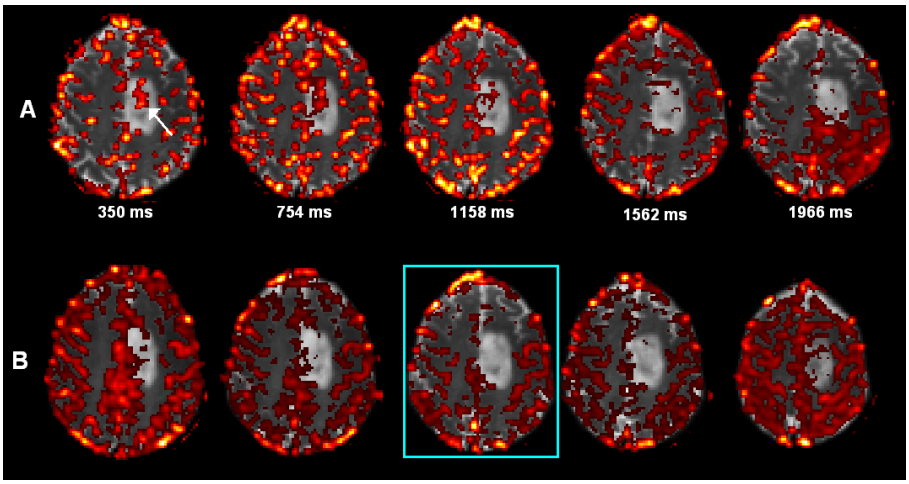

Figure 5-40: (A) LL-TFE data for patient with LGG overlaid on their 3D-FSE image, arrow shows early blood arrival, effective post label delay in ms shown below (B) Single-TI ASL, slice from (A) highlighted.

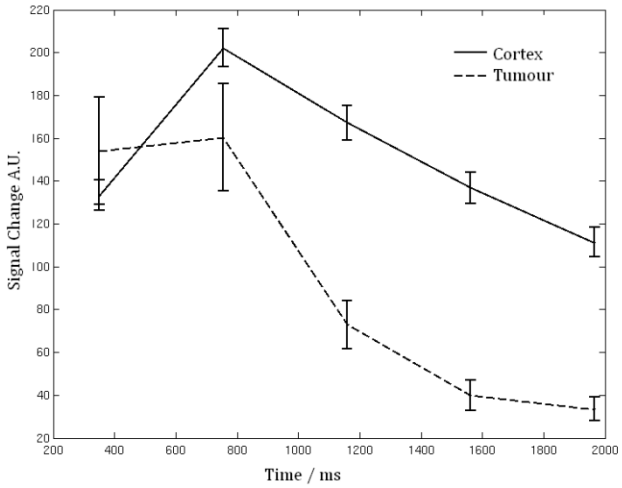

Figure 5-41: LL-TFE timecourse for a ROI in the cortex (solid line) and a ROI in the tumour (broken line), from data shown in Figure 5-40. Error bars represent standard error across voxels in the ROI.

5.3.3.4 Discussion

This study shows the feasibility of using TFE in combination with a Look-Locker readout for ASL at 7 T. This acquisition scheme overcomes the problems associated with susceptibility-based spatial distortion in EPI images, particularly in areas of high susceptibility difference (areas close to sinuses) allowing ASL data to be acquired in any brain region of clinical interest. Further this technique can be used to collect high resolution data and perfusion images can be directly overlaid on anatomical images.

Currently the data has been collected without vascular crushing so the images are weighted by both arterial blood volume (at short delay times) and tissue perfusion (at late delay times), however this does provide an estimate of vascular

viability. Combination of vascular crushing with a TFE readout is not easy due to the multiple excitation pulses [27].

The Look-Locker time course provides an estimate of transit time, allowing PW signals to be examined in clinical situations where transit time may change due to pathology**.** It was seen that the Look-Locker readout provided more information on blood supply than the equivalent single-TI data, as the blood signal has gone by the late delay times of typical single TI ASL.

Further work will model the perfusion signal to give transit time, CBVa and CBF. Currently this technique is limited to a single slice implementation; however with the increased SENSE factor achievable with a 32-channel coil the feasibility of multi-slice LL-TFE will be explored.

5.4 CONCLUSIONS

The experimental work in this chapter has shown several methods for ASL imaging at 7 T. It was demonstrated that gradient echo EPI could be used to acquire ASL data at 1.5 mm in plane resolution without a significant impact on image quality or stability. TFE and bFFE were compared for use as ASL readout methods; bFFE has higher SNR and CNR than TFE, but increases SAR reducing the number of slices that can be achieved. EPI has highest SNR but suffers at 1 mm resolution from image distortions due to a lengthened echo train, whereas TFE and bFFE, with short echo times, are more robust to susceptibility differences. 3D-EPI was shown to increase the slice coverage achievable whilst maintaining perfusion signal across the slices.

Look-Locker methodologies for the assessment of the temporal characteristics of the perfusion response were shown to be applicable at 7 T, even with increased SAR compared to lower field strengths. LL-EPI was used to measure arterial blood volume at rest and during a motor task with results in agreement to those measured at 3 T. The combination of 3D EPI with a Look-Locker ASL scheme was shown, providing increased spatial coverage through the use of parallel acceleration and Partial Fourier along two acquisition axes. LL-3D-EPI provides greater flexibility of the Look Locker technique, with fewer restrictions on slice coverage. Finally, the combination of TFE with a LL readout was shown to be feasible and to provide extra information in the assessment of Low Grade Gliomas compared to a single TI method.

5.5 REFERENCES

1. Teeuwisse, W.M., A.G. Webb, and M.J.P. Van Osch, *Arterial Spin Labeling at Ultra-High Field: All That Glitters is Not Gold.* Int J Imaging Syst Technol, 2010. **2**: p. 62-70.
2. Gardener, A.G., P.A. Gowland, and S.T. Francis, *Implementation of Quantitative Perfusion Imaging Using Pulsed Arterial Spin Labeling at Ultra-High Field.* Mag. Res. Med., 2009. **61**: p. 874-882.
3. Wright, P.J., O.E. Mougin, J.J. Totman, A.M. Peters, M.J. Brookes, R. Coxon, P.G. Morris, M. Clemence, S.T. Francis, R. Bowtell, and P.A. Gowland, *Water Proton T1 Measurements in Brain Tissue at 7, 3 and 1.5T using IR-EPI, IR-TSE and MPRAGE: results and optimisation.* Magn. Reson. Mater. Phy, 2008. **21**: p. 121-130.
4. Rooney, W.D., G. Johnson, X. Li, E.R. Cohen, S.-G. Kim, K. Ugurbil, and C.S. Springer, *Magnetic Field and Tissue Dependancies of Human Brain Longitudinal ^1H_2O Relaxation in Vivo.* Mag. Res. Med., 2007. **57**: p. 308-318.
5. van der Zwaag, W., S. Francis, K. Head, A. Peters, P. Gowland, P. Morris, and R. Bowtell, *fMRI at 1.5, 3 and 7 T: Characterising BOLD signal changes.* Neuroimage, 2009. **47**(4): p. 1425-1434.
6. Parent, A. and M.B. Carpenter, *Human Neuroanatomy.* 1995, Baltimore M.D.: Williams & Wilkins.
7. Grossman, E.J., K. Zhang, J. An, A. Voorhees, M. Inglese, Y. Ge, N. Oesingmann, J. Xu, K.A. Mcgorty, and Q. Chen, *Measurement of Deep Gray Matter Perfusion Using a Segmented True-Fast Imaging with Steady-State Precession (True-FISP) Arterial Spin-Labeling (ASL) Method at 3T.* JMRI, 2009. **29**: p. 1425-1431.
8. Duong, T.Q., E. Yacoub, G. Adriany, X. Hu, K. Ugurbil, J.T. Vaughan, H. Merkle, and S.-G. Kim, *High-Resolution, Spin-Echo BOLD, and CBF fMRI at 4 and 7T.* Mag. Res. Med., 2002. **48**: p. 589-593.
9. Feinberg, D., S. Ramanna, and M. Gunther. *Evaluation of new ASL 3D GRASE sequences using Parallel Imaging, Segmented and Interleaved k-space at 3T with 12- and 32-channel Coils.* in *Proceedings of the 17th Annual Meeting of ISMRM*. 2009. Hawaii, USA: 623.
10. Duyn, J.H., P. van Gelderen, L. Talagala, A. Koretsky, and J.A. De Zwart, *Technological Advances in MRI Measurement of Brain Perfusion.* JMRI, 2005. **22**: p. 751-753.
11. Chen, J.J., M.R. Smith, and R. Frayne, *The impact of partial-volume effects in dynamic susceptibility contrast magnetic resonance perfusion imaging.* Journal of Magnetic Resonance Imaging, 2005. **22**(3): p. 390-399.
12. van Osch, M.J.P., E. Vonken, C.J.G. Bakker, and M.A. Viergever. *Correcting partial volume artifacts of the arterial input function in quantitative cerebral perfusion MRI*. in *Proceedings of the 7th Annual Meeting of ISMRM*. 2001. Philadelphia, Pennsylvania: 477-485.
13. Donahue, M.J., H.Z. Lu, C.K. Jones, J.J. Pekar, and P.C.M. van Zijl, *An account of the discrepancy between MRI and PET cerebral blood flow measures. A high-field MRI investigation.* Nmr in Biomedicine, 2006. **19**(8): p. 1043-1054.
14. Figueiredo, P., Y. Zhang, S. Smith, and P. Jezzard. *Accounting for Partial Volume Effects in Perfusion Measurements using ASL Techniques*. in *Proceedings of the 9th Annual Meeting of ISMRM*. 2001. Scotland, UK: 1567.
15. Asllani, I., A. Borogovac, and T.R. Brown, *Regression Algorithm Correcting for Partial Volume Effects in Arterial Spin Labeling MRI.* Magnetic Resonance in Medicine, 2008. **60**(6): p. 1362-1371.
16. Poole, M. and R. Bowtell, *Volume parcellation for improved dynamic shimming.* Magnetic Resonance Materials in Physics Biology and Medicine, 2008. **21**(1-2): p. 31-40.
17. Sanchez Panchuelo, R.M., *High Resolution Anatomical and Functional Imaging*, in *Physics*. 2009, University of Nottingham: Nottingham.
18. Garcia, D.M., G. Duhamel, and D.C. Alsop, *Efficiency of inversion pulses for background suppressed arterial spin labeling.* Magnetic Resonance in Medicine, 2005. **54**(2): p. 366-372.
19. Triantafyllou, C., R.D. Hoge, G. Krueger, C.J. Wiggins, A. Potthast, G.C. Wiggins, and L.L. Wald, *Comparison of physiological noise at 1.5 T, 3 T and 7 T and optimization of fMRI acquisition parameters.* Neuroimage, 2005. **26**(1): p. 243-250.
20. Herscovitch, P. and M.E. Raichle, *What Is the Correct Value for the Brain-Blood Partition Coefficient for Water?* Journal of Cerebral Blood Flow and Metabolism, 1985. **5**: p. 65-69.
21. Geyer, S., A. Schleicher, and K. Zilles, *The somatosensory cortex of human: Cytoarchitecture and regional distributions of receptor-binding sites.* Neuroimage, 1997. **6**(1): p. 27-45.
22. Geissler, A., R. Lanzenberger, M. Barth, A.R. Tahamtan, D. Milakara, A. Gartus, and R. Beisteiner, *Influence of fMRI smoothing procedures on replicability of fine scale motor localization.* Neuroimage, 2005. **24**(2): p. 323-331.

23. Fernandez-Seara, M.A., J. Wang, Z. Wang, M. Korczykowski, M. Gunther, D. Feinberg, and J.A. Detre, *Imaging Mesial Temporal Lobe Activation During Scene Encoding: Comparison of fMRI Using BOLD and Arterial Spin Labeling.* Hum Brain Mapp, 2007. **28**: p. 1391-1400.
24. Luh, W.-M. and P.A. Bandettini. *Estimation of Pure Gray Matter Perfusion using Pseudo-Continuous Arterial Spin Labeling and Partial Volume Correction*. in *Proceedings of the 17th Annual Meeting of ISMRM*. 2009. Hawaii, USA: 3641.
25. St. Lawrence, K.S. and J. Wang, *Effects of the apparent transverse relaxation time on cerebral blood flow measurements obtained by arterial spin labeling.* Magnetic Resonance in Medicine, 2005. **53**(2): p. 425-433.
26. Preibisch, C. and A. Haase, *Perfusion Imaging Using Spin-Labeling Methods: Contrast-to-Noise Comparison in Functional MRI Applications.* Magnetic Resonance Imaging, 2001. **46**: p. 172-182.
27. Pell, G.S., D.P. Lewis, and C.A. Branch, *Pulsed Arterial Spin Labeling Using TurboFLASH With Suppression of Intravascular Signal.* Magnetic Resonance in Medicine, 2003. **49**: p. 341-350.
28. Pell, G.S., D.P. Lewis, R.J. Ordidge, and C.A. Branch, *TurboFLASH FAIR Imaging with Optimized Inversion and Imaging Profiles.* Mag. Res. Med., 2004. **51**: p. 46-54.
29. Jahng, G.-H., M.W. Weiner, and N. Schuff, *Improved Arterial Spin Labeling Method: applications for measurements of cerebral blood flow in human brain at high magnetic field MRI.* Med Phys, 2007. **34**(11): p. 4519-4525.
30. Schepers, J., M.J.P. van Osch, and K. Nicolay, *Effect of Vascular Crushing on FAIR Perfusion Kinetics, Using a BIR-4 Pulse in a Magnetization Prepared FLASH Sequence.* Mag. Res. Med., 2003. **50**: p. 608-613.
31. Hatabu, H., P.A. Wielopolski, and E. Tadamura, *An attempt of pulmonary perfusion imaging utilizing ultrashort echo time turbo FLASH sequence with signal targeting and alternating radio-frequncy (STAR).* Eur. J. Radiol., 1999. **29**: p. 160-163.
32. Boss, A., P. Martirosian, U. Klose, T. Nagele, C.D. Claussen, and F. Schick, *FAIR-TrueFISP Imaging of Cerebral Perfusion in Areas of High Magnetic Susceptibility Differences at 1.5 and 3 Tesla.* Journal of Magnetic Resonance Imaging, 2007. **25**: p. 924-931.
33. Grossman, E.J., K. Zhang, J. An, A. Voorhees, M. Inglese, Y. Ge, N. Oesingmann, J. Xu, K.A. Mcgorty, and Q. Chen, *Measurement of Deep Gray Matter Perfusion Using a Segmented True-Fast Imaging with Steady-State Precession (True-FISP) Arterial Spin-Labeling (ASL) Method at 3T.* Journal of Magnetic Resonance Imaging, 2009. **29**: p. 1425-1431.
34. Martirosian, P., U. Klose, I. Mader, and F. Schick, *FAIR TrueFISP Perfusion Imaging of the Kidneys.* Magnetic Resonance Imaging, 2004. **51**: p. 353-361.
35. Schraml, C., N.F. Schwenzer, P. Martirosian, C.D. Claussen, and F. Schick, *Perfusion imaging of the pancreas using an arterial spin labeling technique.* Journal of Magnetic Resonance Imaging, 2008. **28**(6): p. 1459-1465.
36. Ge, Y., M.B. Patel, Q. Chen, E.J. Grossman, K. Zhang, L. Miles, J.S. Babb, J. Reaume, and R.I. Grossman, *Assessment of thalamic perfusion in patients with mild traumatic brain injury by true FISP arterial spin labelling MR imaging at 3T.* Brain Injury, 2009. **23**(7): p. 666-674.
37. Zun, Z., E.C. Wong, and K.S. Nayak, *Assessment of Myocardial Blood Flow (MBF) in Humans Using Arterial Spin Labeling (ASL): Feasibility and Noise Analysis.* Mag. Res. Med., 2009. **62**: p. 975-983.
38. Wang, J., L. Li, A.C. Roc, D.C. Alsop, K. Tang, N.S. Butler, M.D. Schnall, and J.A. Detre, *Reduced susceptibility effects in perfusion fMRI with single-shot spin-echo EPI acquisitions at 1.5 tesla.* Magnetic Resonance Imaging, 2004. **22**(1): p. 1-7.
39. Crelier, G.R., R.D. Hoge, P. Munger, and G.B. Pike, *Perfusion-Based Functional Magnetic Resonance Imaging With Single-Shot RARE and GRASE Acquisitions.* Magnetic Resonance in Medicine, 1999. **41**: p. 132-136.
40. Liu, H.-L., P. Kochunov, J. Hou, Y. Pu, S. Mahankali, C.-M. Feng, S.-H. Yee, Y.-L. Wan, P.T. Fox, and J.-H. Gao, *Perfusion-weighted imaging of interictal hypoperfusion in temporal lobe epilepsy using FAIR-HASTE: Comparison with H(2)(15)O PET measurements.* Magnetic Resonance in Medicine, 2001. **45**(3): p. 431-435.
41. Duhamel, G. and D.C. Alsop. *Single-Shot Susceptibility Insensitive Whole Brain 3D fMRI with ASL*. in *ISMRM*. 2004: 518.
42. Wong, E.C., W.-C. Wu, and J. Bykowski. *Whole Brain 3D Velocity Selective Arterial Spin Labeling using a Background Suppressed Flow Weighted Spiral Fast Spin Echo Acquisition.* in *ISMRM*. 2006: 3427.
43. Fernandez-Seara, M.A., Z. Wang, J. Wang, H.-Y. Rao, M. Guenther, D.A. Feinberg, and J.A. Detre, *Continuous Arterial Spin Labeling Perfusion Measurements Using Single Shot 3D GRASE at 3T.* Magnetic Resonance in Medicine, 2005. **54**: p. 1241-1247.
44. Birn, R.M., J.A. Bodurka, N. Petridou, and P.A. Bandettini. *Experimental determination of the effect of T2' changes in spin-echo EPI*. in *International Soceity of Magnetic Resonance in Medicine*. 2004. Kyoto: 997.

45. Harmer, J., R.M. Sanchez-Panchuelo, R. Bowtell, and S.T. Francis, *Spatial location and strength of BOLD activation in high spatial resolution fMRI of the motor cortex: a comparison of SE and GE fMRI at 7T.* NMR in Biomedicine, 2011(IN PRESS).
46. Feinberg, D.A., S. Ramanna, and M. Gunther. *Evaluation of new ASL 3D GRASE sequences using Parallel Imaging, Segmented and Interleaved k-space at 3T with 12- and 32- channel coils.* in *International Soceity of Magnetic Resonance in Medicine*. 2009. Hawaii,: 623.
47. Peters, A.M., M.J. Brookes, F.G. Hoogenraad, P.A. Gowland, S.T. Francis, P.G. Morris, and R. Bowtell, *T2* Measurements in Human Brain at 1.5, 3 and 7T.* Magnetic Resonance Imaging, 2007. **25**: p. 748 - 753.
48. Deichmann, R., C.D. Good, O. Josephs, J. Ashburner, and R. Turner, *Optimization of 3-D MP-RAGE sequences for structural brain imaging.* NeuroImage, 2000. **12**(1): p. 112-127.
49. Dobre, M.C., K. Ugurbil, and M. Marjanska, *Determination of blood longitudinal relaxation time (T1) at high magnetic field strengths.* Mag. Res. Med., 2007. **25**: p. 733-735.
50. Gunther, M., K. Oshio, and D.A. Feinberg, *Single-Shot 3D Imaging Techniques Improve Arterial Spin Labeling Perfusion Measurements.* Magnetic Resonance in Medicine, 2005. **54**: p. 491-498.
51. Owen, D.G., Y. Bureau, A.W. Thomas, F.S. Prato, and K.S. St. Lawrence, *Quantification of pain-induced changes in cerebral blood flow by perfusion MRI.* Pain, 2008. **136**: p. 85-96.
52. Kim, J., J. Whyte, J. Wang, H.-Y. Rao, K.Z. Tang, and J.A. Detre, *Continuous ASL perfusion fMRI investigation of higher cognition: Quantification of tonic CBF changes during sustained attention and working memory tasks.* NeuroImage, 2006. **15**(1): p. 376-385.
53. Talagala, S.L., F.Q. Ye, P.J. Ledden, and S. Chesnick, *Whole-Brain 3D Perfusion MRI at 3.0T Using CASL With a Separate Labeling Coil.* Magnetic Resonance in Medicine, 2004. **52**: p. 131-140.
54. Goerke, U., H.E. Moller, D.G. Norris, and C. Schwarzbauer, *A comparison of signal instability in 2D and 3D EPI resting state fMRI.* NMR Biomed, 2005. **18**: p. 534-542.
55. Poser, B.A., P.J. Koopmans, T. Witzel, L.L. Wald, and M. Barth, *Three dimensional echo-planar imaging at 7 Tesla.* NeuroImage, 2010. **51**: p. 261-266.
56. van der Zwaag, W., J.P. Marques, T. Kober, G. Glover, R. Gruetter, and G. Krueger, *Temporal SNR characteristics in segmented 3D-EPI at 7T.* Magnetic Resonance in Medicine, IN PRESS: p. n/a-n/a.
57. Gai, N.D., S.L. Talagala, and J.A. Butman, *Whole-brain cerebral blood flow mapping using 3D echo planar imaging and pulsed arterial tagging.* Journal of Magnetic Resonance Imaging, 2011. **33**(2): p. 287-295.
58. Francis, S.T., R. Bowtell, and P.A. Gowland, *Modeling and Optimization of Look-Locker Spin Labeling for Measuring Perfusion and Transit Time Changes in Activation Studies Taking into Account Arterial Blood Volume.* Mag. Res. Med., 2008. **59**: p. 316-325.
59. Stocker, T. and N.J. Shah, *MP-SAGE: A New MP-RAGE Sequence With Enhanced SNR and CNR for Brain Imaging Utilizing Square-Spiral Phase Encoding and Variable Flip Angles.* Mag. Res. Med., 2006. **56**: p. 824-834.
60. Busse, R.F., A.C.S. Brau, A. Vu, C.R. Michelich, E. Bayram, R. Kijowski, S.B. Reeder, and H.A. Rowley, *Effects of Refocusing Flip Angle Modulation and View Ordering in 3D Fast Spin Echo.* Mag. Res. Med., 2008. **60**(3): p. 640-649.
61. Gallichan, D. and P. Jezzard, *Variation in the shape of pulsed arterial spin labeling kinetic curves across the healthy human brain and its implications for CBF quantification.* Magnetic Resonance in Medicine, 2009. **61**(3): p. 686-695.
62. Wong, E.C., R.B. Buxton, and L.R. Frank, *Quantitative Imaging of Perfusion Using a Single Subtraction (QUIPSS and QUIPSS II).* Mag. Res. Med., 1998. **39**(5): p. 702-708.
63. Look, D.C. and D.R. Locker, *Time saving in measurement of NMR and EPR relaxation times.* Rev. Sci. Instrum., 1970. **41**: p. 250-1.
64. Gunther, M., M. Bock, and L.R. Schad, *Arterial Spin Labeling in Combination With a Look-Locker Sampling Strategy: Inflow Turbo-Sampling EPI-FAIR (ITS-FAIR).* Mag. Res. Med., 2001. **46**: p. 974-984.
65. Petersen, E.T., T. Lim, and X. Golay, *Model-Free Arterial Spin Labeling Quantification Approach for Perfusion MRI.* Mag. Res. Med., 2006. **55**: p. 219-232.
66. Hoad, C., E. Cox, D. Anblagan, and S.T. Francis. *Multiphase True-FISP ASL in the Kidney*. in *ISMRM*. 2010. Stockholm: 327.
67. Brookes, M.J., P.G. Morris, P.A. Gowland, and S.T. Francis, *Noninvasive Measurement of Arterial Cerebral Blood Volume Using Look-Locker EPI and Arterial Spin Labeling.* Mag. Res. Med., 2007. **58**: p. 41-54.
68. Ho, Y.-C.L., E.T. Petersen, and X. Golay, *Measuring arterial and tissue responses to functional challenges using arterial spin labeling.* NeuroImage, 2010. **49**(1): p. 478-487.
69. Ho, Y.-C.L., E.T. Petersen, I. Zimine, and X. Golay, *Similarities and differences in arterial responses to hypercapnia and visual stimulation.* J Cereb Blood Flow Metab, 2011. **31**(2): p. 560-571.

70. Kamagata, K., Y. Motoi, M. Hori, M. Suzuki, A. Nakanishi, K. Shimoji, S. Kyougoku, R. Kuwatsuru, K. Sasai, O. Abe, Y. Mizuno, S. Aoki, and N. Hattori, *Posterior hypoperfusion in parkinson's disease With and without dementia measured with arterial spin labeling MRI.* Journal of Magnetic Resonance Imaging, 2011. **33**(4): p. 803-807.
71. Buxton, R.B., E.C. Wong, and L.R. Frank, *Dynamics of blood flow and oxygenation changes during brain activation: The balloon model.* Magnetic Resonance in Medicine, 1998. **39**(6): p. 855-864.
72. Lee, S.-P., T.Q. Duong, G. Yang, C. Iadecola, and S.-G. Kim, *Relative changes of cerebral arterial and venous blood volumes during increased cerebral blood flow: Implications for BOLD fMRI.* Magnetic Resonance in Medicine, 2001. **45**(5): p. 791-800.
73. Knutsson, L., D. van Westen, E.T. Petersen, K.M. Bloch, S. Holtas, F. Stahlberg, and R. Wirestam, *Absolute quantification of cerebral blood flow: correlation between dynamic susceptibility contrast MRI and model-free arterial spin labeling.* Magnetic Resonance Imaging, 2010. **28**: p. 1-7.
74. Yoshiura, T., A. Hiwatashi, T. Noguchi, K. Yamashita, Y. Ohyagi, A. Monji, E. Nagao, H. Kamano, O. Togao, and H. Honda, *Arterial spin labelling at 3-T MR imaging for detection of individuals with Alzheimer's disease.* European Radiology, 2009. **19**(12): p. 2819-2825.
75. Zur, Y., M.L. Wood, and L.J. Neuringer, *Spoiling of Transverse Magnetization in Steady-State Sequences.* Magnetic Resonance in Medicine, 1991. **21**: p. 251-263.
76. Gunther, M., K. Oschio, and D.A. Feinberg, *Single-Shot 3D Imaging Techniques Improve Arterial Spin Labeling Perfusion Measurements.* Magnetic Resonance in Medicine, 2005. **54**: p. 491-498.
77. Wang, Y., S.-E. Kim, E.V.R. DiBella, and D.L. Parker, *Flow measurement in MRI using arterial spin labeling with cumulative readout pulses - Theory and validation.* Medical Physics, 2010. **37**(11).

6 THE EFFECT OF HYPERCAPNIA ON BRAIN FUNCTION

6.1 OUTLINE

This chapter describes the effect of hypercapnia, an increase in concentration of carbon dioxide (CO_2) in the blood, on perfusion and neuronal activity. Hypercapnia is a modulation often used for calibrated BOLD studies [1], where it is assumed to only act on the vasculature and not induce metabolic or neuronal activation. The primary aim of the experiments described in this Chapter is to investigate the physiology behind hypercapnia, and whether the assumptions of calibrated BOLD are valid.

Firstly, the known effects of hypercapnia on physiology and hence the BOLD signal are reviewed and the system used to induce hypercapnia in human volunteers is detailed. Two experiments are then presented; (i) the measurement of cerebral blood flow and transit time using ASL at 7 T during hypercapnia for the measurement of $CMRO_2$ using calibrated BOLD, and (ii) the effect of hypercapnia on resting and stimulus induced magnetoencephalography (MEG) signals (published in Hall *et al.* NeuroImage 58 (2011) 1034-1043).

6.2 INTRODUCTION

Hypercapnia is the term used for the state of increasing the concentration of carbon dioxide in the blood (P_aCO_2). This can be achieved through breath holding, inhalation of carbon dioxide or the administration of certain pharmaceuticals (e.g. Remifentanil [2]).

The effects of hypercapnia that are reported in the literature include increased cerebral blood flow [3], cerebral blood volume [4] and baseline BOLD signal [5]. However, stimulus-evoked BOLD signal changes are reduced during hypercapnia (e.g. [6-8]). This effect can be explained by the deoxyhaemoglobin dilution model of Hoge *et al.* [9] where the increased flow "washes out" deoxyhaemoglobin, increasing the MR signal. If a neuronal stimulus is applied during a hypercapnic challenge, which has caused the flow to increase substantially from baseline, the BOLD change is reduced compared to that in the absence of hypercapnia, as demonstrated in Figure 6-1. The flow increases substantially for a combined hypercapnic and motor task compared to a motor challenge alone, but with no

change in $CMRO_2$ the resulting BOLD response compared to hypercapnic baseline is reduced.

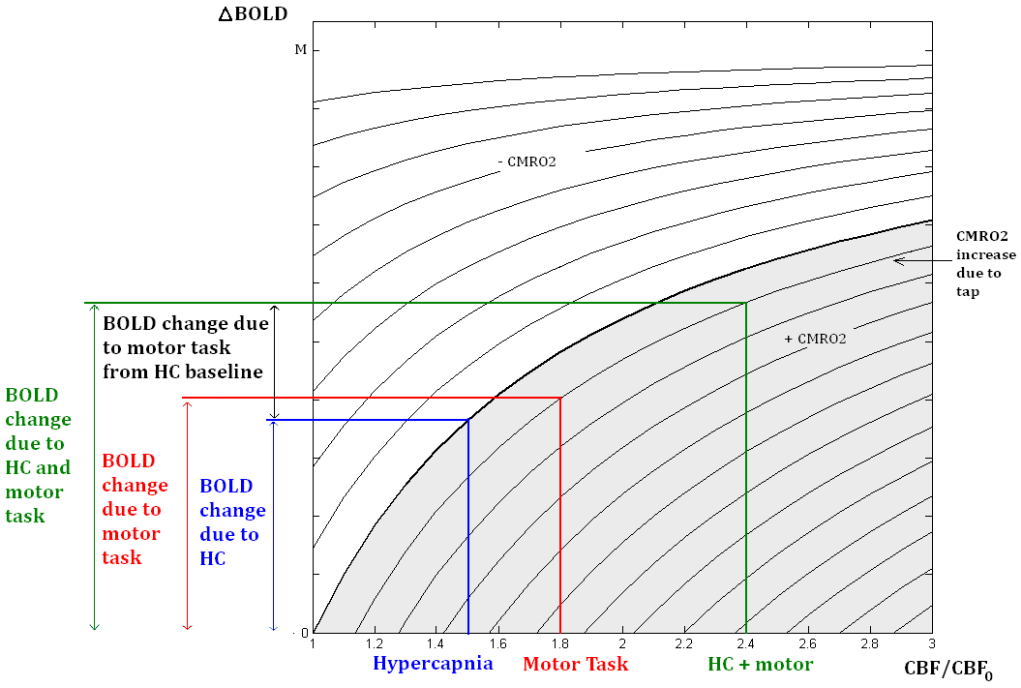

Figure 6-1: Schematic of Hoge's deoxyhaemoglobin model, demonstrating that the stimulus evoked BOLD is reduced on hypercapnia compared to normocapnia. Black lines indicate contours of constant $CMRO_2$, thick black line demonstrates no $CMRO_2$ change. Grey shaded region indicates a $CMRO_2$ increase.

Posse *et al.* [10] showed that the functional response to a visual stimulus in humans decreased with both hypocapnia and hypercapnia (20 – 70 mmHg partial pressure of end tidal CO_2 ($P_{ET}CO_2$)) and that BOLD functional contrast was almost completely eliminated at 70 mmHg $P_{ET}CO_2$. This effect has also been confirmed in the human motor cortex [11]. Gauthier *et al.* [7] showed that the BOLD response to a visual stimulus in humans can be eradicated by combined hypercapnia and hyperoxia (10 % CO_2, 90 % O_2 inhaled concentration). Cohen *et al.* [6] showed that increased $P_{ET}CO_2$ lengthened the onset and the time to peak of the BOLD response in human visual cortex.

The effect of hypercapnia on CBF has been used to provide a method of normalising the BOLD signal for variations in baseline CBF [12] and is widely used for calibrating the BOLD signal in terms of $CMRO_2$ (cerebral metabolic rate of oxygen consumption) [1, 13].

In 1997 Bandettini and Wong [13] first proposed hypercapnia based normalisation of the BOLD fMRI response. The aim of that study was to remove non neuronal-activation based effects from BOLD fMRI responses. The response

to a functional task was normalised by the BOLD response in that area of cortex to hypercapnia (inspired concentration of CO_2 ($FiCO_2$) = 5 %). This was shown to lead to the peak voxel of the finger tap BOLD response to move from a voxel containing a vessel to the cortex.

The more quantitative method of BOLD calibration is the Davis model [1] which was introduced in 1998. Using this model, the cerebral rate of oxygen consumption ($CMRO_2$) can be derived from BOLD and perfusion measures, $CMRO_2$ is a measure thought to be more closely coupled to the underlying neural activity. The relationship between BOLD, CBF, CBV and $CMRO_2$ has been formulated as:

$$\Delta R_2^*(t) \propto CBV(t)\left(\frac{CMRO_2(t)}{CBF(t)}\right)^{\beta} - CBV(0)\left(\frac{CMRO_2(0)}{CBF(0)}\right)^{\beta}, \quad \textbf{6-1}$$

where CBV(t) is the fractional blood volume at time t, CBF is the cerebral blood flow, $CMRO_2$ is the cerebral metabolic rate of oxygen metabolism and β is a power factor relating BOLD signal change and magnetic susceptibility ($\Delta R_2^* = \Delta\chi^{\beta}$) [1]. Through Monte Carlo simulations β has been shown to be 1.5 at 1.5 T [1], β reduces with field strength and is closer to 1 at 7 T [5].

The coupling between CBF and CBV can be used to replace CBV in Equation 6-1. Grubb *et al.* [3] investigated the coupling between CBF and CBV in anaesthetised rhesus monkeys using ^{15}O labelled water and haemoglobin. They showed the coupling between cerebral blood volume and cerebral blood flow was:

$$CBV = 0.8 \cdot CBF^{\alpha}, \quad \textbf{6-2}$$

where α = 0.38. Ito *et al.* [4] found a coupling constant of 0.29 between CBF and CBV in humans, measured using PET. However, the BOLD response is predominantly from the venous side, Chen et al. [14] found that the coupling between CBF and vCBV was 0.18 in humans, measured using MRI. The value Grubb derived is most commonly used to replace CBV in Equation 6-1, and this can be rewritten,

$$\frac{\Delta\text{BOLD}}{BOLD_0} = M\left(1 - \left(\frac{CMRO_2}{CMRO_{2,0}}\right)^{\beta}\left(\frac{CBF}{CBF_0}\right)^{\alpha-\beta}\right), \quad \textbf{6-3}$$

where ΔBOLD is the change in BOLD signal, $BOLD_0$ is baseline signal; subscript 0 represents resting values and M is the maximum BOLD signal achievable. M is generally calculated using a hypercapnic (increased CO_2) challenge, which is assumed not to change metabolism at the concentrations used (typically inspired concentration of CO_2 is 5 % e.g. [13]). By rearranging Equation 6-3, assuming no change in metabolism on hypercapnia, M can be derived as

$$M = \frac{\frac{\Delta BOLD_{HC}}{BOLD_0}}{1 - \left(\frac{CBF_{HC}}{CBF_0}\right)^{\alpha-\beta}}. \quad \textbf{6-4}$$

If CBF and BOLD are measured during hypercapnia (HC) and normocapnia (0, baseline) M can be calculated. This can then be used to find the change in $CMRO_2$ due to a stimulus;

$$\frac{CMRO_2}{CMRO_{2,0}} = \frac{1 - {\Delta BOLD}/{M \cdot BOLD_0}}{\left(\frac{CBF}{CBF_0}\right)^{\alpha-\beta}}. \quad \textbf{6-5}$$

However, the Davis model relies on several assumptions. The model is derived from Fick's law, stating that oxygen delivery is proportional to blood flow and to the arteriovenous oxygen difference. It also incorporates Grubb's law [3], α, and the relationship between ΔR_2^* and blood oxygenation given by Yablonskiy *et al.* [15], Boxerman *et al.* [16] and Ogawa *et al.* [17]. Results to date have given wide inter-subject and inter-study variability for values of M and the $CMRO_2$:CBF coupling ratio measured at 3 T as outlined in Table 6-1. M will increase with field strength as M is directly proportional to BOLD signal change which is known to increase with B_0 (e.g. [18]).

Study	M	$CMRO_2$:CBF Coupling Ratio	Brain Area
Hoge *et al.* [9]	15 ± 6 %	0.5 ± 0.1	Visual
Stefanovic *et al.* [11]	7.6 ± 1.3 %	0.22 ± 0.11	Visual
Chiarelli *et al.* [19]	6.6 ± 3.4 %	0.34 ± 0.03	Visual
Kastrup *et al.* [20]	9 ± 3 %	0.2 ± 0.1	Motor
Uludag *et al.* [21]	25 %	0.45 ± 0.15	Motor
Stefanovic *et al.* [11]	6.1 ± 1.1 %	0.49 ± 0.13	Motor
Chiarelli *et al.* [19]	4.3 ± 3.5 %	0.24 ± 0.03	Motor

Table 6-1: Literature values of the BOLD calibration constant M and coupling between $CMRO_2$ and CBF (adapted from [19]), all acquired at 3 T.

The measurement of metabolic changes in response to a neuronal stimulus should allow for easier comparison across patient and control groups or in groups with perturbed baseline flow (e.g. due to pharmacological agents such as caffeine), as the impact of different baseline physiology will have been removed. A direct measure of a physiological parameter such as CBF is more useful than a compound effect like BOLD. However, BOLD is widely used due to the ease of performing the measurement and analysing the data.

In addition to hypercapnia based calibration, there are other calibration methods used, with interest growing in the area of hyperoxia (increased levels of oxygen in the blood) based calibration. Chiarelli *et al.* [22] proposed a model that expressed the BOLD signal change in terms of changes in CBF and venous deoxyhaemoglobin, the constants of α and β are still used. The calibration constant M is similarly used to scale the BOLD signal change, and this is calculated using hyperoxia by assuming that hyperoxia does not cause a blood flow change. The value for M is equivalent to that calculated using hypercapnia calibration and Equation 6-5 is still valid. Hyperoxia is better tolerated by subjects compared to hypercapnia making this attractive for patient studies. However as with hypercapnia based methods there are several assumptions in the formulation of the model that are still being investigated and recent reports are investigating the combination of hypercapnia and hyperoxia calibration (e.g. [23]).

A fundamental assumption of BOLD calibration using hypercapnia is that there is no neuronal response to hypercapnia, therefore in addition to the effect on haemodynamics recent interest has considered the impact of hypercapnia on

electrophysiology as a marker of this. For example, Zappe *et al.* [24] demonstrated that hypercapnia caused a reduction in the invasive electrophysiological signals (multi-unit activity and beta/gamma spontaneous activity) in the visual cortex of anaesthetised monkeys. They hypothesised that this reduction could be suggestive of a $CMRO_2$ change with hypercapnia. If there is a direct $CMRO_2$ change to hypercapnia itself the method of calculating M in the Davis model would be invalid. The Davis model assumes that hypercapnia is isometabolic allowing for M to be calculated by only measuring BOLD and CBF (Equation 6-4).

MEG has rarely been used to study the neural response to hypercapnia. Schellart and Reits [25] investigated MEG and EEG responses to long breath holds to induce hypercapnia and hypoxia, and showed a frequency shift in the alpha band and an increase in the peak amplitude. Changes were not statistically significant, which is likely to be a result of breath holding being an unreliable way of inducing hypercapnia. DC-MEG measurements have shown changes under respiratory challenges. Carbon *et al.* [26] used hyperventilation to induce hypocapnia and showed a 1.1 – 6.2 pT increase in the global DC-MEG signal, however P_aCO_2 (arterial concentration of CO_2) was not recorded and P_aO_2 was not controlled, making it difficult to separate these effects. There was also large variability in the response, possibly due to the difficulty in inducing repeatable hypocapnia by hyperventilation. Blockley *et al.* [27] demonstrated a change in the MEG sustained field between controlled hypo- and hypercapnia at rest. A recent study of the effect of hypercapnia on the EEG signal [28] found a global reduction in oscillatory power in the alpha band during hypercapnia compared to normocapnia. In the same study, BOLD mediated functional connectivity in the default mode network was shown to be reduced (an effect also shown in the motor network [29]). Similarly [30] showed a reduction in alpha power, and also an increase in delta power, measured by EEG due to hypercapnia. Bloch-Salisbury *et al.* [31] showed in humans that the EEG evoked response to an auditory stimulus was unaffected by $P_{ET}CO_2$.

6.3 THE RESPIRACT™

In order to investigate the effects of hypercapnia it is necessary to have a precise and accurate way of inducing hypercapnia without causing any other effects. Using breath holding or inhalation of fixed concentration gases to control levels

of carbon dioxide in the blood is not ideal. Breath holding is not reliable and is very dependant on the subject, plus concentrations of CO_2 cannot be easily monitored during apnea (breathing cessation) as this is commonly performed using a nasal cannula (e.g. [11]). Breath holding also induces hypoxia, a reduction in the concentration of oxygen in the blood as the body is metabolising oxygen during the breath hold with no replenishment [32]. Fixed concentration inhalation also gives variable results within and between subjects [33]. Ideally oxygen concentrations should remain unchanged whilst the CO_2 level is modulated so that the effects of the two can be uncoupled.

The RespirAct™ (*Thornhill Research Inc, Toronto, Canada*) is a gas blending system that targets end-tidal CO_2 ($P_{ET}CO_2$) and O_2 ($P_{ET}O_2$) separately. The aim of the RespirAct™ is to allow prospective, independent, targeting of $P_{ET}CO_2$ and $P_{ET}O_2$ levels [34]. The system consists of a sequential gas delivery (SGD) circuit, Figure 6-2, attached to a non-vented face mask and a gas blender.

The SGD circuit comprises two gas reservoirs and three valves, schematically represented in Figure 6-2. When the fresh gas bag is full, this provides all the inhaled gas. Exhaled gas always goes into the exhaled gas reservoir, which if full will expel air through a hole. If the fresh gas bag collapses during inhalation, previously exhaled gas is drawn from the exhaled gas reservoir. This is considered to be *neutral gas* as it has already equilibrated with the blood and does not contribute to gas exchange. The system relies on the subject emptying the fresh gas bag with each breath, as this ensures that on each breath the subject receives the calculated amount of fresh gas, topped up with neutral gas.

The face mask has two connections back to the RespirAct™, one to measure the end tidal concentrations of CO_2 and O_2, the other to measure the pressure to detect periods of inspiration and expiration.

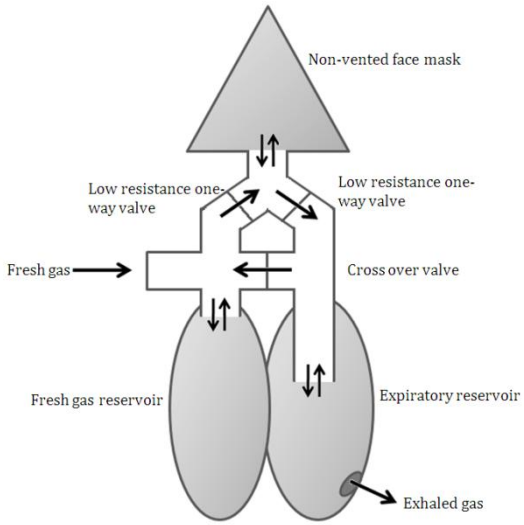

Figure 6-2 Schematic diagram of RespirAct face mask and SGD circuit.

The RespirAct™ uses four supply gases;

100 % O_2

Medical air: 21 % O_2, 79 % N_2

Gas A: 10 % O_2 90 % N_2

Gas B: 10 % O_2 20 % CO_2 70 % N_2

These all have a minimum of 10 % O_2 and a maximum of 20 % CO_2 for safety. The RespirAct™ has further safety functions; 100 % O_2 is delivered in the event of software failure / power cuts, the software ensures the correct gases have been connected prior to setting up a sequence and there is an emergency button to deliver 100 % O_2. Initial calibration of the system is performed using the [100 % O_2] and a gas mixture of [9 % CO_2, 91 % nitrogen]. This is connected to a different port, and the cylinder is removed before a mask is connected.

Sequences to vary $P_{ET}CO_2$ and $P_{ET}O_2$ can be simply designed; they are calculated based on each subject's metabolic parameters (determined using their height, weight and gender), their resting $P_{ET}CO_2$ and $P_{ET}O_2$ (approximately 40 mmHg and 100 mmHg [35], but measured on the day) and the typical and maximum flow rates. The typical flow rate is chosen so that the subject can comfortably empty the fresh gas bag with each breath. The maximum flow rate is the largest flow rate that can be used to induce transitions – if this is low it can take several breaths to achieve the desired change, but a flow rate that is too high can cause a build up of gas in the fresh gas bag as the subject is unable to inspire it.

6.4 THE EFFECT OF HYPERCAPNIA ON CBF AND BOLD: APPLICATION TO CALIBRATED BOLD

ASL measurements of perfusion under hypercapnia are often used for the estimation of $CMRO_2$ using the model of Davis *et al.* [1]. The most common implementation of ASL is to use a single-TI pulsed ASL sequence as this is the easiest method to implement. However, it has been shown that hypercapnia shortens the transit time of the label (e.g. [2, 36]) which can confound single TI perfusion methods as they lack temporal information.

This has been highlighted by Tancredi *et al*. [37] who show that there is a weak CBF increase in response to CO_2 as measured with ASL compared to visual stimulation using single TI PASL. They attributed this to a shortening of transit time causing the CBF response to CO_2 to be reduced.

This experiment aims to measure the perfusion change due to both a hypercapnic challenge and motor task at 7 T using a multiple TI Look-Locker EPI FAIR ASL sequence to account for and measure transit time changes. These measures are used together with BOLD signal changes to estimate the $CMRO_2$ change associated with finger tapping in healthy human subjects using the Davis model of calibrated BOLD. The value of M, the Davis calibration constant, is determined at 7 T. Calibrated BOLD analysis is performed to assess the feasibility of voxelwise analysis to form $CMRO_2$ maps as compared to region-of-interest (ROI) analysis, which is the standard method at 1.5 and 3 T (e.g. [19]).

6.4.1 EFFECTS OF TRANSIT TIME ON CALIBRATED BOLD: SIMULATIONS

To assess the impact of using only a single TI ASL acquisition for calibrated BOLD, simulations were performed to assess the effect of transit time changes. Transit time here refers to the time it takes the labelled blood to traverse from the arterioles to the tissue bed (Δ_{tissue}, equivalent to $\delta+\Delta_a$ in Figure 4-10). In addition to transit time, the bolus duration is also modelled. The bolus duration is the temporal duration of the labelled blood, and is governed by the non-selective thickness.

The effect of perfusion and transit time changes on the shape of the ASL perfusion curves for both an (i) infinite and a (ii) finite bolus are shown in Figure

6-3 for (A) a perfusion increase only and (B) a perfusion increase and transit time decrease.

To quantitatively assess the impact of transit time changes on a single TI measure of perfusion, the % perfusion signal change at TI = 1.5 s was used to estimate the flow change. Simulation parameters were $T_{1,b}$ = 2.1 s, $T_{1,tissue}$ = 2.1 s, at baseline it was assumed that perfusion, f = 90 ml/100g/min, transit delay Δ_{tissue} = 0.4 s and bolus duration W = 1.5 s [38]. The effects of T_2* decay were assumed to be negligible. To simulate activation, flow was increased with a corresponding decrease in transit time (e.g. $CBF_{act} = A.CBF_0$, $\Delta_{act} = \Delta_0 / A$). Figure 6-4 shows that as activation induced flow change increases, the error in the measured flow change also increases. The flow change is overestimated and the magnitude of the measurement error was reduced at short transit times.

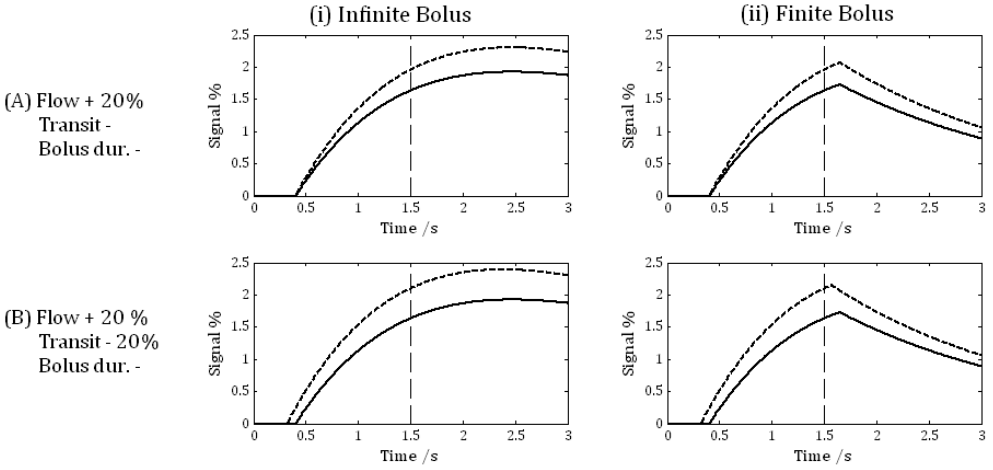

Figure 6-3: Simulated perfusion curves for 7 T [38] with (i) an infinite bolus and (ii) a finite bolus. (A) a perfusion increase of 20 % with no change in transit time or bolus duration (broken line) and (B) a perfusion increase of 20 % and transit time decrease of 20 %. The perfusion curve at rest is shown by the solid black line. Common simulated parameters λ = 0.98 ml/g, $T_{1,b}$ = 2.1 s, $T_{1,tissue}$ = 2.1 s, rest parameters f = 90 ml/100g/min, Δ_{tissue} = 0.4 s, W = 1.25 s). Vertical dashed line indicates typical single TI measurement time of 1.5 s.

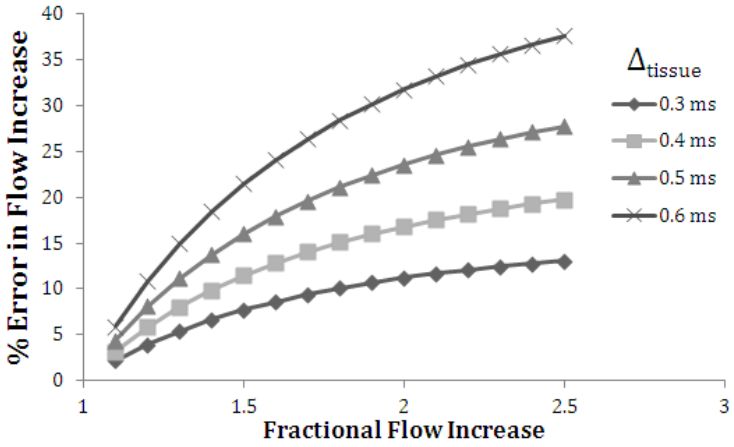

Figure 6-4: % error in measured flow increase as a function of flow increase for different tissue arrival times.

To quantitatively assess the impact on calibrated BOLD the % perfusion signal change at TI = 1.5 s for all cases was used to calculate M and $CMRO_2$ using the equations from the Davis model (Equations 6-3 and 6-4).

The simulations of effects of transit time changes on calibrated BOLD were split into four sections to address the effect of a single TI readout: (A) the error in M caused by error in the flow increase measured to hypercapnia, with different baseline transit delay (Δ_{tissue}) (B) the error in $CMRO_2$ as a function of the flow increase to hypercapnia, assessing the impact of Δ_{tissue} assuming no error in M, (C) the error in $CMRO_2$ caused by an error in M, assessing the impact of the magnitude of the BOLD response to the finger tap and M and (D) the combined effect of errors in the measurement of the flow response to hypercapnia and the finger tap on $CMRO_2$, assuming Δ_{tissue} = 0.5 ms and W = 1.5 s. For clarity, the simulations performed have been summarised in Table 6-2.

Figure	Description	Additional Variables	Assumptions
Figure 6-5 A	Error in M due to flow increase to hypercapnia	Δ_{tissue}	W = 1.5s
Figure 6-5 B	Error in $CMRO_2$ due to flow increase to tap	Δ_{tissue}	No account for error in M, W = 1.5s
Figure 6-5 C	Error in $CMRO_2$ due to error in M	$BOLD_{TAP}$ and M	No account for error due to flow increase from tap
Figure 6-6 A	Error in $CMRO_2$ due to flow increase to hypercapnia and finger tap	$BOLD_{HC}$	Assumes values of Δ_{tissue}, W
Figure 6-6 B	Error in $CMRO_2$ due to flow increase to hypercapnia and finger tap	$BOLD_{TAP}$	Assumes values of Δ_{tissue}, W

Table 6-2: Summary of simulations performed.

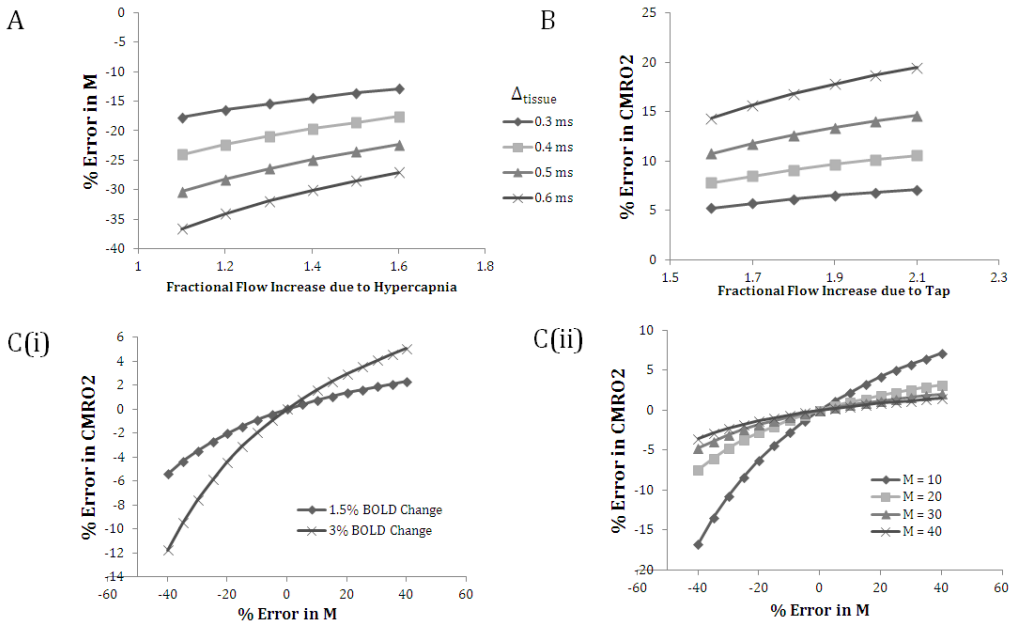

Figure 6-5: Simulation results assessing the impact of a single TI measurement on calibrated BOLD. (A) The error in M as a function of the flow increase to hypercapnia for different transit times (B) The error in $CMRO_2$ as a function of the flow increase due to the finger tap for different transit times (C) The error in $CMRO_2$ measurement due to errors in M with (i) different BOLD change to a finger tap and (ii) different values of M. The BOLD signal changes due to hypercapnia and the finger tap did not affect the % changes in M or $CMRO_2$ for the simulations A,B and C(ii).

The results of the simulations are shown in Figure 6-5 and Figure 6-6. Figure 6-5 A shows that the use of a single TI model has a significant impact on the error in M. B demonstrates that as the response to the tap increases there is an increase in the error in $CMRO_2$, with $CMRO_2$ being overestimated. However this is small compared to the errors in M shown in A. Plots B did not take into account an underlying error in M, as seen in A. Plots C (i) and (ii) demonstrate how an error in M contributes to an error in $CMRO_2$. They show that a large % error in M, causes a much lower % error in $CMRO_2$ which is reduced if the BOLD response to the motor task is small or M is large.

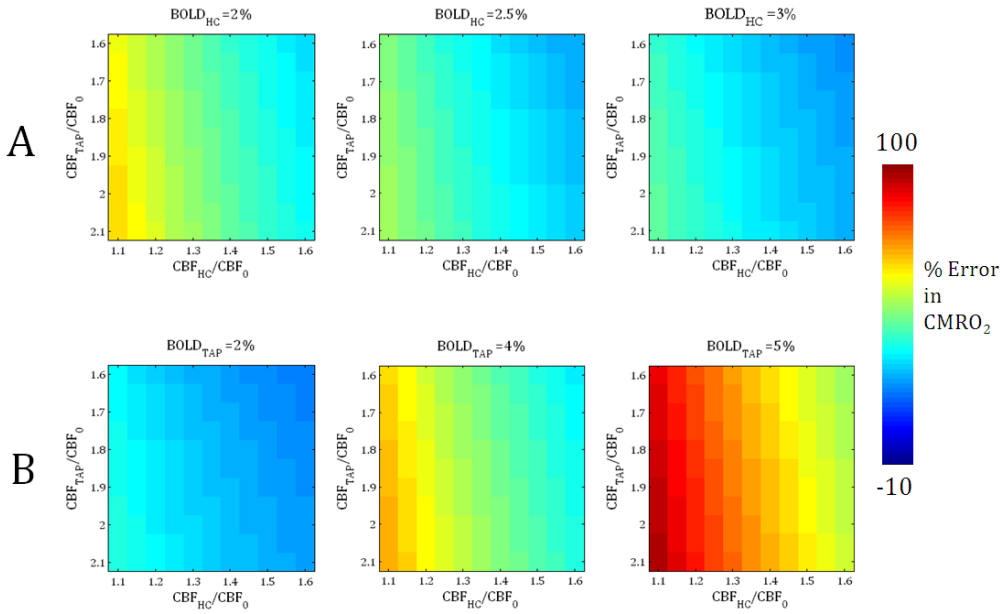

Figure 6-6: Simulation results showing the % error in $CMRO_2$ due to transit time errors in the measurement of the flow response to both hypercapnia and the finger tap, as a function of (A) the BOLD response to hypercapnia (assuming $BOLD_{TAP}$ = 3 %) and (B) the BOLD response to the finger tap (assuming $BOLD_{HC}$ = 2.5 %). Simulation parameters, at rest f = 90 ml/100g/min, Δ_{tissue} = 0.5 ms, W = 1.5 s.

The results of the final simulations are shown in Figure 6-6. These show that the resulting error in $CMRO_2$ is very dependant on the four measures (BOLD and CBF responses to hypercapnia and the finger tap). Typically the combined error in $CMRO_2$ is between -10 and +30 %. However, with certain parameter combinations, e.g. a high $BOLD_{TAP}$ response, and high CBF_{HC} response, the error can exceed + 50 %.

These simulations demonstrate that single TI PASL can cause significant errors in measured flow changes as the shape of the perfusion curve is not taken into account. As shown in Figure 6-4, the flow change can be significantly overestimated which causes values of M to be significantly under or underestimated. However the $CMRO_2$ estimate is relatively more robust to errors in the measured flow change due to the tap, and is also quite robust to errors in M.

From Figure 6-5 C it can be seen that a large error in M does not lead to a corresponding large error in $CMRO_2$. From Equation 6-5 it can be seen that as $\Delta BOLD/(BOLD_0\, M) \rightarrow 0$,

$$\frac{CMRO_2}{CMRO_{2,0}} \rightarrow \left(\frac{CBF}{CBF_0}\right)^{1-\frac{\alpha}{\beta}} \qquad \textbf{6-6}$$

This demonstrates that $CMRO_2$ tends towards a limit, restricting the range that $CMRO_2$ can take for large M as demonstrated in Figure 6-7. The final $CMRO_2$ value is then only dependant on the flow response to the motor task and the constants α and β. This would only occur in areas where the BOLD response to the neuronal stimulus is small compared to M, which could be due to an underestimated perfusion change to hypercapnia increasing M.

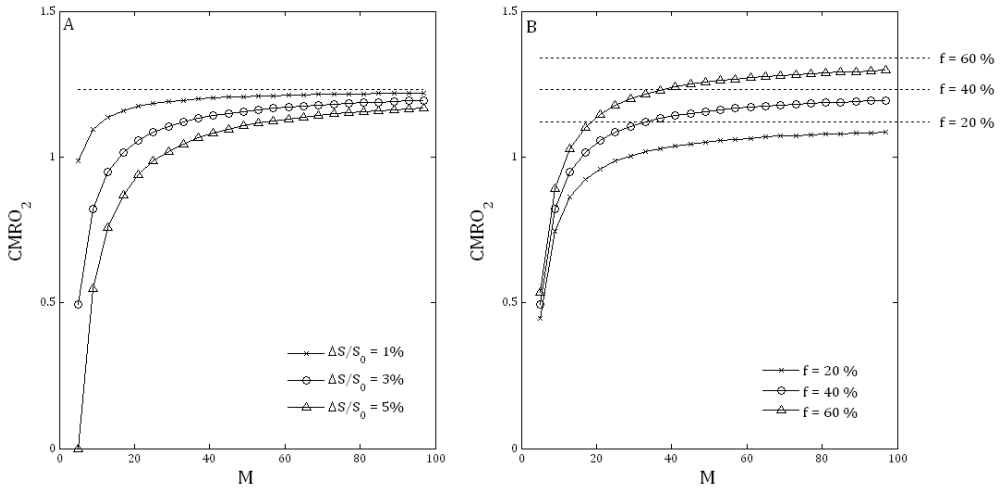

Figure 6-7: Dependence of $CMRO_2$ on M, dashed line represents the limit described in Equation 6-6 for (A) different values of the BOLD signal change and (B) the flow increase.

The simulations demonstrate that using a single TI method in the presence of transit time changes can lead to large errors in CBF measurement and hence M and $CMRO_2$. To reduce such errors a method of perfusion measurement that accounts for transit time changes is required. For the following experimental work a Look-Locker ASL method is used to measure CBF and transit time during hypercapnia, and a motor task to allow assessment of M and $CMRO_2$ using the Davis model [1].

6.4.2 IN VIVO STUDY: EXPERIMENTAL METHOD

5 healthy subjects participated in the study (3 female, age range 24 – 52 years), which was approved by the local ethics committee, and all subjects gave informed written consent. Data were acquired using a Philips Achieva 7 T system with head volume transmit coil and 16-channel SENSE receive coil.

A FAIR ASL scheme (selective 10 mm wider than imaging volume, 250 mm non-selective) with WET pre-sat and sinc post-sat pulses was used. LL-EPI-FAIR acquisition parameters were TI/ΔTI/TR = 350/300/3000 ms with 8 readouts per TR; vascular crushing was applied using bipolar gradients with v_{enc} = 50 mms^{-1}.

The image acquisition module comprised a GE-EPI readout; 5 contiguous axial slices, 2 x 2 x 3 mm^3, FOV = 192 x 192 mm^2, FA = 35°, TE = 23 ms, SENSE factor 2, partial k–space factor 0.8. An equilibrium EPI image with long TR and an inversion recovery EPI data set with 11 TIs (100 ms – 4000 ms) from which to form a T_1 map were also acquired.

Functional protocol: The hypercapnic challenge started with 2 min of subject specific baseline $P_{ET}CO_2$ followed by 90s of hypercapnia (baseline + 10 mmHg $P_{ET}CO_2$) and 90s of baseline. This was then repeated 4 times. $P_{ET}O_2$ was targeted to remain at baseline throughout.

In a separate LL-FAIR experiment a bilateral motor task was performed with 5 cycles of 30s rest / 30s tapping. A schematic of the experimental protocol is shown in Figure 6-8.

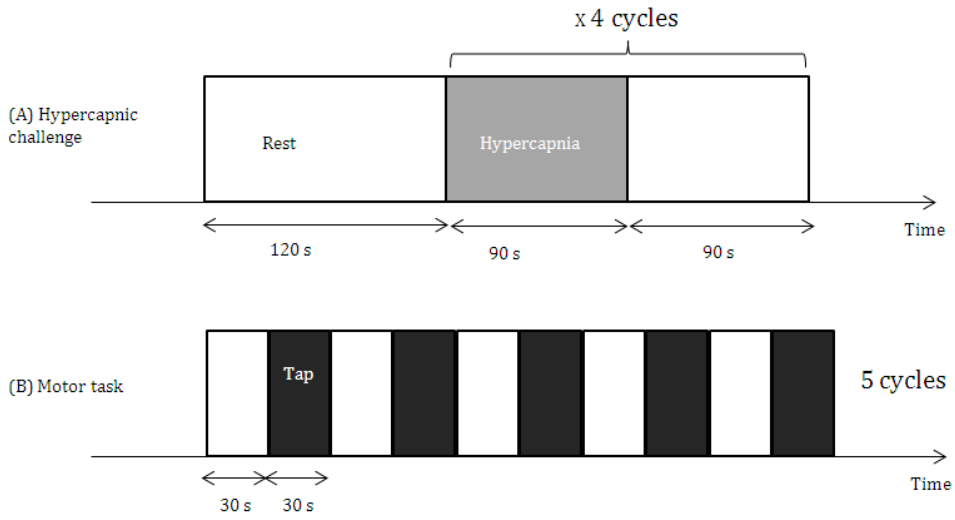

Figure 6-8: Schematic of the two functional paradigms performed, (A) a hypercapnic challenge and (B) a motor task comprising a bilateral finger tapping task.

Data Analysis

For the hypercapnic challenge, the first 30 seconds of each step was discarded and the average of the remaining $P_{ET}CO_2$ data taken to allow the average CO_2 increase to be determined.

For the motor task, BOLD and CBF regions of interest (ROI) in the motor cortex were determined using FEAT (FSL, FMRIB, Oxford). To increase CNR for defining active voxels, CBF perfusion weighted data was averaged over the first 5 readout phases to give one data point per TR, as shown schematically in Figure 6-9. The first 5 readouts were used as these points usually show the most difference

between rest and activation as shown in Figure 6-3 and Figure 6-12. The last readout of the control data was used for BOLD data analysis. Thus CBF and BOLD datasets had an effective temporal resolution of 6 s. BOLD data was smoothed with a 3 mm FWHM Gaussian kernel and CBF data was smoothed with a 5 mm FWHM Gaussian kernel due to lower SNR, both were temporally filtered with a highpass filter (cutoff 60s). The GLM analysis used a boxcar to represent the motor task, and a map of Z score was produced (cluster threshold with $P<0.05$). The ROI was selected as voxels with Z score greater than 60 % of the max Z score, to give a CBF ROI and a BOLD ROI.

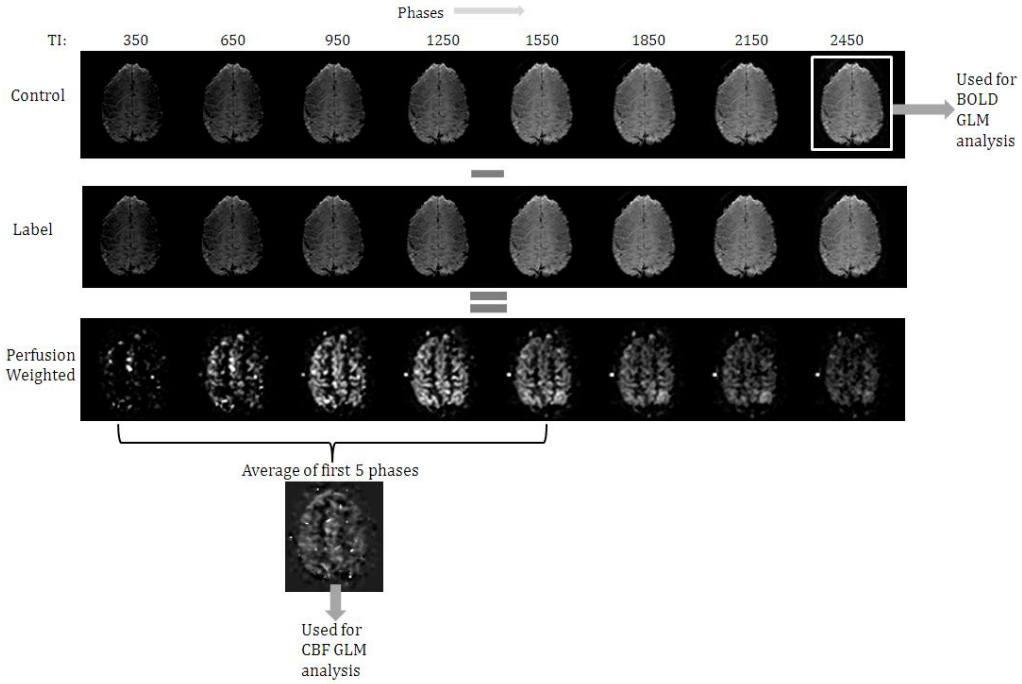

Figure 6-9: Schematic of analysis of the LLEPI data to determine CBF and BOLD ROI using GLM analysis.

The 8 phase LL-EPI data was separated into hypercapnic and normocapnic periods by discarding the first 30s of each transition and averaging over the remainder. Similarly the motor task was divided into periods of tap and rest. The LL-EPI data was normalised globally by $M_{0,b}$ estimated from the grey matter long TR EPI images signal intensity to give fractional signal change. All the LL-EPI data was smoothed using a Gaussian kernel (FWHM of 3 mm) before fitting to a complex model. The ASL data was fitted (using the Powell algorithm) for CBF, transit time (Δ_a) and exchange time (δ) (from which arrival time at the tissue can be estimated ($\Delta_{tissue}= \Delta_a+\delta$), and label duration using the model of Francis *et al*. [39], both voxelwise data and the average LLEPI timecourses from the ROIs were fitted for CBF and transit time.

The BOLD data was spatially smoothed with a Gaussian kernel (FWHM 3 mm) and linearly detrended to remove drift. As for the ASL data, BOLD signal changes due to hypercapnia and the finger tap task were calculated voxelwise and for both the ROIs.

CVR (cerebrovascular reactivity) measures were made voxelwise using both the % BOLD and % CBF changes due to hypercapnia over the entire grey matter scaled by the subject's $P_{ET}CO_2$ change. The grey matter mask was formed from the inversion recovery data, which was fitted to form a T_1 map; these were then thresholded to generate a grey matter mask (threshold of 1900 – 2300 ms).

Analysis of M and $CMRO_2$ was then performed in two ways (i) voxelwise (1 subject was excluded from voxelwise analysis due to low SNR) with results then averaged over the voxels in each of the two ROI's and (ii) on a ROI basis, fitting the average signal curves from the ROI, for both the BOLD and CBF ROI.

CBF and BOLD changes due to hypercapnia were used to determine M using the formula outlined in the Davis model [40] (Eqn. 6-4, using $\alpha = 0.38$ [3] and $\beta = 1$), both voxelwise and using the CBF and BOLD ROIs. For the voxelwise analysis voxels were excluded from the ROI if they displayed a low hypercapnic reactivity (CBF increase due to hypercapnia < 5 % or BOLD increase due to hypercapnia < 1 %).

The $CMRO_2$ change due to the finger tap relative to baseline $CMRO_2$ was then calculated using the Davis model (Eqn. 6-5) for (i) a voxel wise analysis using M maps and (ii) the M values for the ROI analysis.

6.4.3 RESULTS

An example RespirAct trace is shown in Figure 6-10. The hypercapnic challenge caused the $P_{ET}CO_2$ to increase by 6.6 ± 0.5 mmHg (averaged across subjects and repeats).

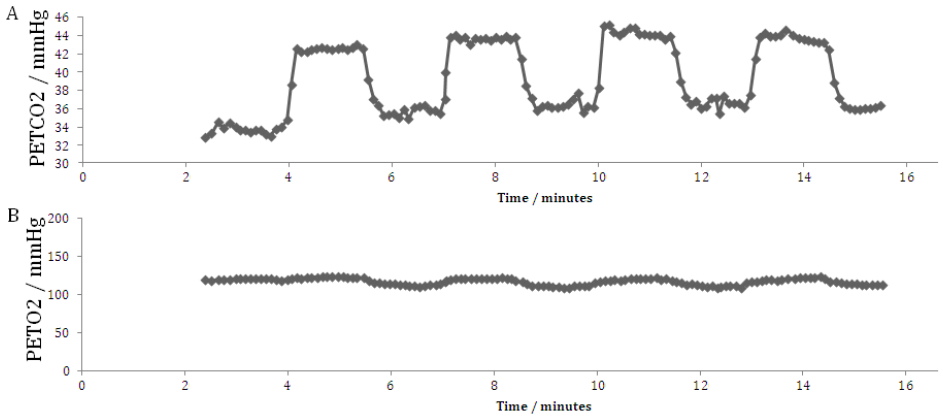

Figure 6-10: RespirAct traces from a single representative subject showing (A) $P_{ET}CO_2$ and (B) $P_{ET}O_2$.

The motor ROI for all 5 subjects for BOLD and CBF data are shown in Figure 6-11. Good correspondence is seen between the two. The CBF ROI tended to be smaller and to not include the supplementary motor area (SMA) probably due to SNR limitations. It is expected that the BOLD ROI will include more voxels and include large veins as these produce large BOLD signal changes, but such changes would not be seen in the ASL data.

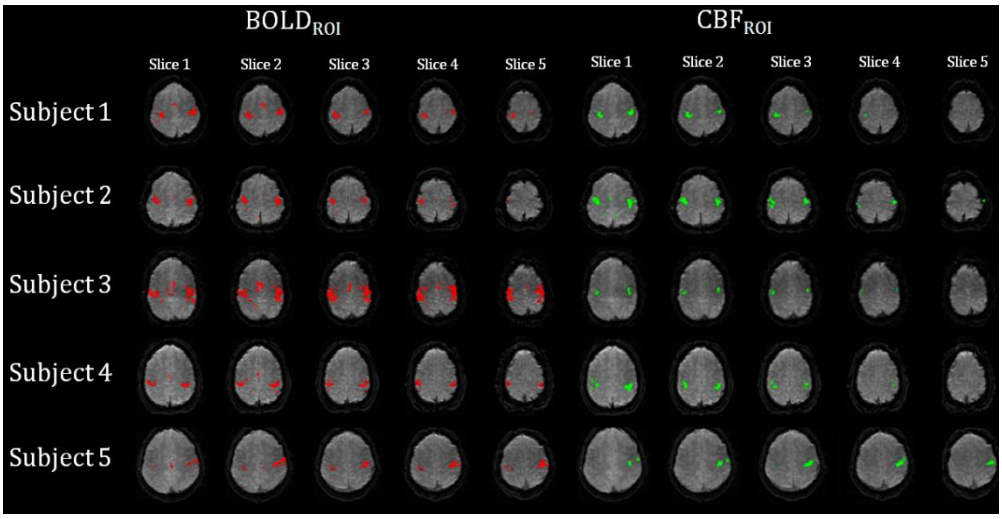

Figure 6-11: BOLD and CBF ROI defined from GLM analysis for all 5 subjects. The ROI was formed from thresholding the GLM Z stat maps at 60 % of their maximum value.

6.4.3.1 Cerebrovascular Reactivity – Effect of Hypercapnia on Perfusion and BOLD

Example LL-EPI timecourses are shown in Figure 6-12. The shift in transit time and the change in perfusion between the three states are clearly visible. Hypercapnia caused the arrival time to reduce significantly ($P < 0.05$, Wilcoxon sign rank) from 484 ± 60 ms to 442 ± 65 ms (mean ± standard error, average

reduction of 9 %). Finger tapping caused a significant reduction in the arrival time to 420 ± 73 ms, an average reduction of 14 % compared to baseline ($P < 0.05$). This highlights the need for a perfusion technique that accounts for transit time when studying hypercapnia or activation states.

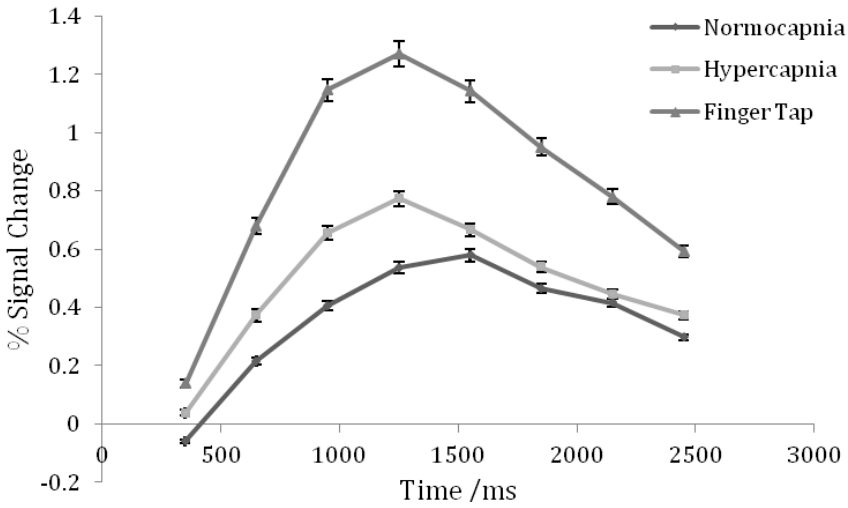

Figure 6-12: LL-EPI FAIR timecourses at normocapnia, hypercapnia and finger tap, for a representative subject in the CBF ROI (66 voxels).

Example BOLD and CBF maps in response to hypercapnia are shown in Figure 6-13. In grey matter, CBF reactivity was determined to be 5 ± 1 % / mmHg and BOLD CVR was 0.56 ± 0.06 % / mmHg (average across 5 subjects).

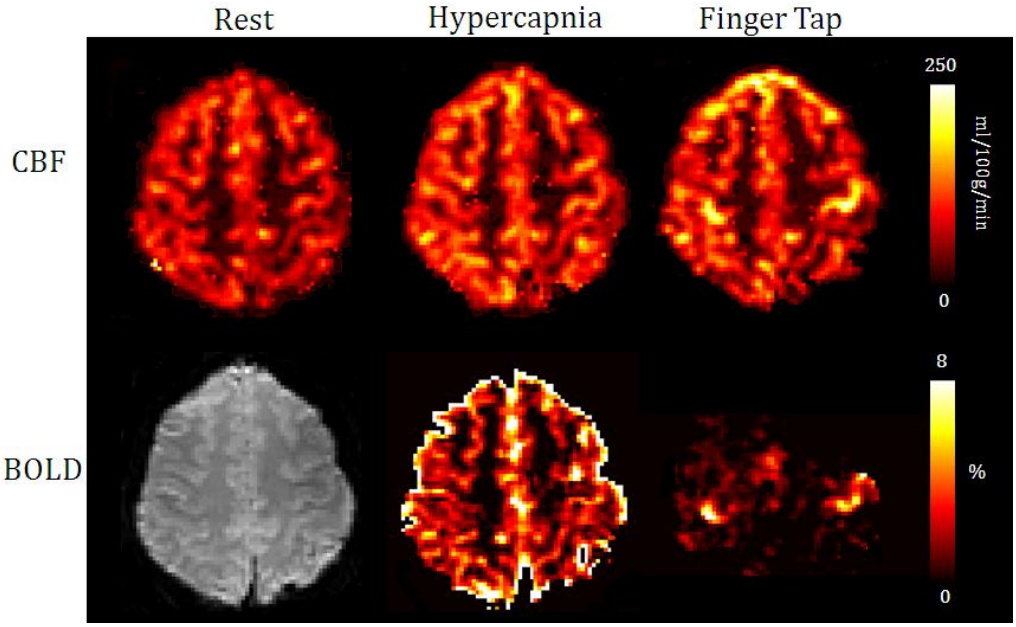

Figure 6-13: CBF maps, equilibrium EPI and % BOLD changes due to hypercapnia and a finger tap in a single representative subject.

6.4.3.2 Comparison of Voxelwise and ROI Analysis for Calibrated BOLD

Two ROIS were defined from the (A) CBF and (B) BOLD GLM analysis. Initially voxels where the reactivity to hypercapnia was low (CBF < 5 %, BOLD < 1 %) were excluded from the ROI defined from the GLM for the voxelwise analysis. The percentage of the voxels excluded was 26 ± 3 % in the BOLD ROI and 25 ± 3 % in the CBF ROI.

An example map of M values is shown in Figure 6-14. It can be seen that M varies across the brain. Large values of M likely correspond to voxels with a large vein where the BOLD response to hypercapnia will be large but there will be a corresponding small CBF response.

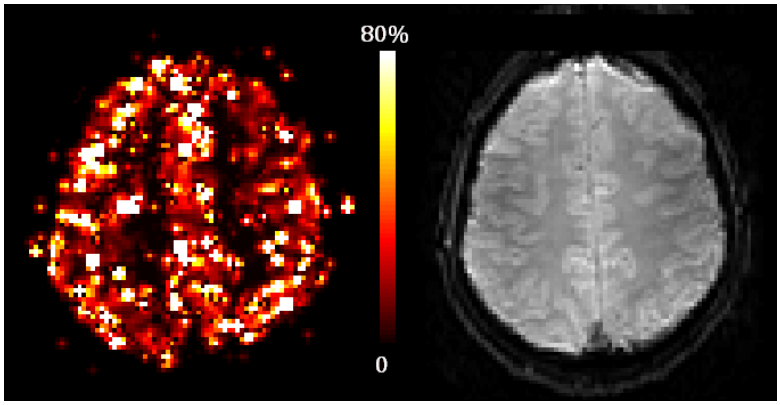

Figure 6-14: Example map of the calibration constant M as a % (left), for a representative subject, alongside their long TR EPI image (right) for anatomical reference.

To assess the distribution of M, the histogram of M values within a grey matter and white matter mask was taken. The masks were defined from the T_1 maps with grey matter defined in the range 1900 – 2,400 ms and white matter 1100 – 1400 ms [41, 42]. Figure 6-15 shows that grey matter (solid line) exhibits the largest M values, as expected. White matter shows a shift to lower M values, as expected as the BOLD response to hypercapnia is reduced in the white matter [5].

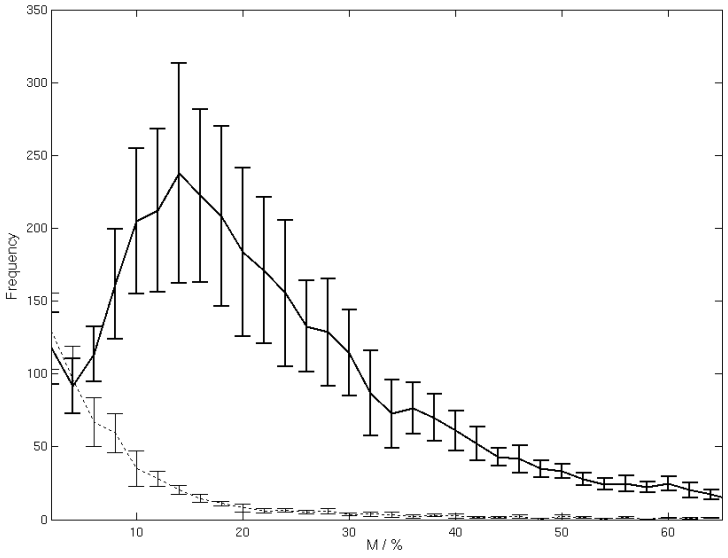

Figure 6-15: Histogram of M values, averaged over the 4 subjects. Histograms shown for grey matter (solid line) and white matter (broken line). Error bars represent standard error across subjects.

Figure 6-16 A shows the results for the voxelwise analysis averaged over the 4 subjects for the BOLD ROI (dark grey) and CBF ROI (light grey). This shows a slight reduction in the BOLD signal change and M for the CBF ROI compared to the BOLD ROI. Only small differences were seen in the CBF measurements between the two ROIs.

Figure 6-16 B shows the results of the ROI analysis for the BOLD and CBF ROI. A significant difference in the BOLD signal change due to both hypercapnia and the motor task was seen between the BOLD and CBF ROI, BOLD changes being significantly greater for the BOLD ROI. A significant difference in the calibration constant, M, can also be seen with a greater value of M for the BOLD ROI. No significant differences were seen in the CBF or $CMRO_2$ measures between the two ROIs.

Comparing the voxelwise and ROI based analysis the main difference is in the M values. The M values were more consistent between the two ROIs for the voxelwise analysis, this is because the voxelwise analysis excluded voxels where the CBF and BOLD responses to hypercapnia were low. Large M, as seen in the BOLD ROI analysis, results from a large BOLD response to hypercapnia accompanied by a small flow response to hypercapnia, as might be expected if large veins are present.

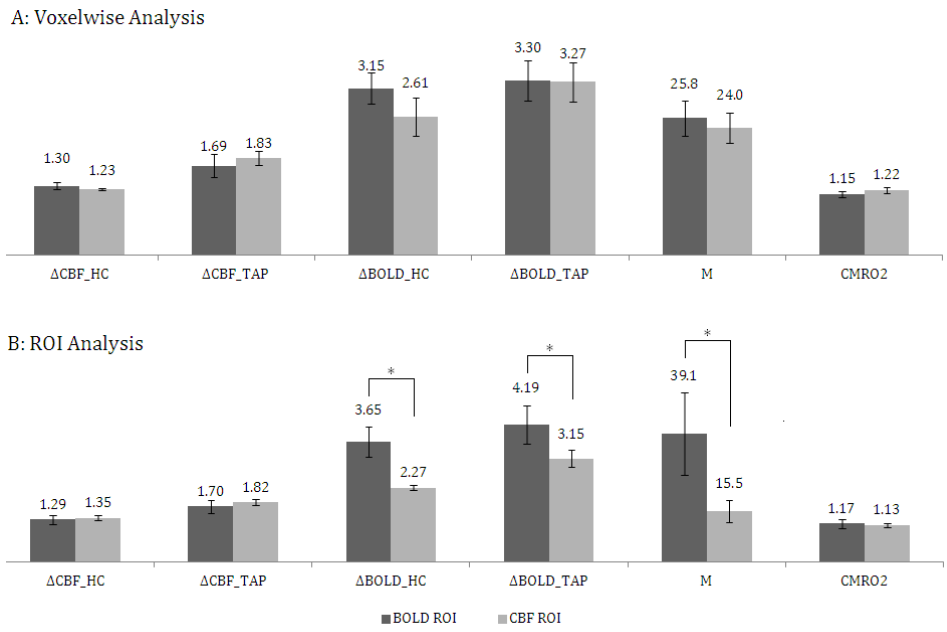

Figure 6-16: Subject averaged fractional CBF and percentage BOLD changes due to hypercapnia and finger tap, calibration constant M and $CMRO_2$ for (A) voxelwise and (B) ROI analysis. * represents significant difference between ROI values. Dark coloured bars are for the BOLD ROI and light gray bars are the CBF ROI. Error bars represent standard error across subjects.

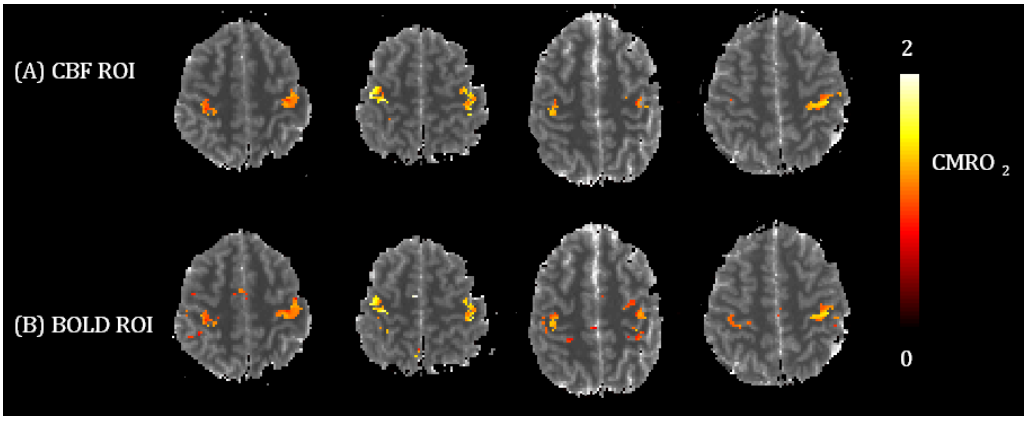

Figure 6-17: $CMRO_2$ maps overlaid onto equilibrium EPI images for the 4 subjects in the voxelwise analysis for both ROIs.

Figure 6-17 shows the $CMRO_2$ maps for the four subjects used in the voxelwise analysis overlaid onto their equilibrium EPI images. Voxelwise analysis has the benefit of showing local variation of $CMRO_2$ over the cortex.

6.4.3.3 Alternative Measures for M

As demonstrated in Figure 6-16, a large variation in M does not result in large variation in $CMRO_2$. As M requires a separate experiment to measure this parameter, in addition to a functional finger tap task, it is important to consider alternatives to M for calculating the $CMRO_2$ change. Figure 6-18 correlates

baseline CBF with the calculated value of M over the motor cortex for 4 subjects, defined from the CBF ROI. This demonstrates a positive correlation between M and CBF_0 over the CBF ROI (R^2 of fit, range of 0.4 – 0.66).

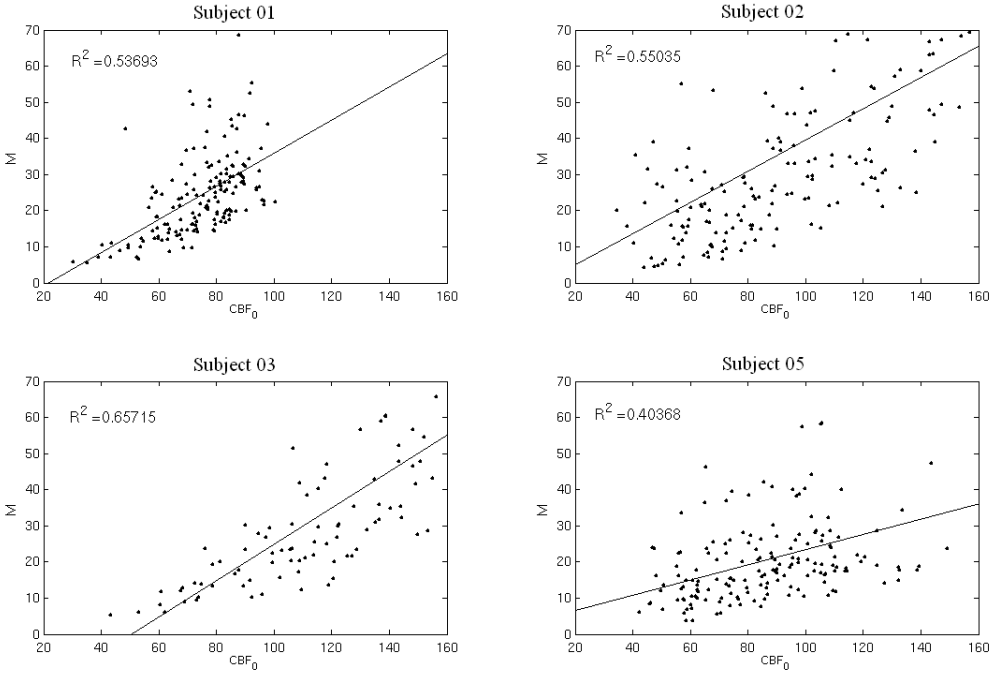

Figure 6-18: Voxelwise plot of M versus baseline CBF (CBF_0) for 4/5 subjects linear trendlines for the CBF ROI. R^2 values of fit displayed.

In the earlier discussion it was shown that as M increases, $CMRO_2$ does not increase greatly. Figure 6-19 shows how $CMRO_2$ varies with M, for small M $CMRO_2$ is quickly varying but tends towards an upper limit as M increases. If $\Delta S/(S_0\, M) \rightarrow 0$ then $CMRO_2$ tends to a limit only dependant on the evoked flow response to the finger tap. The experimental data, and the limit described in Equation 6-6, are shown in Figure 6-20. This shows that the $CMRO_2$ limitation model (Equation 6-6, red line) overestimates, but describes the data well.

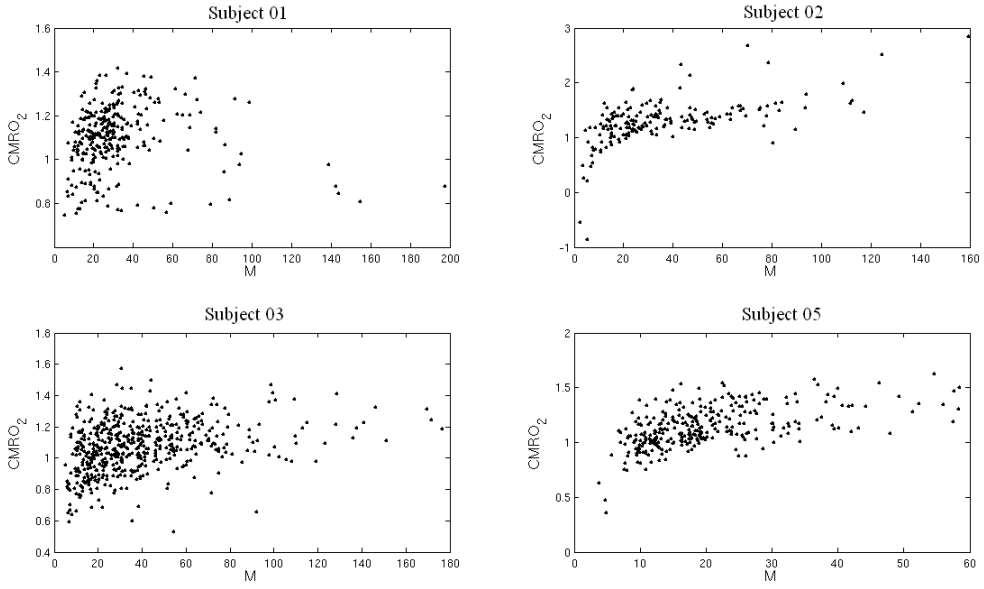

Figure 6-19: $CMRO_2$ as a function of M for the BOLD ROI (data from the 4 subjects shown).

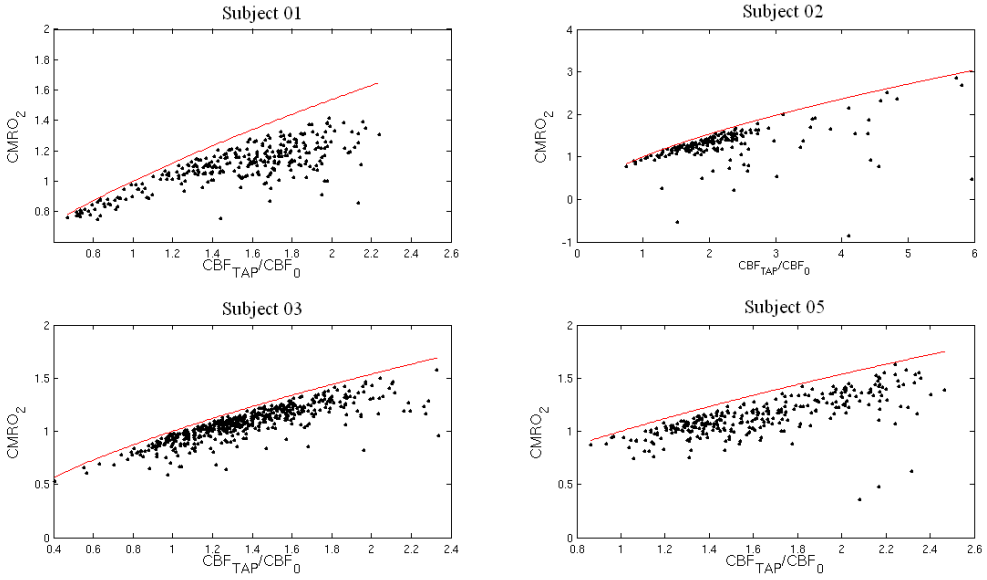

Figure 6-20: $CMRO_2$ as a function of the evoked CBF response to the finger tap for the BOLD ROI (black dots). Red line is the relationship given in Equation 6-6, (data from the 4 subjects shown).

6.4.4 DISCUSSION

Calibrated BOLD is a common technique used to estimate $CMRO_2$ through the measurement of BOLD and perfusion changes. With this technique, a hypercapnic challenge is used to determine the calibration constant, M. This technique has been widely used at 3 and 1.5 T, however few studies have performed calibrated BOLD at higher field strengths in humans. The aim of this experiment was to measure the perfusion change and transit time change using LL-EPI ASL due to hypercapnia and a motor task. These results were then used to determine M and

$CMRO_2$ changes using the Davis model at 7 T both on a voxelwise basis and using an ROI method that is typically performed.

An increase in cerebral perfusion and reduction in blood arrival time in response to the hypercapnic challenge was found, changes in both of these parameters were less than the response to the motor task. CBF reactivity was found to be 5 ± 1 % / mmHg and is comparable to that found by St Lawrence *et al.* (4 % / mmHg) [43] and Mark *et al.* (3 % / mmHg) [33]. BOLD CVR studies to hypercapnia have not been widely performed at 7 T. Driver *et al.* [5] measured R_2* reactivity at 7 T and 3 T, and found a factor of 2 increase between the CVR measures made at the two field strengths, from 0.066 s^{-1}/ mmHg to 0.141 s^{-1} / mmHg. BOLD CVR measures at 3 T have been found to be approximately 0.3 % / mmHg [33, 44]. As expected, this study found a higher BOLD CVR (0.56 ± 0.06 % / mmHg), a factor of 1.9 increase, due to the increased BOLD signal at 7 T.

The ROI calibrated BOLD analysis demonstrates a significant dependence of the results on ROI definition [45]. The BOLD ROI showed an increased measured BOLD change and a larger value of M compared to the CBF ROI. This is likely to be due to the inclusion of large veins in the BOLD ROI. The voxelwise analysis was less affected by the ROI as further discrimination of the individual voxel data is available – voxels that are largely veins or white matter will be excluded due to low hypercapnic CBF reactivity.

Voxelwise analysis produced maps of M, the Davis model calibration constant (Figure 6-14). This demonstrates that voxelwise analysis is feasible at 7 T and crucially it demonstrates that M varies over the brain. This highlights the fact that studies should measure M for the region under investigation and not average over entire grey matter or use an assumed value. There are no other reported measures of M at 7 T that can be compared with the values measured here (24 % voxelwise in the CBF ROI). However, it is known that M is largely variable across and within subjects. For example, Leontiev and Buxton measured M values ranging between 5 and 20 % at 3 T [45].

The large increase in M that was found for the BOLD ROI compared to the CBF ROI for the ROI analysis did not lead to a corresponding change in $CMRO_2$. Equation 6-6 demonstrates that $CMRO_2$ tends towards a limit, restricting the range $CMRO_2$ can take for large M as demonstrated in Figure 6-7. The final $CMRO_2$ value is then only dependant on the flow response to the motor task and the

constants α and β. Figure 6-7 A demonstrates that with a small BOLD response to the finger tap, the values of $CMRO_2$ are close to the limit even with smaller values of M. The closer values of $\Delta BOLD/M.BOLD_0$ are to 0, the closer that $CMRO_2$ is to the limiting value. Experimentally this was shown in Figure 6-20, where the upper limit expression of $CMRO_2$ was shown to describe the data well but overestimated.

This result is counter intuitive as it is expected that as M increases there is a corresponding increase in the evoked BOLD response such that $\Delta BOLD/M.BOLD_0$ does not tend towards 0. For voxels that are predominantly white matter, the BOLD and flow changes due to hypercapnia and the functional task will be low, equally for veins the BOLD response to hypercapnia will be high, but the flow response will be low ($\sim$ 1), so both white matter and veins are removed in the voxelwise analysis due to low CBF response to hypercapnia. The remaining voxels should be cortical grey matter but there is still a mismatch between M and evoked BOLD. Large M arises from a large BOLD response to hypercapnia coupled with a small flow response, then a relatively small BOLD response to the functional challenge to cause $\Delta BOLD/M.BOLD_0$ to tend to 0.

The relationship in Equation 6-6 shows that $CMRO_2$ is independent of the hypercapnia measurements; the voxelwise analysis was interrogated further to assess the dependence of M on basal CBF (Figure 6-18). Figure 6-18 suggests a positive correlation between M and CBF_0. If the average linear relationship between M and CBF_0 was used to estimate M and hence $CMRO_2$, the value for $CMRO_2$ would be 1.17 ± 0.07 which corresponds well with the other results (1.13 – 1.22). The origin of this dependence on M with basal CBF can be interrogated by taking the Taylor series of M as a function of $f_{HC} = CBF_{HC} / CBF_0$ about a value of 1.2;

$$M_{Taylor} = M(f_{HC} = 1.2) + \left.\frac{dM}{df}\right|_{f_{HC}=1.2} \cdot (f_{HC} - 1.2) + \left.\frac{d^2M}{df^2}\right|_{f_{HC}=1.2} \cdot (f_{HC} - 1.2)^2 \qquad \textbf{6-7}$$

Assuming that α = 0.38, β = 1, that $(f_{HC} - 1.2)^2 \sim 0$ and that $CBF_{HC} - CBF_0 = \delta$, where δ is independent of CBF_0 (approximated from experimental data), it can be shown that

$$M_{Taylor} \approx 17.6BOLD_{HC} - \frac{40.39BOLD_{HC}\delta}{CBF_0} \qquad \textbf{6-8}$$

where $BOLD_{HC}$ is the % BOLD change due to hypercapnia. Figure 6-21 shows graphs of this relationship as a function of CBF_0, for different values of $BOLD_{HC}$ and δ. This demonstrates a relationship that has linear sections for higher CBF_0 values.

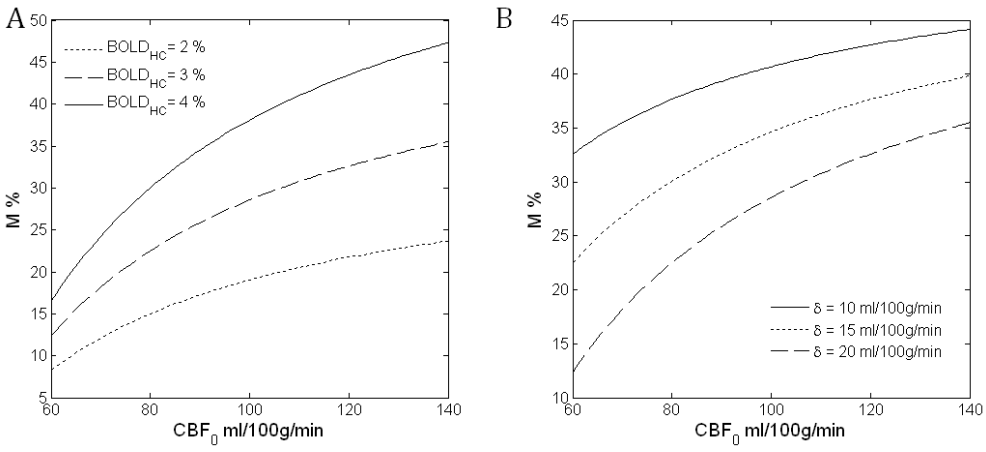

Figure 6-21: Taylor series approximation for the relationship between M and CBF_0, with variable (A) BOLD response to hypercapnia with δ = 20 ml/100g/min and (B) δ, the absolute flow increase due to hypercapnia with $BOLD_{HC}$ = 3 %.

Further consideration of this relationship should be investigated, as if M could be approximated by CBF_0 this would simplify the experiment time. In addition, the functional task (e.g. motor) could be extended to ensure high SNR in the CBF measurements. This would make calibrated BOLD a more flexible technique for general use and for example for the study of longer fMRI tasks (e.g. cognitive) or in the study of patients where movement can significantly affect data quality.

6.4.5 CONCLUSION

This experiment has shown the marked effect of hypercapnia on cerebral blood flow and the BOLD effect at 7 T. These characteristics have been used in the Davis model to estimate the $CMRO_2$ increase due to a simple finger tapping task. Through the standard ROI analysis and then voxelwise analysis it was shown that ROI definition can have significant effect on BOLD and M measurements but does not impact greatly upon $CMRO_2$ [45].

Voxelwise analysis was seen to be more robust to ROI choice as further discrimination can be applied to reduce the impact of large vessels in the ROI. Voxelwise analysis allows for further interrogation of the relationship between the underlying physiological measurements and the metrics of the Davis model. This analysis demonstrated that M does not greatly impact $CMRO_2$ measures and

further experiments are required to probe the feasibility of Davis model calibrated BOLD without hypercapnia measures. This would reduce experiment time, giving greater flexibility in the effects being investigated.

6.5 THE EFFECT OF HYPERCAPNIA ON MEG SIGNALS

The Davis model assumes that hypercapnia is isometabolic allowing for M to be calculated by only measuring BOLD and CBF (Equation 6-4) as demonstrated in the first experiment. However recent work by Zappe *et al.* [24] demonstrated that hypercapnia caused a reduction in multi-unit activity measured with invasive electrophysiology in anaesthetised monkeys. They hypothesised that this reduction could be suggestive of a $CMRO_2$ change with hypercapnia. The following experiment was designed to investigate whether this is true in humans.

Non-invasive measurement of human neuronal activity can be performed using electroencephalography (EEG) or magnetoencephalography (MEG). In the following study, MEG is used for assessment of neuronal activity. This was because the MEG system has more channels (275 compared to 64 in the available EEG system) and higher signal-to-noise. EEG is also further complicated by the inhomogeneous conductivity across the skull/scalp distorting the electric field produced by neurons; this makes source localisation in EEG more difficult [46].

6.5.1 MEG INSTRUMENTATION

The MEG system uses superconducting loops to pick up the weak currents produced by the small neuromagnetic fields. These pick up coils are coupled to super-conducting quantum interference devices (SQUIDs) to produce a voltage output proportional to the current flowing in the pick up coil [46], schematically represented in Figure 6-22. An array of these detectors are used to give whole head coverage.

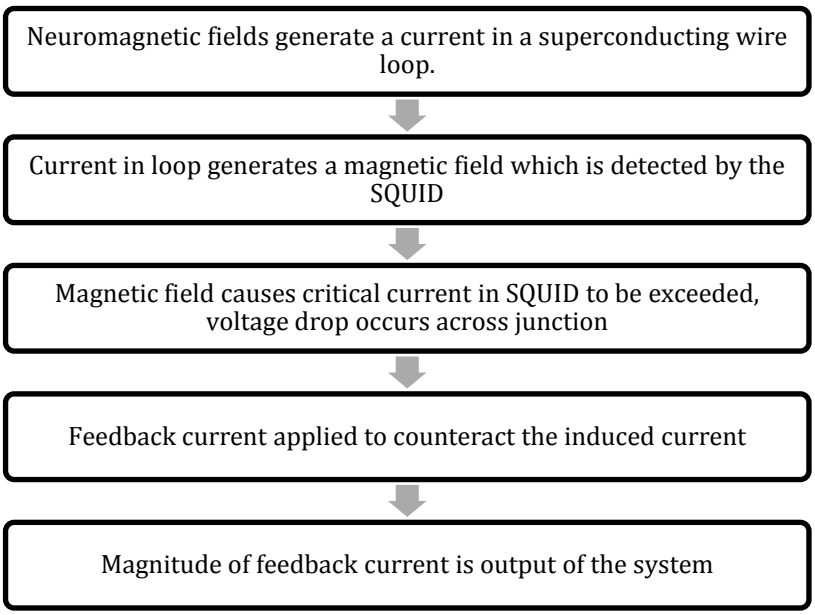

Figure 6-22: Schematic flow chart of MEG detection of neuronally generated magnetic fields, adapted from [46].

As the neuronally generated magnetic field is very small (fT) compared to environmental magnetic noise (e.g. from computers and other lab equipment) MEG scanners are housed within magnetically shielded rooms to reduce interference. The shielded rooms are made from materials of high magnetic permeability (mu-metal – a nickel-iron alloy) to reduce static field noise, and aluminium to reduce eddy current magnetic fields. To stop the introduction of noise within the shielded room subject's need to remove any metal as this can create magnetic fields if it moves (e.g. with breathing).

Furthermore, gradiometers are used to remove background magnetic field contributions, as the brain's magnetic field will fall off quickly a few centimetres from the head ($1/r^2$ dependence) – whereas other sources of magnetic field are likely to originate further away and will be approximately constant across the detector coil. First-order gradiometers have two loops of wire connected in series but wound in opposite directions. These will produce two equal but opposite current for magnetic fields that are constant between the two loops, cancelling out the effect.

The MEG data are dominated by neural oscillatory effects characterised by rhythmic electrical activity in cell assemblies. These signals can be broken down into specific frequency bands; these bands are associated with different activities or states, summarised in Table 6-3.

Name	Frequency	Information
Delta, δ	< 4 Hz	Most pronounced during deep sleep
Theta, θ	4 – 8 Hz	Associated with sleep, and cognitive processing (e.g. [47])
Alpha, α	8 – 13 Hz	Most pronounced in awake relaxed subjects, interrupted by stimulation (e.g. visual, motor)
Beta, β	13 – 30 Hz	Predominantly associated with motor cortex
Gamma, γ	30 – 100 Hz	Predominantly associated with visual cortex

Table 6-3: Characteristic frequency bands, adapted from [48].

The MEG data are acquired in *sensor space* by detectors placed around the scalp and ideally need the measurements to be transformed into *source space* (i.e. in the brain) for interpretation. There are a number of different methods of source space projection; here a scalar beamformer is employed. For the scalar beamformer (e.g. [49, 50]) the strength of a source, y, at a particular location and orientation, $\boldsymbol{\theta}$, and point in time, t, is given by a weighted sum of measurements ($\boldsymbol{x}$) from the MEG sensors,

$$y_\theta(t) = \boldsymbol{W}^T(\boldsymbol{\theta}).\boldsymbol{x}(t). \qquad \textbf{6-9}$$

The weights, $\boldsymbol{W}$, are derived from the lead fields, $\boldsymbol{L_\theta}$, a measurement of the sensitivity of each MEG sensor to a current source at location and orientation $\boldsymbol{\theta}$ and the covariance matrix, $\boldsymbol{C}$, of the measured data [48], (superscript T represents matrix transpose).

$$\boldsymbol{W^T}(\boldsymbol{\theta}) = \frac{\boldsymbol{L_\theta^T C^{-1}}}{\boldsymbol{L_\theta^T C^{-1} L_\theta}} \qquad \textbf{6-10}$$

The current orientation is determined based on a non-linear search for maximum signal-to-noise. By using Equation 6-9 at each point in time, a timecourse of source strength can be found. Such timecourses will contain many independent signals from the different frequency bands. Hence band pass filters are applied to interrogate specific frequency bands, the main bands are given in Table 6-3. When looking at stimulus induced changes, the analytic signal can be used to form the envelope of an oscillatory signal. The envelope is calculated as

$$E(t) = \sqrt{(y_\theta(t))^2 + (H(y_\theta(t)))^2} \qquad \textbf{6-11}$$

where E is the envelope of the signal, H indicates the Hilbert transform [48]. Figure 6-23 demonstrates the envelope derived from the analytic signal of a

simulated oscillatory signal. This allows for calculation of amplitude changes in the signal due to a stimulus. For example in a motor task a reduction in beta power is expected, corresponding to a stimulus induced decrease in the beta band envelope.

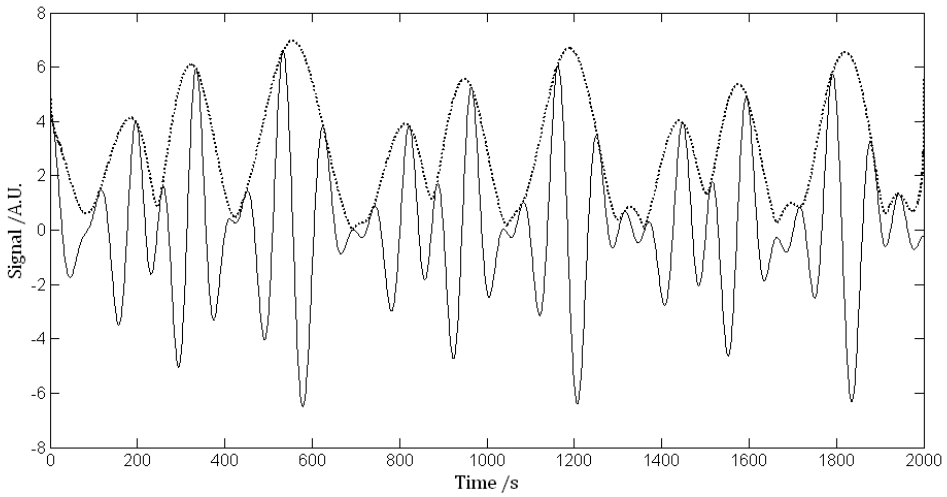

Figure 6-23: Example of the signal envelope derived from Hilbert transform, signal (solid line) and envelope (broken line) shown.

6.5.2 EXPERIMENTAL METHOD

Six healthy subjects (4 male, age range 24 – 33 years) took part in the study which was approved by the University of Nottingham Medical School Ethics Committee. All subjects gave informed, written consent.

MEG Acquisition: MEG data were acquired using the synthetic third order gradiometer configuration of a 275-channel CTF MEG system (*MISL, Port Coquitlam, BC, Canada*), at a sample rate of 600 Hz and with a 150 Hz anti-aliasing hardware filter.

The location of the subject's head within the MEG system was measured before and after each experiment by energising electromagnetic coils placed at 3 fiducial points on the head (nasion, left preauricular and right preauricular). Prior to data acquisition, the positions of these coils on the subject's head were measured using a 3D digitiser (*Polhemus isotrack*). An MPRAGE structural image was acquired on a Philips Achieva 3 T MRI scanner (1 mm^3 isotropic resolution, 256 x 256 x 160 matrix size, TE/TR/TI = 3.9/8.3/960 ms, FA = 8°, shot interval = 3s, and SENSE factor = 3). The locations of the fiducial markers and MEG sensors with respect to the brain anatomy was determined by matching the digitised head surface to the head surface extracted from the structural MRI.

Experimental Paradigm: The RespirAct™ (*Thornhill Research Inc, Toronto, Canada)* was used for end-tidal targeting [34]. Three experiments were performed during which $P_{ET}O_2$ was targeted to remain constant:

Experiment 1: Subjects were instructed to fixate their eyes on a dot. The gas challenge comprised an initial 2 minute period of baseline (defined as each subject's resting $P_{ET}CO_2$), followed by 3 cycles of 2 minutes of hypercapnia ($P_{ET}CO_2$ level raised to baseline + 10 mmHg) and 2 minutes of baseline. The total duration of this experiment was 14 minutes.

Experiment 2: Subjects fixated on the dot during a second gas challenge which comprised an initial 1 minute of baseline followed by 2 cycles, each comprising 2 minutes of hypercapnia (baseline + 10 mmHg) and 5 minutes of baseline. The total experimental duration was 15 minutes. Experiment 2 was used to investigate the recovery of the MEG signal after hypercapnia.

Experiment 3: Here, the gas challenge was identical to Experiment 1, but during the experiment the subject was presented with a visual stimulus and performed a motor task. The visual stimulus was a drifting sinusoidal grating (3 cycles/degree; 8 Hz drift rate; Michelson contrast of 1; shown in Figure 6-24) presented in a circular window which was central in the visual field (visual angle 6 degrees). A single trial comprised 5 s of visual stimulation followed by 5 s of rest during which the subjects viewed the fixation dot. Subjects were instructed to press a button using the index finger of their left hand (motor response) immediately after cessation of the visual stimulus.

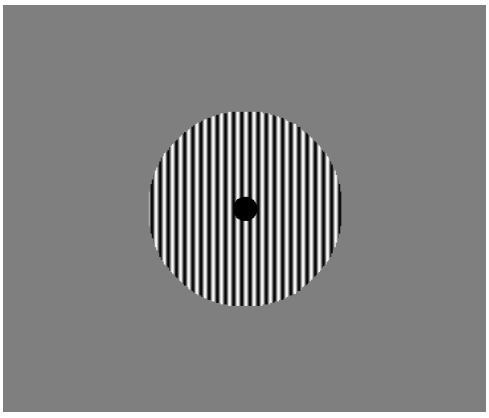

Figure 6-24: Visual stimulus used in Experiment 3.

Experiments 1 and 3 were performed in the same session on all 6 subjects. Experiment 2 was carried out in 5 of the 6 subjects in a separate session three

weeks later to further investigate the timecourse of changes in neural oscillatory activity induced by hypercapnia.

Data Analysis

RespirAct™ data: End tidal RespirAct™ data were used to quantify the average $P_{ET}CO_2$ and $P_{ET}O_2$ change between hypercapnia and baseline.

In order to assess the effect of hypercapnia on reaction time, the time between stimulus cessation and the button press was calculated for each subject.

MEG data: Raw MEG data were visually inspected and trials with excessive noise were discarded. DC offsets were removed on a trial-by-trial basis and data filtered into frequency bands of interest: theta (4 – 8 Hz), alpha (8 – 13 Hz), beta (13 – 30 Hz) and low gamma (30 – 50 Hz). For all three experiments, data were processed using an adaptive beamformer [50-54]. The output comprises a timecourse estimate of electrical activity at the location specified, and sequential application to all voxels yields a set of timecourses that can be further analysed to create volumetric images of change in electrical activity (e.g. [55]). Covariance matrices were regularised as described previously [50]. This algorithm yields accurate source localisation across a large brain volume, but has also been shown to be an excellent means to attenuate channel level interference in MEG signals caused by environmental magnetic noise.

Experiments 1 and 2

The beamformer was used to produce images of the change in spontaneous neural oscillatory activity due to hypercapnia. A pseudo-T-statistical (~~T~~) approach was employed in which the oscillatory amplitude in an active time window (hypercapnic periods) was contrasted with that in a control time window (normocapnic periods),

$$\mathcal{T}_\theta = \frac{y_\theta^a - y_\theta^c}{v_\theta^a + v_\theta^c} \qquad \textbf{6-12}$$

where y is the source power, and v the noise, a is the active window (hypercapnia) and c the control window (normocapnia) [50].

The number of samples in the active and control periods were equal to ensure no bias between measurements [56]. Covariance matrices were regularised with a

value of 4 times the minimum singular value of the unregularised matrix. Voxels were placed on a regular 5 mm grid spanning the entire brain.

For each voxel, the timecourse of electrical activity was derived; its associated Hilbert envelope was also computed. The mean envelope amplitude in the active and control windows was then computed and the difference normalised by the control value. This was computed for all voxels, and independently for each frequency band. For each frequency band the statistical significance of frequency change was assessed using a Monte Carlo technique [47, 57, 58] in which 50 'fake' pseudo-T statistical images were calculated with active and control windows randomly switched. Voxels were identified as having statistically significant changes in oscillatory amplitude if they fell in the upper 5^{th} percentile of T-values computed in the randomised images. These maps, which depict change in oscillatory activity induced by hypercapnia, are termed *reactivity maps*. Each subjects' MR image was co-registered to MNI space using FLIRT (FSL, Oxford) and the transform applied to the reactivity maps, which were then averaged across subjects.

Following computation of average reactivity maps, three brain locations were further investigated. The first (location 1) was the voxel with peak value in the beta band reactivity maps, location 2 was in the visual cortex (based on the location of visual activation found in Experiment 3) and chosen specifically to draw direct comparisons with the work of [24] and location 3 was in the medial frontal area (MNI [-2 36 32] mm, an area associated with cognitive processing in working memory [47]). MEG data were frequency filtered into the following 17 frequency bands; 1 – 4, 2 – 6, 4 – 8, 6 – 10, 8 – 13, 10 – 15, 13 – 20, 15 – 25, 20 – 30, 25 – 35, 30 – 40, 35 – 45, 40 – 50, 45 – 55, 50 – 60, 55 – 65 and 60 – 80 Hz. Weights were constructed independently in each band for the three brain locations and the Hilbert envelope was derived for each band. Hilbert envelopes were averaged across hypercapnic and normocapnic periods yielding two spectra, the difference between which gives the change in neural oscillatory amplitude due to hypercapnia as a function of frequency. These spectra were averaged across subjects and significant differences between normocapnia and hypercapnia tested using a non-parametric Wilcoxon signed rank test.

To assess dynamic changes the data were filtered in the 8 – 40 Hz band (based on results presented below), and the Hilbert envelope at location 1 computed and

down-sampled to an effective temporal resolution of 1 s to increase its signal-to-noise ratio. Timecourses of the evolution of oscillatory amplitude across the experiment were then averaged across subjects.

Experiment 3

MEG data recorded during Experiment 3 were initially processed using a standard commercial implementation of synthetic aperture magnetometry (SAM) (*MISL, Port Coquitlam, BC, Canada*), a scalar beamformer technique widely used in MEG studies [50, 55]. Pseudo-T statistical images were computed [55] localising the induced changes in oscillatory power due to both the visual stimulus and the button press. To localise visual effects, the active window was defined as 0.5 – 4.5 s with respect to trial onset and the control window as 5.5 – 9.5 s with respect to trial onset. To localise motor effects, the active window was 0 – 0.75 s following the button press whilst the control window was 2 – 2.75 s following the button press. A regularisation value of 2 was used for weghts calculation for both stimuli, including a regularisation factor increases the signal to noise but also increases the spatial smoothness of the data [50]. Data were processed in the 30 – 50 Hz, 50 – 70 Hz and 70 – 90 Hz bands to localise visual cortex activity whilst beta band filtered data were used to localise the motor areas. Resulting images, termed *functional maps*, were subsequently transformed to MNI space and averaged across subjects.

Locations of interest in visual and motor cortices were derived from peaks in the functional maps and Hilbert envelope data computed for each location in the frequency bands used above. Trials were divided into two sets, those in which the stimulus was presented during hypercapnia, and those in which the stimulus was presented during normocapnia. For each dataset, data within each trial were divided into active and rest time periods (for visual analysis the active period was taken as 0.5 – 4.5 s and the control was 5.5 – 9.5 s; for motor analysis the periods were 5 – 6 s and 7.5 – 8.5 s respectively).

For both hypercapnia and normocapnia, the average change in oscillatory amplitude between the active and control periods was computed to give absolute change in mean amplitude, this was then normalised by the control value to give % change in mean amplitude due to the stimulus under the two conditions. These values were then averaged across subjects and significant differences between normocapnia and hypercapnia assessed using a Wilcoxon sign rank test. The

average timecourse of the Hilbert envelope in the 8 - 25 Hz frequency band was also computed for hypercapnic and normocapnic trials. Finally the visual evoked response (from the peak in visual cortex) was analysed by filtering the data in the 1 – 40 Hz band. Beamformer timecourse estimates (without Hilbert envelope computation) were averaged across hypercapnic and normocapnic trials.

6.5.3 RESULTS

The average step in $P_{ET}CO_2$ for all three experiments was 7 ± 1 mmHg (average and standard error across both experiments and all subjects); $P_{ET}O_2$ increased from 111 ± 4 mmHg to 115 ± 4 mmHg between hypercapnia and baseline.

No significant difference (470 ± 40 ms at normocapnia, 490 ± 70 ms at hypercapnia) was found in reaction time between hypercapnic and normocapnic trials.

Figure 6-25 shows the group average reactivity maps depicting percentage change in the alpha, beta and low gamma (30 – 50 Hz) bands due to hypercapnia for Experiment 1 (A, B and C) and Experiment 2 (D, E and F). Widespread loss in mean oscillatory amplitude was observed in all three frequency bands.

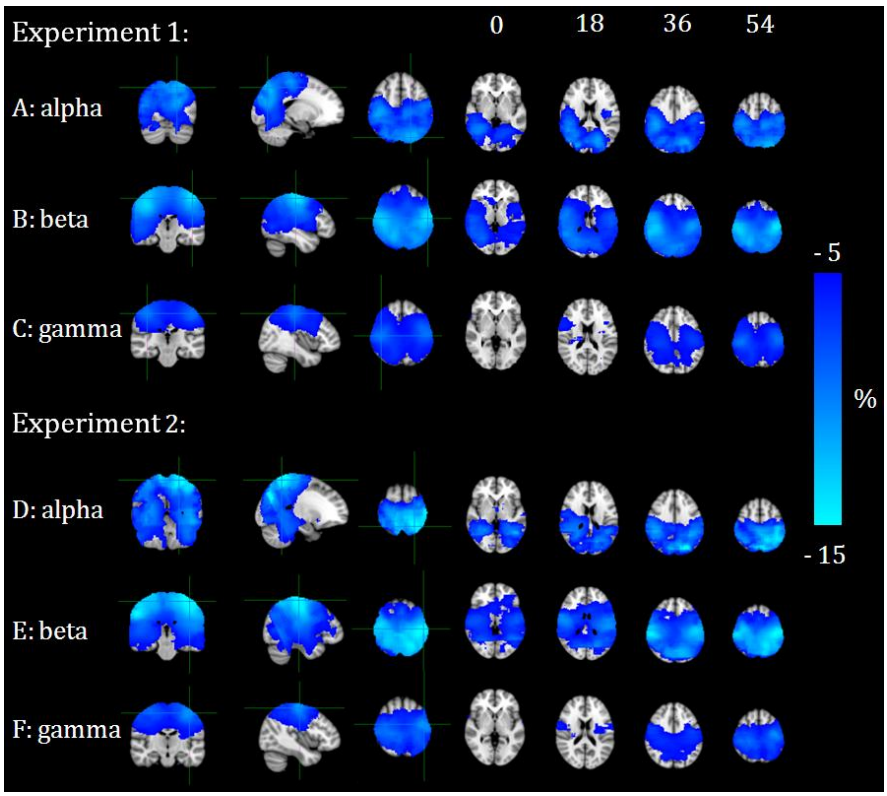

Figure 6-25: % Change in spontaneous MEG signals for Experiment 1 (A-C) and Experiment 2 (D - F).

	Experiment 1		*Experiment 2*	
	MNI	% Change	MNI	% Change
Alpha	[-18 -74 50]	-13 ± 4	[-22 -54 66]	-16 ± 4
Beta	[-46 -22 56]	-14 ± 2	[-42 -24 62]	-15 ± 2
Low Gamma	[40 -24 54]	-10 ± 1	[-40 -16 60]	-11 ± 3

Table 6-4: MNI positions of peaks in the reactivity maps for Experiments 1 and 2, with corresponding signal changes. Change expressed as % with respect to normocapnia, mean ± standard error across subjects.

Alpha band changes were most apparent across the posterior parietal and occipital regions, including the medial and lateral visual areas, MNI coordinates of peaks are shown in Table 6-4. Beta band changes are most apparent in sensorimotor regions with areas of significant change spanning the sensorimotor strip and posterior parietal areas. Significant gamma band changes were less widespread and appeared more focal to the hand area of the sensorimotor.

Figure 6-26 A shows the frequency characteristics of change in neural oscillatory activity in response to hypercapnia for: 1) the position of peak change in beta power in the sensorimotor cortex from Experiment 1 (MNI [-46 -22 56] mm) (blue); 2) the primary visual cortex (MNI [-8 -80 -6] mm) derived from the visual stimulus data in Experiment 3 (red) and 3) the medial frontal cortex (MNI [-2 36 32] mm [47]) (green). In location 1 significant power loss is observed in the 8 – 60 Hz band, with highest power loss being found at 20 Hz. Location 2 demonstrates significant power loss in the 8 - 30 Hz band with the peak at 10 Hz. Changes were smaller in the location 3 as expected from the images shown in Figure 6-25, but significant power loss was observed in the alpha, high beta and gamma range. Interestingly a significant increase in theta power was also observed in medial frontal cortex.

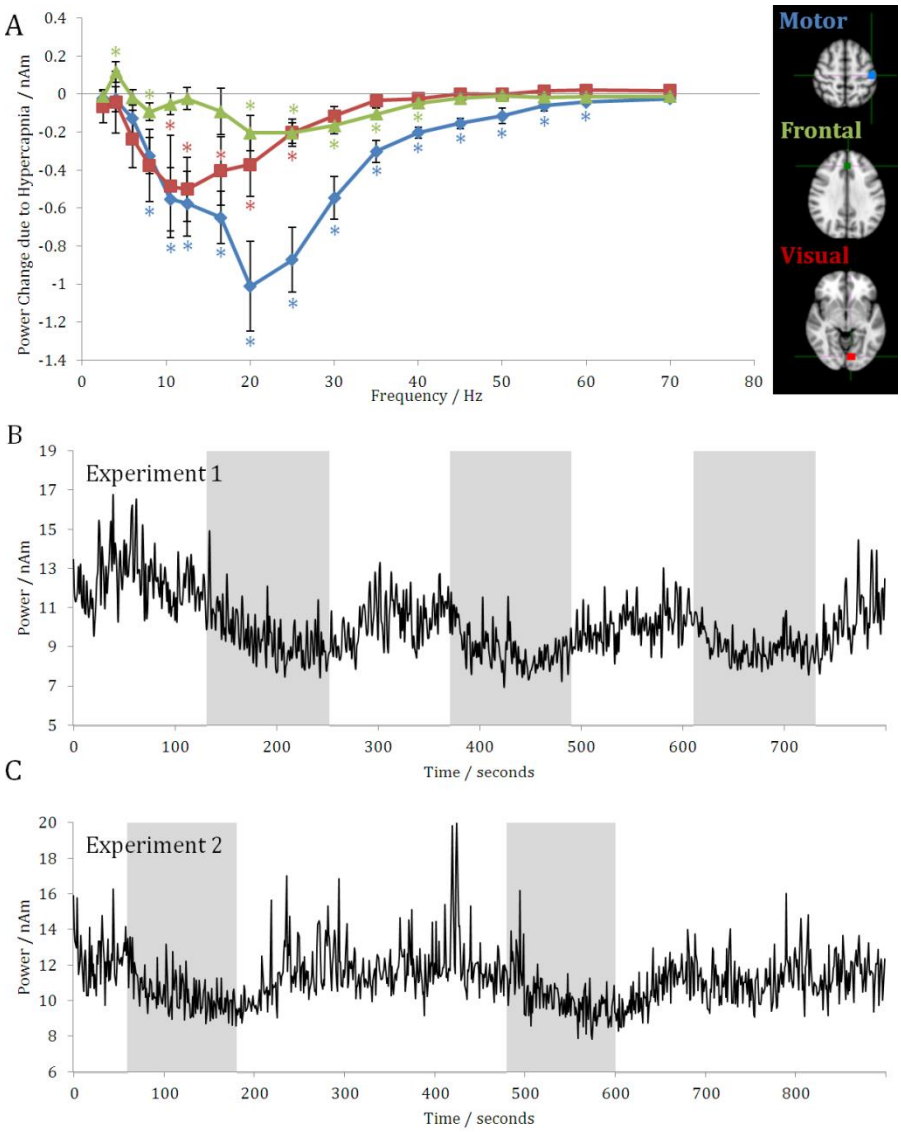

Figure 6-26 (A) Power change due to hypercapnia at 3 brain locations, * indicates significant power change (P < 0.05) (B) Timecourse in 8 - 40 Hz for Experiment 1 (C) Timecourse in 8 - 40 Hz for Experiment 2. Shaded areas indicate the periods of hypercapnia.

Figure 6-26 B shows the group average time evolution of oscillatory amplitude in the 8 - 40 Hz frequency band across the duration of Experiment 1 extracted from the location of maximum beta band power change. Figure 6-26 C shows the equivalent timecourse for Experiment 2. Figure 6-26 C also shows a significant delay of approximately 100 s in the recovery of the MEG signal to baseline following hypercapnia

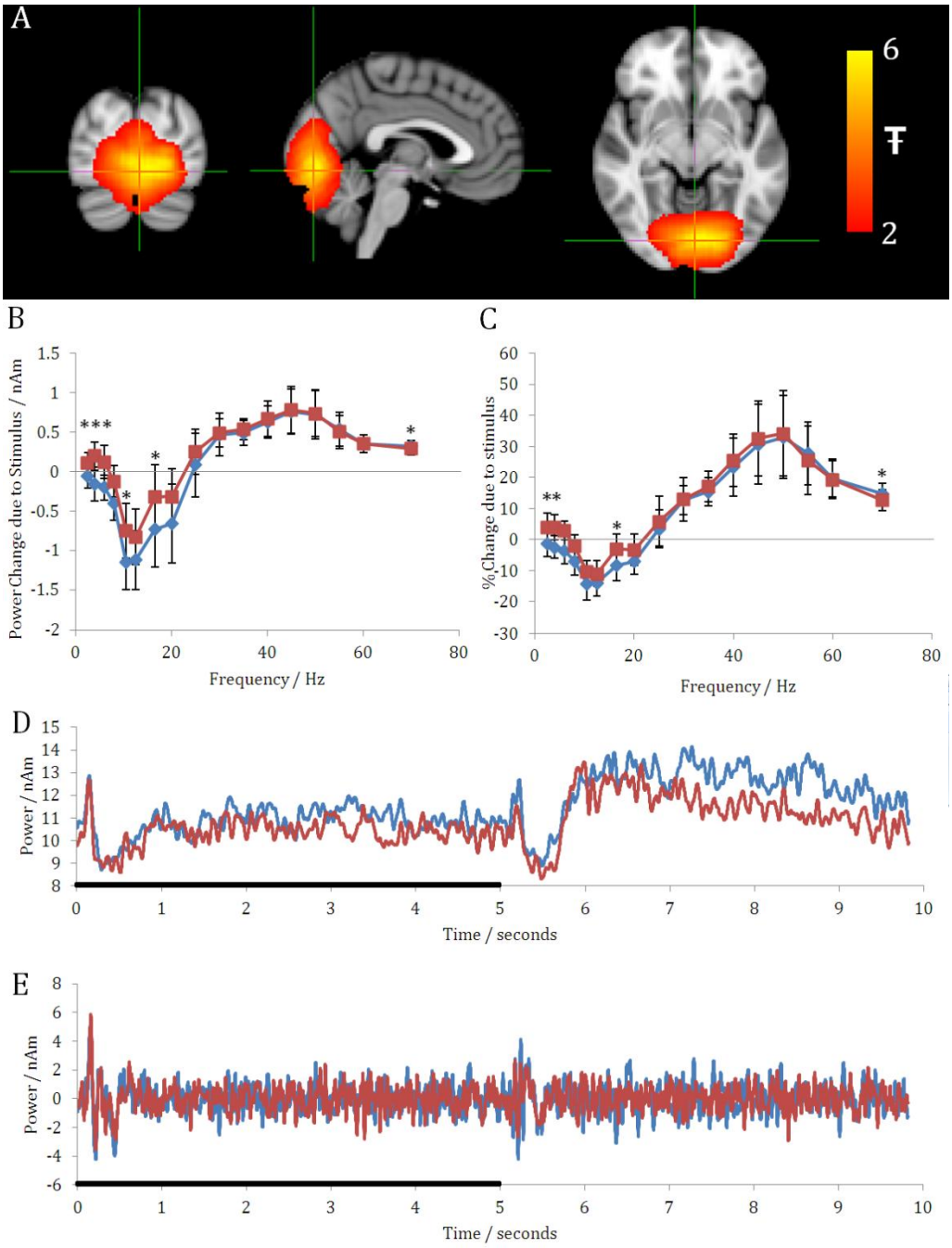

Figure 6-27 (A) Group average pseudo T-statistic images for the visual stimulus (B) Power change due to stimulus at hypercapnia (red ■) and normocapnia (blue ♦) (C) % change due to stimulus (D) Time course in 8 – 25 Hz range, thick black line indicates stimulus (E) Visual evoked response. All averaged across subjects. * Indicates significant difference between hypercapnia and normocapnia. Error bars represent standard error across subjects.

Figure 6-27 A shows the group averaged functional map showing the location of change in gamma oscillations (30 Hz – 50 Hz range) due to visual stimulation. Functional maps are overlaid onto the standard brain and the MNI coordinate for the peak pseudo T-statistic in the group average map is [-8 -80 -6] mm. Figure 6-27 B shows the absolute power change and C the corresponding percentage change in amplitude due to visual stimulation at normocapnia (blue) and

hypercapnia (red) plotted as a function of frequency. In both cases, a characteristic increase in gamma oscillations accompanied with a loss in amplitude in the lower frequency bands can be seen in response to the visual stimulus. Although the percentage change in oscillatory amplitude due to visual stimulation is similar for normocapnia and hypercapnia (C), hypercapnia reduced the visual induced change in low frequency (alpha and beta band) oscillations.

Figure 6-27 D further characterises this effect by showing the Hilbert envelope, computed in the 8 – 25 Hz range, for the average stimulus cycle for normocapnia and hypercapnia. During the rest period (7 – 10 s), the average oscillatory amplitude in the visual cortex was 13 ± 1 nAm for normocapnia and this fell to 11 ± 1 nAm for the hypercapnic trials (mean ± standard error across subjects) ($P < 0.03$), consistent with results of Experiment 1 (Figure 6-26 A). Despite this baseline change, the oscillatory amplitude following stimulus onset (0.3 s to 0.8 s window) falls to the same level for normocapnic (9.6 ± 0.7 nAm) and hypercapnic (9.3 ± 0.5 nAm) trials (no significant difference across subjects). Figure 6-27 E shows the visual evoked response, averaged across all normocapnic (red) and hypercapnic (blue) trials. It is worth noting that no significant differences were observed in the evoked response between normocapnia and hypercapnia.

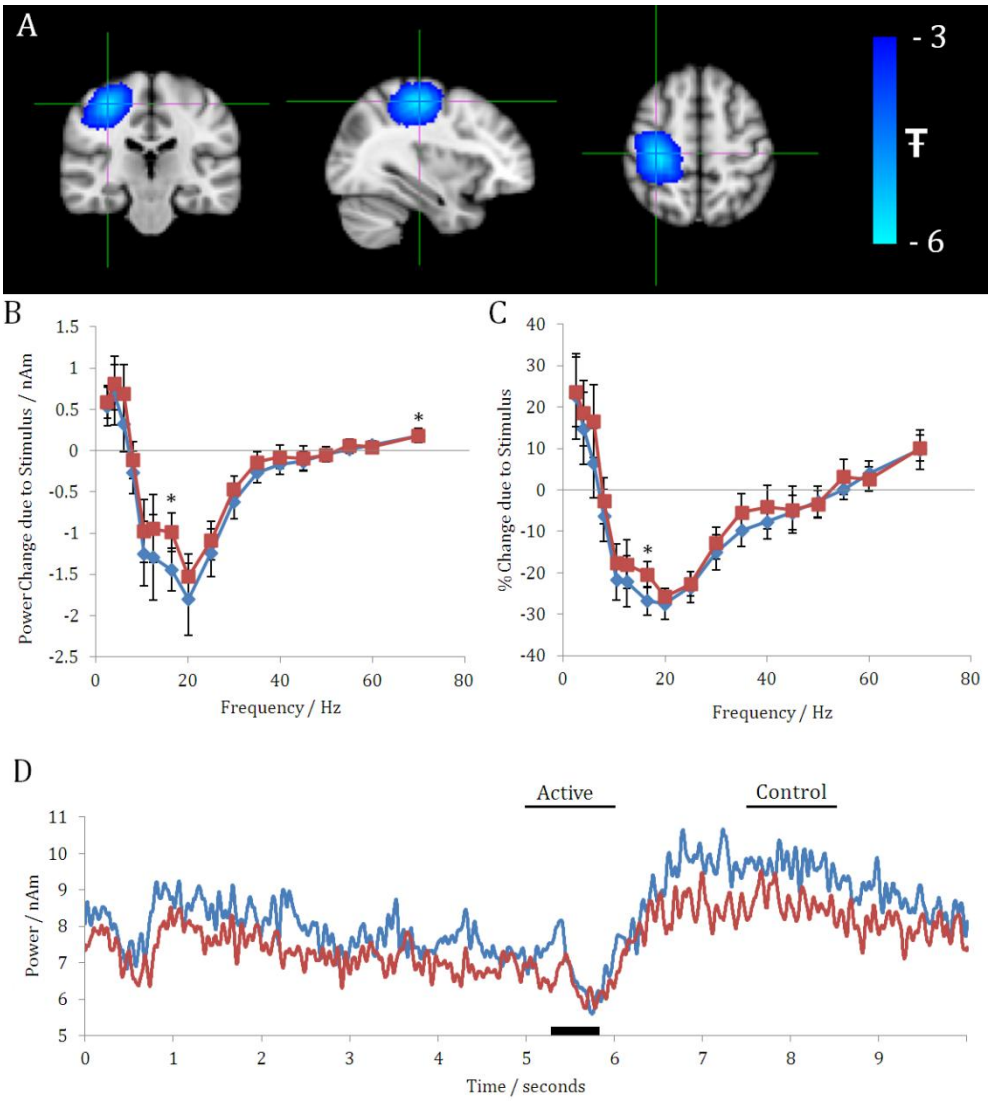

Figure 6-28 (A) Group average pseudo-T statistic image of the response to the button press (B) Power change due to stimulus at hypercapnia (red ■) and normocapnia (blue ♦) (C) % change due to stimulus (D) Timecourse in 8 - 25 Hz range, thick black line indicates time of button press, timing of active and control windows also shown. All averaged across all subjects. Error bars represent standard error across subjects.

Figure 6-28 A shows the group average functional map depicting the spatial distribution of loss in beta power in response to the button press. As expected, the left hand button press induced the largest change in the right primary motor cortex (average MNI coordinate [34 -24 54] mm). Figure 6-28 B shows the absolute change and Figure 6-28 C the corresponding percentage change in oscillatory amplitude due to the finger movement at normocapnia (blue) and hypercapnia (red). Characteristic loss in beta band oscillations due to the button press is clearly evident in both cases. Again, some difference was observed between normocapnia and hypercapnia; this difference is accentuated in the absolute values compared to percent change values and this agrees with findings in the visual cortex. Figure 6-28 D shows the Hilbert envelope (8 – 25 Hz band)

with a clear desynchronisation at the time of the button press (~ 5 s). Again the effect of hypercapnia can be observed with the average oscillatory amplitude (8 - 25 Hz) in the 7 - 10 s time window being significantly reduced ($P < 0.03$ computed across subjects) from 9 ± 1 nAm for normocapnia to 8 ± 1 nAm for the hypercapnic trials. In agreement with the visual task, despite the change in baseline values, the oscillatory amplitude falls to the same value in response to the button press (6.2 ± 0.6 nAm for normocapnia and 6.1 ± 0.4 nAm for hypercapnia computed between 5.4 s and 5.8 s, no significant difference across subjects).

6.5.4 DISCUSSION

This experiment has shown that a hypercapnic stimulus causes significant and widespread changes in the level of spontaneous neural oscillations in a number of frequency bands, in agreement with previous studies [24, 28, 30, 59]. The changes in neural oscillations induced by hypercapnia are spatially specific, with the spatial pattern changing as a function of frequency band. Also, despite a difference in resting state baseline, the absolute oscillatory amplitude immediately following visual or motor events is unaffected by $P_{ET}CO_2$.

The reduction in oscillatory amplitude during hypercapnia was highly robust, exhibited by its repeatability across subjects and between Experiments 1 and 2. The spatial distribution of desynchronisation was predominantly bilateral with the greatest effects in the parietal and occipital lobes. The largest beta band effects were close to the hand area of sensorimotor cortices which could be due, in-part, to the predominance of beta oscillations in these regions. The alpha shift was highest in the occipital lobe, which again could again be because the largest alpha signals originate in this region.

The precise cause of the desynchronisation observed in response to hypercapnia remains unknown. Zappe *et al.* [24] suggested a pH decrease caused by hypercapnia could affect neuronal excitability and therefore be responsible for the reduction in spiking and LFP activity. Participants reported an acidic taste due to the CO_2 which is likely to have activated sensory areas. This effect would implicate sensory cortices; however this effect would be expected to induce maximal effects in the insula and inferior areas of somatosensory cortex which was not the case in the reactivity maps. Another possible explanation could result from the subject's awareness of the hypercapnia (e.g. taste, increased heart rate,

or need to breathe deeply). Beta desynchronisation in the motor network is not only associated with movement, but also with the intention to move (e.g. [60]). If, during unpleasant periods of hypercapnia, subjects contemplated movement (for example, removal of the mask) this might explain some of the effects observed.

Another finding is that following hypercapnia-induced oscillatory power loss, the signal took ~ 100 s to return to baseline. The $P_{ET}CO_2$ stimulus was a square wave and hence cannot explain the protracted recovery observed in this study. This slow recovery of the oscillatory amplitude should be a topic for future investigation.

The motivation for Experiment 3 was to assess the effect of hypercapnia on stimulus induced changes in neural oscillations in the visual and motor systems. Whilst large robust changes in spontaneous oscillatory activity were observed in response to hypercapnia, Figure 6-27 and Figure 6-28 show that hypercapnia had a smaller effect on visual and motor task induced changes in neural oscillations. They show that percentage changes due to the stimulus with respect to baseline were similar for hypercapnic and normocapnic trials. However, absolute measures of oscillatory amplitude showed that stimulus induced changes were smaller under hypercapnia compared to normocapnia. This agrees with the electrophysiology study by Zappe *et al.* [61], who showed that the percentage response to visual stimulation relative to baseline, was unchanged by hypercapnia. Whilst Jones *et al.* [59] showed a decrease in current source density, which was measured as an absolute change. Taken together, these results suggest that absolute power change due to a stimulus differs at hypercapnia compared to normocapnia, whilst the relative change remains approximately constant which could account for the apparent discrepancy between the previous results of [59] and [61]. The reason for the difference between absolute and relative change is apparent from Figure 6-27 D and Figure 6-28 D. In both cases there are significant ($P < 0.05$) differences in the baseline oscillatory amplitude between normocapnia and hypercapnia, however on stimulation both exhibit a reduction to the same level (no significant differences were observed in the amplitude of oscillations following stimulation in either the visual or the motor task).

Whilst a direct link between oscillatory amplitude change and $CMRO_2$ has not yet been shown, a number of studies have suggested a link between BOLD measurements (related to $CMRO_2$) and oscillations [49, 62-66]. A loss of neuronal

oscillatory synchrony is not necessarily indicative of an associated metabolism change. Hence, it is important for future studies to explore the mechanism behind these hypercapnia induced changes in neural oscillations. If the mechanism originates due to subject awareness of the CO_2 then it is possible that these effects do not scale with the level of hypercapnia. Many fMRI calibration methods employ a graded hypercapnic stimulus using more than one $P_{ET}CO_2$ level [9], and a graded hypercapnic stimulus should be assessed in future MEG studies to assess the mechanism behind these effects.

6.6 CONCLUSION

These two experiments have demonstrated the global brain response to hypercapnia. The results from the MEG experiment have supported the recent literature reports that hypercapnia affects $CMRO_2$ by demonstrating a change in neuronal activity. With this in mind the use of hypercapnia to calculate M for the Davis model [1] could invalidate the $CMRO_2$ calculations. However, the first experiment highlighted how the values of $CMRO_2$ can be unaffected by M due to the form of the Davis model relationship where values of M are large and how basal CBF and M could be related without the use of hypercapnia.

6.7 REFERENCES

1. Davis, T.L., K.K. Kwong, R.M. Weisskoff, and B.R. Rosen, *Calibrated functional MRI: Mapping the dynamics of oxidative metabolism.* Neurobiology, 1998. **95**: p. 1834-1839.
2. MacIntosh, B.J., K.T.S. Pattinson, D. Gallichan, I. Ahmad, K.L. Miller, D.A. Feinberg, R.G. Wise, and P. Jezzard, *Measuring the effects of remifentanil on cerebral blood flow and arterial arrival time using 3D GRASE MRI with pulsed arterial spin labelling.* J Cereb Blood Flow Metab, 2008. **28**(8): p. 1514-1522.
3. Grubb, R.L., M.E. Raichle, J.O. Eichling, and M.M. Ter-Pogossian, *The Effects of Changes in PaCO2 on Cerebral Blood Volume, Blood Flow, and Vascular Mean Transit Time.* Stroke, 1974. **5**: p. 630-639.
4. Ito, H., I. Kanno, M. Ibaraki, J. Hatazawa, and S. Miura, *Changes in Human Cerebral Blood Flow and Cerebral Blood Volume During Hypercapnia and Hypocapnia Measured by Positron Emission Tomography.* Journal of Cerebral Blood Flow & Metabolism, 2003. **23**: p. 665-670.
5. Driver, I., N. Blockley, J. Fisher, S.T. Francis, and P.A. Gowland, *The change in cerebrovascular reactivity between 3T and 7T measured using graded hypercapnia.* NeuroImage, 2010. **51**: p. 274-279.
6. Cohen, E.R., K. Ugurbil, and S.-G. Kim, *Effect of Basal Conditions on the Magnitude and Dynamics of the Blood Oxygenation Level-Dependent fMRI Response.* Journal of Cerebral Blood Flow & Metabolism, 2002. **22**: p. 1042-1053.
7. Gauthier, C.J., C. Madjar, F.B. Tancredi, B. Stefanovic, and R.D. Hoge, *Elimination of visually evoked BOLD responses during carbogen inhalation: Implications for calibrated MRI.* NeuroImage, 2010. **54**: p. 1001-1011.
8. Sicard, K.M. and T.Q. Duong, *Effects of hypoxia, hyperoxia, and hypercapnia on baseline and stimulus-evoked BOLD, CBF, and $CMRO_2$ in spontaneously breathing animals.* NeuroImage, 2005. **25**: p. 850-858.
9. Hoge, R.D., J. Atkinson, B. Gill, G.R. Crelier, S. Marrett, and G.B. Pike, *Investigation of BOLD Signal Dependence on Cerebral Blood Flow and Oxygen Consumption: The Deoxyhaemoglobin Model.* Magnetic Resonance in Medicine, 1999. **42**: p. 849-863.

10. Posse, S., L.J. Kemna, B. Elghahwagi, S. Wiese, and V.G. Kiselev, *Effect of Graded Hypo- and Hypercapnia on fMRI Contrast in Visual Cortex: Quantification of T_2^* Changes by Mutliecho EPI.* Magnetic Resonance in Medicine, 2001. **46**: p. 264-271.
11. Stefanovic, B., J.M. Warnking, K.M. Rylander, and G.B. Pike, *The effect of global cerebral vasodilation on focal activation hemodynamics.* NeuroImage, 2006. **30**: p. 726-734.
12. Cohen, E.R., E. Rostrup, K. Sidaros, T.E. Lund, O.B. Paulson, K. Ugurbil, and S.-G. Kim, *Hypercapnic normalization of BOLD fMRI: comparison across field strengths and pulse sequences.* NeuroImage, 2004. **23**(2): p. 613-624.
13. Bandettini, P.A. and E.C. Wong, *A Hypercapnia-Based Normalization Method for Improved Spatial Localization of Human Brain Activation with fMRI.* NMR in Biomedicine, 1997. **10**: p. 197-203.
14. Chen, J.J. and G.B. Pike, *MRI measurement of the BOLD-specific flow-volume relationship during hypercapnia and hypocapnia in humans.* Neuroimage, 2010. **53**(2): p. 383-391.
15. Yablonskiy, D.A. and M. Haacke, *Theory of NMR Signal Behaviour in Magnetically Inhomogeneous Tissues: The Static Dephasing Regime.* Mag. Res. Med., 1994. **32**: p. 749-763.
16. Boxerman, J.L., L.M. Hamberg, B.R. Rosen, and R.M. Weisskoff, *MR Contrast due to Intravascular Magnetic Susceptibility Perturbations.* Mag. Res. Med., 1995. **34**: p. 555-566.
17. Ogawa, S., R.S. Menon, D.W. Tank, S.-G. Kim, H. Merkle, J.M. Ellerman, and K. Ugurbil, *Functional brain mapping by blood oxygenation level-dependent contrast magnetic resonance imaging. A comparison of signal characterstics with a biophysical model.* Biophysical Journal, 1993. **64**(3): p. 803-812.
18. van der Zwaag, W., S. Francis, K. Head, A. Peters, P. Gowland, P. Morris, and R. Bowtell, *fMRI at 1.5, 3 and 7 T: Characterising BOLD signal changes.* Neuroimage, 2009. **47**(4): p. 1425-1434.
19. Chiarelli, P.A., D.P. Bulte, D. Gallichan, S.K. Piechnik, R.G. Wise, and P. Jezzard, *Flow-Metabolism Coupling in Human Visual, Motor, and Supplementary Motor Areas Assessed by Magnetic Resonance Imaging.* Magnetic Resonance in Medicine, 2007. **57**: p. 538-547.
20. Kastrup, A., G. Kruger, T. Neumann-Haefelin, G.H. Glover, and M.E. Moseley, *Changes of cerebral blood flow, oxygenation, and oxidative metabolism during graded motor activation.* Neuroimage, 2002. **15**: p. 74-82.
21. Uludag, K., D.J. Dubowitz, E.J. Yoder, K. Restom, T.T. Liu, and R.B. Buxton, *Coupling of cerebral blood flow and oxygen consumption during physiological activation and deactivation measured with fMRI.* Neuroimage, 2004. **23**: p. 148-155.
22. Chiarelli, P.A., D.P. Bulte, R. Wise, D. Gallichan, and P. Jezzard, *A calibration method for quantitative BOLD fMRI based on hyperoxia.* Neuroimage, 2007. **37**(3): p. 808-820.
23. Bulte, D.P., M. Kelly, M. Germuska, J. Xie, M.A. Chappell, T.W. Okell, M.G. Bright, and P. Jezzard, *Quantitative measurement of cerebral physiology using respiratory-calibrated MRI.* Neuroimage, 2012. **60**(1): p. 582-591.
24. Zappe, A.C., K. Uludag, A. Oeltermann, K. Ugurbil, and N.K. Logothetis, *The Influence of Moderate Hypercapnia on Neural Activity in the Anesthetized Nonhuman Primate.* Cerebral Cortex, 2008. **18**: p. 2666-2673.
25. Schellart, N.A.M. and D. Reits, *Voluntary breath holding affects spontaneous brain activity measured by magnetoencephalography.* Undersea and Hyperbaric Medical Society, 1999. **26**(4): p. 229-234.
26. Carbon, M., G. Wubbeler, L. Trahms, and G. Curio, *Hyperventilation-induced human cerebral magnetic fields non-invasively monitored by multicannel 'direct current' magnetoencephalography.* Neuroscience Letters, 2000. **287**: p. 227-230.
27. Blockley, N.P., T.P. White, C.M. Stevenson, M.J. Brookes, S.T. Francis, P.A. Gowland, and P.G. Morris, *Modulation of the MEG sustained field by a controlled hypercapnic stimulus.* Biomagnetism - Transdisciplinary reasearch and exploration, 2008: p. 18-20.
28. Xu, F., J. Uh, M.R. Brier, J. Hart Jr, U.S. Yezhuvath, H. Gu, Y. Yang, and H. Lu, *The influence of carbon dioxide on brain activity and metabolism in conscious humans.* Journal of Cerebral Blood Flow & Metabolism, 2011. **31**: p. 58-67.
29. Biswal, B., A.G. Hudetz, F.Z. Yetzin, V.M. Haughton, and J.S. Hyde, *Hypercapnia reversibly suppresses low-frequency fluctuations in the human motor cortex during rest using echo-planar imaging.* Journal of Cerebral Blood Flow & Metabolism, 1997. **17**: p. 301-308.
30. Halpern, P., M.Y. Neufeld, K. Sade, A. Silbiger, O. OSzold, N.M. Bornstein, and P. Sorkine, *Middle cerebral artery flow velocity decreases and electroencephaolgram (EEG) changes occur as acute hypercapnia reverses.* Intensive Care Med, 2003. **29**: p. 1650-1655.
31. Bloch-Salisbury, E., R. Lansing, and S. S.A., *Acute changes in carbon dioxide levels alter the electroencephalogram without affecting cognitive function.* Psychophysiology, 2000. **37**: p. 418-426.
32. van den Aardweg, J.G. and J.M. Karemaker, *Repetitive apneas induce periodic hypertension in normal subjects through hypoxia.* Journal of Applied Physiology, 1992. **72**(3): p. 821-827.

33. Mark, C.I., M. Slessarev, S. Ito, J. Han, J.A. Fisher, and G.B. Pike, *Precise control of end-tidal carbon dioxide and oxygen improves BOLD and ASL cerebrovascular reactivity measures.* Magnetic Resonance in Medicine, 2010. **64**(3): p. 749-756.
34. Slessarev, M., J. Han, A. Mardimae, E. Prisman, D. Preiss, G. Volgyesi, C. Ansel, J. Duffin, and J.A. Fisher, *Prospective targeting and control of end tidal CO2 and O2 concentrations.* J. Physiol., 2007. **581**(3): p. 1207-1219.
35. Klabunde, R.E., *Cardiovascular Physiology Concepts*. 2005, Baltimore: Lippincott Williams & Wilkins.
36. Wegener, S., W.-C. Wu, J.E. Perthen, and E.C. Wong, *Quantification of Rodent Cerebral Blood Flow (CBF) in Normal and High Flow States Using Pulsed Arterial Spin Labeling Magnetic Resonance Imaging.* JMRI, 2007. **26**: p. 855-862.
37. Tancredi, F.B., C.J. Gauthier, C. Madjar, and R.D. Hoge. *Does pulsed arterial spin-labeling selectively underestimate responses to global challenges?* in *ISMRM*. 2010. Stockholm.
38. Gardener, A.G., P.A. Gowland, and S.T. Francis, *Implementation of Quantitative Perfusion Imaging Using Pulsed Arterial Spin Labeling at Ultra-High Field.* Mag. Res. Med., 2009. **61**: p. 874-882.
39. Francis, S.T., R. Bowtell, and P.A. Gowland, *Modeling and Optimization of Look-Locker Spin Labeling for Measuring Perfusion and Transit Time Changes in Activation Studies Taking into Account Arterial Blood Volume.* Mag. Res. Med., 2008. **59**: p. 316-325.
40. Davis, T.L., K.K. Kwong, R.M. Weisskoff, and B.R. Rosen, *Calibrated functional MRI: Mapping the dynamics of oxidative metabolism.* Proc. Natl. Acad. Sci. USA, 1998. **95**: p. 1934-1839.
41. Rooney, W.D., G. Johnson, X. Li, E.R. Cohen, S.-G. Kim, K. Ugurbil, and C.S. Springer, *Magnetic Field and Tissue Dependancies of Human Brain Longitudinal ^1H_2O Relaxation in Vivo.* Mag. Res. Med., 2007. **57**: p. 308-318.
42. Wright, P.J., O.E. Mougin, J.J. Totman, A.M. Peters, M.J. Brookes, R. Coxon, P.G. Morris, M. Clemence, S.T. Francis, R. Bowtell, and P.A. Gowland, *Water Proton T1 Measurements in Brain Tissue at 7, 3 and 1.5T using IR-EPI, IR-TSE and MPRAGE: results and optimisation.* Magn. Reson. Mater. Phy, 2008. **21**: p. 121-130.
43. St. Lawrence, K.S., F.Q. Ye, B.K. Lewis, D.R. Weinberger, J.A. Frank, and A.C. McLaughlin, *Effects of indomethacin on cerebral blood flow at rest and during hypercapnia: An arterial spin tagging study in humans.* Journal of Magnetic Resonance Imaging, 2002. **15**(6): p. 628-635.
44. Yezhuvath, U.S., K. Lewis-Amezcua, R. Varghese, G. Xiao, and H. Lu, *On the assessment of cerebrovascular reactivity using hypercapnia BOLD MRI.* NMR in Biomedicine, 2009. **22**(7): p. 779-786.
45. Leontiev, O. and R.B. Buxton, *Reproducibility of BOLD, Perfusion, and $CMRO_2$ Measurements with Calibrated-BOLD fMRI.* NeuroImage, 2007. **35**(1): p. 175-184.
46. Orrison, W.W., J.D. Lewine, J.A. Sanders, and M.F. Hartshorne, *Functional Brain Imaging*. 1995, St-Louis: Mosby.
47. Brookes, M.J., J.R. Wood, C.M. Stevenson, J.M. Zumer, T.P. White, P.F. Liddle, and P.G. Morris, *Changes in brain network activity during working memory tasks: A magnetoencephalography study.* NeuroImage, 2010.
48. Brookes, M.J., *A Multi-Modal Approach to Functional Neuroimaging*, in *Physics*. 2005, University of Nottingham: Nottingham.
49. Brookes, M.J., A.M. Gibson, S.D. Hall, P.L. Furlong, G.R. Barnes, A. Hillebrand, K.D. Singh, I.E. Holliday, S.T. Francis, and P.G. Morris, *GLM-beamformer method demonstrates stationary field, alpha ERD and gamma ERS co-localisation with fMRI BOLD response in visual cortex.* Neuroimage, 2005. **26**: p. 302-308.
50. Robinson, S. and J. Vrba, *Functional Neuroimaging by synthetic aperture magnetometry*. 1998, Sendai: Tohoku University Press.
51. Gross, J., J. Kujala, M. Hamalainen, L. Timmermann, A. Schnitzler, and R. Salmelin, *Dynamic imaging of coherent sources: Studying neural interactions in the human brain.* Proceedings of the National Academy of Science USA, 2001. **98**: p. 694-699.
52. Sekihara, K., S.S. Nagarajan, D. Peoppel, A. Marantz, and Y. Miyashita, *Reconstructing Spatio-Temporal Activities of Neural Sources Using an MEG Vector Beamformer Technique.* IEEE Transactions on Biomedical Engineering, 2001. **48**: p. 760-771.
53. Van Drongelen, W., M. Yuchtman, B.D. Van Veen, and A.C. Van Huffelen, *A Spatial Filtering Technique to Detect and Localize Multiple Sources in the Brain.* Brain Topography, 1996. **9**: p. 39-49.
54. Van Veen, B.D., W. Van Drongelen, M. Yuchtman, and A. Suzuki, *Localisation of brain electrical activity via linearly constrained minimum variance spatial filtering.* IEEE Transactions on biomedical engineering, 1997. **44**: p. 867-880.
55. Vrba, J. and S.E. Robinson, *Signal processing in magnetoencephalography.* Methods, 2001. **25**(2): p. 249-271.

56. Brookes, M.J., J. Vrba, S.E. Robinson, C.M. Stevenson, A.P. Peters, G.R. Barnes, A. Hillebrand, and P.G. Morris, *Optimising experimental design for MEG beamformer imaging* Neuroimage, 2008. **39**: p. 1788-1802.
57. Cheyne, D., W. Gaetz, L. Garnery, J.-P. Lachaux, A. Ducorps, D. Schwartz, and F. Varela, *Neuromagnetic imaging of corticaloscillations accompanying tactile stimulation.* Cognitive Brain Research, 2003. **17**: p. 599-611.
58. Nichols, T.E. and A.P. Holmes, *Non-parametric permutation tests for functional neuroimaging: a primer with examples.* Human Brain Mapping, 2002. **15**: p. 1:25.
59. Jones, M., J. Berwick, N. Hewson-Stoate, C. Gias, and J. Mayhew, *The effect of hypercapnia on the neural and hemodynamic responses to somatosensory stimulation.* NeuroImage, 2005. **27**: p. 609-623.
60. Bai, O., Z. Mari, S. Vorbach, and M. Hallett, *Asymmetric spatiotemporal patterns of event-related desynchronisation preceding voluntary sequential finger movements: a high resolution EEG study.* Clinical Neurophysiology, 2005. **116**: p. 1213-1221.
61. Zappe, A.C., K. Uludag, and N.K. Logothetis, *Direct measurement of oxygen extraction with fMRI using 6% CO_2 inhalation.* Magnetic Resonance Imaging, 2008. **26**: p. 961-967.
62. Zumer, J.M., C.M. Stevenson, M.J. Brookes, S.T. Francis, and P.G. Morris, *Deconvolved fMRI correlates with source-localised MEG as a function of neural frequency oscillation.* Neuroimage, 2009. **49**(2): p. 1479-1489.
63. Stevenson, C.M., M.J. Brookes, and P.G. Morris, *Beta band correlates of the fMRI BOLD response.* Human Brain Mapping, 2011. **32**: p. 182-197.
64. Attwell and Laughlin, *An Energy Budget for Signaling in the Grey matter of the Brain.* Journal of Cerebral Blood flow and Metabolism, 2001. **21**: p. 1133-1145.
65. Logothetis, N.K., J. Pauls, M. Augath, T. Trinath, and A. Oeltermann, *Neurophysiological investigation of the basis of the fMRI signal.* Nature, 2001. **412**(6843): p. 150-7.
66. Singh, K., D, Barnes, G.,R, Hillebrand, A., *Group imaging of task-related changes in cortical synchronisation using nonparametric permutation testing.* Neuroimage, 2003. **19**(4): p. 1589-1601.

7 LOOK-LOCKER T_1 IMAGING: FAST MEASUREMENT OF CEREBRAL BLOOD VOLUME AND OPTIMISATION OF ANATOMICAL IMAGING AT 7 T

7.1 OUTLINE

This chapter outlines the theory behind T_1 mapping and how developments have led to more rapid, larger volume coverage sequences. A sequence for fast, B_1 independent, measurement of the change in R_1 is introduced. The sequence is applied to monitor gadolinium contrast agent uptake and to measure cerebral blood volume (CBV) in Multiple Sclerosis (MS) patients at 7 T.

Furthermore the sequence is optimised for high spatial resolution (0.6 mm isotropic) anatomical imaging at 7 T. The sequence is designed to allow maximal contrast between grey and white matter using Phase Sensitive Inversion Recovery (PSIR) and bias field correction to remove artefacts from an inhomogeneous transmit field.

7.2 INTRODUCTION

The longitudinal relaxation time, T_1, introduced in Chapter 2 can be used for monitoring the uptake of contrast agent. Contrast agents, as discussed in Chapter 4, are the standard clinical tool for the assessment of cerebral blood volume (CBV), perfusion (CBF) and blood brain barrier (BBB) permeability. They are often used in diseases, such as tumours (e.g. [1]), stroke (e.g. [2]) and multiple sclerosis [3-5].

Multiple sclerosis (MS) is an inflammatory disease of the central nervous system, characterised by lesions predominantly in the white matter [6]. MS has many different symptoms, including vision problems, dizziness, spasms and memory problems. The degree and time of onset of these is dependant on the individual and the type of MS. The three types of MS are relapsing remitting (RRMS), primary progressive (PPMS) and secondary progressive (SPMS). Relapsing remitting MS is where symptoms appear over a short period of time, and then usually completely recover. RRMS often eventually progresses into secondary progressive MS. SPMS is a gradual increase in disability, incomplete recovery occurs after symptom onset. Primary progressive MS is where the initial symptoms continue and worsen with time with no periods of remission [7].

Clinically isolated syndrome (CIS) describes the first neurological symptoms caused by inflammation or demyelination. If this is accompanied by a lesion, the patient has a high likelihood of further symptoms and thus being diagnosed with MS in subsequent years [8].

MRI is a useful tool in the monitoring of the progression of MS, and determining if structural abnormalities (i.e. number/volume of lesions) are correlated to disability. Current MR imaging in MS covers many different methods. For example; T_2 weighted imaging [6], T_1 histogram analysis [9] and gadolinium contrast for studying enhancing lesions [3-5]. The use of higher field for studying MS patients is also a growing area of research [6, 10].

Traditionally, T_1 was measured by an inversion-recovery (IR) sequence, as introduced in Chapter 2. The longitudinal magnetisation is inverted then sampled at a time TI later. This is repeated for different values of TI, allowing full recovery of the magnetisation between each inversion. This is then fitted to an exponential recovery curve,

$$S = S_0\left(1 - 2exp\left(-\frac{TI}{T_1}\right)\right), \quad \textbf{7-1}$$

where S_0 is the equilibrium signal (this takes into account readout flip angle, transverse decay and M_0). To account for imperfect inversion a further parameter, K, can be used:

$$S = S_0\left(1 - \mathrm{K}exp\left(-\frac{TI}{T_1}\right)\right), \quad \textbf{7-2}$$

where $\mathrm{K} = 1 - \cos(\theta)$, θ is the inversion angle achieved. Equations 7-1 and 7-2 assume full recovery of the longitudinal relaxation between each measurement ($\sim 5T_1$), which makes scan times long. This is exacerbated at higher field strengths as T_1 lengthens [11, 12].

7.3 Look-Locker Methods

To reduce acquisition time, Look and Locker [13] suggested the technique of making multiple readouts per inversion: continually sampling the magnetisation as it recovered. This would allow for the entire IR curve to be sampled in one shot, thus reducing the acquisition time. However in doing so, the recovery is perturbed (demonstrated in Figure 7-1) and does not follow a simple relationship as in Equation 7-1.

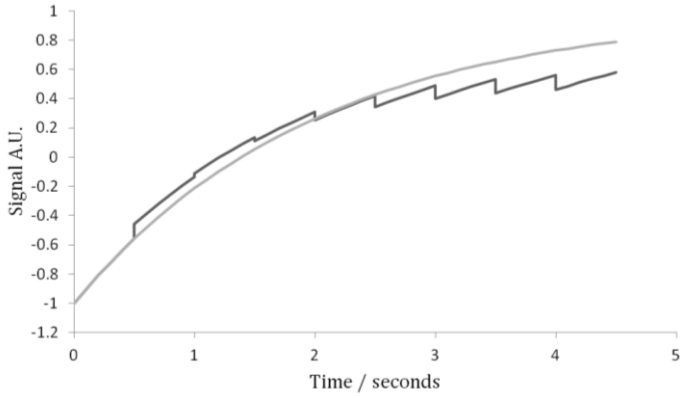

Figure 7-1: Longitudinal signal recovery curve for a standard inversion recovery experiment (light grey line) and a Look-Locker experiment (dark grey). Parameters T_1 = 2 s (grey matter at 7 T), flip angle = 35°, TR = 0.5s.

The model of Look and Locker iteratively applied the Bloch equations to calculate the complex relationship between the measured signal and T_1. Kaptein *et al.* [14] proposed a simplification of the model for the recovery curve allowing for the recovery to be fitted to an exponential recovery curve with relaxation time T_1*. The relaxation time T_1* is related to T_1 by

$$\frac{1}{T_1} = \frac{1}{T_1^*} + \frac{\ln(\cos(\alpha))}{TR}, \qquad \textbf{7-3}$$

where α is the readout flip angle, and TR is the time between the RF pulses. T_1* is always shorter than T_1, so the sample appears to recover faster (demonstrated in Figure 7-1). This allows for quantification of T_1 providing there is precise knowledge of the flip angle. The need for accurate flip angle quantification is shown in Figure 7-2 where a 40 % overestimation of flip angle would lead to a 150 % overestimation in T_1.

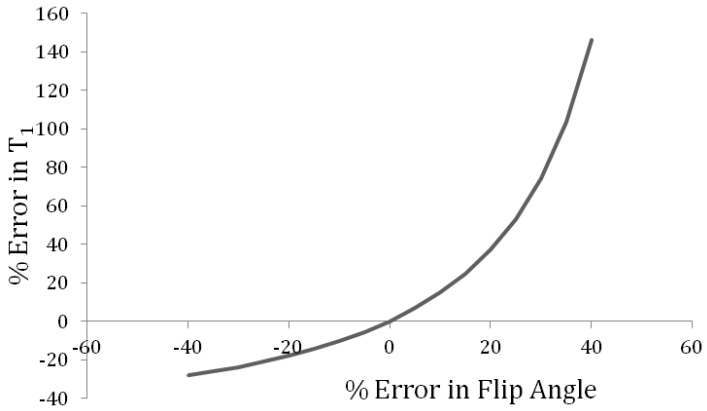

Figure 7-2: Example of the dependence of T_1 quantification on accurate flip angle knowledge. Simulated with T_1 = 2000 ms, TR = 50 ms and FA = 10°.

These two techniques were proposed for NMR sampling, and were soon adapted for MRI. Some of the first demonstrations of the Look-Locker technique were by

Young *et al.* in 1987 [15] who acquired T_1 maps of the brain at 0.15 T. In 1990, Brix *et al.* [16] acquired 32 IR images for single-slice T_1 mapping at 1.5 T at a resolution of 1.8 x 1.8 x 5 mm^3. Their model did not assume total relaxation between inversion pulses, instead they allowed for a steady state to be established by repeated application of closely spaced RF pulses. This gave a total scan time of ~ 4 minutes; to obtain the equivalent using a standard IR approach allowing 5 seconds between inversion pulses would take approximately 5 hours. The approach of Brix *et al.* is similar to the implementation shown by Kay and Henklemann in 1991 [17].

Figure 7-3: T_1 map produced using Look-Locker methods at 1.5 T in 1991, reproduced from [17]. A single slice T_1 map took 8.5 minutes to acquire (FOV 30 cm, resolution 2.5 x 2.5 x 7 mm^3) with 20 readouts per shot. Image reproduced with kind permission from John Wiley & Sons.

Deichmann and Haase [18] in 1992 proposed using SNAPSHOT-FLASH with Look-Locker sampling. By assuming equally spaced pulses, and that TR << T_1* < T_1 they derived a simplified form of the recovery curve allowing for T_1 quantification without knowledge of the flip angle of the readout pulse assuming that the flip angle is small so that cos(α) ≈ 1.

$$M(t) = M_0^* - (M_0 + M_0^*)\exp\left(-\frac{t}{T_1^*}\right), \quad \textbf{7-4}$$

where M_0* is $M_0\, T_1^*/T_1$, this leads to a form similar to that in Equation 7-2:

$$M(t) = A - Bexp\left(-\frac{t}{T_1^*}\right), \quad \textbf{7-5}$$

where A = M_0* and B = M_0 + M_0*. As M_0* is $M_0\, T_1^*/T_1$ an expression for T_1 in terms of the three parameters in Equation 7-5 can be formed;

$$\Rightarrow T_1 = T_1^*\left(\frac{B}{A} - 1\right). \quad \textbf{7-6}$$

By fitting the IR data to a simple 3 parameter exponential recovery, T_1 can be determined from the 3 fitted parameters without knowledge of the flip angle. For their experimental design [18] it was determined through simulation that the flip angle must be less than 10° to maintain contrast between the T_1 values of interest (1 – 2 s). The suppression of the relaxation of longitudinal magnetisation by the train of RF pulses can cause T_1* to converge at higher FA values ($\theta \geq 10°$). Also the assumption made that $\cos(\theta) \approx 1$ causes errors in T_1 measurement to increase with the flip angle of the RF pulse train (Figure 7-4). In addition Equation 7-6 only works for pulse sequences that have equally spaced RF pulses.

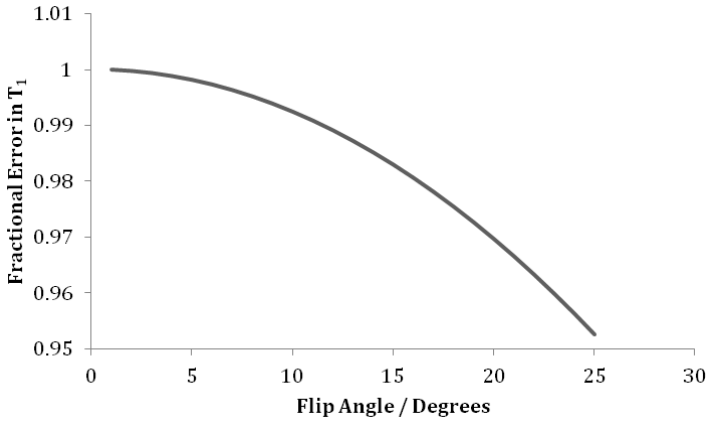

Figure 7-4: Error in T_1 as a function of increasing flip angle using the Deichmann and Haase method [18]. Simulated with T_1 = 2000 ms, TR = 50 ms.

Previously the image acquisition has been limited to simple gradient-echo where one line of k-space is acquired with each RF pulse, and the experiment is repeated stepping through the phase encode lines. In 1993, this was improved upon by Gowland and Mansfield [19] where an EPI readout was combined with the Look-Locker sampling for T_1 measurement at 0.5 T. This allowed for the entire image to be acquired with a single RF pulse, allowing for a T_1 map to be acquired in 3 seconds.

From this point, Look-Locker based sequences have developed – using different image readout schemes, and methods for further shortening the acquisition time. For example, Deichmann [20] suggested a method of acquiring 2D slices in an interleaved fashion thus allowing for the magnetisation to fully recover, but still offering a reduction in the scan time. Shah *et al*. [21] implemented a saturation pulse prior to the 180° so that the magnetisation was in the same state prior to each inversion pulse, without requiring complete recovery to reduce scan time. However, for this method there needs to be a sufficient pause between the

saturation and inversion pulses to give adequate SNR, reducing the benefit of not waiting for full recovery.

7.4 SIMULATING THE LL-TFEPI SIGNAL

The aim of this work is to develop a T_1 mapping sequence that can be used to produce high resolution, large volume coverage T_1 maps of the brain at 7 T to monitor the uptake of a Gadolinium based contrast agent in MS patients, and to measure total cerebral blood volume. The sequence is an inversion recovery Look-Locker combined with a 3D-TFEPI readout [22] and is shown in Figure 7-5.

For high volume coverage and high resolution in short scan times a Look-Locker method is necessary. The low EPI readout factor of 3 reduces the acquisition time by a factor of 3 without introducing susceptibility artefacts which are associated with EP images.

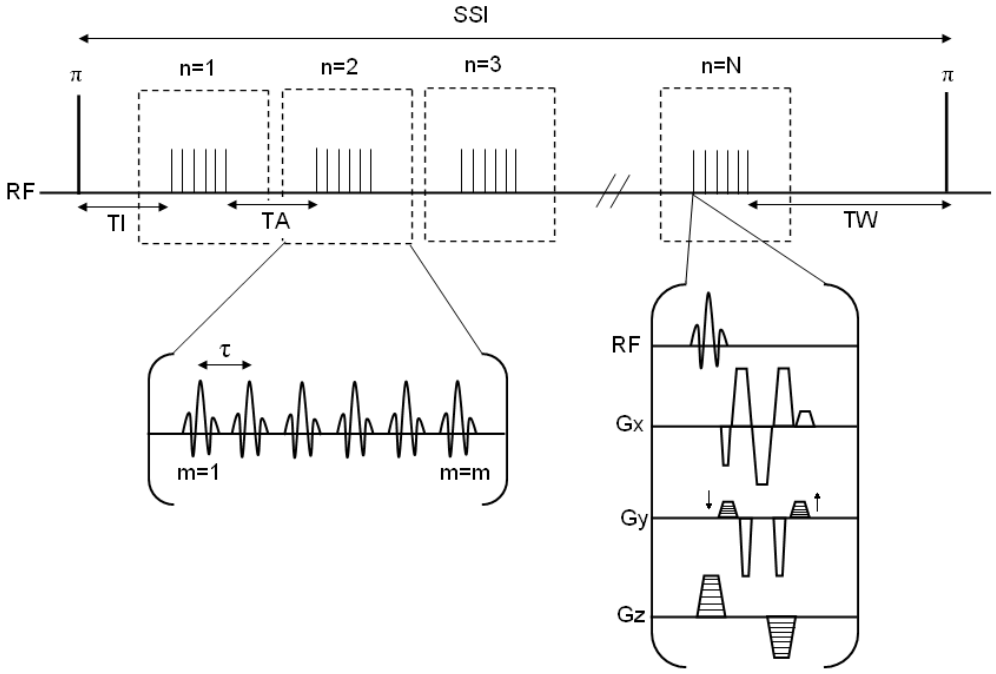

Figure 7-5: Schematic diagram of the LL-TFEPI sequence. SSI is the shot-to-shot interval, TI is the inversion delay, TA is the time between the Look-Locker readouts, N is the number of readouts per shot, τ is the time between RF pulses in a block, m is the number of pulses per block, TA is the time between readout blocks and TW is the time between the last readout pulse and the next inversion pulse.

To fit the data a model had to be developed to describe the recovery of the signal due to the perturbation by the successive readout pulses. It is assumed that all transverse magnetisation is spoiled between each successive RF pulse; this is achieved through RF spoiling. Therefore only the longitudinal magnetisation is modelled. The centre of k-space, where the bulk image contrast arises, is taken as

defining the signal in the image. This sequence uses a low-high k-space acquisition where the centre of k-space is collected first. It was assumed that full relaxation does not occur between shots and that a steady-state will have been established that is not equal to M_0.

The following terms are defined to simplify the subsequent equations:

$$\begin{aligned}
&\alpha = \cos(\theta),\\
&\beta = exp\left(-\frac{\tau}{T_1}\right),\\
&\gamma = exp\left(-\frac{TI}{T_1}\right),\\
&\delta = exp\left(-\frac{TW}{T_1}\right),\\
&\phi = exp\left(-\frac{TA}{T_1}\right).
\end{aligned} \qquad \textbf{7-7}$$

θ is the readout flip angle, the other symbols are defined in Figure 7-5. The expression for longitudinal magnetisation prior to the first small RF pulse is

$$X_1^- = M_0^+\gamma + M_e(1-\gamma), \qquad \textbf{7-8}$$

where M_0^+ is the steady state magnetisation (the magnetisation after the inversion pulse once steady state has been established) and M_e is the equilibrium magnetisation. By fully modelling the entire sequence, the expression for M_0^+ can be determined

$$M_0^+ = M_e\cos(\theta_{inv})\frac{\big((1-\delta)+\alpha\delta(D+E+F)\big)}{1-\cos(\theta_{inv})\,\alpha\delta(\phi\alpha(\alpha\beta)^{m-1})^{N-1}\gamma(\alpha\beta)^{m-1}}, \qquad \textbf{7-9}$$

where

$$\begin{aligned}
&D = \left(\frac{(1-\beta)(1-(\alpha\beta)^{m-1})}{(1-\alpha\beta)}\right)\cdot\left(1+\frac{\alpha\phi(\alpha\beta)^{m-1}(1-(\phi\alpha(\alpha\beta)^{m-1})^{N-1})}{(1-\phi\alpha(\alpha\beta)^{m-1})}\right),\\
&E = (\phi\alpha(\alpha\beta)^{m-1})^{N-1}(\alpha\beta)^{m-1}(1-\gamma),\\
&F = \frac{(\alpha\beta)^{m-1}(1-\phi)(1-(\phi\alpha(\alpha\beta)^{m-1})^{N-1})}{1-\phi\alpha(\alpha\beta)^{m-1}},
\end{aligned} \qquad \textbf{7-10}$$

and where θ_{inv} is the angle of inversion (ideally 180°). The signal at the centre of k-space is modelled, which arises from the first pulse of each of the N readout blocks. For the first readout block (n = 1) the longitudinal signal prior to the first pulse is X_1^-, and for the second readout block (n = 2) this is the signal prior to the m+1th small RF pulse and is given by X_2^-:

$$X_2^- = M_e(1-\phi) + \alpha\phi(\alpha\beta)^{m-1}X_0^- + \frac{\alpha\phi M_e(1-\beta)(1-(\alpha\beta)^{m-1})}{1-\alpha\beta}. \quad \textbf{7-11}$$

This can be generalised to

$$X_n^- = X_1^-(\alpha\phi(\alpha\beta)^{m-1})^{n-1} + \left(m_e(1-\phi) + \frac{\alpha\phi M_e(1-\beta)(1-(\alpha\beta)^{m-1})}{1-\alpha\beta}\right) \cdot \left(\frac{1-(\alpha\phi(\alpha\beta)^{m-1})^{n-1}}{1-\alpha\phi(\alpha\beta)^{m-1}}\right), \quad \textbf{7-12}$$

for n = 1, 2 … N. This is converted to the signal measured in the transverse plane (neglecting transverse decay)

$$S_n = \sin(\theta)\cdot X_n^-. \quad \textbf{7-13}$$

S_n expresses the measured signal of the nth TFE block, where n = 1, 2 … N. This will be referred to as the *full model* in subsequent discussion. However S_n can be re-expressed in terms of an effective relaxation term;

$$S_n = \sin(\theta)\left(X_0^- t^{n-1} + A\left(\frac{1-t_{eff}^{n-1}}{B}\right)\right) = \sin(\theta)\left(t_{eff}^{n-1}\left(X_0^- - \frac{A}{B}\right) + \frac{A}{B}\right), \quad \textbf{7-14}$$

where $t_{eff}^{n-1} = \exp\left(-\frac{TA}{T_1}\right)(\cos(\theta))^m\left(exp\left(-\frac{\tau}{T_1}\right)\right)^{m-1}$. Expressing this as an effective relaxation term, $t_{eff}^{n-1} = exp\left(-\frac{n-1}{T_1^*}\right)$, where

$$\frac{1}{T_1^*} = \frac{1}{T_1}(TA + (m-1)\tau) - m\cdot\ln(\cos(\theta)). \quad \textbf{7-15}$$

This takes into account the fact that the small flip angle pulses are not applied at equal spacings, but in groups of pulses. This gives a simple expression to fit to:

$$S_j = A' - B' exp\left(-\frac{j}{T_1^*}\right), \quad \textbf{7-16}$$

where $A' = \frac{\sin(\theta)A}{B}$, $B' = \sin(\theta)\left(\frac{A}{B} - X_0^-\right)$, j = 0 , 1 .. N-1. The data is fitted for A', B' and T_1*, and T_1 calculated from Equation 7-15, providing knowledge of θ. This will be referred to as the *effective relaxation model*.

7.4.1 Measuring the Change in R_1 and Cerebral Blood Volume

Often the motivation behind measuring T_1 is to monitor the change in T_1 (ΔT_1) due to the administration of a contrast agent, most commonly a Gadolinium based compound. If the change in R_1 (ΔR_1) is only required then precise

knowledge of B_1 is not required [23], since from Equation 7-15 it can be seen that:

$$\Delta R_1^* = \Delta R_1(\mathrm{TA} + (m-1)\tau). \quad \textbf{7-17}$$

ΔR_1 can be found by scaling the change in R_1* by a factor of (TA + (m-1) τ). This is valid providing the patient/sample does not move greatly between scans so that the B_1 in each voxel is approximately the same. This allows for quantification without knowledge of the flip angle, which can be difficult to quantify (see Section 7.5) and requires a separate scan to do so. This will speed up the acquisition time which is important in clinical protocols where the patients are undergoing several different scans in one session.

ΔR_1 can be converted to regional blood volume (RBV) using the method of Schwarzbauer *et al.* [24]. RBV is defined as the fractional intravascular volume. Two measurements of T_1 are taken, one prior to administration of an intravascular contrast agent (T_1), the other when the contrast agent has reached equilibrium (T_1^{eq}). The RBV is quantified through the relative changes in T_1 between tissue (T_1) and blood ($T_{1,b}$);

$$RBV = \frac{T_1^{-1} - T_1^{eq\,-1}}{T_{1,b}^{-1} - T_{1,b}^{eq\,-1}},$$

$$RBV = \frac{\Delta R_1}{\Delta R_{1,b}}. \quad \textbf{7-18}$$

It can be seen from Equations 7-17 and 7-18 that

$$RBV = \frac{\Delta R_1^*}{\Delta R_{1,b}^*}, \quad \textbf{7-19}$$

which is independent of both B_1 and the scan parameters. The blood measurement can be formed from a blood sample or a large vessel if present in the imaging volume. This allows simple quantification of RBV, in this application CBV, from two T_1 or R_1 maps acquired pre- and post-contrast agent administration. Due to the B_1 independence of the measurement of ΔR_1 the measurement of CBV at 7 T could be achieved with only two scans.

7.5 B_1 Mapping

It has been shown that ΔR_1 or cerebral blood volume can be mapped using contrast enhanced LL-TFEPI without knowledge of the flip angle. This is advantageous because mapping of the B_1 field requires a separate scan,

increasing the total scan time required. However, if in addition to measuring ΔR_1, absolute T_1 is required, then accurate knowledge of the flip angle is needed or errors in T_1 measurement increase (e.g. Figure 7-2 and Figure 7-4). B_1 field homogeneity decreases with increasing magnetic field strength, due to the increase in Larmor frequency reducing the RF wavelength required. This reduced wavelength is comparable to the length scale of the human body (~ 1m), increasing interactions between the RF radiation and the dielectric tissues in the body. This results in higher flip angles being achieved in the centre of the image, than at the edges. This spatial variation can be visible in the maps of T_1 produced. To overcome this, maps of the flip angle variation can be used.

The most accurate way of mapping the B_1 field is to acquire several images at different flip angles and fit $M_0\sin(c.\alpha)$ where c is the scale and α is the flip angle requested to each voxel. This gives a map of c which will vary for 7T typically between 0.5 and 1.5 and can then be used to convert T_1* to T_1. To implement this a long TR between RF pulses must be used to remove saturation effects from the measured signal intensity. For a TFE/FLASH acquisition with a 256 x 256 x 50 matrix this would take over a day to acquire! However the B_1 map can be acquired at a lower resolution as it is a smooth, slowly varying function. An alternative is to use an EPI readout, however the spatial distortions may not match those of the T_1 acquisition, making it hard to realign. Also, for Philips scanners, if care is not taken, the RF pulse parameter (set by the scanner automatically) can change dependant on the readout used, further complicating the use of a faster method of B_1 mapping.

Hence, fast B_1 methods have been proposed which attempt to overcome this. A popular method, with many variants upon it, is the dual angle method (DAM). Two sets of images, S_1 and S_2, are acquired with flip angles of α and 2α. This relies on full relaxation to eliminate terms dependant on T_1. The ratio of the two images is taken and this can be related back to the flip angle θ assuming TR << T_1;

$$\theta = arccos\left(\left|\frac{S_2}{2S_1}\right|\right). \qquad \textbf{7-20}$$

Cunningham *et al.* [25] modified this by preceding the image readout with a 'reset' module (saturation pulse) to remove the period of recovery. This was designed to ensure the magnetisation was in the same state at the beginning of each TR period for both flip angles. However, this will rely on good saturation

pulses, and scan time will be long due to the period of time needed to allow the magnetisation to recover after the saturation pulse to give adequate SNR.

Standard B_1 mapping on the Philips system uses Actual Flip-angle Imaging (AFI), as proposed by Yarnykh [26]. The pulse sequence consists of two identical RF pulses with two delays TR_1 and TR_2, as shown in Figure 7-6, which generate two signals S_1 and S_2.

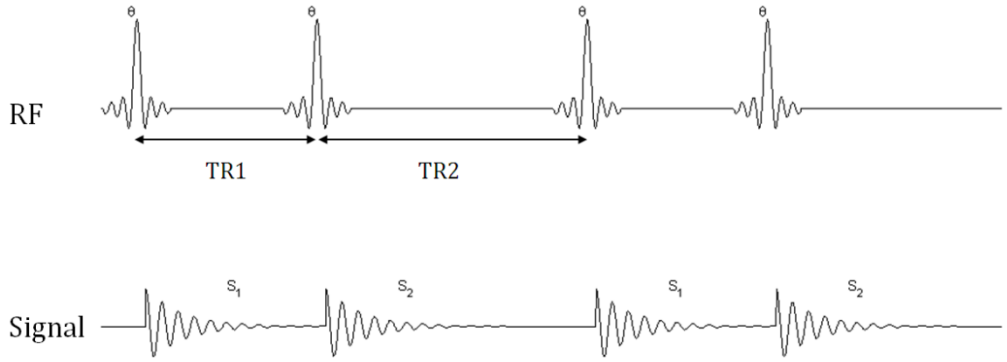

Figure 7-6: Timing diagram for the B_1 mapping sequence of Yarnykh [26] showing RF pulses and detected signals.

The method allows for the lack of complete relaxation of the longitudinal magnetisation in the period TR2, which allows for a shorter acquisition. With TR1 < TR2 < T_1 a new steady state is established which is accounted for. It is assumed that the transverse magnetisation is completely spoiled after each acquisition. Using the Bloch equations, expressions for the measured signals S_1 and S_2 can be derived,

$$S_1 = M_0 \frac{1 - E_2 + (1 - E_1)E_2 \cos(\theta)}{1 - E_1 E_2 (\cos(\theta))^2} \exp\left(-\frac{TE}{T_2^*}\right) \sin(\theta),$$

$$S_2 = M_0 \frac{1 - E_1 + (1 - E_2)E_1 \cos(\theta)}{1 - E_1 E_2 (\cos(\theta))^2} \exp\left(-\frac{TE}{T_2^*}\right) \sin(\theta), \qquad \textbf{7-21}$$

where $E_{1,2}=\exp(-TR_{1,2}/T_1)$. The ratio between these signals is

$$\frac{S_2}{S_1} = \frac{1 - E_1 + (1 - E_2)E_1 \cos(\theta)}{1 - E_2 + (1 - E_1)E_2 \cos(\theta)}. \qquad \textbf{7-22}$$

By first order approximation of the exponential terms as $1\text{-}TR_{1,2}/T_1$, Equation 7-22 can be simplified to

$$\frac{S_2}{S_1} \approx \frac{1 + \frac{TR2}{TR1}\cos(\theta)}{\frac{TR2}{TR1} + \cos(\theta)}. \qquad \textbf{7-23}$$

This can be rearranged to give an expression for the flip angle θ;

$$\theta \approx arccos\left(\frac{\frac{S_2}{S_1}\cdot\frac{TR2}{TR1}-1}{\frac{TR2}{TR1}-\frac{S_2}{S_1}}\right). \quad \textbf{7-24}$$

An example slice from a B_1 map acquired using this method at 7 T is shown in Figure 7-7. Clear structural information can be seen, which should not be present in the B_1 map. This is indicative of tissue weighting in the B_1 map which would introduce significant error into T_1 quantification; the maps shown in Yarnykh [26] were acquired at 1.5 T and did not have any visible brain structure. Further investigation of the origin of this signal is described below.

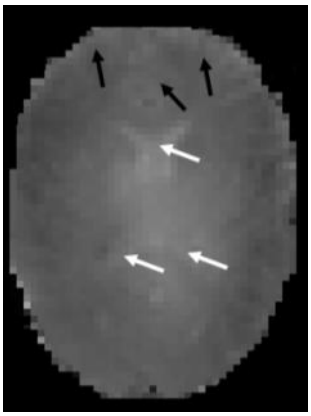

Figure 7-7: An example B_1 map using the AFI method at 7 T. White arrows show structure from the ventricles, black arrows show grey/white matter boundary that is visible.

At 7 T, B_1 inhomogeneities are increased relative to 1.5 and 3 T. To investigate the appearance of structure in the B_1 maps acquired at 7 T phantom and in vivo experiments were performed.

7.5.1 PHANTOM EXPERIMENTS

In Figure 7-7 it was seen that the B_1 map produced using AFI displayed brain structure. To investigate the origin of this and the effect of the different scan parameters of the AFI B_1 mapping technique was assessed on a phantom.

7.5.1.1 Methods

A quadrant phantom of agar gel doped with gadolinium where each quadrant has a different T_1 and T_2 were used (T_1 range 300 – 2,800 ms, T_2 range 30 – 100 ms). The sequence used was AFI (Figure 7-6) with standard scan parameters: 3 x 3 x 5 mm^3 voxel size, FOV 200 x 200 x 75 mm^3, TE 5 ms, TR1 / TR2 = 23 / 103 ms, gradient spoil factor 5, flip angle 60°.

The scan parameters under investigation are TE, TR1, TR2, gradient spoil factor and flip angle. Each scan parameter was varied, keeping the remaining parameters constant at the value provided above.

The average B_1 scaling factor (termed *B_1 value*) was averaged separately over each quadrant to look at the impact of the different scan parameters on B_1 estimation.

7.5.1.2 Results

Firstly, the standard B_1 map was investigated to assess the dependence of the measured B_1 value on T_1 and T_2, Figure 7-8. This suggests that the B_1 value will increase with increasing T_1, which corresponds to the B_1 map in Figure 7-7, where grey matter with longer T_1 has higher B_1 value than the neighbouring white matter. There was not a strong correlation with T_2.

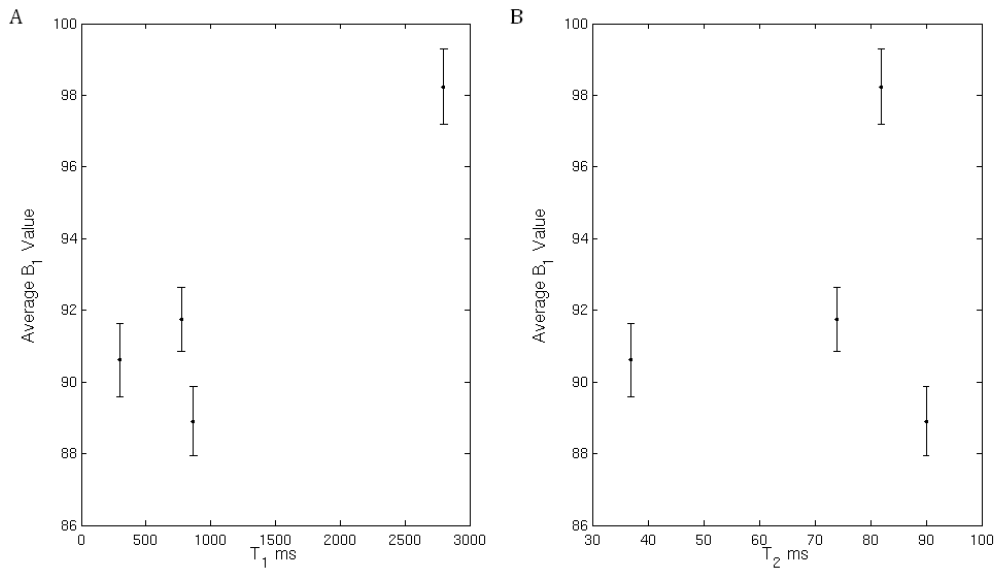

Figure 7-8: Dependence of measured B_1 value on (A) T_1 and (B) T_2. Error bars represent standard error across voxels in the ROI.

Spoil factor, TR1 and echo time did not greatly impact B_1 quantification – measured values were stable across the values assessed, Figure 7-9 A, B and D. Both flip angle and TR2 affected B_1 values strongly (Figure 7-9 C, E).

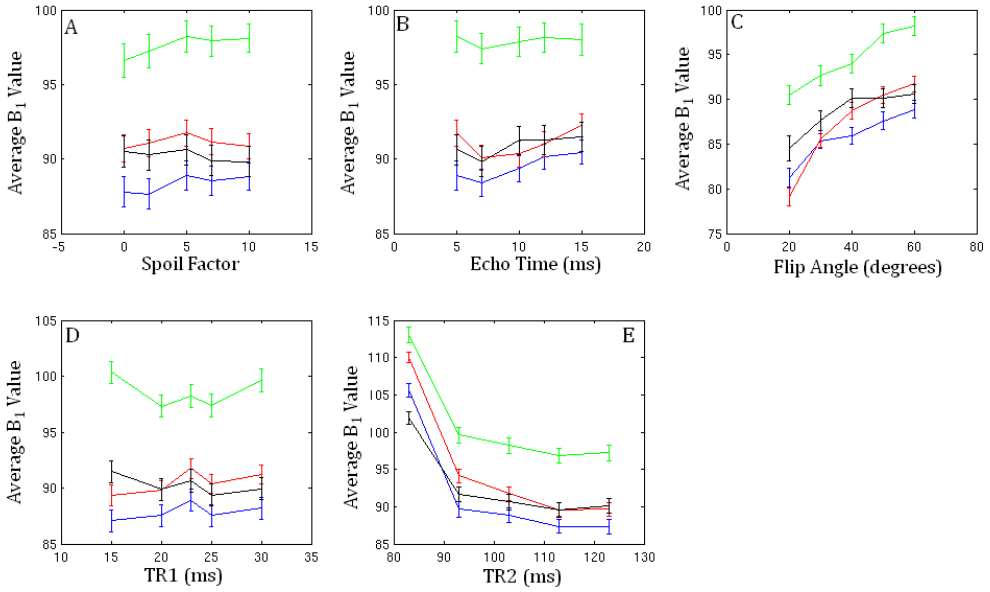

Figure 7-9: Effect of (A) spoil factor, (B) echo time (C) flip angle (D) TR1 and (E) TR2 and on average B_1 value. The four quadrants are plotted in different colours. Error bars represent standard error across voxels in the ROI.

7.5.2 IN VIVO INVESTIGATION

To verify the large effect of TR2 seen in the phantom data, in-vivo, B_1 maps were acquired on one healthy volunteer. In addition, comparative B_1 maps were acquired with a variable flip angle approach and in an additional healthy volunteer.

7.5.2.1 Methods

One healthy volunteer was scanned with the standard Philips B_1 mapping sequence (TR2 = 103 ms) and with a reduced TR2 of 83 ms. In addition, a variable flip angle gradient echo EPI acquisition was performed to map the flip angle. A single slice, 3 mm isotropic, TE = 16 ms, 192 x 192 mm^2 FOV GE-EPI was acquired with flip angles of 10 - 140°. A TR of 30 s was used to ensure full relaxation between acquisitions. The RF transmit bandwidth was fixed across the flip angles. The slice was positioned through the ventricles to allow CSF as well as grey and white matter to be interrogated. The EPI data was fitted in Matlab (The Mathworks, MA, USA) to $S_0\sin(c.\theta)$ where c is the B_1 scaling factor and θ is the requested flip angle.

A further healthy volunteer was scanned, an EPI B_1 map, using parameters above, and an AFI B_1 map with the standard parameters were acquired in the cortical grey matter to assess if any structural information was present.

7.5.2.2 Results

The histograms of the two AFI B_1 maps acquired with TR2 of 83 and 103 ms are shown in Figure 7-10. These demonstrate that, in agreement with the phantom, by reducing TR2 the B_1 value increases by approximately 15 %. 98 % of brain voxels showed an increase in B_1 value when TR2 was reduced.

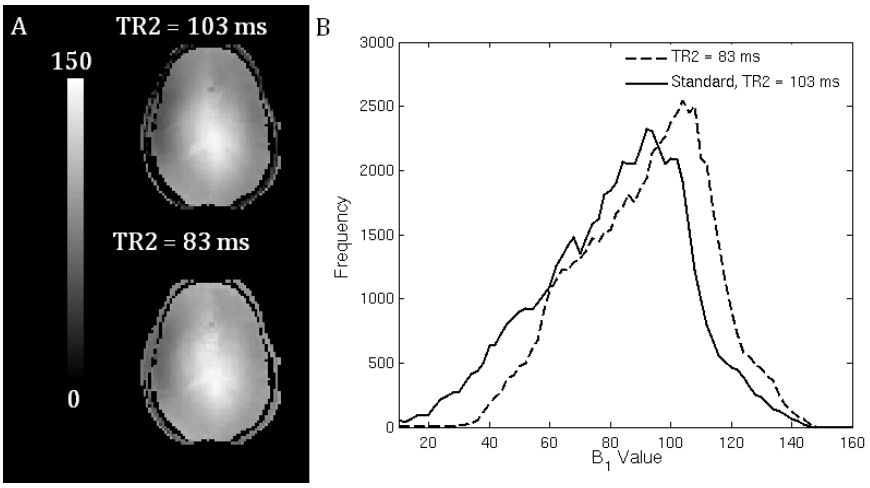

Figure 7-10: (A) Example slice from AFI B_1 maps acquired with TR2 = 103 ms (standard parameter) and 83 ms. (B) Whole brain histogram of AFI B_1 maps acquired in-vivo with TR2 of 83 ms (broken line) and 103 ms (solid line).

The EPI flip angle maps acquired in two volunteers are shown in Figure 7-11 alongside the AFI map acquired with the standard parameters. These EPI B_1 maps demonstrate quite a slow variation in the flip angle with little brain structure visible. The ventricles are still distinguishable, but this could be due to flow in the CSF rather than a T_1/T_2 effect. This demonstrates that the AFI maps should not display significant structure, as expected. The EPI maps give lower B_1 values than AFI, however the RF pulse shape is different for the two methods which could lead to different pulse profiles.

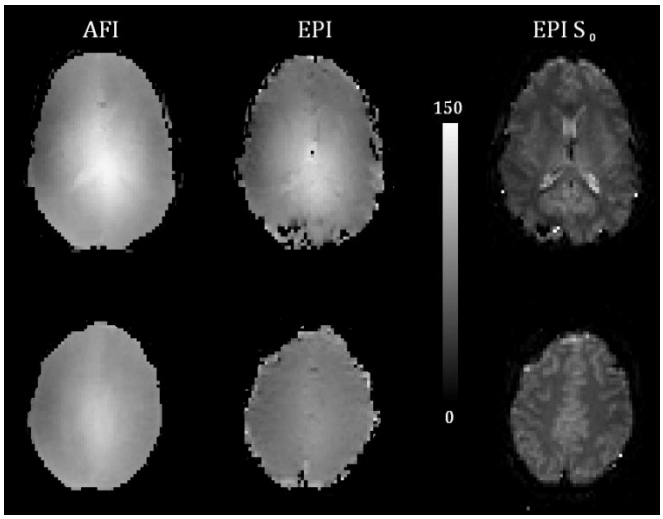

Figure 7-11: EPI B_1 maps acquired on two healthy volunteers using AFI and EPI, grey scale is the B_1 value (%), and the corresponding S_0 EPI image shown.

7.5.3 SIMULATIONS

To investigate the possibility of spoiling impacting on AFI, simulations were performed. Using real anatomical data, the AFI signals were simulated to give images of S_1 and S_2 which were converted to B_1 maps.

The signal was simulated using rotation and relaxation operators to model the effect of the train of RF pulses on the three components of magnetisation [M_x, M_y, M_z]. The input B_1 field was modelled by a 2D Gaussian ($exp\left(-\left((x-x_0)^2/2\sigma_x^2 + (y-y_0)^2/2\sigma_y^2\right)\right)$) with peak in the image centre, with σ_x = 80 and σ_y = 60 pixels (Figure 7-12 A) to give a distribution (similar to that obtained in vivo, as in Figure 7-11). A 1 mm isotropic MPRAGE image was segmented into grey matter, white matter and CSF partial volume maps (FAST, FSL, FMRIB) to give structural information. T_1 was taken to be 2100, 1300, 4000 ms [11, 12], T_2 40, 33 and 125 ms [27, 28] and M_0 1.2, 1 and 1.6 [29] for grey matter, white matter and CSF respectively. The simulations were performed voxelwise to give a flip angle map. 100 pulses were simulated to model the steady state condition; the two signals (S_1 and S_2) were then used to calculate the flip angle map using Equation 7-24.

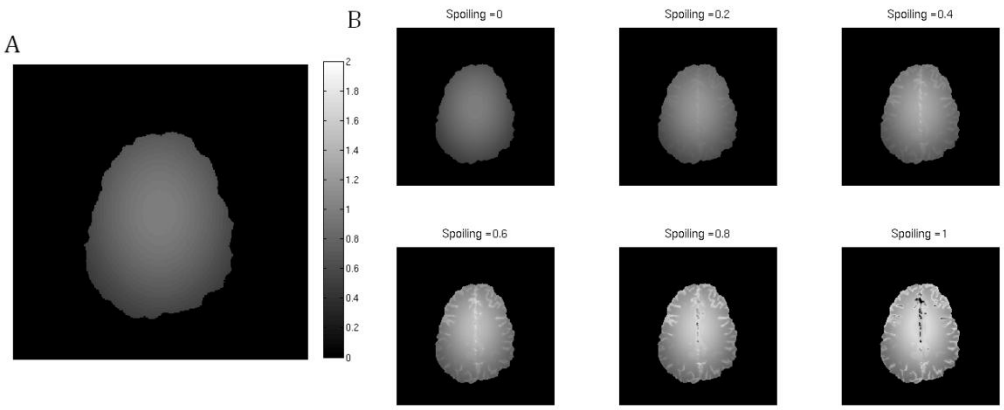

Figure 7-12: (A) Simulated B_1 profile and (B) modelled B_1 maps as a function of spoiling factor.

To model insufficient spoiling prior to the next RF pulse, the magnitude of the transverse signal was reduced by a factor ranging from 0 to 1, where 0 is complete spoiling and 1 is no spoiling. The simulated B_1 maps obtained using the standard scan parameters with different spoiling factors are shown in Figure 7-12 B. It is clearly seen that the amount of transverse magnetisation that remains prior to the subsequent RF pulse has significant impact on the resultant B_1 map, with structure clearly visible with incomplete spoiling.

7.5.4 DISCUSSION

The B_1 maps produced from AFI show structure (demonstrated in Figure 7-7) suggesting that the method is not working correctly as B_1 is a slowly varying spatial function as shown in the EPI B_1 maps (Figure 7-11). The EPI method of B_1 mapping is slow, taking 7 minutes to acquire one slice, due to the need for complete recovery between RF pulses to eliminate T_1 effects. Here only a single slice was acquired to prevent subsequent slice acquisitions affecting the spins (e.g. through magnetisation transfer). In addition, the distortions are more pronounced in the EPI which would be hard to match to the LL-TFEPI acquisition to correct the T_1* values. The EPI B_1 maps would require distortion correction using a B_0 field map, further increasing scan time; hence EPI maps are not an option for B_1 mapping here.

From the phantom experiments it can be seen that the scan parameters can have significant effect on the resultant B_1 value measured using AFI. The effect of flip angle used on measured B_1 could be due to pulse length changing (hence B_1 profile has changed). The assumptions in the mathematical description of AFI are

that TR1 < TR2 << T_1 and that the transverse signal is adequately spoilt between successive RF pulses. The assumption TR1 < TR2 << T_1 is used to allow simplification of the exponential terms to a Maclaurin series. With the lowest T_1 expected in-vivo at 7 T of ~1 s there is less than a 1 % difference between the exponential term and the approximation, suggestive that this assumption holds. The significant impact of TR2 on all four quadrants of the phantom (T_1 values ranging from 300 – 2,800 ms), and the in-vivo data may be due to inadequate spoiling. With a reduced TR2, less transverse signal has decayed due to T_2/T_2*. The simulations support the fact that residual transverse signal may have significant impact on the estimated B_1 resulting in structural information being visible. However, the phantom data did not show a correlation between T_2 and B_1, but the phantom has some short T_1 (< 1s) compartments possibly invalidating the Maclaurin series assumption, and so competing effects could be present.

With sequences, such as AFI, where TR < T_2 the transverse magnetisation does not decay completely prior to the next RF pulse. With a train of pulses this signal can be rephased to give partial echoes and stimulated echoes in addition to the FID. The coherence plot in Figure 7-13 shows the evolution of the phase of the transverse signal and the impact of RF pulses. After an RF pulse there are three components; the transverse signal component that rephases, the transverse signal component that continues to dephase and a longitudinal signal component. Hahn/spin echoes and stimulated echoes are formed when the phase of the spin is zero (shown in Figure 7-13). It is assumed that components with non-zero phase will vectorally add to zero and not contribute to the signal [30].

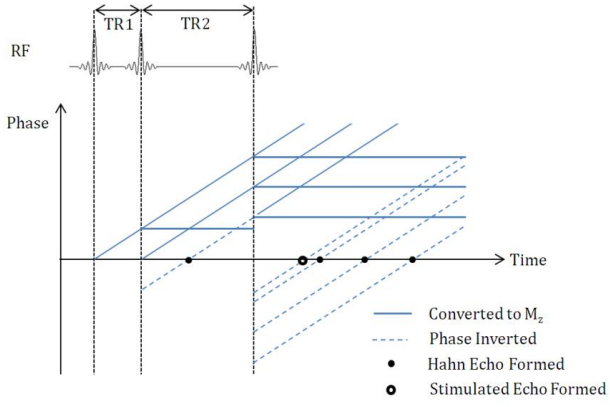

Figure 7-13: Coherence plot showing the evolution of phase of the transverse signal over time due to the application of three RF pulses and how these form spin (filled circle) and stimulated echoes (unfilled circle). After the RF pulse the signal has three components (1) longitudinal magnetization and the phase remains unchanged shown by solid horizontal line, (2) phase inverted and begins to rephase, broken line, or (3) continue to be dephased. Adapted from [31].

A main assumption of AFI is that all the transverse signal is spoiled between RF pulses. To achieve this, two methods of spoiling are used; gradient and RF spoiling. Gradient spoiling uses additional gradients on the read and frequency encode axes after each RF pulse to spoil the transverse signal. This is achieved as the phase, ϕ , of a spin at a position **r** is equal to

$$\phi(\boldsymbol{r}) = \gamma \boldsymbol{r} \int_0^{TR} \boldsymbol{G}(t)dt, \qquad \textbf{7-25}$$

where **G** is the applied gradient and TR is the time between successive RF pulses. Gradient spoiling dephases the signal but does not prevent the formation of Hahn echoes, as shown in Figure 7-14. The AFI sequence spoil factor varies the duration of these gradients, altering the degree of dephasing. Varying the strength of the gradients with the different RF pulses would reduce the amount of rephasing with sequential spoiler gradients.

RF spoiling uses phase cycling of the RF excitation pulses to reduce the transverse signal, this adds a φ_n term (where n is the number of the RF pulse) to the expression for phase in Equation 7-25, demonstrated by the shift in Figure 7-14 B;

$$\phi(\boldsymbol{r}) = \gamma \boldsymbol{r} \int_0^{TR} \boldsymbol{G}(t)dt + \varphi_n. \qquad \textbf{7-26}$$

The phase of the RF excitation pulse is incremented with each pulse, this reduces phase coherence of the spins resulting in reduced net residual transverse magnetisation. Optimisation of the phase cycling of the RF pulses leads to improved signal spoiling [30].

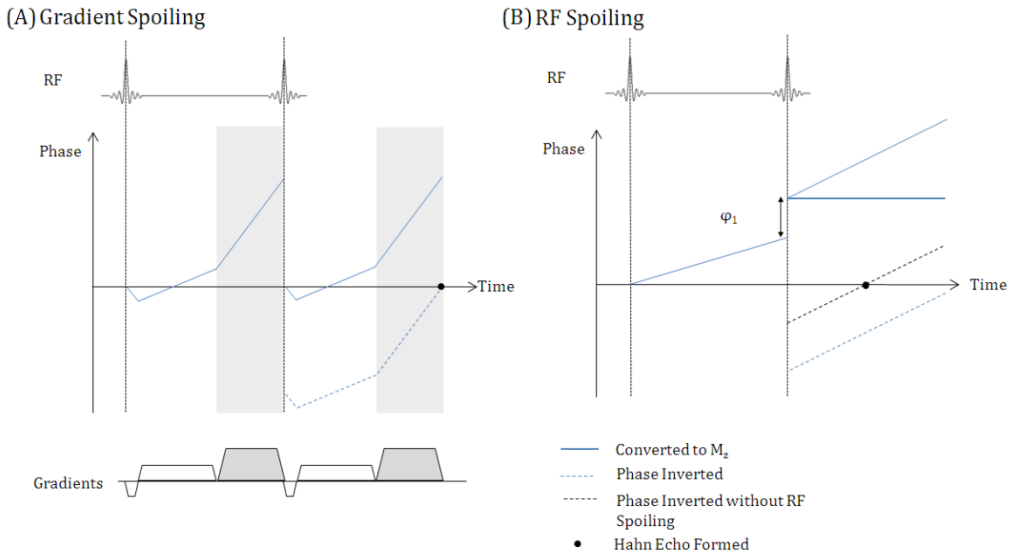

Figure 7-14: Coherence plot showing the evolution of phase over time due to the application of two RF pulses, with (A) gradient spoiling, the grey shaded areas show the application of a spoiler gradient, (read and associated spoiler gradient waveform shown, not all phase pathways shown for clarity) and (B) RF spoiling, black broken line shows how a spin echo would have been formed if the phase had not been incremented. Adapted from [31].

From the results, it can be seen that the standard B_1 mapping technique currently implemented on the Philips 7 T system has tissue weighting resulting in B_1 being dependent on the scan parameters. From the effect of TR2, and simulations, this could be due to incomplete spoiling of the transverse signal. Further investigation as to the performance of the spoiling implemented for the AFI needs to be explored. Possibilities include implementing gradient spoiling that varies between the shots to avoid refocusing of the signal, and implementing spoilers on a third axes. The optimisation of RF spoiling can be tailored to the specific pulse sequence to see if an improvement is seen.

Another area for further investigation is alternative methods for B_1 mapping that do not rely on such assumptions. The most promising is the recently proposed method of B_1 mapping by Sacolick *et al.* which utilises the Bloch-Seigert shift [32]. This method encodes B_1 information into the phase of the signal by applying off-resonance RF pulses (kHz range) after spin excitation. The off-resonance pulse causes a change in precession frequency, this shift is dependant on the B_1 field. This was shown to produce B_1 maps with reduced T_1 effects in them at 3 T in the brain, abdomen, shoulder and knee compared to the dual-angle method (DAM).

7.6 Investigating the Effect of Parameter Choice on Sequence Sensitivity to Random Noise

Monte Carlo simulations were performed to assess the impact of the LL-TFEPI sequence parameters on random errors in fitting for R_1*. The first simulations took each parameter in turn (N, m, τ, TI, TA and FA, it was assumed that TW = TA as the readouts were spaced evenly through the SSI) and varied that parameter keeping the remainder constant. 1000 LL-TFEPI curves were simulated using the full model and Gaussian random noise added with zero mean and standard deviation of $0.01M_0$ to model the noise present in-vivo. These were fitted to Equation 7-15 (fitting for R_1*), the percentage difference between the fitted value and ideal value was then calculated. The variance in the 1000 measures was taken and the results are shown in Figure 7-15 (solid lines).

The second set of Monte Carlo simulations took into account that the sequence parameters are not independent of one another, except for flip angle. A formula for scan time, t_{total}, was calculated;

$$t_{total} = \frac{SSI.FOV.N_{slice}.1.15}{6m.VOX}, \quad \textbf{7-27}$$

where FOV is the field of view in mm, N_{slice} is the number of slices, 1.15 is the oversample factor, m is the number of RF pulses per block, VOX is the in-plane voxel size and 6 takes into account the EPI factor and the SENSE reduction factor. SSI is the shot-to-shot interval, given by

$$SSI = TI + N.TA + (m-1).\tau, \quad \textbf{7-28}$$

where the symbols are the sequence timings given in Figure 7-5. The scan time, t_{total}, was chosen to be 5 minutes, with a FOV/VOX ratio of 160. When m, τ or N were varied then TA changed to maintain SSI, using Equation 7-28, and hence the scan time. When TA was varied, SSI and hence M was changed correspondingly. The effect of TI was not simulated as the initial simulations demonstrated little effect of this on the error in the fit. The results of these simulations are illustrated in Figure 7-15 with the broken lines.

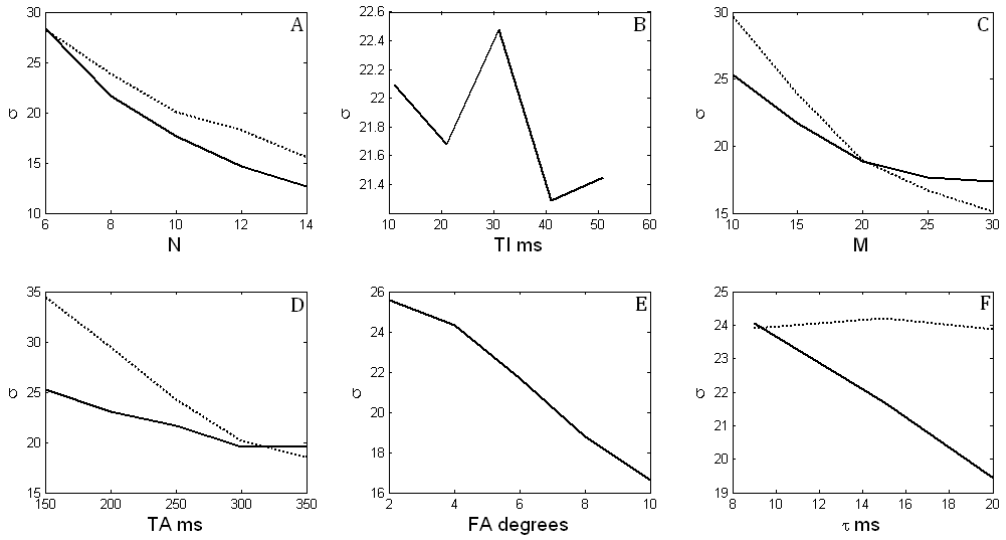

Figure 7-15: Standard deviation in fitted R_1* values due to (A) number of readouts, N (B) Inversion time, TI (C) TFE factor, m (D) readout spacing TA (E) flip angle and (F) pulse spacing τ. Solid lines show basic simulations, broken lines show time optimised simulations.

Figure 7-15, shows that TI and τ, when scan time is maintained, do not significantly effect the error in R_1* quantification. N, m, TA and FA need to be kept large to minimise fitting errors in R_1*.

To investigate the sensitivity to errors in the expected flip angle in the quantification of R_1, the systematic error in R_1 was calculated as a function of the sequence parameters. Errors were estimated using partial differentiation of Equation 7-15 and results are shown in Figure 7-16. This demonstrates that a 5 % error in the flip angle could lead to a 40 % error in R_1 (e.g. Figure 7-16 A, m = 15). Error in R_1 due to errors in knowledge of the flip angle is reduced if m and expected FA are kept small, and τ and TA are kept large. However, this shows that precise knowledge of the flip angle is critical, and that assessing the change in R_1 is preferable, as the B_1 term is then removed.

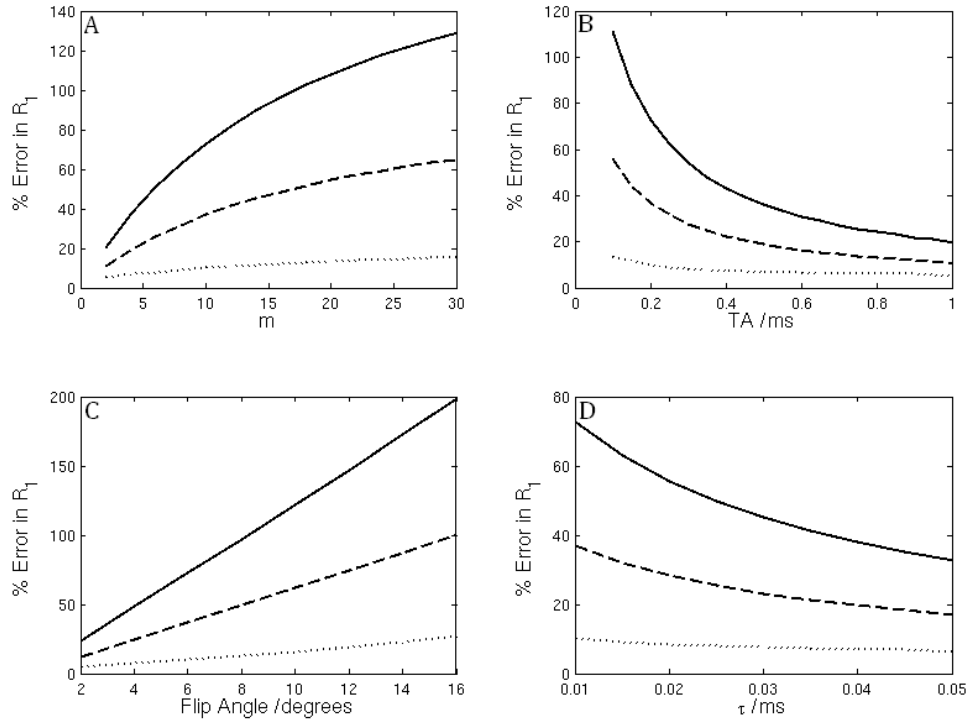

Figure 7-16: Error in R_1 due to error in flip angle estimate – variation with (A) TFE factor, m (B) readout spacing time, TA (C) flip angle and (D) pulse spacing, τ. The solid line represents a 10 % error in the expected flip angle, dashed line a 5 % error and the dotted line a 1 % error.

Further consideration when deciding on scan parameters is SAR and acoustic noise. SAR can be minimised by reducing the number of pulses per SSI and keeping the flip angle low. Acoustic noise, which can make the scan uncomfortable for patients and increase movement, can be reduced by keeping m and N low, or TA high.

Accounting for all the simulations, the following conclusions were drawn when finalising the sequence parameter choice for the experimental work. The minimum value of TI and τ were used as these were not found to impact greatly on fitting. A large flip angle would cause large errors if R_1 or T_1 were calculated directly, however increasing flip angle would improve the fit for R_1*. To allow investigation into the quantification of R_1 as well as ΔR_1* for CBV measurement, the flip angle was kept at 6°, providing adequate SNR for voxelwise fitting, but increasing the chances of accurate T_1 quantification. TA was chosen to be the maximum possible within the SSI, as this reduced both the error in fitting for R_1* and the systematic error in R_1. SSI and m were balanced to allow short scan time (low SSI, high m) and lower levels of acoustic noise (long SSI, low m), also reducing m reduces the systematic error in R_1. For the first in-vivo experiment, m

was kept low (15), with SSI = 3s, the longest SSI possible within a scan time of 5 minutes 45 seconds, to improve estimation of R_1. For the second in-vivo experiment, where the aim was fast high-resolution mapping of CBV and not absolute R_1 quantification, m was increased to 31.

7.7 Using LL-TFEPI To Monitor Gadolinium Uptake and to Measure Cerebral Blood Volume

Here two studies are performed to assess the measurement of the change in R_1 (ΔR_1) with the administration of a contrast agent and to use this to measure CBV. The first experiment studies six MS patients using the 16-channel coil. The second study on eleven MS patients uses the 32 channel coil which increases SNR allowing the spatial resolution to be increased.

7.7.1 *Measuring Relative Cerebral Blood Volume in MS using a Gadolinium Contrast Agent*

7.7.1.1 Methods

Six subjects took part in the study (3 females, 3 males, age 40 ± 11 years old), and all gave informed written consent. 5 subjects had Clinically Isolated Syndrome (CIS) and 1 had clinically confirmed relapsing remitting (RR) multiple sclerosis (MS). The scanning was performed on a Philips 7 T system with head volume transmit, and 16-channel SENSE receive coil. Patients were positioned in the magnet with foam padding to reduce head motion.

Two LL-TFEPI scans were performed, one prior to contrast agent administration and one after the administration of a Gadolinium contrast agent (Gadovist, Bayer Healthcare) as a bolus at 0.1 mmol / kg body weight. The LL-TFEPI scan parameters were: SSI = 3s, N = 8, m = 15, P = 3, $\alpha = 6°$, $\tau = 9$, TA = 245 ms, TI = 21 ms, TW = 242 ms, SENSE = 2, FOV = 200 x 170 x 72 mm^3 with 1.25 mm isotropic voxels, and low-high Cartesian k-space acquisition order. This gave a total scan time of 5 minutes 45 seconds. Magnitude and phase data were saved allowing for sign correction.

A B_1 field map was also acquired using the AFI method of Yarnkyh [26] with 3D GE imaging parameters: 3 x 3 x 5 mm^3 voxel size, FOV 200 x 200 x 75 mm^3, TE 5 ms, TR1 / TR2 = 23 / 103 ms, gradient spoil factor 5, flip angle 60°.

7.7.1.2 Data Analysis

To define grey and white matter masks the modulus images were segmented using SPM8 (*www.fil.ion.ucl.ac.uk*). Lesions were included in the grey matter masks due to their longer T_1, so these were then excluded manually (*Analyze 9, Mayo Clinic, US*) to avoid lesions affecting mean T_1 measures.

The phase data was used to sign correct the modulus data. The data were then fitted voxelwise for R_1* in Matlab (*The Mathworks, MA, USA*). The B_1 maps were realigned and resampled to the LL-TFEPI matrix size using the affine transformation in FLIRT, (FSL, FMRIB, Oxford). These were then used to produce maps of T_1 pre- and post-contrast. The post-contrast inversion recovery images were realigned to the pre-contrast images to account for small movement between scans, and this transform applied to the post-contrast R_1 and R_1* maps. The R_1* maps were subtracted to give ΔR_1 maps independent of B_1. The mean B_1, ΔR_1, and pre- and post-contrast R_1* and T_1, in grey and white matter was calculated.

The ΔR_1* maps were then converted to cerebral blood volume maps using Equation 7-19. The change in blood R_1 was determined by applying a threshold to the ΔR_1 map, as the blood vessels have the largest ΔR_1. The threshold was chosen so that the sagittal sinus was visible and the average ΔR_1 in these voxels was taken to give blood ΔR_1. The resulting CBV maps were spatially smoothed with a Gaussian kernel (FWHM = 2.5 mm). The average CBV in the grey and white matter masks was then calculated.

Wilcoxon signed rank test was used to assess differences between pairs of results for R_1*, T_1 and B_1. ΔR_1 is tested using a two tailed t-test for non-zero mean (SPSS v19, IBM).

7.7.1.3 Results

The high quality of the images and high SNR are shown in Figure 7-17. Figure 7-17 A are the magnitude images for an example slice over the 8 readouts. Figure 7-17 B is an example, single-voxel, inversion-recovery curve from grey matter (broken line) and white matter (solid line). The locations of the voxels are shown in A.

An example fitted R_1^* map is shown in Figure 7-18; pre- (A) and post-contrast (B). MS lesions are highlighted in the pre-contrast images. The post contrast sagittal

view is chosen to highlight blood vessels, whose R_1* is increased greatly post contrast due to the gadolinium.

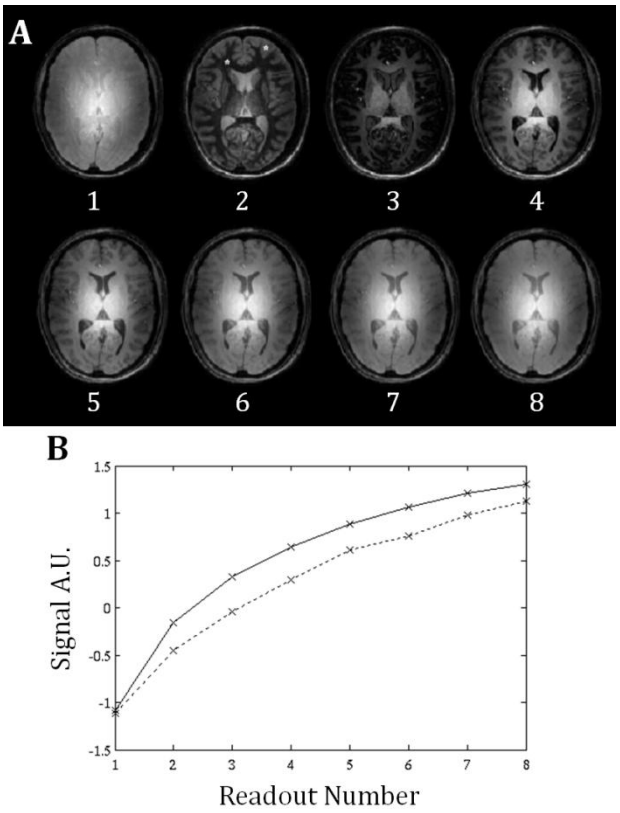

Figure 7-17 (A) Example LL-TFEP IR images with readout number shown below (B) IR curves from a grey matter (broken line) and white matter (solid line) voxel marked in (A).

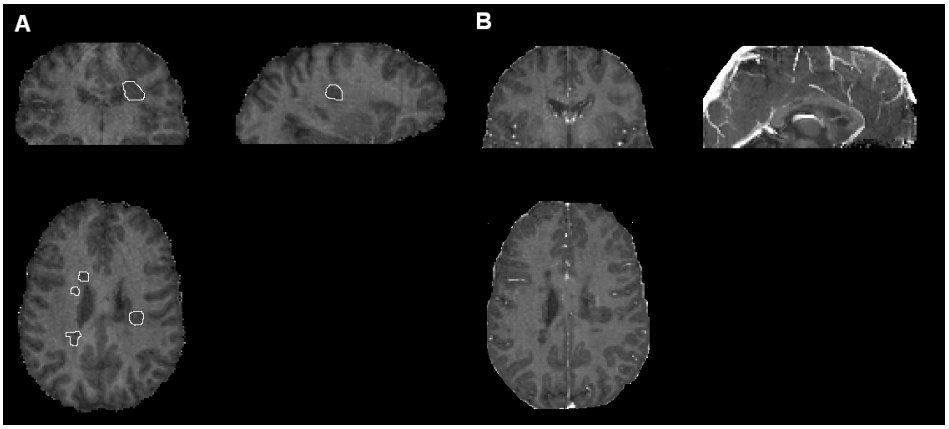

Figure 7-18 (A) R_1* map pre-contrast, MS lesions highlighted by white ROI (B) R_1* map post contrast showing enhancement in the vessels.

The CBV maps calculated from the change in R_1 are shown in Figure 7-19 for a single subject. These show that the grey matter (GM) has higher CBV than the white matter (WM). The average measured CBV was 5.1 ± 0.3 % and 2.5 ± 0.2 % in the grey and white matter respectively. CBV was significantly higher in the GM

than WM ($P < 0.05$, Wilcoxon sign rank test). As most of the patient group were diagnosed with CIS at time of scanning, few enhancing lesions were seen. One subject had a contrast enhancing lesion, shown in Figure 7-20.

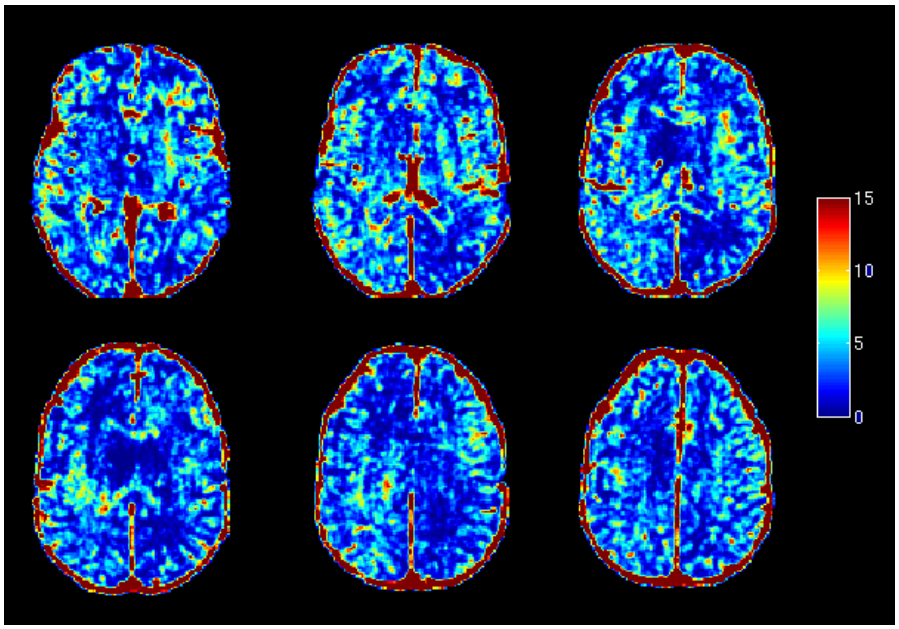

Figure 7-19: CBV maps from a single subject, (colour bar in %)

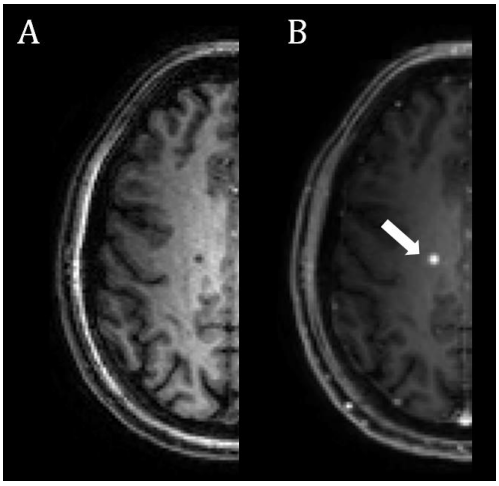

Figure 7-20: One subject had an enhancing lesion shown on 4th readout image (TI ~ 900 ms) (A) pre contrast and (B) post contrast LL-TFEPI image. White arrow indicates contrast enhancing lesion.

The group results for the 6 patients are shown in Figure 7-21. The results show a significant difference between white and grey matter for all metrics. Grey matter had a significant change in T_1 and ΔR_1, but not white matter. The grey matter has significantly higher CBV, and hence will show a great change in R_1. This is expected as the contrast agent is distributed in the blood, and will not leak into the tissue unless there is a break down of the blood brain barrier (BBB).

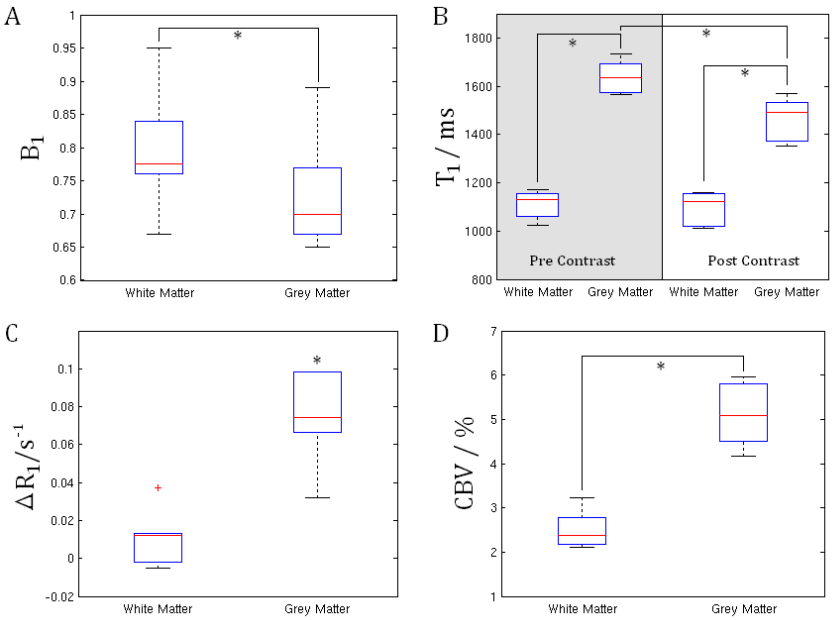

Figure 7-21: Results from gadolinium contrast experiment showing (A) average B_1 scaling factor (B) T_1 pre and post gadolinium, shaded area indicates pre contrast values, (C) ΔR_1 due to gadolinium and (D) CBV in white and grey matter. * indicates a significant difference, P<0.05.

7.7.1.4 Discussion

The baseline measured T_1 values in grey (1639 ± 30 ms) and white matter (1112 ± 26 ms) are lower than would be anticipated at 7 T given the results of previous studies (e.g. [11, 12]). This could be due to an inaccurate B_1 map giving the incorrect flip angle when converting from effective T_1/R_1 to actual T_1 and R_1 values. The average B_1 scaling factor in the grey and white matter is given in Figure 7-21 A. All the average B_1 values were below 1, suggesting that the flip angle achieved is always lower than the expected flip angle. The average B_1 value is higher in the white matter; this is expected as the white matter is predominantly in the centre of the brain where the flip angle profile is highest. There is a large variation in the B_1 scaling values for both tissue types; this is due to the large volume covered by the B_1 map (7 cm thick section). As the T_1 values are low, it is suggestive of an underestimated B_1 factor (increase FA to increase T_1 estimate, Figure 7-22). For contrast agent uptake, the change in R_1 is normally adequate, and hence this method of measuring the change in R_1 can be used, as no B_1 information is required.

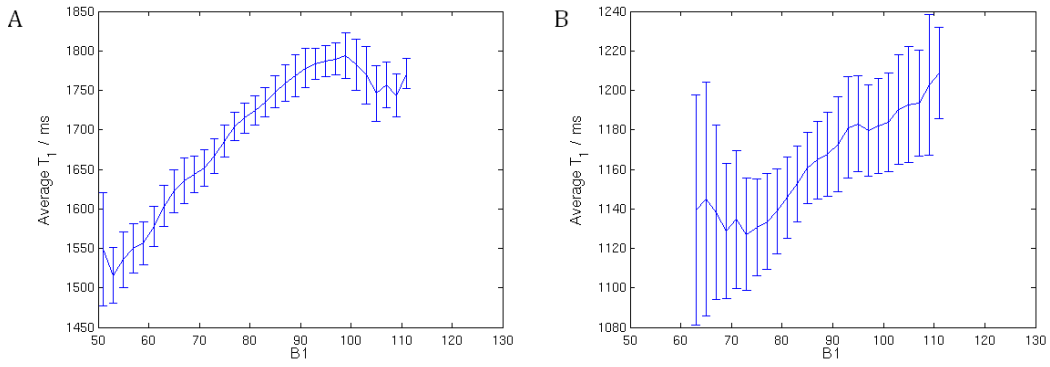

Figure 7-22: Relationship between calculated T_1 value and B_1 in (A) grey matter and (B) white matter. Data shown subject averaged, error bars represent standard error across subjects.

7.7.2 HIGH RESOLUTION MAPPING OF CBV IN MS PATIENTS USING GADOLINIUM

The second study was implemented to assess the change in R_1 due to the administration of a Gadolinium based contrast agent in Multiple Sclerosis, with the emphasis on high resolution (1 mm isotropic).

7.7.2.1 Methods

11 subjects took part in the study (6 females, 5 males, age range 28 - 58 years old), and all gave informed written consent. 5 subjects had Clinically Isolated Syndrome, 5 had clinically confirmed relapsing remitting (RR) multiple sclerosis (MS) and 1 secondary progressive MS. The scanning was performed on a Philips 7 T system with head volume transmit, and 32-channel SENSE receive coil. Patients were positioned in the magnet; foam padding was used to reduce head motion.

Two LL-TFEPI scans were performed, one prior to contrast agent administration and one after the administration of a Gadolinium contrast agent at 0.1 mmol / kg body weight. The LL-TFEPI scan parameters were: SSI = 3 s, N = 8, m = 31, P = 3, $\alpha = 6^{\circ}$, $\tau = 9$, TA = 245 ms, TI = 21 ms, SENSE = 2, FOV = 200 x 170 x 72 mm^3 with 1 mm isotropic voxels with a low-high Cartesian k-space acquisition. This gave a total scan time of 4 minutes 21 seconds.

7.7.2.2 Data Analysis

The data was analysed as in Section 7.7.1.2 to give CBV maps. Average CBV in grey and white matter was calculated.

7.7.2.3 Results

The image quality achieved with the high resolution LL-TFEPI scan is demonstrated in Figure 7-23. Using the 32-channel coil is acquire higher spatial resolution data has not noticeably affected the SNR ratio of the acquired images.

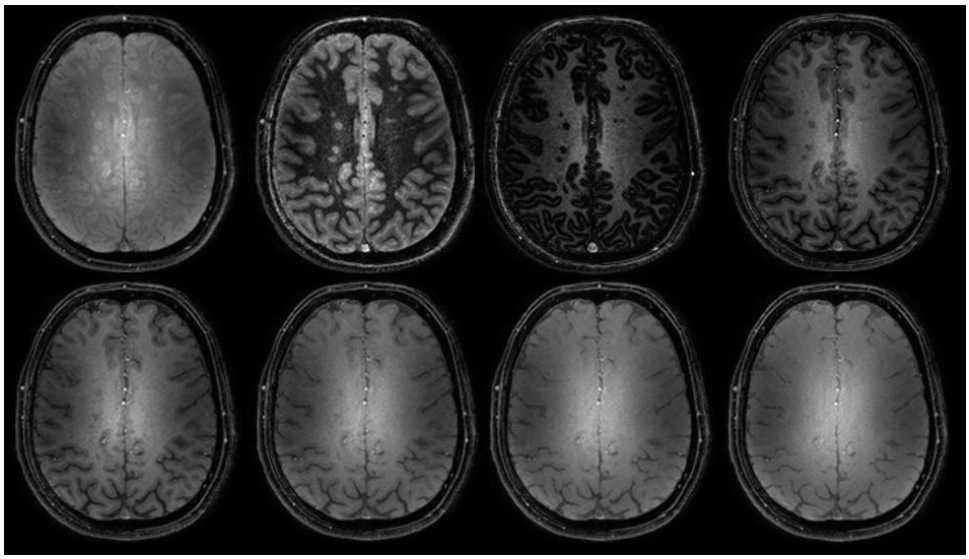

Figure 7-23: Example images from a representative subject for the high resolution LL-TFEPI sequence over the 8 readouts.

Figure 7-24 shows an example CBV map acquired using the high resolution LL-TFEPI scan. The expanded section shows how the cortical detail is maintained in the final CBV map. Over the eleven subjects, GM CBV was 5.2 ± 0.3, and WM CBV was 1.9 ± 0.1 %. These values agree well to the results obtained with the lower resolution scan. Only three subjects had any contrast enhancing lesions and examples are shown in Figure 7-25.

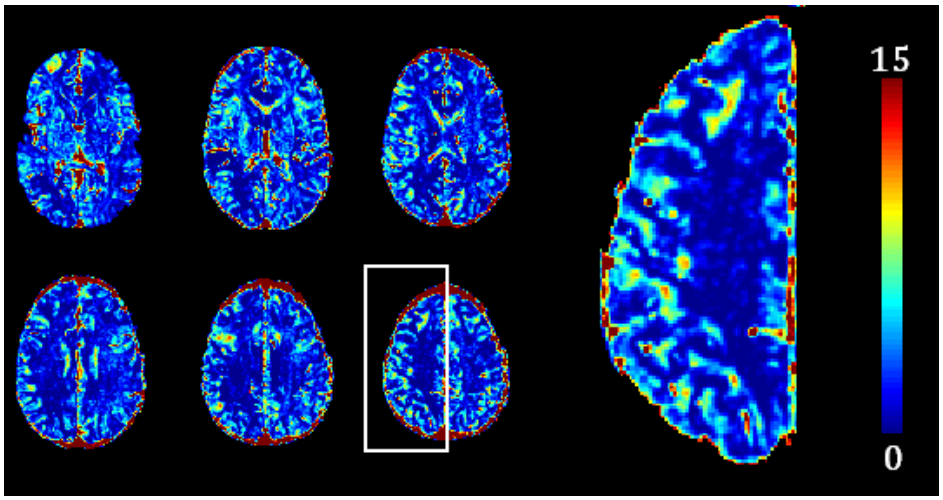

Figure 7-24: High resolution CBV maps from a representative subject. White box shows expanded section. Colour bar is CBV in %.

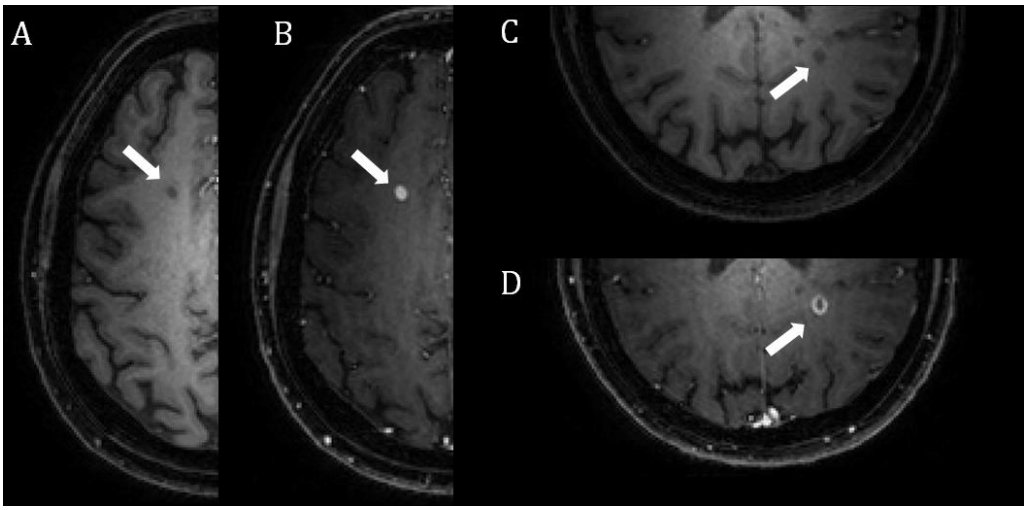

Figure 7-25: Two enhancing lesions in the same subject, 4th phase pre (A, C) and post (B, D) contrast LL-TFEPI images. White arrows indicate contrast enhancing lesion.

7.7.3 DISCUSSION

These experiments have shown that the LL-TFEPI sequence can be used to achieve high spatial resolution, large volume coverage ΔR_1 maps following gadolinium contrast agent without dependence on the B_1 field. The ΔR_1 maps can be used to assess the uptake of gadolinium and converted into cerebral blood volume maps.

The patients scanned demonstrated few enhancing lesions, likely due to the patient subgroups that were examined and the small sample size. Patients with CIS are least likely to have enhancing lesions, as they will only have presented with one neurologic episode up to that point.

A possible confound for the CBV quantification is the choice of threshold to determine the change in R_1 of the blood. Here, the threshold was chosen by visual inspection of the data so that the sagittal sinus was included in the mask but excluding minor vessels by increasing the threshold. To assess the impact of the threshold chosen on CBV this value was varied, the results are shown in Figure 7-26. As the threshold increases the average CBV value decreases as this causes $\Delta R_{1,blood}$ to increase. An alternative would be manually segment vessels, however this would be time consuming and an automated method is preferable when analysing multiple subject data sets. In addition the values found here from the two studies (GM 5.1 - 5.2 % and WM 1.9 – 2.5 %) agree well with literature values (GM 4.8 – 5.5 %, and WM 1.4 – 2.7 % from [33]).

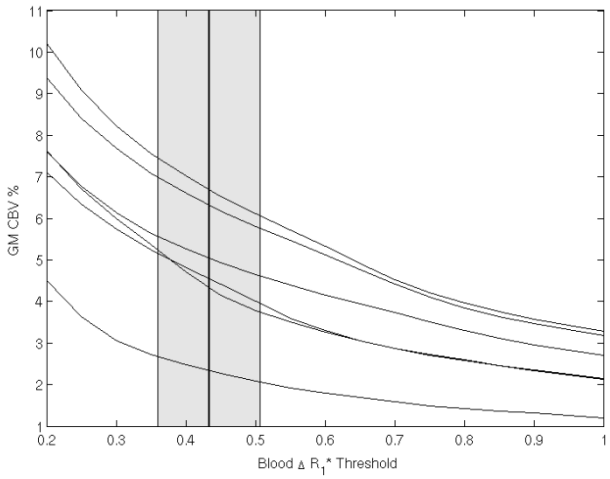

Figure 7-26: Effect of blood ΔR_1 threshold on GM CBV quantification. Vertical line shows the mean threshold used for final CBV quantification, shaded region is mean ± standard error. All six subjects from the low resolution study shown.

7.8 HIGH RESOLUTION BIAS FIELD CORRECTED ANATOMICAL IMAGING

Anatomical imaging using T_1 weighted contrast is very common in both clinical and research protocols as it allows for delineation of different tissue types (e.g. grey and white matter) and anatomical localisation. Many different types of T_1 weighted image sequences exist, with some inversion recovery based sequences summarised in Table 7-1.

Name of Sequence	Brief Description
MPRAGE – Magnetisation Prepared Rapid Gradient Echo	Inversion pulse prior to a rapid GE sequence. TI can be altered for different contrast.
FLAIR – FLuid Attenuated Inversion Recovery	Single inversion prior to imaging, TI is chosen to null the signal from fluid (e.g. CSF)
DIR – Dual Inversion Recovery	Two inversion pulses, timing optimised to null signal from two tissue types
STIR – Short TI Inversion Recovery	A short inversion time is used to null signal from fat to reduce fat artefacts

Table 7-1: Common inversion recovery based T_1 weighted imaging sequences.

T_1 weighted images (e.g. MPRAGE) are displayed as modulus images; this can mean discarding information from the inversion recovery, as different tissue types can have the same magnitude values but be on opposite sides of the null point due to different T_1 values. The dynamic range of an image can be improved by incorporating the phase information, termed Phase Sensitive Inversion Recovery (PSIR) [34]. PSIR imaging is commonly used in heart imaging, such as for the study of myocardial infarction [35]. However, it is also used in neuroimaging [36], including the identification of intracortical lesions in Multiple Sclerosis [37].

To enable the correction of the modulus images for PSIR imaging, the phase needs to be calculated. However a single phase image cannot be used, as the phase images do not give absolute quantities. Hence a reference image is collected, when all tissue types have recovered, this allows calculation of the phase change between the two images. The PSIR sequence is shown schematically in Figure 7-27. It is equivalent to the LL-TFEPI sequence but with only two readouts per inversion (N = 2). For example, Figure 7-28 shows PSIR images generated from data shown in Section 7.7.2. This demonstrates how the PSIR contrast changes with the effective post-inversion delay.

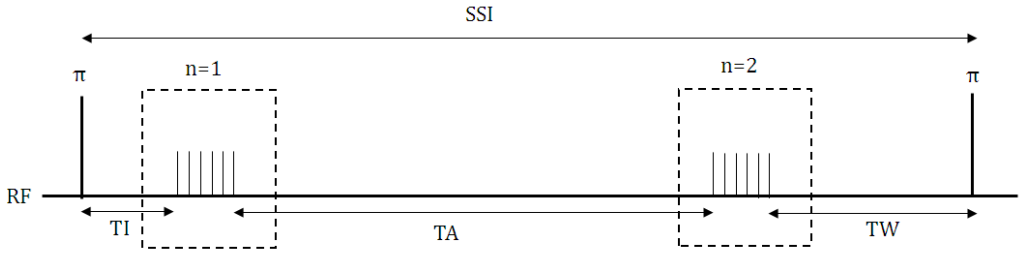

Figure 7-27: Schematic of the RF pulses for the PSIR sequence.

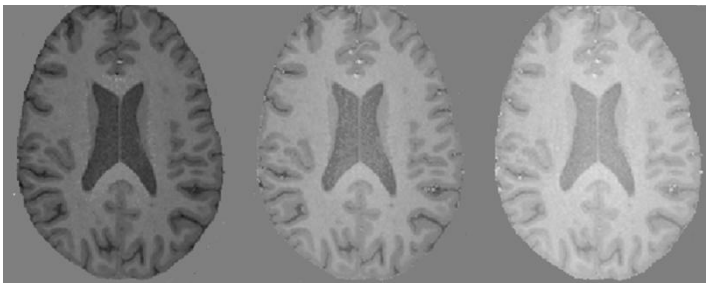

Figure 7-28: Example PSIR images created from LL-TFEPI data at three successive post inversion delays.

Marques *et al.* [38] proposed an alternative scheme entitled MP2RAGE, where two MPRAGE images were collected as in Figure 7-27. Rather than phase correct the first image using the phase information in the second the complex signals for the two images were combined using the following relationship

$$MP2RAGE = real\left(\frac{x^{*}y}{|x|^{2}+|y|^{2}}\right), \qquad \textbf{7-29}$$

where x is the signal from the 1st acquisition and y the 2nd, and * denotes the complex conjugate. This keeps the phase information, and allows for correction of transmit inhomogeneities, but it restricts the dynamic range of the image between -0.5 and +0.5. They obtained images at resolutions of 0.5 – 1 mm at 7 T, to achieve large coverage (160 slices) in a scan time of 12 minutes required

partial Fourier factor of 0.75 and parallel imaging factor of 3. PSIR requires a simpler reconstruction method whilst maintaining phase information and correction for B_1 effects.

The aim of this work is to develop a high resolution sequence that maximises contrast between grey and white matter structures for use in patient protocols, for example MS or Alzheimer's disease. Hence it was also required that the scan was short, approximately 10 minutes, to reduce the impact of motion, of particular concern for patient studies. Large volume coverage, potentially whole brain, would be preferably as MS and Alzheimer's can affect the entire brain.

7.8.1 BIAS FIELD CORRECTION

Magnitude images, such as that in Figure 7-29 A, can display signal variations due to underlying inhomogeneities in the static magnetic field and the transmit and receive fields. These can be seen as bright areas in the centre of the image from the flip angle profile, or signal voiding from poor shim. Field inhomogeneities can make it difficult to see the fine structure in the centre of the image, for example deep gray matter structures, or structures low down (e.g. cerebellum).

These inhomogeneities will be transmitted to phase corrected images, Figure 7-29 B is the phase corrected image of A. This shows increased dynamic range of the image, but the inhomogeneities are clearly seen. To reduce this effect, the image is normalised to the reference image (C), '*flattening'* out the images. This is most effective in the centre of the image, such as around the ventricles where structures are now more clearly delineated and any asymmetry in the raw images has also been removed. This was shown to be effective at correcting MPRAGE images acquired at 7 T [39].

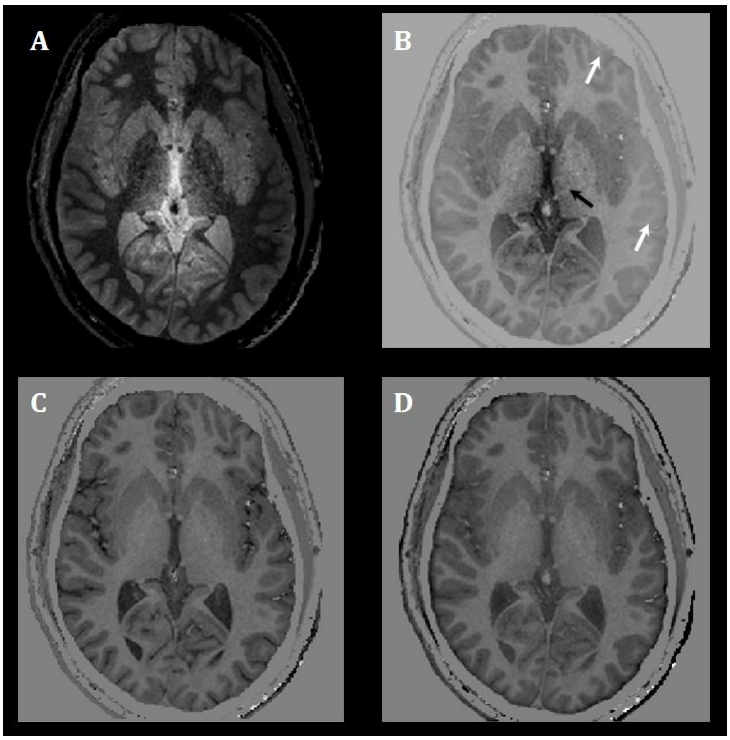

Figure 7-29: (A) Raw modulus image (B) Phase corrected version of (A), arrows represent signal abnormalities caused by underlying image inhomogeneity (C) PSIR normalised to reference image and (D) PSIR normalised to smoothed reference image.

7.8.2 COMPARISON OF PSIR AND MP2RAGE

PSIR and MP2RAGE both use the same acquisition sequence and only differ in the reconstruction of the images. To assess which sequence is the most appropriate the signal and contrast properties of the two was simulated.

As highlighted in Marques *et al.* [38] the theoretical signal to noise of the MP2RAGE is higher due to the noise propagation in the PSIR, as summarised in Table 7-2.

	PSIR	MP2RAGE
Signal, S	$\frac{x}{y}$	$\frac{xy}{x^2+y^2}$
Noise, σ	$\delta\sqrt{\frac{x^2+y^2}{y^4}}$	$\delta\sqrt{\frac{(x^2-y^2)^2}{(x^2+y^2)^3}}$
$SNR = \frac{Signal}{Noise}$	$\frac{x}{y\delta}\sqrt{\frac{y^4}{x^2+y^2}}$	$\frac{xy}{\delta(x^2+y^2)}\sqrt{\frac{(x^2+y^2)^3}{(x^2-y^2)^2}}$
$\left\lvert\frac{SNR_{MPRAGE}}{SNR_{PSIR}}\right\rvert$	$\left\lvert\frac{x^2+y^2}{x^2-y^2}\right\rvert \geq 1$	

Table 7-2: Signal and noise characteristics of the PSIR and MP2RAGE sequences, where x and y are the signal from the tissue from the two images, it is assumed that the absolute error in x is equal to the absolute error in y, which is equal to δ.

In addition to the SNR of the sequence, an important characteristic is the contrast to noise (CNR) between different tissue types for discrimination of different tissues, important in the study of Multiple Sclerosis lesions as the T_1 differs from the surrounding normal appearing white matter (NAWM). The contrast to noise between two tissues is defined as

$$CNR = \frac{S_{tissue,1} - S_{tissue,2}}{\sqrt{\sigma_{tissue,1}^2 + \sigma_{tissue,2}^2}}, \qquad \textbf{7-30}$$

where S is the signal from either the PSIR or MP2RAGE sequence, and σ is the noise. The CNR for both sequences can be calculated using Table 7-2:

$$CNR_{PSIR} = \frac{\frac{x_1}{y_1} - \frac{x_2}{y_2}}{\delta\sqrt{\frac{x_1^2 + y_1^2}{y_1^2} + \frac{x_2^2 + y_2^2}{y_2^2}}},$$

$$CNR_{MP2RAGE} = \frac{\frac{x_1 y_1}{x_1^2 + y_1^2} - \frac{x_2 y_2}{x_2^2 + y_2^2}}{\delta\sqrt{\frac{(x_1^2 - y_1^2)^2}{(x_1^2 + y_1^2)^3} + \frac{(x_2^2 - y_2^2)^2}{(x_2^2 + y_2^2)^3}}}, \qquad \textbf{7-31}$$

where x_1, y_1 and x_2, y_2 are the signals from tissue 1 and tissue 2 respectively. The ratio of $CNR_{PSIR}/CNR_{MP2RAGE}$ is shown in Figure 7-30, demonstrating that the CNR between two tissue types is always greater for PSIR than MP2RAGE, with an improvement of a factor of 5 for PSIR. The range of the simulations are that $y_1 > x_1$ and $y_2 > x_2$, shown here is the case where $y_1 \geq 0.8$ (as CNR is symmetric, e.g. $CNR(x_1/y_1 = a, x_2/y_2 = b) = CNR(x_1/y_1 = b, x_2/y_2 = a)$, y_2 is kept equal to 1). For smaller values of y the improvement in CNR increases.

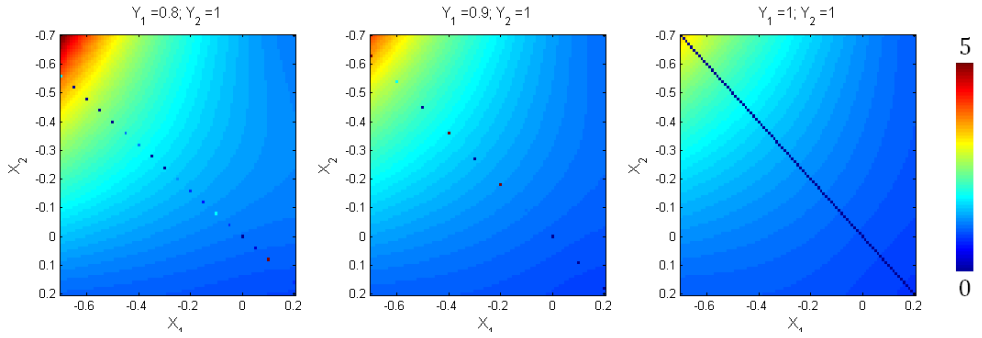

Figure 7-30: Ratio of $CNR_{PSIR}/CNR_{MP2RAGE}$ for different signal intensity combinations. Dark blue pixels identify the areas where the two tissue types are the same.

An example PSIR and MP2RAGE image are shown in Figure 7-31, with the corresponding image histograms. It can be seen that MP2RAGE is confined

between -0.5 and +0.5 whereas PSIR has a larger dynamic range. The histogram of the PSIR easily allows identification of the different tissue types whereas the histogram of the MP2RAGE is more ambiguous. The PSIR histogram may allow identification of deep gray matter structures, due to the small peak at low positive values as the average signal intensity in the putamen from Figure 7-31 is 0.077 ± 0.003 and in the caudate nucleus 0.067 ± 0.007.

For the identification of lesions the improved CNR between tissue types that is afforded by the PSIR is crucial. The MP2RAGE, with the improved SNR, may be more appropriate if looking to quantify T_1, as demonstrated in [38], where high SNR will be important. Whereas for tissue type discrimination (e.g. segmentation or lesion identification) the improved CNR of PSIR is more important.

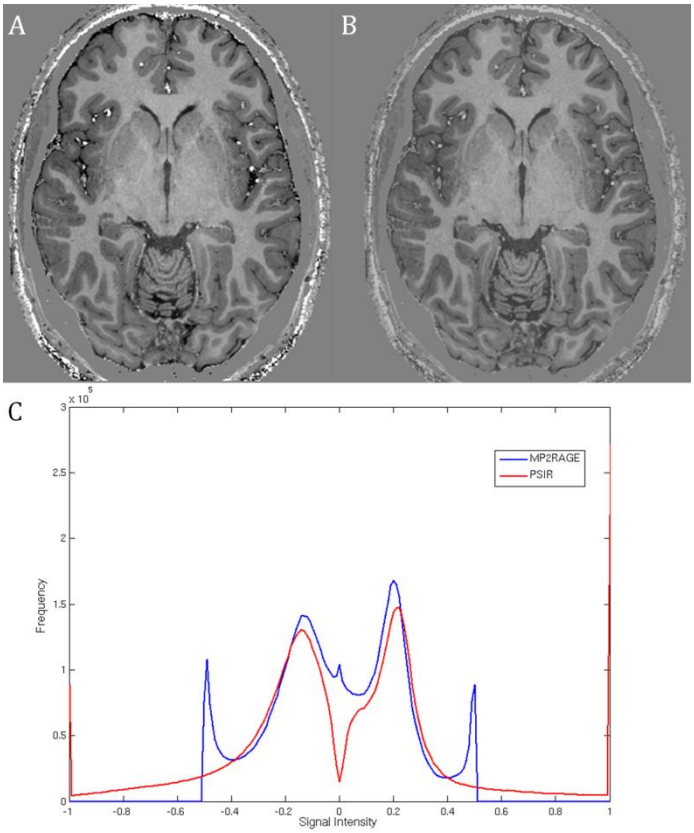

Figure 7-31: (A) PSIR image and (B) equivalent MP2RAGE image, (C) is the signal intensity histogram of PSIR (red) and MP2RAGE (blue).

7.8.3 *OPTIMISATION OF PSIR FOR GREY-WHITE MATTER CONTRAST*

The PSIR signal was simulated, as described in Section 7.4, using the full model with N = 2. A steady state was established by simulating several shots. The optimisation criteria was to maximise

$$S_{PSIR} = |x_1 - x_2|, \quad \textbf{7-32}$$

where subscript 1 represents grey matter and 2 white matter. The signal ratio (x/y) was not optimised as the reference image (y) has little contrast remaining ($y_1 \approx y_2$) due to the high TFE factor required to acquire high resolution images in short scan times. The theoretical time taken for the scan (Equation 7-27) must be less than 12 minutes, for patient comfort and to reduce motion artefacts, and x_1 and x_2 must be of opposite polarity (opposite sides of the null point) to benefit from PSIR. The scan optimised was of 0.6 mm isotropic resolution, FOV 192 x 172 mm with 160 slices (coverage 9.6 cm), using an EPI factor of 3 and SENSE reduction factor of 2.5.

The parameters of interest were TI, TA, TW, FA and m. τ was fixed to the minimum achievable value, as from previous simulations it was known to not greatly impact on the signal curves over a realistic range of values. The parameters were varied over a large range (TI 50 - 550 ms, TA 50 – 550 ms, TW = 100 – 4,000 ms, FA = 2 - 12° and m = 40 - 150) to find the optimum sequence parameter combination. The sequence was chosen to have linear k-space ordering to allow shorter values of TI, but still allowing GM and WM signals to have opposite sign.

Table 7-3 shows the results of the optimisation for GM/WM CNR for two different values of grey matter T_1 (from literature values 1939 [12] and 2,132 ms [11],). T_1 of white matter was simulated as 1300 ms, with M_0 simulated as 1.2 for GM and 1 for WM [29].

Parameter	T_1 = 2100 ms	T_1 = 1900 ms
Flip Angle [degrees]	9	10
TI [ms]	550	250
TW [ms]	2000	3000
TA [ms]	1300	600
m	69	69

Table 7-3: Optimised parameters for two different values of the T_1 of grey matter.

Further optimisation was performed for a scan that does not use the EPI factor but increases the SENSE reduction factor to maintain a short scan time but

reduces any distortions due to the lengthened echo time of LL-TFEPI. This gave TI/TA/TW= 150/400/3000 ms and m = 110 with τ = 13 ms, total scan time of 12 minutes with SENSE of 2/2.5 applied in two directions.

7.8.4 METHODS

Data Acquisition

All experiments were performed on a Philips 7 T Achieva system with volume transmit and 32 channel SENSE receive coil.

Two healthy volunteers were scanned, one using the PSIR LL-TFEPI scan optimised for a T_1 of 2100 ms and the other for a T_1 of 1900 ms.

Further healthy volunteers were scanned with the PSIR LL-TFE scan to assess methods for reduction of flow artefacts. Two methods were compared; flow compensation and the use of saturation or rest slabs. Flow compensation uses gradients to ensure that the phase accumulated during the imaging is zero, by applying the same gradients but with opposite polarity should cancel the phase accumulated by the moving spins and not affect the stationary spins either [31]. This increases the echo time (hence the minimum pulse spacing), so will reduce the signal, here the echo time changes from 7 to 10 ms so the effect will be negligible. The rest slab saturates the signal using a 90° pulse inferior to the imaging volume prior to the acquisition of the images. This should reduce the signal from the blood, and also cause the phase to change less rapidly across the acquisition.

A male patient with Multiple Sclerosis was scanned with the optimised LL-TFE PSIR scan (TI/TA/TW= 150/400/3000 ms, M = 110, τ = 13 ms, total scan time of 12 minutes with SENSE of 2/2.5 applied in two directions). In addition, an MPRAGE was acquired for comparison. The MPRAGE scan parameters were FOV = 205 x 192 x 140 mm^3, 0.5 mm isotropic resolution, TE/TR/TI = 7/15/275 ms with a flip angle of 8°. Total scan duration 10 minutes.

Data Analysis

The images were converted to PSIR by sign correcting the first image using the phase information. The phase corrected image was then normalized to the smoothed second image (3D Gaussian smoothing kernel, 9 voxel extent, σ = 90 mm). The reference image was smoothed to reduce transmission of noise to the

PSIR image, as there is little structural information present in the reference image (Figure 7-33 D/E) smoothing has little impact on the PSIR image (Figure 7-29 C/D) [39].

The PSIR images were converted to give an angiogram using similar methodology to [39]. The vessels are extracted by applying a threshold (PSIR signal > 0.5) to the PSIR images (interpolated to 0.3 mm isotropic), to exclude tissue and CSF. Mean intensity projections (MIP) of the vessels are then produced along the three axes.

7.8.5 RESULTS

The PSIR images using the optimised values for a grey matter T_1 of 2100 ms are shown in Figure 7-32. The B_1 receive inhomogeneity has been removed by normalising to the smoothed reference image. However, after phase correction both grey and white matter are positive. This means that the phase correction has not improved the dynamic range of the image (except for CSF which has intensity < 0).

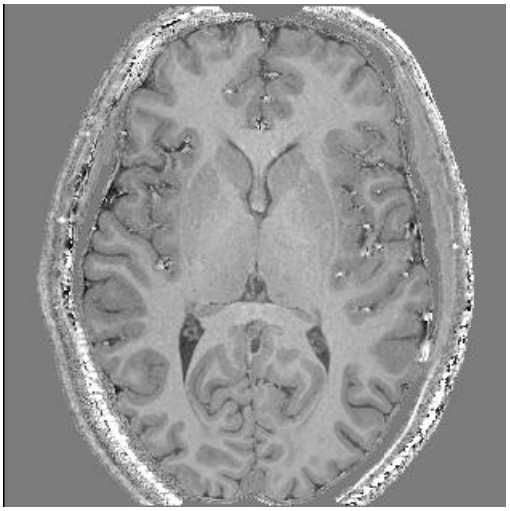

Figure 7-32: Example PSIR Image using optimised parameters for T_1 of grey matter = 2.1s.

The PSIR images using the second set of optimised parameters, where $T_{1,GM}$ = 1900 ms are shown in Figure 7-33 A. Here grey matter has not crossed the null so is negative in the PSIR image – increasing the dynamic range and contrast of the resultant images compared to the modulus image shown in Figure 7-33 B and the previous PSIR in Figure 7-32. The B_1 field correction has removed the hyper intensity shown in the middle of the images and the signal drop out on the right and left sides of the images in C-E.

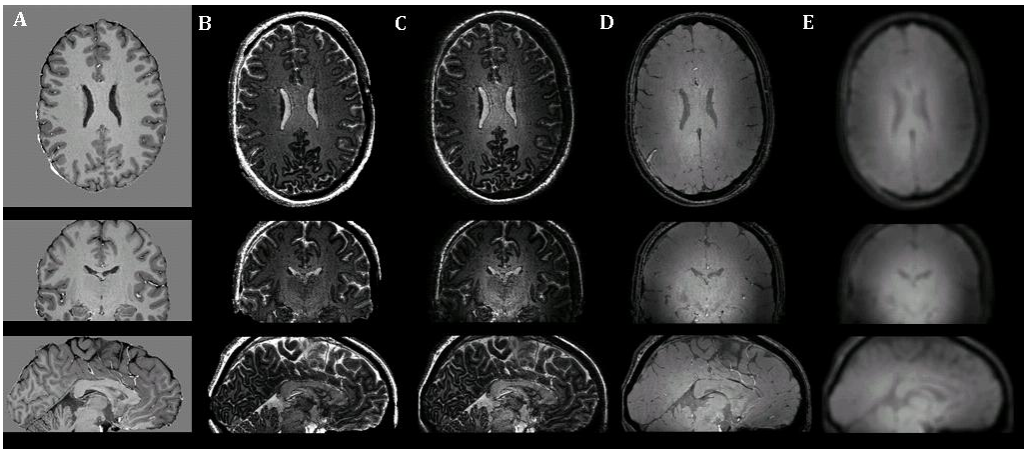

Figure 7-33: (A) PSIR image (B) Modulus of (A), (C) and (D) are raw images (E) smoothed images of (D) used for bias field correction.

Taking a histogram of the PSIR image from this scan shows two clear peaks on either side of 0 for grey and white matter. No clear peak is seen for CSF, this could be due to partial voluming between grey matter and CSF at the tissue boundaries. The deep gray matter is shown as the small positive peak (intensities of 0 – 0.1). The clear peaks allow for tissue segmentation using a simple threshold technique as demonstrated in Figure 7-34.

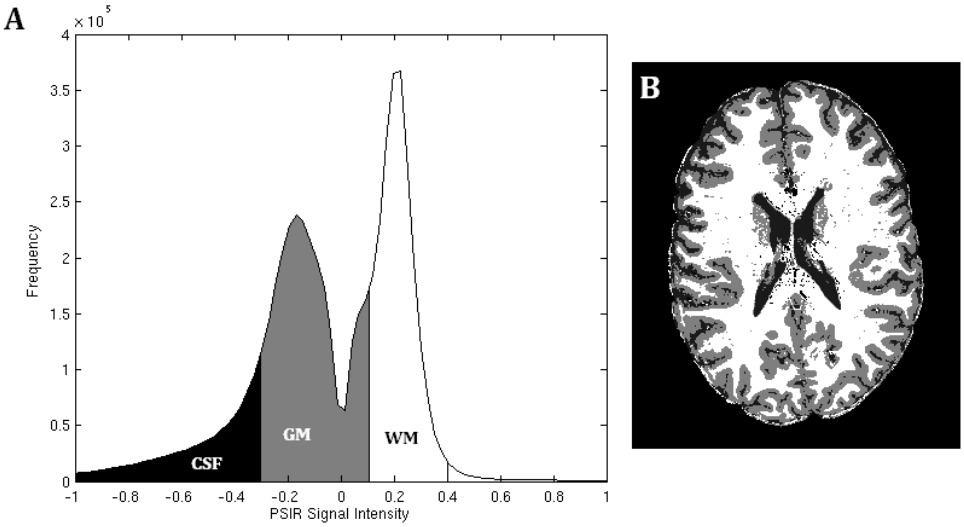

Figure 7-34: (A) Histogram of whole head PSIR image (B) Example slice of segmented PSIR, black is CSF, GM is gray and white matter is white.

The PSIR images show some artefacts, displayed as ripples, seen in the frontal regions of Figure 7-32. Removing the EPI factor, so that the scan was LL-TFE with a standard gradient echo readout, was found to remove these ripples (Figure 7-35). In addition an artefact from the blood vessels, which appears as a line across the image, was visible, shown by the black arrow in Figure 7-35. This is caused by blood flowing through a vessel during the applied gradients causing

ranging resonant frequencies, the phase acquired will cause the signal to be spatially misplaced in the phase encode direction – resulting in a band across the image in the PE direction (here right-left) [31].

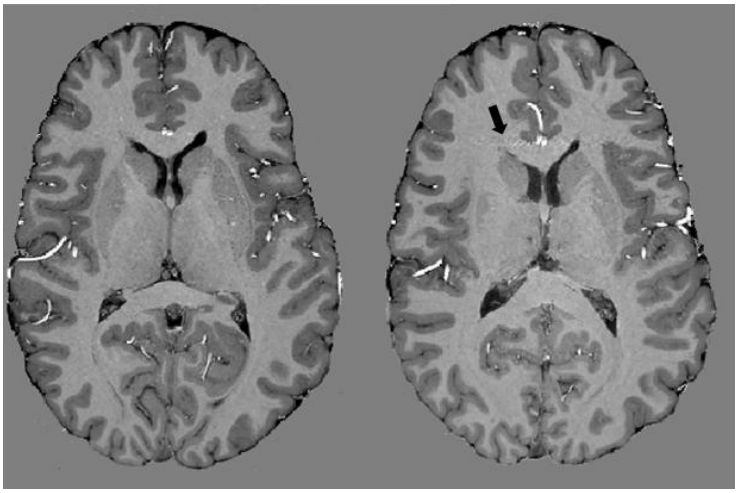

Figure 7-35: Example PSIR images from a single subject using LL-TFE, black arrow indicates blood artefact.

Flow compensation was found not to significantly reduce the artefact due to the flow, and it had the disadvantage of increasing the TR which would increase the readout duration. Using a rest slab was found to reduce the artefact significantly, Figure 7-36. This has the benefit of not increasing the pulse spacing as it is performed prior to the readout. The optimised LL-TFE PSIR with 160 slices, 0.6 mm isotropic resolution acquired with rest slabs is shown in Figure 7-37. This demonstrates whole brain coverage whilst maintaining good contrast between the white and grey matter.

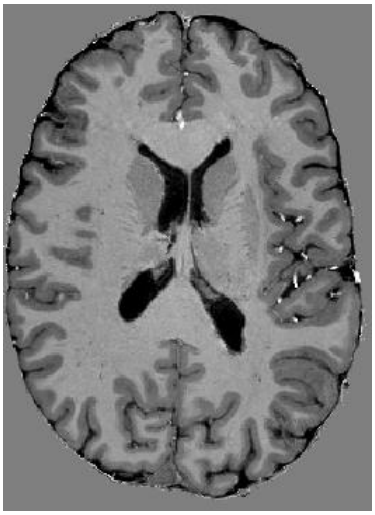

Figure 7-36: PSIR image where a rest slab has been used to reduce artefactual signal from the blood vessel.

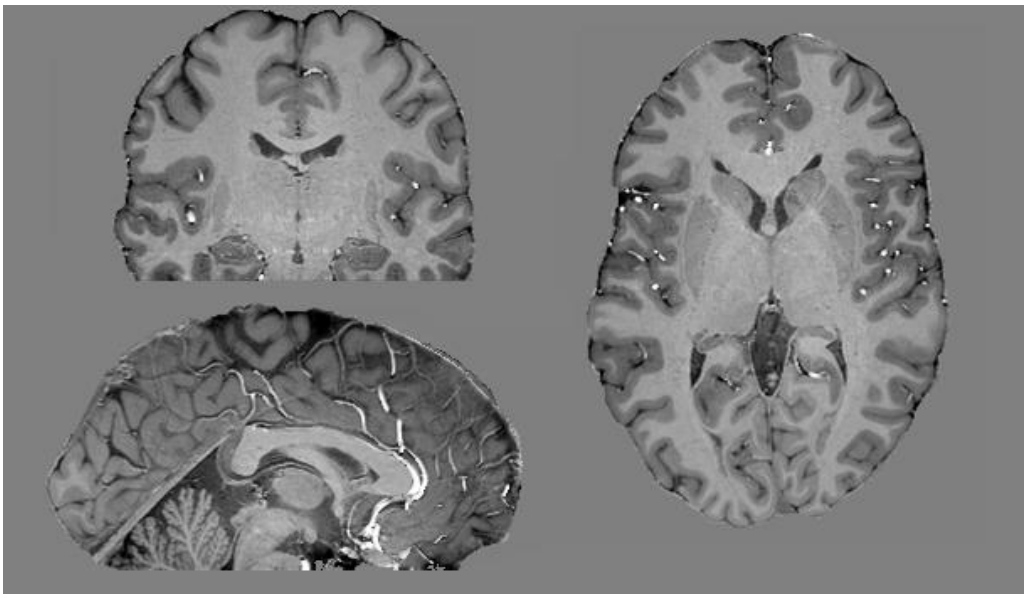

Figure 7-37: PSIR images acquired using LL-TFE with 0.6 mm isotropic voxels and 160 slices, with SENSE factor 2/2.5.

The mean intensity projections (MIP) produced along the three axes are shown in Figure 7-38. These clearly show vessel structure and could be used in patient groups where arterial vasculature is affected.

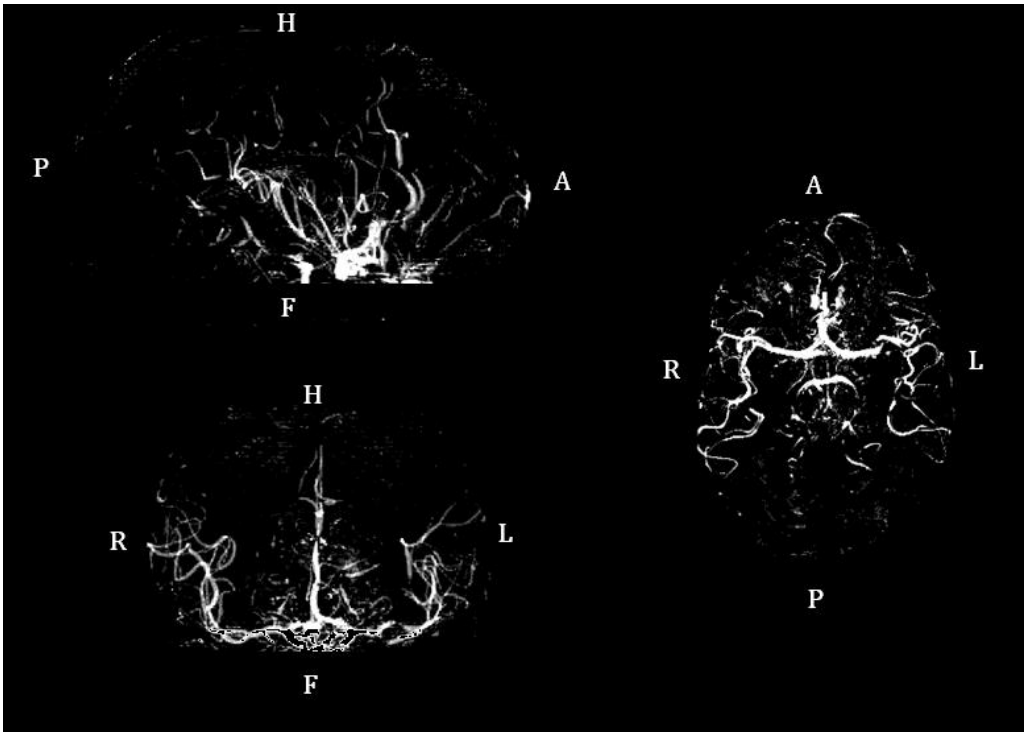

Figure 7-38: MIP produced from the PSIR image demonstrated in Figure 7-37.

Figure 7-39 demonstrates the PSIR acquired in a male patient with MS and a corresponding MPRAGE. The MPRAGE displays large inhomogeneities in the image intensity due to the bias field, whereas the PSIR contrast is more

homogenous across the slice allowing for easier tissue type discrimination. In this patient MS lesions are visible in the white matter surrounding the ventricles and this area on the MPRAGE is corrupted by the large scale inhomogeneities making lesion identification difficult. This demonstrates how PSIR could be useful in the assessment of clinical conditions.

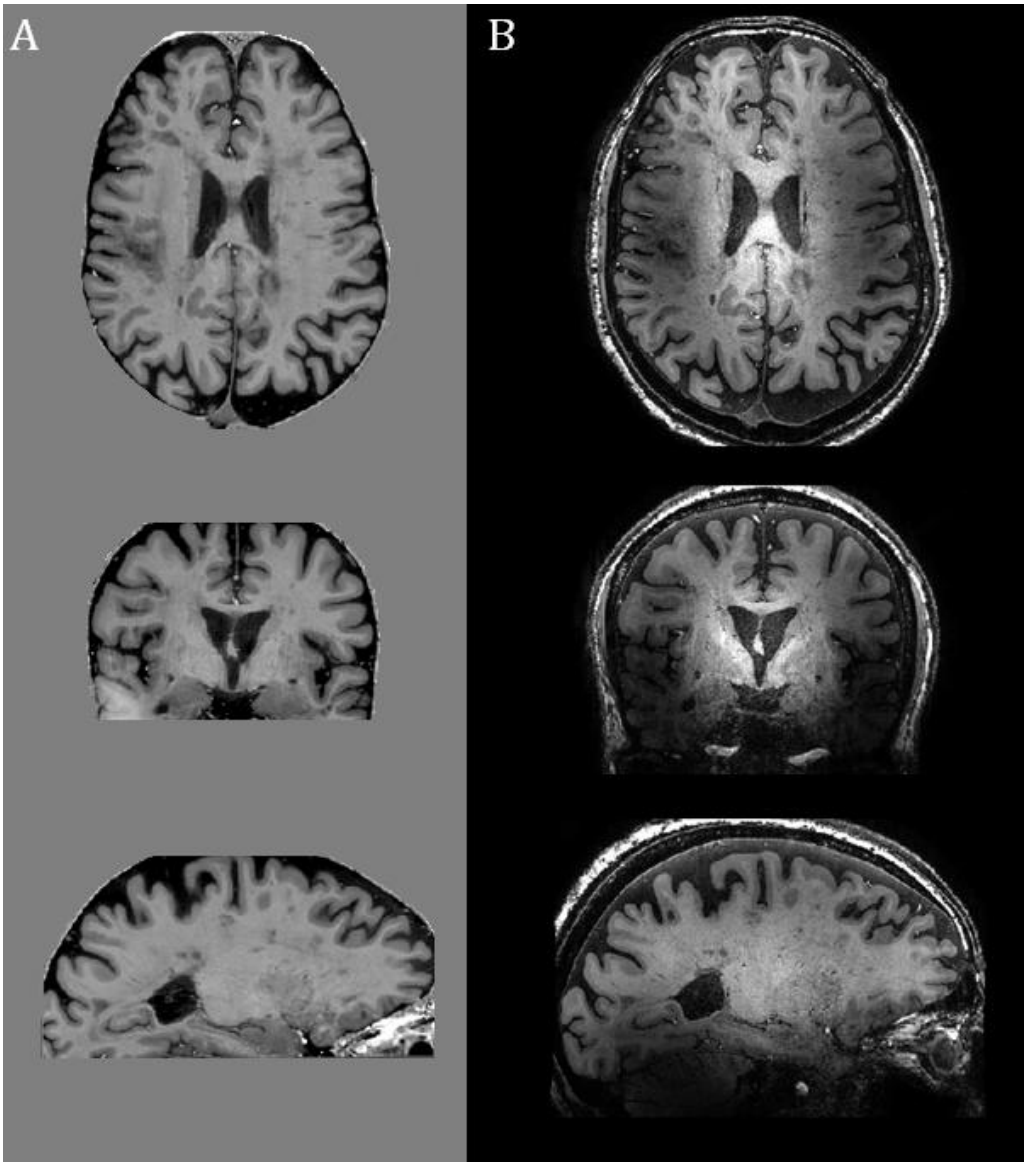

Figure 7-39: Anatomical images acquired in an MS patient using (A) PSIR and (B) MPRAGE.

7.8.6 DISCUSSION

LL-TFEPI has been shown to provide fast, high resolution T_1 weighted images that can be phase and bias field corrected using a dual readout scheme. Through simple CNR optimisation parameters were found to allow phase information to increase the dynamic range of the images improving CNR between grey and

white matter. A whole head, B_1 invariant scan, with 0.6 mm isotropic resolution was achieved in 12 minutes.

This scan can be used for tissue segmentation (as shown in Figure 7-34) due to high resolution and reduced B_1 artefacts, with applications in the study of pathology, such as Multiple Sclerosis, Figure 7-39, to aid in the identification of lesions.

7.9 CONCLUSION

The work in this chapter has shown the development of a sequence to measure ΔR_1 due to the administration of a gadolinium based contrast agent to allow measurement of CBV. The difficulties associated with quantitative T_1 mapping at ultra high field due to transmit inhomogeneity were demonstrated, as well as the problems with mapping the transmit field. An optimised method for bias field corrected, high resolution whole brain T_1 weighted anatomical imaging at 7 T has been demonstrated allowing for ease of tissue segmentation and arteriogram imaging.

7.10 REFERENCES

1. Roberts, H.C., T.P.L. Roberts, R.C. Brasch, and W.P. Dillon, *Quantitative Measurement of Microvascular Permeability in Human Brain Tumors Achieved Using Dynamic Contrast-enhanced MR Imaging: Correlation with Histologic Grade.* American Journal of Neuroradiology, 2000. **21**(5): p. 891-899.
2. Rother, J., F. Guckel, W. Neff, A. Schwartz, and M. Hennerici, *Assessment of Regional Cerebral Blood Volume in Acute Human Stroke by Use of Single-Slice Dynamic Susceptibility Contrast-Enhanced Magnetic Resonance Imaging.* Stroke, 1996. **27**(6): p. 1088-1093.
3. Miller, D.H., F. Barkhof, and J.J.P. Nauta, *Gadolinium enhancement increases the sensitivity of MRI in detecting disease activity in multiple sclerosis.* Brain, 1993. **116**(5): p. 1077-1094.
4. Kermode, A.G., A.J. Thompson, P. Tofts, D.G. Macmanus, B.E. Kendall, D.P.E. Kingsley, I.F. Moseley, P. Rudge, and W.I. McDonald, *Breakdown of the Blood-Brain Barrier Precedes Symptoms and other MRI Signs of New Lesions in Multiple Sclerosis.* Brain, 1990. **113**(5): p. 1477-1489.
5. Silver, N.C., C.D. Good, G.J. Barker, D.G. MacManus, A.J. Thompson, I.F. Moseley, W.I. McDonald, and D.H. Miller, *Sensitivity of contrast enhanced MRI in multiple sclerosis: Effect of gadolinium dose, magnetisation transfer contrast and delayed imaging.* Brain, 1997. **120**: p. 1149-1161.
6. Kollia, K., S. Maderwald, N. Putzki, M. Schlamann, J.M. Theysohn, O. Kraff, M.E. Ladd, M. Forsting, and I. Wanke, *First Clinical Study of Ultra-High-Field MR Imaging in Patients with Multiple Sclerosis: Comparison of 1.5T and 7T.* AJNR, 2009. **30**: p. 699-702.
7. MS_Society. http://www.mssociety.org.uk/. 2011 [cited 2011 14/11].
8. National_Multiple_Sclerosis_Society. http://www.nationalmssociety.org/. 2011 [cited 2011 15/11].
9. Davies, G.R., A. Hadjiprocopis, D.R. Altmann, D.T. Chard, C.M. Griffin, W. Rashid, G.J. Parker, P.S. Tofts, R. Kapoor, A.J. Thompson, and D.H. Miller, *Normal-appearing grey and white matter T1 abnormality in early relapsing-remitting multiple sclerosis: a longitudinal study.* Multiple Sclerosis, 2007. **13**: p. 169-177.
10. Tallantyre, E.C., M.J. Brookes, J.E. Dixon, P.S. Morgan, N. Evangelou, and P.G. Morris, *Demonstrating the perivascular distribution of MS lesions in vivo with 7-Tesla MRI.* Neurology, 2008. **70**(22): p. 2076-2078.

11. Rooney, W.D., G. Johnson, X. Li, E.R. Cohen, S.-G. Kim, K. Ugurbil, and C.S. Springer, *Magnetic Field and Tissue Dependancies of Human Brain Longitudinal ^1H_2O Relaxation in Vivo.* Mag. Res. Med., 2007. **57**: p. 308-318.
12. Wright, P.J., O.E. Mougin, J.J. Totman, A.M. Peters, M.J. Brookes, R. Coxon, P.G. Morris, M. Clemence, S.T. Francis, R. Bowtell, and P.A. Gowland, *Water Proton T1 Measurements in Brain Tissue at 7, 3 and 1.5T using IR-EPI, IR-TSE and MPRAGE: results and optimisation.* Magn. Reson. Mater. Phy, 2008. **21**: p. 121-130.
13. Look, D.C. and D.R. Locker, *Time saving in measurement of NMR and EPR relaxation times.* Rev. Sci. Instrum., 1970. **41**: p. 250-1.
14. Kaptein, R., K. Dijkstra, and C.E. Tarr, *Single-Scan Fourier Transform Method for Measuring Spin-Lattice Relaxation Times.* Journal of Magnetic Resonance, 1976. **24**(2): p. 295-300.
15. Young, I.R., A.S. Hall, and G.M. Bydder, *The design of a multiple inversion recovery sequence for T1 measurement.* Magnetic Resonance in Medicine, 1987. **5**(2): p. 99-108.
16. Brix, G., L.R. Schad, M. Deimling, and W.J. Lorenz, *Fast and Precise T1 Imaging Using a TOMROP Sequence.* Magnetic Resonance Imaging, 1990. **8**: p. 351-356.
17. Kay, I. and R.M. Henkelman, *Practical Implementation and Optimization of One-shot T1 imaging.* Magnetic Resonance in Medicine, 1991. **22**(2): p. 414-424.
18. Deichmann, R. and A. Haase, *Quantification Of T1 Values By Snapshot-FLASH NMR Imaging.* Journal of Magnetic Resonance, 1992. **96**(3): p. 608-612.
19. Gowland, P. and P. Mansfield, *Accurate Measurement Of T(1) In-Vivo In Less Than 3 Seconds Using Echo-Planar Imaging.* Magnetic Resonance in Medicine, 1993. **30**(3): p. 351-354.
20. Deichmann, R., *Fast high-resolution T1 mapping of the human brain.* Magnetic Resonance in Medicine, 2005. **54**(1): p. 20-27.
21. Shah, N.J., M. Zaitsev, S. Steinhoff, and K. Zilles, *A new method for fast multislice T-1 mapping.* Neuroimage, 2001. **14**(5): p. 1175-1185.
22. Chikui, T., K. Tokumori, R. Zeze, T. Shiraishi, T. Ichihara, M. Hatakenaka, and K. Yoshiura, *A fast Look-Locker method for T_1 mapping of the head and neck region.* Oral. Radiol., 2009. **25**: p. 22-29.
23. McKenzie, C.A., R.S. Pereira, F.S. Prato, Z. Chen, and D.J. Crost, *Improved contrast agent bolus tracking using T_1 FARM.* Mag. Res. Med., 1999. **41**: p. 429-435.
24. Schwarzbauer, C., J. Syha, and A. Haase, *Quantification of Regional Blood Volume by Rapid T1 Mapping.* Mag. Res. Med., 1993. **29**: p. 709-712.
25. Cunningham, C.H., J.M. Pauly, and K.S. Nayak, *Saturated Double-Angle Method for Rapid B_1+ Mapping.* Mag. Res. Med., 2006. **55**: p. 1326-1333.
26. Yarnykh, V.L., *Actual Flip-Angle Imaging in the Pulsed Steady State: A Method for Rapid Three-Dimensional Mapping of the Transmitted Radiofrequency Field.* Mag. Res. Med., 2007. **57**: p. 192-200.
27. Grenier, D., D. Pelletier, M. Normandeau, D. Newitt, S. Nelson, D.E. Goodkin, and S. Majumdar, *T2 Relaxation Time Histograms in Multiple Sclerosis.* Magnetic Resonance Imaging, 2002. **20**: p. 733-741.
28. Cox, E.F. and P. Gowland, *Simultaneous Quantification of T2 and T2' Using a Combined Gradient Echo-Spin Echo Sequence at Ultrahigh Field.* Mag. Res. Med., 2010. **64**: p. 1441-1446.
29. Asllani, I., A. Borogovac, and T.R. Brown, *Regression Algorithm Correcting for Partial Volume Effects in Arterial Spin Labeling MRI.* Magnetic Resonance in Medicine, 2008. **60**(6): p. 1362-1371.
30. Zur, Y., M.L. Wood, and L.J. Neuringer, *Spoiling of Transverse Magnetization in Steady-State Sequences.* Magnetic Resonance in Medicine, 1991. **21**: p. 251-263.
31. McRobbie, D.W., E.A. Moore, M.J. Graves, and M.R. Prince, *MRI: From Picture to Proton*. 2010, Cambridge: Cambridge University Press.
32. Sacolick, L.I., F. Wiesinger, I. Hancu, and M.W. Vogel, *B1 mapping by Bloch-Siegert shift.* Magnetic Resonance in Medicine. **63**(5): p. 1315-1322.
33. Lu, H., M. Law, G. Johnson, Y. Ge, P.C.M. van Zijl, and J.A. Helpern, *Novel approach to the measurement of absolute cerebral blood volume using vascular-space-occupancy magnetic resonance imaging.* Magnetic Resonance in Medicine, 2005. **54**(6): p. 1403-1411.
34. Moran, P.R., N.G. Kumar, N. Karstaedt, and S.C. Jackels, *Tissue contrast enhancement: Image reconstruction algorithm and selection of TI in inversion recovery MRI.* Magnetic Resonance Imaging, 1986. **4**(3): p. 229-235.
35. Huber, A., K. Bauner, B.J. Wintersperger, S.B. Reeder, F. Stadie, E. Mueller, M. Schmidt, E. Winnik, M.F. Reiser, and S.O. Schoenberg, *Phase-Sensitive Inversion Recovery (PSIR) Single-Shot TrueFISP for Assessment of Myocardial Infarction at 3 Tesla.* Investigative Radiology, 2006. **41**(2): p. 148-153.
36. Hou, P., K.M. Hasan, C.W. Sitton, J.S. Wolinsky, and P.A. Narayana, *Phase-Sensitive T1 Inversion Recovery Imaging: A Time-Efficient Interleaved Technique for Improved Tissue Contrast in Neuroimaging.* American Journal of Neuroradiology, 2005. **26**(6): p. 1432-1438.

37. Nelson, F., A.H. Poonawalla, P. Hou, F. Huang, J.S. Wolinsky, and P.A. Narayana, *Improved Identification of Intracortical Lesions in Multiple Sclerosis with Phase-Sensitive Inversion Recovery in Combination with Fast Double Inversion Recovery MR Imaging.* American Journal of Neuroradiology, 2007. **28**(9): p. 1645-1649.
38. Marques, J.P., T. Kober, G. Krueger, W. van der Zwaag, P.-F.o. Van de Moortele, and R. Gruetter, *MP2RAGE, a self bias-field corrected sequence for improved segmentation and T1-mapping at high field.* Neuroimage. **49**(2): p. 1271-1281.
39. Van de Moortele, P.-F., E.J. Auerbach, C. Olman, E. Yacoub, K. Ugurbil, and S. Moeller, *T1 weighted brain images at 7 Tesla unbiased for Proton Density, T2 contrast and RF coil receive B1 sensitivity with simultaneous vessel visualization.* Neuroimage, 2009. **46**(2): p. 432-446.

8 CONCLUSIONS

This thesis has outlined work exploring MRI techniques at ultra high field (7 T) to measure aspects of cerebral haemodynamics and to assess the underlying mechanisms. This chapter summarises the conclusions of work presented in this thesis and describing possible future work arising from these findings.

8.1 ARTERIAL SPIN LABELLING AT 7T

Chapter 5 described methodological development of arterial spin labelling for ultra high field imaging, concentrating on readout strategies and multi-phase ASL. It was demonstrated how 7 T allows for improved resolution 2D-EPI ASL which reduces partial volume effects and improves anatomical information of the cortical structure in perfusion images. 3D-EPI was optimised for high SNR and large slice coverage acquisition, whilst maintaining image quality and perfusion sensitivity. 3D-EPI ASL allows for large volume coverage, an advantage for whole brain studies e.g. resting state, pharmacological or patient studies. TFE and bFFE were demonstrated to be more robust to field inhomogeneities than 2D-EPI, with bFFE having higher SNR than TFE but being limited by SAR to only a single slice acquisition. These will be most useful when studying areas of the brain near the sinuses or other air interfaces. In addition, due to reduced spatial distortions when compared to EPI these can be more easily compared to other sequences (e.g. MPRAGE, FSE) for anatomical comparison such as tumours.

Look-Locker readout methods were shown to give temporal information to the vascular response (Δ_a and δ), which aided in functional tasks where transit times reduce or in pathology where the vascular structure is different to healthy controls. LL-EPI was used to measure arterial blood volume and the effect of a motor task on haemodynamic parameters. 7 T allows for high resolution aCBV maps to be acquired in less than 1 minute. Look-Locker TFE was applied in patients with Low Grade Gliomas where the increased temporal resolution allowed for identification of different vascular compartments compared to a single TI acquisition. Further development would investigate modelling the perfusion signal of 3D-EPI and TFE Look-Locker methods for CBF or CBVa quantification.

Future work should assess the reproducibility of these measurements. The possibility of ASL becoming a common alternative to contrast agent based

measures of blood flow requires robust, reliable techniques. These methods could then be applied to study perfusion differences between healthy controls and patient groups. ASL would be useful in the study of patients with renal disease, a contraindication of gadolinium based contrast agents. 7 T would allow the use of high resolution to maintain anatomical information and to improve upon previous ASL studies made at 1.5 and 3 T.

8.2 Effect of Hypercapnia on Brain Function

The Look Locker ASL methods developed in Chapter 5 were applied in the calibrated BOLD work presented in Chapter 6 which demonstrates that voxelwise implementation of the Davis model is feasible at 7 T. This allows for estimation of the change in $CMRO_2$ due to a motor task. $CMRO_2$ changes can be used to compare functional responses across subject groups where baseline haemodynamics may be different (e.g. caffeine studies or patients with Cerebrovascular disease). The voxelwise comparison showed a possible positive correlation between baseline blood flow and the calibration constant (M). Further work should concentrate on this relationship, as a surrogate metric for M which does not require a hypercapnic challenge would increase the applicability of calibrated BOLD. Further mapping of M, across further brain regions would be required to assess the spatial distribution to determine if this relationship holds in other brain areas, e.g. visual cortex.

The MEG study demonstrated a widespread change in MEG signal due to hypercapnia. However the mechanism behind this change is not fully understood and the impact on calibrated BOLD is also unknown. To probe the mechanism further a graded hypercapnia experiment would make it possible to determine if there is a component of perception to the MEG response as the desynchronisation was predominant around sensory/motor areas; applying levels of hypercapnia above and below the perception threshold would allow these two effects to be uncoupled.

The impact of MEG results on calibrated BOLD would depend on whether the MEG response is accompanied by a metabolic change, which would make the assumptions used in the Davis model [1] no longer valid. Magnetic resonance spectroscopy (MRS) could be used to probe the metabolic effects of hypercapnia, using carbon-13 or phosphorous-31 MRS. In addition; it has been shown that MEG responses can correlate with MRS metrics in the proton spectrum (e.g.

GABA [2]). Hence looking at the neurochemical effect of hypercapnia may help explain the origins of the MEG response and hence the full impact on models of calibrated BOLD.

8.3 LL-TFEPI: CBV AND PSIR

Look-Locker techniques were shown to give high resolution cerebral blood volume maps with the administration of a Gadolinium contrast agent using a B_1 independent measure of ΔR_1. In addition, Look-Locker TFE was shown to produce bias field corrected T_1 weighted images. Using the phase information the dynamic range of an inversion recovery image can be recovered and image inhomogeneities arising from the B_1 transmit field were removed by normalising to a reference image. Images with 0.6 mm isotropic resolution and whole head coverage were acquired in 12 minutes.

From the work in Chapter 7 it was seen that the standard B_1 mapping technique currently used on the 7 T system gave tissue weighting in the calculated B_1 maps. This means that they cannot be used to correct T_1 maps for the effect of the transmit field, which is essential for fast T_1 mapping techniques such as Look-Locker. Indications were that the problem was associated with spoiling of the transverse signal. Further work would concentrate on both improving the AFI method and the investigation of other B_1 mapping techniques such as the Bloch-Siegert shift [3]. This would benefit more sequences than T_1 mapping; it could aid in the modelling of ASL, specifically Look-Locker ASL where many RF pulses perturb the perfusion signal.

High resolution anatomical imaging with phase sensitive inversion recovery (PSIR) was optimised for 7 T imaging. It was demonstrated that PSIR would be beneficial in Multiple Sclerosis patients due to improvements in the visualisation of periventricular MS lesions. Further work applying the PSIR imaging technique in pathology, such as MS, and drawing comparison with standard anatomical imaging techniques such as MPRAGE would be beneficial. The PSIR developed here, is shown to be more easily interpreted than the MPRAGE sequence, which is often used for anatomical imaging and the improved anatomical information due to higher SNR and spatial resolution would make 7 T imaging attractive for clinical applications.

8.4 FINAL OVERVIEW

7 T MRI has developed significantly over the 11 years since the first human imaging study [4]. However there are still challenges associated with RF inhomogeneity, static field inhomogeneities and image distortions. In this thesis, developments were presented for arterial spin labelling, contrast agent monitoring and anatomical imaging that overcame some of these problems that arise at ultra-high field. This allows the advantages of 7 T, such as increased signal to noise, to be realised. Furthermore, these developments were applied to monitor functional brain activity, perfusion in healthy volunteers and those with Low Grade Gliomas, and CBV measurements in MS patients. Through such developments, 7 T imaging can be seen to be more clinically relevant.

8.5 REFERENCES

1. Davis, T.L., K.K. Kwong, R.M. Weisskoff, and B.R. Rosen, *Calibrated functional MRI: Mapping the dynamics of oxidative metabolism.* Neurobiology, 1998. **95**: p. 1834-1839.
2. Muthukumaraswamy, S.D., R.A. Edden, D.K. Jones, J.B. Swettenham, and K.D. Singh, *Resting GABA concentration predicts peak gamma frequency and fMRI amplitude in response to visual stimulation in humans.* PNAS, 2009. **106**(20): p. 8356-8361.
3. Sacolick, L.I., F. Wiesinger, I. Hancu, and M.W. Vogel, *B1 mapping by Bloch-Siegert shift.* Magnetic Resonance in Medicine. **63**(5): p. 1315-1322.
4. Vaughan, J.T., M. Garwood, C.M. Collins, W. Liu, L. DelaBarre, G. Adriany, P. Andersen, H. Merkle, R. Goebel, M.B. Smith, and K. Ugurbil, *7T vs. 4T: RF power, homogeneity, and signal-to-noise comparison in head images.* Magnetic Resonance in Medicine, 2001. **46**(1): p. 24-30.